The Influence of Alloying GeTe with Sn and Mn on Magnetic Interactions and Magnetotransport Effects

A dissertation
Submitted to the Institute of Physics of the
Polish Academy of Sciences (IP PAS)
in partial fulfillment of the requirements
for the degree of
doctor of philosophy

Submitted by
MSc. Abdul Khaliq
Principal supervisor: Dr hab. Łukasz Kilański
Auxiliary supervisor: Dr Andrei Avdonin
2023, Warsaw, Poland

ABSTRACT

Over the past several decades, rapid development based on metal-spintronics (utilizing both charge and spin of the carriers) has seen massive efforts which are associated with the detection of giant magnetoresistance phenomenon in thin metallic films [1,2]. Among a number of applications, several apparent uses are magnetic hard drives, random-access magnetic memories [3,4], race-track memories [5], spin-transfer nanooscillators [6], and many others. The pursuit to develop materials based on ferromagnetic semiconductors which could realize highly desirable semiconductor spintronic applications at room temperature has witnessed extensive research efforts. In addition to its metallic counterparts, semiconductor spintronics research is very promising due to several reasons e.g. spin-coherence times at room temperature are remarkably long and about three times longer in semiconductor spintronics than in metallic spintronics devices [7], motion of the spin-density packets in semiconductors is faster comparative to metals [8], electrical control of the ferromagnetic order is possible in semiconductors [9], among several others. The family of diluted magnetic semiconductors in which paramagnetic magnetic ions such as Mn are incorporated into semiconducting lattice was first coined in the mid twentieth century to integrate the electrical and magnetic characteristics of distinct materials into a common $A^{II}MnB^{VI}$ solid solution [10–12]. This was an important step towards inducing magnetic ordering in the semiconductor lattice via randomly placed Mn ions which would eventually lay foundation of semiconductor spintronics. This new materials design pioneered a vast research playground which rapidly expanded to state of the art compositions such as (II-VI) $Cd_{1-y}Mn_yTe$ [13], (III-V) $Ga_{1-y}Mn_yAs$ and $In_{1-y}Mn_yAs$ films [14,15], and others. In addition, the wide-gap (II-VI) and (III-V) oxides/nitrides incorporated with transition metals, e.g. $Zn_{1-y}Mn_yO$ [16] and $Ga_{1-y}Mn_yN$ [17], respectively, were developed. Apart from the above mentioned materials, the discovery of ferromagnetism in Mn doped narrow bandgap IV-VI semiconductors such as $Pb_{1-x-y}Sn_xMn_yTe$ [18], $Ge_{1-y}Mn_yTe$ [19] and $Sn_{1-y}Mn_yTe$ [20] provided more possibilities in regard to semiconductor spintronics research. One of the major milestones in regard to room temperature semiconductor spintronics has been the development of epitaxial growth of thin films such as $Ga_{1-y}Mn_yAs$ with ferromagnetic Curie temperature, $T_C \approx 200$ K obtained for these samples processed with the use of nanostructure patterning [21]. In addition, $Ge_{1-y}Mn_yTe$ epitaxial thin films have achieved ferromagnetic Curie temperature, $T_C = 200$ K for $y = 0.5$ which makes this IV-VI material very promising candidate for room temperature semiconductor spintronics [22].

In addition to ferromagnetic order, certain representatives of IV-VI materials with narrow bandgap, E_g such as GeTe ($E_g \approx 0.6 - 0.7$ eV) [23,24] and SnTe ($E_g \approx 0.18$ eV) [25] hold superior characteristics such as spontaneous ferroelectricity for GeTe occurring below $T \approx 720$ K that arises from low symmetry rhombohedral phase [24], whereas for layered SnTe, ferroelectric critical

temperature was enhanced from $T \approx 98$ K to room temperature [26], topological edge states were observed in SnTe [27], high temperature thermoelectric features of SnTe [28] and GeTe [29] are important from applications point of view, and control of spin-texture via ferroelectric polarization was achieved [30]. Owing to the above exciting features, IV-VI semiconductors alloyed with magnetic ions offer a wide range of possibilities to realize energy efficient semiconductor candidates for spintronics. Furthermore, the combination of ferromagnetic and ferroelectric orders can lead to Zeeman splitting and Rashba type splitting effects, respectively in a single system [31]. Therefore, diluted magnetic semiconductors such as $Ge_{1-x-y}Sn_xMn_yTe$ studied in this thesis offer exciting possibilities towards spectacular discoveries related to the interplay between electronic states, spin/orbital degrees of freedom, and coupling between ferroelectric and ferromagnetic orders [31].

In this thesis, comprehensive structural characterizations followed by state of the art magnetic and magnetotransport investigations of $Ge_{1-x-y}Sn_xMn_yTe$ crystals were executed. The foremost purpose of this thesis was centered on studying and tuning the magnetic order induced by paramagnetic “Mn” and diamagnetic “Sn” ions, low temperature charge scattering and localization phenomena. The increase of Sn content in $Ge_{1-x-y}Sn_xMn_yTe$ crystals caused transition from polar rhombohedral (R3m) symmetry distorted along $\langle 111 \rangle$ direction to coexistence of rhombohedral + rock salt (Fm-3m) phases and eventually to pure (Fm-3m) phase for high contents of Sn and Mn ions. In the low concentration limits of $y \leq 0.04$, the crystals behave like paramagnet down to liquid helium temperature. In the Sn-rich regime, $Ge_{1-x-y}Sn_xMn_yTe$ crystals demonstrated large variation in the nature of magnetic ordering. A magnetically disordered state depicting properties close to a canonical spin-glass was observed in the intermediate level of $y \approx 0.05$, cluster-glass state for $0.052 \leq y \leq 0.07$, and ferromagnetic order for higher Mn contents was observed. The appearance of a cluster-glass state can be justified by phenomenological laws using both static and dynamic magnetometric results. The spin-dynamics and potential barrier analysis demonstrate that the cluster-glass state constitute small size frozen ferromagnetic-like clusters with spin relaxation time just above the spin-glass limit. Double maxima in dynamic magnetic susceptibility observed for the crystal with $x \approx 0.2$, $y = 0.06$ manifested frequency dependent maximum at $T \approx 21.5$ K which shifts to higher values as frequency increases. The second maximum at $T \approx 8$ K is independent of variation in the frequency of the applied magnetic field. The frequency independent maximum might be attributed to ferromagnetic-like clusters. This variation in the behavior of susceptibility maxima over a few Kelvins reflects that the magnetic clusters might be of different sizes. The magnetic clusters switch from small (frequency dependent maximum) to comparatively large size which opposes any change in the susceptibility maximum on the temperature scale with frequency variation. Apart from that, the sublinear dependence of effective magnetic moment, μ_{eff} on the Mn concentration suggests that the tuning of magnetic interactions is influenced by both Mn and Sn contents. The appearance of ferromagnetic-like Mn clusters is responsible for the slow spin dynamics in the Sn rich crystals when a large fraction of Ge is replaced by Sn.

In the second part of the thesis, the magnetotransport studies of $Ge_{1-x-y}Sn_xMn_yTe$ crystals are presented in the temperature range, $T \approx 1.6 - 300$ K, as a function magnetic field up to $|H| = 130$ kOe. The scattering mechanisms responsible for temperature dependence of resistivity, $\rho_{xx}(T)$, and hole mobility, $\mu_h(T)$, are analyzed. For $Ge_{1-x-y}Sn_xMn_yTe$ crystals, the $\rho_{xx}(T)$ results take contributions from mixed scattering mechanisms such as phonons and polarons. Also, the $\mu_h(T)$ curves reveal phonon scattering of carriers with polar lattice optical modes with possible polaron-induced scattering at high temperatures. From high field magnetotransport data, the anomalous Hall resistivity is discussed with a modified scaling law to separate the residual and temperature dependent scattering mechanisms. Such analysis allows distinguishing between the parameters resulting from residual and phononic scattering processes related to skew scattering, and quadratic term emanating from side jump/intrinsic mechanism which cannot be obtained using conventional scaling.

ABSTRAKT

W ciągu ostatnich kilkudziesięciu lat szybki rozwój oparty na spintronice metali (wykorzystującej zarówno ładunek, jak i spin elektronów) był możliwy dzięki znacznym postępem wysiłki związanyme z wykrywaniem zjawiska gigantycznego magnetooporu w cienkich warstwach metalicznych [1,2]. Wśród wielu zastosowań kilka oczywistych to magnetyczne dyski twarde, pamięci magnetyczne o dostępie swobodnym [3,4], pamięci typu „race-track” [5], nanooscylatory z transferem spinu [6] i wiele innych. Dążenie do opracowania ferromagnetycznych materiałów półprzewodnikowych pracujących w temperaturze pokojowej, które mogłyby umożliwić realizację wysoce pożądanych zastosowań spintronicznych półprzewodników, było przedmiotem szeroko zakrojonych badań. Oprócz odpowiedników wśród metali badania nad spintroniką półprzewodników są bardzo obiecujące z kilku powodów, m.in. czasy koherencji spinu w temperaturze pokojowej są niezwykle długie i około trzy razy dłuższe w spintronice półprzewodnikowej niż w urządzeniach spintronicznych bazujących na metalach [7], ruch pakietów gęstości spinowej w półprzewodnikach jest szybszy w porównaniu do metali [8], elektryczne sterowanie uporządkowaniem ferromagnetycznym jest możliwy m.in. w półprzewodnikach [9]. Rodzina rozcieńczonych półprzewodników magnetycznych, w których paramagnetyczne jony magnetyczne, takie jak Mn, są wbudowane w sieć krystaliczną półprzewodnika, została po raz pierwszy utworzona w połowie XX wieku w celu zintegrowania właściwości elektrycznych i magnetycznych różnych materiałów w roztwór stały typu $A^{II}MnB^{VI}$ [10–12]. Był to ważny krok w kierunku wywołania uporządkowania magnetycznego w sieci półprzewodnikowej za pomocą losowo rozmieszczonych jonów Mn, co ostatecznie położyło podwaliny pod spintronikę półprzewodnikową. Ten nowy projekt materiałów zapoczątkował rozległy obszar badań, który szybko rozszerzył się na najnowocześniejsze materiały, takie jak cienkie warstwy grup pierwiastków (II-VI) $Cd_{1-y}Mn_yTe$ [13], (III-V) $Ga_{1-y}Mn_yAs$ i $In_{1-y}Mn_yAs$ [14,15] i innych. Ponadto opracowano tlenki/azotki o szerokiej przerwie energetycznej należące do grup (II-VI) i (III-V) zawierające metale przejściowe, np. $Zn_{1-y}Mn_yO$ [16] iczy też $Ga_{1-y}Mn_yN$ [17]. Oprócz wyżej wymienionych materiałów, odkrycie ferromagnetyzmu w domieszkowanych Mn półprzewodnikach IV-VI o wąskim paśmie wzbronionym, takich jak $Pb_{1-x-y}Sn_xMn_yTe$ [18], $Ge_{1-y}Mn_yTe$ [19] i $Sn_{1-y}Mn_yTe$ [20] dało więcej możliwości w zakresie badania spintroniki półprzewodników. Jednym z najważniejszych kamieni milowych w zakresie spintroniki półprzewodników mogących pracować w temperaturze pokojowej był rozwój epitaksjalnego wzrostu cienkich warstw, takich jak $Ga_{1-y}Mn_yAs$, z ferromagnetyczną temperaturą Curie, $T_C \approx 200$ K, uzyskiwaną dla tych próbek przetwarzanych z wykorzystaniem modelowania nanostruktur [21]. Ponadto cienkie warstwy epitaksjalne $Ge_{1-y}Mn_yTe$ osiągnęły ferromagnetyczną temperaturę Curie do

T_C = 200 K dla y = 0,5, co czyni ten materiał bardzo obiecującym kandydatem do spintroniki półprzewodników mogących pracować w temperaturze pokojowej [22].

Oprócz porządku ferromagnetycznego, niektórzy przedstawiciele materiałów IV-VI o wąskim pasmie wzbronionym, np. GeTe ($E_g \approx 0{,}6 - 0{,}7$ eV) [23,24] i SnTe ($E_g \approx 0{,}18$ eV) [25] posiadają interesujące właściwości, takie jak spontaniczna ferroelektryczność dla GeTe występująca poniżej $T \approx 720$ K, która powstaje z fazy romboedrycznej o niskiej symetrii [24], natomiast dla warstwowego SnTe ferroelektryczna temperatura krytyczna została podniesiona z $T \approx 98$ K do temperatury pokojowej [26], w SnTe zaobserwowano topologiczne stany brzegowe [27], wysokotemperaturowe właściwości termoelektryczne SnTe [28] i GeTe [29] są ważne z punktu widzenia zastosowań, a kontrolę tekstury spinu uzyskano poprzez polaryzację ferroelektryczną [30]. Dzięki powyższym ekscytującym cechom stopy półprzewodników IV-VI z jonami magnetycznymi oferują szeroką gamę możliwości w zakresie wytwarzania energooszczędnych półprzewodników do zastosowań w spintronice. Co więcej, połączenie uporządkowania ferromagnetycznego i ferroelektrycznych może prowadzić odpowiednio do efektów rozszczepienia Zeemana i rozszczepienia typu Rashby w jednym układzie [31]. Dlatego też rozcieńczone półprzewodniki magnetyczne, takie jak $Ge_{1-x-y}Sn_xMn_yTe$ badane w tej rozprawie, oferują ekscytujące możliwości w kierunku spektakularnych odkryć związanych z wzajemnym oddziaływaniem stanów elektronowych, spinowymi/orbitalnymi stopniami swobody oraz sprzężeniem między uporządkowaniem ferroelektrycznym i ferromagnetycznym [31].

W niniejszej rozprawie przeprowadzono kompleksową charaktetyzację strukturalną, a następnie szczegółowe badania właściwości magnetycznych i elektronowych kryształów $Ge_{1-x-y}Sn_xMn_yTe$. Najważniejszym celem tej pracy było zbadanie i pokazanie możliwości kontroli porządku magnetycznego indukowanego przez jony paramagnetyczne Mn i diamagnetyczne Sn, rozpraszanie nośników ładunków w niskiej temperaturze oraz zjawiska lokalizacji w niskich temperaturach. Wzrost zawartości Sn w kryształach $Ge_{1-x-y}Sn_xMn_yTe$ spowodował przejście od polarnej symetrii romboedrycznej (R3m) odkształconej w kierunku ⟨111⟩ do współistnienia faz romboedrycznych i soli kamiennej (Fm-3m) i ostatecznie do czystej fazy soli kuchennej (Fm-3m) dla najwyższych zawartości jonów Sn i Mn. W niskich granicach zawartości Mn $y \leq 0{,}04$ kryształy zachowują się jak paramagnetyki aż do temperatury ciekłego helu. W kryształach Ge1–x–ySnxMnyTe o znacznej zawartości Sn wykazywały duże zróżnicowanie natury uporządkowania magnetycznego. Zaobserwowano stan magnetycznie sfrustrowany o właściwościach zbliżonych do kanonicznego szkła spinowego na poziomie pośrednim $y \approx 0{,}05$, stan szkła klasterowego dla $0{,}052 \leq y \leq 0{,}07$, a porządek ferromagnetyczny przy wyższych zawartościach Mn. Pojawienie się stanu szkła-klasterowego można uzasadnić prawami fenomenologicznymi, wykorzystując zarówno statyczne, jak i dynamiczne wyniki magnetometryczne. Analiza dynamiki spinów i bariery potencjału pokazuje, że stan szkła-klasterowego składa się z małych zamrożonych klastrów przypominających ferromagnetyki, z czasem relaksacji spinu tuż powyżej granicy szkła spinowego. Podwójne maksima dynamicznej podatności magnetycznej obserwowane dla kryształu o $x \approx 0{,}2$, $y = 0{,}06$ objawiały się maksimum zależnym od częstotliwości przy $T \approx 21{,}5$ K, które przesuwa się do wyższych wartości wraz ze wzrostem częstotliwości. Drugie maksimum w $T \approx 8$ K jest niezależne od zmian częstotliwości przyłożonego pola magnetycznego. Maksimum niezależne od częstotliwości można przypisać klastrom podobnym do ferromagnetycznych. Ta zmiana w zachowaniu maksimów podatności dla kilku Kelvinów odzwierciedla, że klastery magnetyczne mogą mieć różne rozmiary. Klastery magnetyczne zmieniają się z małych (maksimum podatności magnetycznej zależne od częstotliwości) do stosunkowo dużych rozmiarów, co przeciwdziała wszelkim zmianom maksimum podatności w skali temperatury wraz ze zmianami częstotliwości. Poza tym subliniowa zależność efektywnego momentu magnetycznego μ_{eff} od stężenia Mn sugeruje, że na kontrolę oddziaływań magnetycznych wpływa zarówno zawartość Mn, jak i Sn. Pojawienie się ferromagnetycznych klastrów Mn jest odpowiedzialne za powolną dynamikę spinów w kryształach bogatych w Sn.

W drugiej części pracy przedstawiono badania magnetotransportu kryształów $\mathrm{Ge}_{1-x-y}\mathrm{Sn}_x\mathrm{Mn}_y\mathrm{Te}$ w zakresie temperatur $T \approx 1{,}6 - 300$ K, w funkcji pola magnetycznego do $|H| \leq 130$ kOe. Analizowane są mechanizmy rozpraszania odpowiedzialne za zależność rezystywności $\rho_{xx}(T)$ od temperatury i ruchliwość dziur przewodnictwa $\mu_h(T)$. W przypadku kryształów $\mathrm{Ge}_{1-x-y}\mathrm{Sn}_x\mathrm{Mn}_y\mathrm{Te}$ wyniki $\rho_{xx}(T)$ uwzględniają udział mieszanych mechanizmów rozpraszania, takich jak fonony i polarony. Krzywe $\mu_h(T)$ ujawniają również rozpraszanie fononowe nośników ładunku z modami optycznymi sieci polarnej z możliwym rozpraszaniem indukowanym polaronem w wysokich temperaturach. Na podstawie danych dotyczących magnetotransportu w silnych polach magnetycznych omówiono anomalną oporność Halla ze zmodyfikowanym prawem skalowania w celu oddzielenia mechanizmów rozpraszania resztkowego i zależnego od temperatury. Taka analiza pozwala na rozróżnienie parametrów wynikających z procesów rozpraszania resztkowego i fononowego związanych z rozpraszaniem skośnym oraz składnika kwadratowego pochodzącego z mechanizmu przeskoku bocznego lub mechanizmu wewnętrznego, którego nie można uzyskać przy użyciu konwencjonalnego skalowania.

Acknowledgements

In making the completion of this thesis possible, first and foremost I would like to thank my supervisor Łukasz Kilański and an honor for being his first Ph.D. student. He consistently and very generously taught me all the way through my doctoral program at the Institute of Physics, Polish Academy of Sciences. I very much appreciate his friendly supervision and plentiful time at each and every phase during this Ph.D. program. I am thankful for his contributions during experimental work even on weekends, data analysis and interpretation. He has well-mentored both my personal and professional skills in continuing my efforts to become a better academic. I am grateful to my auxiliary supervisor Andrei Avdonin who contributed generously during the analysis of experimental results. The support from both my supervisor and auxiliary supervisor has been amazing through this journey whenever I needed.

I am also thankful to the other group members Monika Arciszewska, Beata Brodowska and Sana Zakar who contributed in completing essential parts of this thesis. Monika worked consistently in executing a large part of the magnetometric measurements. I would like to thank Vasyl E. Slynko who prepared the crystals studied in this thesis at the Institute of Materials Science Problems, Ukrainian Academy of Sciences. I might not have completed this thesis without the support of Roman Minikayev from Applied Crystallography Group (SL1.3) who contributed to the structural part of this thesis. I would like to acknowledge the contributions of Sabina Lewińska and A. Ślawska-Waniewska (ON3.5) for their support in obtaining part of the magnetometric results and helpful discussion. In executing both magnetometric and magnetotransport experiments, I thank the members of cryogenic department at Institute of Physics, Polish Academy of Sciences who provided us liquid helium well on time.

Besides my amazing colleagues, I have come a long way having significant support and encouragement of my family. I must gratefully recognize the years-long support and grooming my parents poured on me. During the entire Ph.D. program, I can’t appreciate enough my wife, Saikal Kushubekova who stood tall and patiently cheered my work. I proudly dedicate this work to my little son Kadir Khaliq.

Finally, I appreciate and acknowledge National Science Centre, Poland for financially supporting my Ph.D. program under the project number 2018/30/E/ST3/00309.

Abdul Khaliq
Institute of Physics
Polish Academy of Sciences
(2023)

List of publications during Ph.D. program

This thesis was designed with the original and partial content from the following publications concluded at the Institute of Physics of the Polish Academy of Sciences.

1. A. Khaliq, R. Minikaev, S. Zakar, M. Arciszewska, A. Avdonin, V. E. Slynko, and L. Kilanski, Extrinsic anomalous Hall effect in Mn doped GeSnTe semiconductors in the bad-metal hopping regime, *J. Alloy. Compd.* **976**, 172902 (2023).
2. A. Khaliq, P. Dziawa, B. C. Camargo, S. Lewińska, R. Minikaev, S. Zakar, A. Reszka, A. Avdonin, A. Ślawska-Waniewska, J. Szczytko, and L. Kilanski, Magnetic interactions and high-field magnetotransport properties of Ge$_{1-x-y}$(Sn$_x$Mn$_y$)Te epitaxial layers, *J. Magn. Magn. Mater.* **587**, 171257 (2023).
3. A. Khaliq, S. Lewińska, R. Minikaev, M. Arciszewska, A. Avdonin, B. Brodowska, V. E. Slynko, A. Ślawska-Waniewska, and L. Kilanski, Magnetic phase diagram of Ge$_{1-x-y}$(Sn$_x$Mn$_y$)Te multiferroic semiconductors: Coexistence of ferromagnetic and cluster glass ordering, *J. Alloy. Compd.* **968**, 171893 (2023).
4. A. Khaliq, P. Dziawa, R. Minikaev, M. Arciszewska, A. Avdonin, B. Brodowska, and L. Kilański, Low temperature weak anti-localization effect in the GeTe and SnTe epitaxial layers, *Acta Physica Polonica A* **142**, 657 (2022).
5. A. Khaliq, R. Minikayev, M. Arciszewska, A. Avdonin, B. Brodowska, A. Khan, V. E. Slynko, E. I. Slynko, and L. Kilanski, Spin-glass like magnetic ordering in Ge$_{1-x-y}$(Sn$_x$Mn$_y$)Te multiferroics, *J. Magn. Magn. Mater.* **544**, 168695 (2022).
6. L. Kilanski, M. Arciszewska, A. Khaliq, B. Brodowska, R. Minikayev, and V. E. Slynko, Magnetic exchange constant and ferroelectric anomaly in magnetic susceptibility in Sn$_{1-x-y}$Si$_x$Mn$_y$Te diluted magnetic semiconductors, *Acta Physica Polonica A* **141**, 161 (2022).
7. L. Kilanski, S. Lewińska, A. Khaliq, R. Minikaev, A. Reszka, A. Ślawska-Waniewska, B. J. Kowalski, T. R. Arslanov, and S. F. Marenkin, From ferromagnetic to helical order with a discussion of the low-temperature antiferromagnetism in composite Cd$_{1-x}$Mn$_x$GeP$_2$+MnP semiconductors, *Phys. Rev. B* **104**, 184430 (2021).
8. L. Kilanski, M. Górska, A. Khaliq, F. Bartosik, M. Arciszewska, A. Podgórni, R. Minikayev, B. Brodowska, A. Reszka, B. J. Kowalski, V. E. Slynko, and E. I. Slynko, Magnetic interactions in Ge$_{1-x}$Eu$_x$Te semiconductors: random distribution of magnetic Eu ions vs spinodal decompositions, *Mater. Res. Express* **7**, 036103 (2020).

List of publications before Ph.D. program

9 I. Muhammad, U. Younis, H. Xie, A. A. Khan, A. Khaliq, A. Samad, U. Schwingenschlogl, and Q. Sun, Borophene-based three-dimensional porous structures as anode materials for alkali metal-ion batteries with ultrahigh capacity, *Chem. Mater.* **33**, 2976 (2021).

10 I. Muhammad, U. Younis, W. Wu, H. Xie, A. Khaliq, and Q. Sun, Three-dimensional porous phosphorus-graphdiyne as a universal anode material for both K- and Ca-ion batteries with high performance, *J. Power Sources*, **480**, 228876 (2020).

11 M. H. Saeed, S. Ahmed, I. Muhammad, I. Murtaza, A. Ghani, A. Ali, R. Abdullah, and A. Khaliq, Molybdenum carbide nano-sheet as a high capacity anode material for monovalent alkali metal-ion batteries-theoretical investigation, *Physics Letters A* **384**, 126688 (2020)**.**

12 M. Sheeraz, A. Khaliq, A. Ullah, H. S. Han, A. Khan, A. Ullah, I. W. Kim, T. H. Kim, and C. W. Ahn, Stress driven high electrostrain at low field in incipient piezoelectrics, *J. Eur. Ceram. Soc.* **39**, 4688 (2019).

13 M. Sheeraz, H. J. Kim, K. H. Kim, J. S. Bae, A. Y. Kim, M. Kang, J. Lee, J. Song, A. Khaliq J. Kim, B. G. Cho, S. Y. Joe, J. H. Jung, J. H. Ko, T. Y. Koo, T. W. Noh, S. Cho, S. Lee, S. M. Yang, Y. H. Shin, I. W. Kim, C. W. Ahn, and T. H. Kim, Enhanced ferroelectricity in perovskite oxysulfides, *Phys. Rev. Materials* **3**, 084405 (2019).

14 A. Khaliq, M. Sheeraz, A. Ullah, H. J. Seog, C. W. Ahn, T. H. Kim, S. Cho, and I. W. Kim, Ferroelectric seeds-induced phase evolution and large electrostrain under reduced poling field in bismuth-based composites, *Ceram. Int.* **44**, 13278 (2018).

15 A. Tange, H. S. Kim, A. Khaliq M. Sheeraz, and I. W. Kim, Relaxor-type ferroelectric behavior of $(1-x)Bi_{0.5}(Na_{0.78}K_{0.22})_{0.5}TiO_3xBi(Cu_{0.5}Ti_{0.5})O_3$ lead-free piezoelectric ceramics, *Sci Adv Mater.* **10**, 262 (2018).

16 A. Khaliq, M. Sheeraz, A. Ullah, J. S. Lee, C. W. Ahn, and I. W. Kim, Large strain in $Bi_{0.5}(Na_{0.78}K_{0.22})_{0.5}TiO_3$-$Bi(Mg_{0.5}Ti_{0.5})O_3$ based composite ceramics under low driving field, *Sens. Actuator A: Phys.* **258**, 174 (2017).

Conference presentations during Ph.D. program

1 High field magnetotransport study of $Ge_{1-x-y}Sn_xMn_yTe$ layers, oral presentation at the 13th Joint European Magnetic Symposia (JEMS), Madrid, Spain Aug 27–Sep 01, 2023.

2 Magnetic interactions and high-field magnetotransport properties of $Ge_{1-x-y}Sn_xMn_yTe$ epitaxial layers, oral presentation at the European Conference Physics of Magnetism (PM'23), Poznań, Poland June 26–30, 2023.

3 Low temperature weak anti-localization effect in GeTe–SnTe epitaxial layers, oral presentation at XIV Symposium of PhD Students (IFPAS), Sep 19–20, Zegrze, Poland, 2022.

4 Spin-glass state and Almeida-Thouless line observation in $Ge_{1-x-y}Sn_xMn_yTe$ multiferroics, oral presentation at the Joint European Magnetic Symposia (JEMS), Warsaw, Poland, July 24–29, 2022.

5 Weak localization effect in $Ge_{1-x}Sn_xTe$ epitaxially grown ferroelectric semiconductors, poster presentation at the 50th International School & Conference on the Physics of Semiconductors, Jaszowiec, Szczyrk, Poland, June 4–10, 2022.

6 Spin-glass like magnetic ordering in $Ge_{1-x-y}Sn_xMn_yTe$ diluted magnetic semiconductors, oral presentation at XIII Symposium of PhD Students (IFPAS), Dec 13–15, 2021.

7 Magnetic ordering in $Ge_{1-x-y}Sn_xMn_yTe$ multiferroics, oral presentation at the European School and conference on Magnetism, Romania, Sep 6–17, 2021.

8 Magnetic ordering and frustration in $Ge_{1-x-y}Sn_xMn_yTe$ multiferroic crystals, oral presentation at the 49th International School & Conference on the Physics of Semiconductors, Jaszowiec, Poland Sep 1–10, 2021.

9 Frustrated magnetic ordering in $Ge_{1-x-y}Sn_xMn_yTe$ multiferroics, oral presentation at the European Conference Physics of magnetism (PM'21), Poznań, Poland June 28–July 2, 2021.

Conference presentations before Ph.D. program

10 Tandem organic solar cells with improved electron transport layer, poster presentation at International Conference on Science and Technology of Synthetic Metals, Busan, South Korea July 1–6, 2018.

11 High conductive ZnO as an electron transport layer in organic tandem cells, poster presentation at Korea Polymer Society (KPS), Daejeon, South Korea April 4–6, 2018.

12 HUST-UOU Workshop on Materials Physics, University of Ulsan, South Korea Feb 27, 2018.

13 Large electromechanical response in $Bi_{0.5}(Na_{0.78}K_{0.22})_{0.5}TiO_3$–$Bi(Mg_{0.5}Ti_{0.5})O_3$ based piezoelectric composites, poster presentation at the Brain Korea (BK21) Regional Meeting, Busan, South Korea, Dec 27–28, 2017.

14 Large strain under low driving field obtained in $Bi_{0.5}(Na_{0.78}K_{0.22})_{0.5}TiO_3$–$Bi(Mg_{0.5}Ti_{0.5})O_3$ piezoelectrics, poster presentation at the 11th Korea-Japan Conference on Ferroelectrics, Seoul South Korea, August 7–10, 2016.

15 $Bi_{0.5}(Na_{0.78}K_{0.22})_{0.5}TiO_3$ seeds driven electromechanical response in relaxor ferroelectrics, poster presentation at the Korean Physical Society (KPS) Daejeon, Korea April 20–22, 2016.

16 0-3 type relaxor ferroelectric composites for actuator applications, poster presentation at the National Conference on Dielectrics, Muju, Korea Jan 31–Feb 2, 2016.

17 Piezoelectric solid solutions based on $Bi_{0.5}(Na_{0.78}K_{0.22})_{0.5}TiO_3$ ferroelectric seeds, poster presentation at the Regional Conference on Advancement of Materials, Dong-A University Busan, Korea, Dec 12, 2015.

18 High strain produced by ferroelectric seeds in relaxor matrix, poster presentation at the 3rd International Conference on Advanced Electromaterials, ICC Jeju Korea Nov17–20, 2015.

19 Influence of ferroelectric nucleation on the electromechanical response of relaxor type ferroelectrics, poster presentation at the Korean Physical Society, Gyeongju South Korea, October 2015.

20 Days Joint Korea-Vietnam Workshop on Material Physics, University of Ulsan, Korea August 2015.

21 National Symposium on “Frontiers in Physics” University of Peshawar Pakistan Jan-2013.

List of symbols

a — Edge length of crystallographic unit cell along x-axis

a_{sk} — Coefficient of skew scattering mechanism

α — Angle between lattice constant, a, and c

A — Coefficient related to crystalline defects or leakage

B — Coefficient related to magnetocrystalline anisotropy

B_M — Molecular field

b_{sj} — Coefficient of side jump mechanism

b/a_0 — Radius of potential well

$B_{\mathrm{S}}(\zeta)$ — Modified Brillouin function

c — Edge length of crystallographic unit cell along z-axis

C — Curie-Weiss constant

$d\Omega/4\pi$ — Fractional value of the fluorescent x-ray directed towards the detector

E — Electric field

E_b — Hole binding energy

E_{ex} — Exchange splitting energy

E_g — Bandgap energy

E_{F} — Fermi level

E_{S} — Energy of the singlet state

E_{T} — Energy of the triplet state

E_a/k_B — Potential barrier between two easy magnetic orientations

ΔE_{DX} — Energy gained during exchange interaction

Δ_{eff} — Energy difference between d^4/d^5 level and valence band

f — Frequency of magnetic field

Φ — Exponent related to De Almeida-Thouless equation

Φ_{f} — Angle of reflection of the fluorescent X–ray beam

φ — Incident angle of the primary X–ray beam

g — Lande spin splitting factor

g_L — Fractional value of the measured line of the sample

γ — Parameter related to phonon scattering

$\mathit{\Gamma}$ — Effective factor related to exchange integral

H — Magnetic field

H_{C} — Coercive field/Coercivity

$\widehat{\mathcal{H}}$ — Hamiltonian for the magnetic exchange interaction

I — Electric current

I_L — Line intensity of the composition to be measured

I_0 — Intensity of the primary beam with an effective wavelength, λ_{pri}

J — Magnetic exchange constant

J_L — Total angular momentum

k_B — Boltzmann constant

k_F — Fermi wave vector

κ — Slope of the power law for resistivity

χ_{AC} — AC magnetic susceptibility

χ'_{AC} — Real component of the AC magnetic susceptibility

χ''_{AC} — Imaginary component of the AC magnetic susceptibility

l_{SO} — Spin orbit scattering length

l_{φ} — Phase coherence length

Δl — Lateral displacement of charge carriers during side jump scattering

λ — Wavelength of x-rays

λ_W — Coefficient of Weiss molecular field

λ_d — Exponential damping factor

λ_M — Molecular field constant

λ_{pri} — Effective wavelength of the primary x-ray beam

λ_L — Wavelength of the measured line of the composition

M — Magnetization

M_R — Remnant magnetization/Remanence

M_S — Saturation magnetization

μ — Magnetic moment

μ_B — Bohr magneton

μ_{eff} — Effective magnetic moment

μ_h — Charge carrier mobility

$\mu_{\mathrm{A}}(\lambda_{pri})$ — Mass absorption coefficient of the composition A for λ_{pri}

$\mu_{\mathrm{M}}(\lambda_{pri})$ — Mass absorption coefficient of the matrix for λ_{pri}

$\mu_{\mathrm{M}}(\lambda_L)$ — Mass absorption coefficient of the matrix for λ_L related to the sample

m^* — Effective mass of band carrier

N_0 — Number of cation sites per gram

N_{C} — Coordination number

$N_0\alpha$ — Exchange integral arising from *s*-*d* exchange interaction
n_h — Charge carrier concentration
R — Mydosh parameter/Scaling parameter
R_H — Ordinary Hall coefficient
R_S — Anomalous Hall coefficient
r_A — Absorption edge jump ratio of the sample
ρ_{xx} — Longitudinal resistivity tensor component
ρ_{xy} — Transverse resistivity tensor component
ρ_{xx0} — Residual resistivity
ρ_AH — Anomalous Hall resistivity
$\rho(\varepsilon_\mathrm{F})$ — Density of states at the Fermi level
S — Spin quantum number
$\vec{S}_{i,j}$ — Spin operator of the band carrier
$\vec{S}_L$ — Spin operator of state L
σ_{xx} — Longitudinal conductivity tensor component
σ_AH — Anomalous Hall conductivity
$\varPsi$ — Wavefunction
T_C — Curie temperature
T_N — Néel temperature
T_Irr — Irreversibility temperature
T_g — Spin glass transition temperature
T_{cg} — Cluster glass transition temperature
T_0 — Vogel-Fulcher temperature
T^* — Figure of merit of magnetic clustering
T_F — Spin freezing temperature
T_max — Temperature of the mobility maxima
T_min — Temperature of the maxima in charge carrier concentration
t — Thickness of Hall bar
t_h — Hopping matrix element
τ — Spin relaxation time
θ — Angle between the incoming X–ray beam and crystal planes
Θ — Curie-Weiss temperature
U_eff — Correlation energy
V_{xx} — Longitudinal voltage

V_{xy} — Hall voltage

$V_{(r)}$ — Potential of a square well

v_n — Number of valleys in the band structure

w — Width of Hall bar

x — Concentration of Sn ions

y — Concentration of Mn ions

y_θ — Effective Mn content

z — Concentration of other alloying ions

z_{ij} — Number of nearest neighbors

List of acronyms

AHE — Anomalous Hall effect

AT line — De Almeida-Thouless line

BF — Brillouin function

CG — Cluster glass

DMS — Diluted magnetic semiconductor

DOS — Density of states

DVM — Digital voltmeter

EDXRF — Energy dispersive X-ray fluorescence

FC — Field-cooled magnetization

FM — Ferromagnet

Fm-3m — Rocksalt crystal symmetry

GMR — Giant magnetoresistance

HRXRD — High resolution X-ray diffraction

MR — Magnetoresistance

MRAM — Magnetoresistive random access memory

OHE — Ordinary Hall effect

PM — Paramagnet

PL — Power law

PPMS — Physical property measurement system

RKKY — Ruderman–Kittel–Kasuya–Yosida interaction

R3m — Rhombohedral symmetry

SC — Semiconductors

SG — Spin glass

SJ — Side jump

SS — Skew scattering
SOI — Spin orbit interaction
TM — Transition metal
VSM — Vibrating sample magnetometer
WL — Weak localization
WAL — Weak anti–localization
ZFC — Zero-field-cooled magnetization

Table of Contents

CHAPTER 1

Background and Scope of the Thesis

1.1 Introduction

Global technological needs have sharply surged since the introduction of computing devices over the past several decades. Particularly, the size and efficiency of the electronic devices such as computers have been an active research theme which has witnessed tremendous development till today. The invention of transistor and its continuous miniaturization with advanced capabilities have revolutionized modern electronics. For the past several years, there have been extensive efforts to develop new functional materials which could bring together the computing and storage capabilities in a single system, thus replacing the previously used components with advanced multifunctional materials. In this sense, search for new materials that could integrate the semiconducting (computing power) and magnetic (information storage) characteristics in a single material is essential. This active research area known as spintronics has seen persistent work by scientists and technologists to overcome the issues which are causing hindrance in the implementation of such future devices. However; the successful development of such multifunctional semiconducting materials has not been reported yet due to several obstacles. One such problem in the advancement of semiconductor (SC) spintronics materials is the lack of functionality at room temperature e.g. low ferromagnetic Curie temperature. The material with highest Curie temperature in IV-VI group so far is $Ge_{1-y}Mn_yTe$ semimagnetic semiconductor which has upper functional temperature of about 200 K, far lower than the required room temperature functionality in real world devices. The exploitation of carrier's spin property may realize an efficient new class of spintronic devices with capabilities such as non-volatile memory, higher information processing speed and lower energy consumption.

Since conventional electronic devices are based on the electronic charge and transport, these devices have functional limit in enhancing the processing speed and transistor density. This indication of eventually moving towards saturated performance of the existing materials demands the development of new class of efficient alternatives. In that context, materials which offer manipulation of both electrical charge and spin offer new prospects to develop novel quantum materials for spintronics applications. In order to realize semiconductor spintronics materials with enhanced functional capabilities, two broad research areas have been instrumental; nonmagnetic semiconductors in which scientists concentrate on the studies of spin-related phenomena e.g. spin manipulation and transport, spin polarization, and the spin Hall effect among many others [32–37].

The second active research domain is related to the integration of ferromagnetism and electrical characteristics of a SC by introducing small fraction of magnetic ions as dopants in semiconductor matrix. These desired quantum materials propose a possible direction to develop hybrid devices which could perform several operations such as communication, logic and storage, achieved by the same material's technology.

The search for spintronic materials has witnessed substantial diversity in the context of materials' choice. For example, metallic spintronics which has achieved great success after the discovery of giant magnetoresistive (GMR) [1,2] effect in 1988 in magnetic systems consisting of alternating layers of ferromagnetic and diamagnetic materials. The discovery of GMR greatly enhanced the performance of memory devices like magnetoresistive random access memory (MRAM) [3,4]. Dieny *et al*., [38] detected very large magnetoresistive effect in uncoupled ferromagnetic layers which they named as spin valve. The spin-valve phenomenon was attributed to the presence of nonzero relative angle between the magnetizations associated with two ferromagnetic layers. The above giant magnetoresistive phenomena resulting in spin dependent scattering can be understood by presuming that the spin current can be represented by spin-up and spin-down carriers [38]. Proposed by Mott [39], such two-channel depiction of spin transport explains well the behaviour of devices based on magnetoresistance such as GMR and tunneling magnetoresistance [40,41]. The development of metallic spintronics has been particularly fast as the realization of commercial devices took about one decade after the discovery of breakthrough phenomena on which these devices are based [42].

In addition to metallic spintronics, the emergence of semiconductor spintronics has attracted plentiful of efforts due to the compatibility of these materials with the existing commercial electronic devices which are based on semiconductors. Metallic spintronics devices store data in metal-built magnetic devices which has to be sent and then processed in semiconductor based processor. This costs both energy and time which could be minimized if same types of materials were used for both data storage and processing. Therefore, transition from metallic to semiconductor-based spintronics is essential to realize more efficient electronic devices. Semiconductors allow manipulating carrier density by introducing dopants, capable of tuning bandgap and importantly, longer spin-coherent times have been demonstrated in SC compared to their metallic counterparts [7,43]. Semiconducting spintronics has also seen rapid progress which produced new devices based on the carrier spin i.e. spin field effect transistor [44], spin light emitting diodes [45,46], spin resonant tunneling devices [47] and development of quantum bits desired for applications such as quantum computation [48]. Semiconductor spintronics also offer possibilities which are very unlikely to appear in their metallic counterparts e.g. depletion of charge density which is exceptionally challenging approach in case of metals.

In this regard, a large number of diluted magnetic semiconductors have been studied during the last 5 decades such as II-VI, III-V and IV-VI compounds. In contrast to III-V and II-VI based ferromagnetic semiconductors, narrow gap $IV_{1-y}Mn_yVI$ (for example $Ge_{1-y}Mn_yTe$) [49,50] offer advantages over III-V and II-VI based compounds due to an independent control of charge (hole) density since Mn^{2+} dopant is isoelectric to Ge. The narrow bandgap ($E_g \approx 0.6$ to 0.7 eV) [23,24] crystalline α-GeTe is a degenerate semiconductor which possesses high intrinsic charge (hole) density $\approx 10^{20} - 10^{21}$ cm^{-3} owing to the native cation vacancies [23,51]. Furthermore, the incorporation of Mn ions in GeTe lattice is high and can reach up to 95 % [52] which provides great opportunities to manipulate ferromagnetic order and tune the ferromagnetic transition temperature. Ferromagnetic order in materials such as $Ge_{1-y}Mn_yTe$ is carried by charge carriers which can be manipulated either by external magnetic or electric fields [53]. Ferromagnetic transition temperature remains below room temperature in these materials and therefore has been a hindrance to use these materials in SC spintronics devices. In order to tune the ferromagnetic transition temperature, several works have shown improved outcomes such as $T_C \approx 150$ K for bulk $Ge_{1-y}Mn_yTe$ with $y = 0.5$, [19], T_C of 140 K with $x = 0.51$ [52,54] for thin films of $Ge_{1-y}Mn_yTe$, $T_C = 90$ K with $y = 0.5$ for $Ge_{1-y}Mn_yTe$ films prepared by radio frequency sputtering [50], and $T_C = 200$ K for $Ge_{1-y}Mn_yTe$ thin films with $y = 0.5$ [22]. Although previous works focused over $Ge_{1-y}Mn_yTe$ indicate highest T_C values around $x = 0.5$, it is important to investigate these desired materials considering advanced growth techniques and conditions in the entire range of alloying concentration.

The incorporation of Mn into IV-VI materials provides possibilities to introduce and manipulate ferromagnetic order which makes such materials superior over nonmagnetic semiconductor based spintronics candidates. Owing to the intriguing features of IV-VI SC materials presented above, this thesis is an attempt to study the magnetic and magnetotransport phenomena of Mn alloyed $Ge_{1-y}Sn_yTe$ semiconductors. This family of IV-VI narrow-gap materials also manifests spontaneous ferroelectric polarization due to the distorted rhombohedral crystal. The parent compound α-GeTe sustains spontaneous electric polarization up to $T \approx 720$ K. The ferroelectric Curie temperature drops with the increase of Sn and Mn contents in α-GeTe. For $Ge_{1-x-y}Sn_xMn_yTe$ crystals studied in this thesis, the spontaneous ferroelectric polarization occurs above room temperature up to $x + y \leq 0.45$ [55].

Although carrier mediated ferromagnetism [56] and magnetotransport studies [57] in $Ge_{1-x-y}Sn_xMn_yTe$ crystals have been performed in the past, though the published results on this material are limited. Since ternary $Ge_{1-y}Mn_yTe$ and quaternary $Ge_{1-x-y}Sn_xMn_yTe$ are less explored compositions compared to their II-VI and III-V counterparts, this work is an attempt to analyze the carrier mediated indirect magnetic exchange interaction in a range of $Ge_{1-x-y}Sn_xMn_yTe$ alloys. In this thesis, the alloying concentration of Sn was significantly enhanced to about $x = 0.8$. These crystals with high Sn concentration were studied in order to investigate its influence on both magnetic ordering and electron transport phenomena. Magnetic studies of $Ge_{1-x-y}Sn_xMn_yTe$ crystals can probe important correlation between the concentration of alloying elements and magnetic parameters such as magnetic exchange constant, and type of magnetic order. These investigations of $Ge_{1-x-y}Sn_xMn_yTe$ crystals are aimed to lead to understanding the magnetic order in entire range of Sn content from 0 to 1. Such understanding can then help to tune the exchange coupling between magnetic ions. Furthermore, extensive electron transport studies of $Ge_{1-x-y}Sn_xMn_yTe$ crystals can provide details about charge scattering which arise either from impurities or lattice vibrations (phonons). Detailed magnetotransport enabled requiring knowledge about the origin of anomalous Hall resistivity, magnetoresistance and charge localization phenomena in $Ge_{1-x-y}Sn_xMn_yTe$ crystals.

1.2 Aim of the Thesis

This thesis is aimed to study the quaternary $Ge_{1-x-y}Sn_xMn_yTe$ alloys incorporated with a broad range of Sn and Mn ions in order to gather comprehensive understanding of the magnetic interactions and electron transport phenomena. In the first part, carrier mediated ferromagnetic order was investigated both in Ge-rich and Sn-rich $Ge_{1-x-y}Sn_xMn_yTe$ samples. Particularly, since the magnetic and magnetotransport studies of $Ge_{1-x-y}Sn_xMn_yTe$ crystals are unknown in Sn-rich regime, this thesis is aimed to explore the influence of high Sn concentration on magnetic and transport phenomena.

- Wide variation in Sn concentration between 0 and 1 is anticipated to tune the lattice dimensions of $Ge_{1-x-y}Sn_xMn_yTe$ crystals which in turn can alter the Mn – Mn bond length and hence influence magnetic interactions. Also, Mn content was varied from 0.02 to 0.09 in an attempt to probe the type of magnetic order as a function of the magnetic ions content.
- Magnetic phase diagram $Ge_{1-x-y}Sn_xMn_yTe$ alloys is known in a narrow compositional range, $x \leq 0.13$, this thesis is aimed to construct magnetic phase diagram in a much wider alloying regime from $x = 0.2 – 0.8$ and $y = 0.02 – 0.09$ in order to understand the impact of both Sn and Mn on the magnetic order and present different magnetic phases of $Ge_{1-x-y}Sn_xMn_yTe$ crystals. For the above investigations, in-depth static and dynamic magnetometric techniques followed by data analysis are applied to understand the variation of magnetic order as a function of magnetic ions in quaternary $Ge_{1-x-y}Sn_xMn_yTe$ alloys.
- Also, thorough understanding of magnetic phases in $Ge_{1-x-y}Sn_xMn_yTe$ alloys requires detailed analyses as a function of temperature and magnetic field which is an important part of this thesis. Since the incorporation of Sn into GeTe tunes the magnitude of magnetic exchange constant, it is important to investigate $Ge_{1-x-y}Sn_xMn_yTe$ alloys with high Sn concentration. In that context, magnetic exchange constant is also determined taking into account high alloying concentration of Sn up to $x \approx 0.8$.

The magnetic phase diagram is also related to electrical properties of $Ge_{1-x-y}Sn_xMn_yTe$ crystals; therefore, this thesis was extended to study the magnetotransport phenomena. Investigations of electrical properties of $Ge_{1-x-y}Sn_xMn_yTe$ crystals by means of magnetotransport analysis can probe the influence of alloying on the behavior of GeTe [58]. For instance, magnetic interactions are often manifested by analyzing the anomalous Hall resistivity which might be ascribed to charge scattering mechanisms such as spin-orbit coupling that causes extrinsic side jump and skew scattering. Therefore, the magnetotransport investigations presented in this thesis are aimed to study the following problems.

- Determination of the exact charge scattering mechanisms is studied in $Ge_{1-x-y}Sn_xMn_yTe$ crystals. This part is aimed to understand the charge scattering mechanisms both as a function of temperature and magnetic field.
- The magnetotransport studies are also proposed to understand the driving mechanisms which cause anomalous Hall effect in $Ge_{1-x-y}Sn_xMn_yTe$ crystals. The analysis of electron transport phenomena in the presence of magnetic field is also essential to understand several important quantities for instance, parsing of the anomalous behavior of Hall resistivity, understanding the transverse magnetoresistance and other effects (for example charge localization) induced by charge scattering. Using a modified scaling relation, possible ways to separate and estimate contributions from static and dynamic disorder are analyzed.
- The analysis of negative magnetoresistance by correlating magnetization results to the magnetoresistance isotherms is also presented. Such scaling analysis helped in understanding the origin of negative magnetoresistance in $Ge_{1-x-y}Sn_xMn_yTe$ crystals.
- Furthermore, as magnetic disorder is major issue in these materials, extensive magnetotransport studies are essential for understanding charge scattering from impurities. The investigation of this problem is particularly important in the low temperature regime since lattice vibrations are negligible where contribution to charge scattering comes from impurities. This part of the thesis is meant to estimate and compare the contributions from different carrier scattering mechanisms.

1.3 Outline of the Thesis

Chapter 1 of this thesis presents a brief introduction of the global trend related to the scientific development of diluted magnetic semiconductors and its importance. Comparison between metallic and semiconductor spintronics is described with advantages attached to the later. Encouragement behind the choice of studied material and techniques are narrated which led to the studies of magnetic and electrical properties of these $Ge_{1-x-y}Sn_xMn_yTe$ crystals.

Chapter 2 gives a short history of various groups of diluted magnetic semiconductors and important breakthroughs over the past four to five decades. Selected magnetic exchange mechanisms are reviewed, their role in explaining the presence of ferromagnetic order in different systems, and several types of magnetic order are presented. In the second part of chapter 2, selected concepts related to magnetotransport effects and their analysis are presented.

Chapter 3 describes the samples' growth method and experimental techniques which were used as characterization tools. The principle of vertical Bridgman method and growth conditions applied to obtain $Ge_{1-x-y}Sn_xMn_yTe$ crystals is described. Description of preparing Hall bars and making electrical contacts is presented. For compositional and structural analysis, energy dispersive x-ray fluorescence and x-ray diffraction techniques are described. Working principle of the susceptometer, Weiss magnetometer and magnetotransport setups and conditions applied for the susceptibility/magnetization and electron transport studies of $Ge_{1-x-y}Sn_xMn_yTe$ crystals are illustrated.

Chapter 4 presents the crystal structure of $Ge_{1-x-y}Sn_xMn_yTe$ crystals at room temperature. Variation in lattice constants is illustrated as a function of Sn and Mn concentration, and the influence of alloying on the crystal symmetry.

Chapter 5 Provides extensive studies of magnetic properties of $Ge_{1-x-y}Sn_xMn_yTe$ alloys. This chapter begins with the dynamic susceptibility results including frequency dependent magnetic susceptibility studies. Subsequently, magnetic field and temperature dependent static magnetization results and their analysis are presented. The results of this chapter were published in the Journal of Alloys and Compounds (doi.org/10.1016/j.jallcom.2023.171893) and Journal of Magnetism and Magnetic Materials (doi.org/10.1016/j.jmmm.2021.168695).

Chapter 6 Presents magnetotransport results which are being analyzed with the scaling analysis of the anomalous Hall resistivity/conductivity and transverse magnetoresistance. In this chapter, the charge scattering effects are analyzed based on magnetotransport data in order to explain the temperature and magnetic field dependent behavior of the longitudinal and Hall resistivity. Partial results of this chapter were published in the Journal of Alloys and Compounds (doi.org/10.1016/j.jallcom.2023.172902).

Chapter 7 concludes this thesis with the summary of magnetometric and magnetotransport results.

CHAPTER 2

Selected Concepts Related to Diluted Magnetic Semiconductors

In this chapter, a brief review of diluted magnetic semiconductors and important concepts related to magnetic interactions and electron transport in these materials are presented. The development of inducing ferromagnetism into the semiconducting lattice, diversification of the host materials and impurities, advancements of growth technology and other achievements will be assessed. Particular devotion is paid to different phenomena discovered so far in IV-VI narrow bandgap semiconductors such as α–GeTe and SnTe. This chapter presents two broad sections: (a) lattice structure and carrier mediated magnetic interactions, and (b) charge scattering mechanisms in the presence of magnetic impurities in the semiconductor lattice.

2.1 Diluted magnetic semiconductors – a historical timeline

A new class of magnetic materials emerged [10,11] after a small fraction (a few atomic %) of diamagnetic cations in a host semiconductor was replaced by magnetic impurities. These SCs doped with magnetic ions are known as diluted magnetic semiconductors (DMS) due to the addition of magnetic ions into SC. Before presenting a review of the DMS history, a comparison of non-magnetic (diamagnetic), diluted magnetic and magnetic semiconductors is shown in Fig. 2.1.

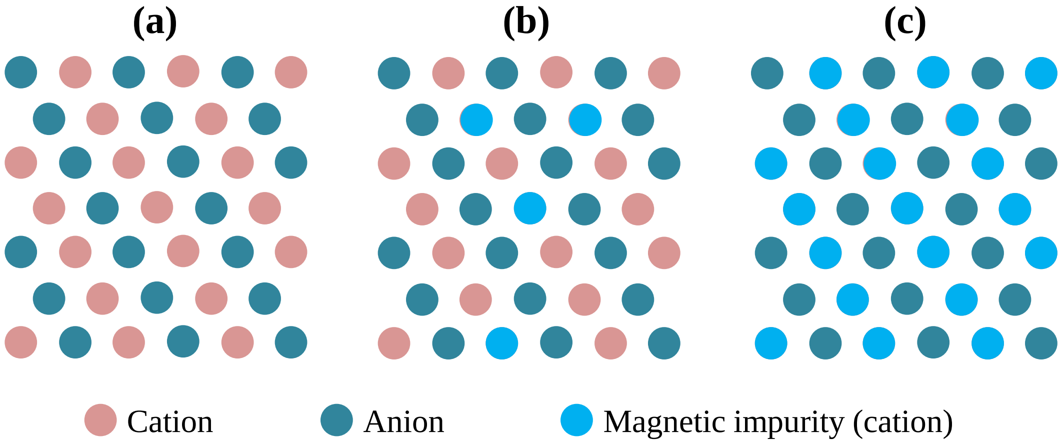

FIG. 2.1 A simplified picture illustrating two dimensional host lattices and incorporated magnetic ions: (a) standard SC (b) DMS in which small amount of magnetic ions replace cation sites (c) magnetic semiconductor where magnetic ions occupy the cation sites [59].

A schematic lattice exemplary of diamagnetic semiconductor is shown in Fig. 2.1(a) consisting of cations and anions without any magnetic impurities. Next is shown the same SC with a small fraction of cations substituted by randomly distributed magnetic ions i.e. Mn which make the compound a DMS, see Fig. 2.1(b). Here the alloyed ions introduce randomly distributed magnetic moments which originate from either unfilled 3*d* or 4*f* shells of the transition metals (TM) or rare earth elements, respectively. Another arrangement of a SC lattice and magnetic ions is shown in Fig. 2.1(c) where paramagnetic ions constitute all cation lattice sites. Such a compound is termed as magnetic SC which is different than DMS due to the difference in the density of magnetic ions. Here the random distribution of alloyed impurities is replaced by a periodic array of magnetic ions. The mostly studied host lattice was usually (among many others) a SC from one of the II-VI, III-V, IV-VI, IV or II-VI-V_2 or wide-gap (>3eV) oxides and nitrides such as II-VI (ZnO) and III-V (GaN). In these materials, magnetic elements such as TM like manganese (Mn), chromium (Cr), iron (Fe), nickel (Ni), cobalt (Co) or others such as rare earths europium (Eu), gadolinium (Gd), or other elements are introduced as dopants. In order for ferromagnetic order to be observable at low temperature in the above materials, a few atomic percent within the solubility range of the host lattice should be added [60]. However; alloying of magnetic ions of the order of $10^{18} - 10^{19}$ cm^{-3} were successfully incorporated in typical bulk III-V materials owing to the low solubility limit which results in phase separation at high alloying concentration [61,62]. For $In_{1-y}Mn_yAs$ thin films, Munekata *et al.*, had achieved a high alloying concentration of $y = 0.18$ by low temperature growth process using molecular beam epitaxy [63]. Randomly distributed magnetic ions with spatial spin alignment can induce interesting magnetic properties in an alloy in a controllable fashion.

The foundation of DMS family was laid with the work of Delves and others in early 1960s [10,11,64,65] who reported the first magnetoresistance and Seebeck effect results of $Hg_{1-x}Mn_xTe$ alloys. During the early years of DMS development, the $II_{1-y}Mn_yVI$ alloys garnered extensive research which surfaced as the most comprehensively understood materials in 1970s [13]. II-VI compounds also attracted wide attention as these DMS could be in some cases, obtained in a broad compositional range e.g. $0 \leq y \leq 1$ where y is the content of magnetic ions [66]. In the preliminary works, magnetooptical and magnetotransport measurements techniques were used to investigate the influence of magnetic impurities on the SC host material which later expanded to magnetization and magnetic susceptibility studies [67–72]. Certain salient features such as colossal magnetoresistance and magneto-optical characteristics such as huge Faraday effect [13] in DMS which arise due to the interaction between localized magnetic moments and electrical properties of the material paved way for further research opportunities. $II_{1-y}Mn_yVI$ DMS saw intense interest also due to the possibility to tune both lattice and band parameters and formation of frustrated magnetic state e.g. low temperature spin-glass due to random distribution of impurity ions [73,74]. Here Mn ions and other 3d transition metals such as Cr, Fe and Co interact via short range antiferromagnetic superexchange which results in low temperature frustrated magnetic states like spin-glass state. Apart from the above, the appearance of magnetic clusters causes such frustration in the magnetic state. Broad interest in $II_{1-y}Mn_yVI$ materials was pushed by possible applications related to the large magneto-optical effects [13], high intensity photoluminescence in the visible region (λ = 600 nm) in $Zn_{1-y}Mn_yS$ [75] and possible optical applications [76] as flat panel displays [77]. These effects were assumed to occur due to the introduction of localized magnetic moments of alloyed magnetic ions within the semiconductor matrix [77,78]. The exchange interaction developed between the *sp* band electrons and the Mn *d*-electrons yielding giant Zeeman splitting of electronic energy levels. Further, large Faraday rotation was proposed to make optical devices such as optical isolators [79] and circulators [80], optical modulation and switching [81]. The magnetic studies of IV-VI DMS also emerged in 1970s with initial work on $Sn_{1-y}Mn_yTe$ and $Pb_{1-y}Gd_yTe$ alloys [19,82]. One of the widely studied IV-VI DMS, $(GeTe)_{1-x}(MnTe)_x$ pseudobinary alloys also find its introductory magnetization study in 1974 as reported by Cochrane *et al* [19]. During the 1960–1990 period, a large number of DMS alloys were studied owing to their integrated electrical and magnetic characteristics [13,83].

The quest to explore functional ferromagnetic compounds took rapid pace which resulted in remarkable developments to induce ferromagnetism in Mn doped SC from which only a few outstanding outcomes are presented below.

2.1.1 II–VI DMS

Among different DMS compounds, a large number of II-VI DMS were investigated with a diverse choice of host materials e.g. Mn/Fe and Co doped Zn/CdS, Zn/CdSe, Zn/CdTe and others like HgTe [84–89]. Conventionally, DMSs were studied in bulk form therefore the synthesis of new structures was urged in order to discover physical properties based on the materials' geometry or confinement of charge carriers. Further investigations of II-VI DMS such as $Cd_{1-y}Mn_yTe$ led to the fabrication of II-VI materials in the form of quantum wells by confining the charge carriers in a two-dimensional system [90]. In 1985, $Cd_{1-y}Mn_yTe$ superlattices with up to 150 layers which consisted of alternate Mn content were grown by molecular beam epitaxy [91]. The introduction of epitaxial grown structures was assumed to open wealth of new discoveries in such compounds e.g. spin dependent tunneling typically between two quantum wells which are separated by a potential barrier, study of the quantum Hall effect and giant spin splitting which occur only in DMS thin films. The excitonic Zeeman effect in zinc-blende II-VI DMS such as $Cd_{1-y}Y_yTe$ (Y = Mn, Co, Fe) was investigated by Alawadhi *et al.*, which is a spectroscopic phenomenon used for studying the magnetization that results from *sp-d* and *d-d* interactions [92]. One of the experimental demonstration of tuning the superlattice potential was seen in the form of spin superlattices (which are periodically stacked SC layers with different energy bandgap) although first proposed in the narrow–gap quantum structures e.g. HgSe/Hg$_{1-y}$Mn$_y$Se [93]. This was later realized in wide–gap structures such as ZnSe/Zn$_{1-y}$M$_y$nSe [94] and Zn$_{1-y}$Mn$_y$Se/Zn$_{1-x-z}$Be$_x$Mg$_z$Se [95]. Until early 2000s, majority of DMS based on II-VI SCs held either spin-glass magnetic state controlled by antiferromagnetic superexchange interactions or paramagnetic state [13]. However; the continuous research efforts and development in growth techniques made possible to design DMS with ferromagnetic order. In one such example, the influence of light on the magnetic properties of modulation doped 8 nm quantum well of Cd$_{1-y}$Mn$_y$Te/Cd$_{1-x-y}$Zn$_x$Mn$_y$Te:N was studied by Haury *et al*. in which photo-tuned ferromagnetic order was demonstrated [96]. Advancements in growth techniques then allowed the development of these materials to show high ferromagnetic Curie temperatures which is important in the context of commercial device applications. In that sense, Zener model for *p*-type II-VI and III-V DMSs was proposed which attracted broad interest due to its suggested explanation of ferromagnetic order at room temperature with 5% of Mn in Zn$_{1-y}$Mn$_y$Te and Ga$_{1-y}$Mn$_y$As with carrier concentration $3.5\text{x}10^{20}$ holes per cm^{-3} [97]. In similar efforts, Saito *et al*. made significant development reporting room temperature intrinsic ferromagnetism in Zn$_{1-z}$Cr$_z$Te based on the *sp-d* exchange interaction [98]. In this work, the highest Curie temperature, $T_C = 300 \pm 10$ K was obtained for Cr concentration, $x = 0.2$.

2.1.2. IV–VI DMS

Among IV-VI group of compounds, Pb$_{1-x-y}$Sn$_x$Mn$_y$Te DMS [18] was first reported by Story *et al*., in which a reversible phase transition between paramagnetic state and carrier mediated ferromagnetic order was demonstrated. Due to variation in hole carrier concentration from $n_h = 1\text{x}10^{20}$ cm^{-3} to $1.4\text{x}10^{21}$ cm^{-3}, a pronounced influence of varying charge concentration on magnetic ordering was observed e.g. transition to a ferromagnetic phase was recorded at $n_h \geq 3\text{x}10^{20}$ cm^{-3}. The magnetic ordering in this DMS compound is governed by the long range Ruderman–Kittel–Kasuya–Yosida (RKKY) indirect interaction which is mediated by free charge carriers [99–101]. The ferromagnetic transition temperature in Pb$_{1-x-y}$Sn$_x$Mn$_y$Te alloys was showed to be $T_C \approx 4.1$ K for $x = 0.72$ and $y = 0.03$. The efforts to increase the ferromagnetic transition temperature which was enhanced to about $T_C = 190$ K ($n_h = 1.57\text{x}10^{21}$ cm^{-3}) in Ge$_{1-y}$Mn$_y$Te epilayers by tuning the hole concentration in the system [102]. Multiferroics such as Ge$_{1-y}$Mn$_y$Te which simultaneously exhibit ferroelectric and ferromagnetic orders were proposed to play a vital role in the interplay between ferroelectric and ferromagnetic orders by tuning the alloy composition [103]. Multiferroic materials like Ge$_{1-y}$Mn$_y$Te offer exciting possibilities for device applications such as magnetoelectric effect which couples switchable magnetization and electrical polarization [104]. These materials have potential to realize electrically controlled spin based devices; spin filter devices which use multiferroic tunnel junction [105] and the emergence of spiral-spin multiferroics where polarization direction could be manipulated by magnetic field and giant magnetoelectric effect [106]. Moreover, the emergence of multiferroic Rashba semiconductors has opened a new path to design IV-VI spintronic devices. In the Rashba multiferroics, both the Zeeman and Rashba type splitting in spin-bands could be observed in a single material [31]. In addition to IV-VI DMS based on ferroelectric GeTe, the discovery of topological surface states in narrow-gap crystalline insulator, SnTe, added another exciting characteristic to the existing known properties [27,107]. The above mentioned works are only a few major research directions based on IV-VI DMS which hold tremendous potential to develop new functional materials for future spintronics applications.

2.1.3. III–V DMS

Based on III-V SC materials, a number of DMS candidates such as $In_{1-y}Mn_yAs$ [108] and $Ga_{1-y}Mn_yAs$ [14] were reported by Ohno *et al*. After the discovery of ferromagnetism in GaAs and InAs based III-V DMS [14,108,109], these compounds are the most extensively studied and understood DMS so far since Mn impurities in III-V compounds have the roles of both localized spins and acceptors at the same time. Particularly for $Ga_{1-y}Mn_yAs$ with $x = 0.1$, above room temperature T_C value was suggested by Zener model [97]. In addition, the above two DMS inspired new research dimension due to the possibility to design a large number of heterostructure configurations. Soon after the emergence of $In_{1-y}Mn_yAs$ as a promising DMS candidate, Koshihara *et al*., demonstrated the photo-generated ferromagnetic order in p–$In_{1-y}Mn_yAs$/GaSb epitaxially grown heterostructures [110]. This photoconductivity effect showed that the ferromagnetic order was maintained below $T = 35$ K even in the absence of light source. In view of the optimization of ferromagnetic transition temperature for device applications, $Ga_{1-y}Mn_yAs$ studies have also achieved great success as $T_C \sim 200$ K was reported for $y = 0.13$ [21]. Following the initial years of research, the next decade saw some intriguing multi-functional achievements for $Ga_{1-y}Mn_yAs$ such as current induced magnetization switching [83], manipulation of magnetization by light [83], and spin injection from $Ga_{1-y}Mn_yAs$ to nonmagnetic compounds like GaAs and many others. The successful fabrication of $Ga_{1-y}Mn_yAs$ based spintronic heterostructure device was reported by Ohno *et al*., who demonstrated injection of spin-polarized charge carriers which can be transported across the heterostructure interfaces over distances greater than 200 nm by applying a forward bias to p–n junction [46]. This was followed by demonstration of a large positive magnetoresistance due to spin-polarized current from a DMS into a nonmagnetic semiconductor which arises as a result of the suppression of a spin channel in the nonmagnetic semiconductor [111]. In addition to the above exciting discoveries, many more interesting reports were shown for III-V compounds such as control of ferromagnetic order in layered semiconductors [20], observation of spin-valve like effect of tunneling anisotropic magnetoresistance in a thin film semiconducting alloy of $Ga_{1-y}Mn_yAs$ [112], domain wall switching leading to magnetization reversal by means of current were demonstrated [113] and many others. The above DMS highlights present only few of many major milestones in terms of materials and transition temperatures that were achieved in order to integrate ferromagnetic order with semiconducting characteristics.

2.2 Crystal Structure of selected IV-VI DMS

In this section, a brief review of known crystal structures of IV-VI DMS is presented with a discussion of both host SC lattice and the impact of magnetic ions on the crystal structure. To begin with previous investigations, the structural transitions in binary and ternary semiconductor single crystals e.g. SnTe and $Pb_{1-y}Sn_yTe$, respectively, were examined via neutron diffraction method [114]. In this study, the cubic phase of SnTe single crystal showed a displacive (rearrangement of atoms from one crystal structure to another without altering the density of the material) phase transformation to a rhombohedral symmetry at T = 97 K. In 1980s, empirical pseudopotential approach was applied using Hohenberg-Kohn-Sham local-density approximation to investigate the crystal symmetry of selected IV-VI structures [115]. These calculations revealed that several tellurides of IV-VI compounds crystallize in the rocksalt cubic symmetry at high temperatures. Certain tellurides have the tendency to switch from rocksalt (face-centered-cubic Bravais lattice) to a rhombohedral structure as the temperature decreases e.g. GeTe and SnTe whereas PbTe was shown to remain in the rocksalt structure down to absolute zero [115]. For $Sn_{1-z}Pb_zTe$, $Pb_{1-z}Ge_zTe$, and $Ge_{1-x}Sn_xTe$ mixed crystals, phase diagrams in terms of ferroelectric Curie temperatures were calculated as a function of alloying content, x which showed phase transition from rhombohedral to cubic symmetry. The important results obtained from these calculations showed that; since GeTe crystallizes in rhombohedral (R3m) symmetry below $T \approx 720$ K, the introduction of Sn into GeTe reduces the ferroelectric Curie temperature to $T \approx 80$ K for pure SnTe. At room temperature, the R3m symmetry switches to rock salt (Fm-3m) phase at $x \approx 0.7$ in $Ge_{1-x}Sn_xTe$. $Sn_{1-z}Pb_zTe$ with its R3m symmetry below $T \approx 80$ K further drops the T_C value as the concentration of Pb is increased. For PbTe which does not show R3m symmetry at all, the incorporation of Ge ions into $Pb_{1-z}Ge_zTe$ lattice leads to an increase in the Curie temperature beyond room temperature when the Ge content approaches $z \approx 0.5$.

In addition to the calculated transition temperature values for IV-VI alloys presented above, the experimental study of quaternary IV-VI DMS such as $Pb_{1-x-y}Sn_xMn_yTe$ showed rock salt structure at room temperature with $a = 6.331$ Å for $x = 0.72$ and $y = 0.03$ [116]. For GeTe-SnTe alloys, the room temperature structural transition was experimentally investigated by Bierly *et al*., via X-ray diffraction [117] whereas A. I. Lebedev *et al*., used X-ray absorption fine structure (EXAFS) characterizations [118]. As a result of these studies, the pseudo-binary alloy GeTe-SnTe revealed a transition from face centered rhombohedral to cubic symmetry at 0.32GeTe−0.68SnTe at room temperature. These experimental results are consistent with calculated values presented in the previous paragraph.

In this part, crystal structure of DMS crystals which are a subject of this thesis e.g. $Ge_{1-y}Mn_yTe$-$Sn_{1-y}Mn_yTe$ mixed crystals is presented. In Fig. 2.2(a), the influence of alloying Sn on the crystal structure of GeTe is shown. As mentioned in the above paragraph, both theoretical [115] and experimental [117,118] investigations showed room temperature R3m to Fm-3m transition at $x \approx 0.7$. In case of $Ge_{1-y}Mn_yTe$, room temperature transition from R3m to Fm-3m symmetry was earlier investigated by Przybylińska *et al*., which shows ferroelectric to paraelectric crossover at $x \approx 0.3$ [103]. In Fig. 2.2(b), the transition from R3m to Fm-3m is shown for $Ge_{1-y}Mn_yTe$ as a function of the Mn content. Below T_C, the corner angle, α, decreased below 90˚ whereas an electric dipole moment, $\boldsymbol{P}_{el}$ is formed along ⟨111⟩ direction [103]. The R3m phase of $Ge_{1-y}Mn_yTe$ is typically identified as rocksalt structure in which inversion symmetry is broken by 2 degrees [31,103].

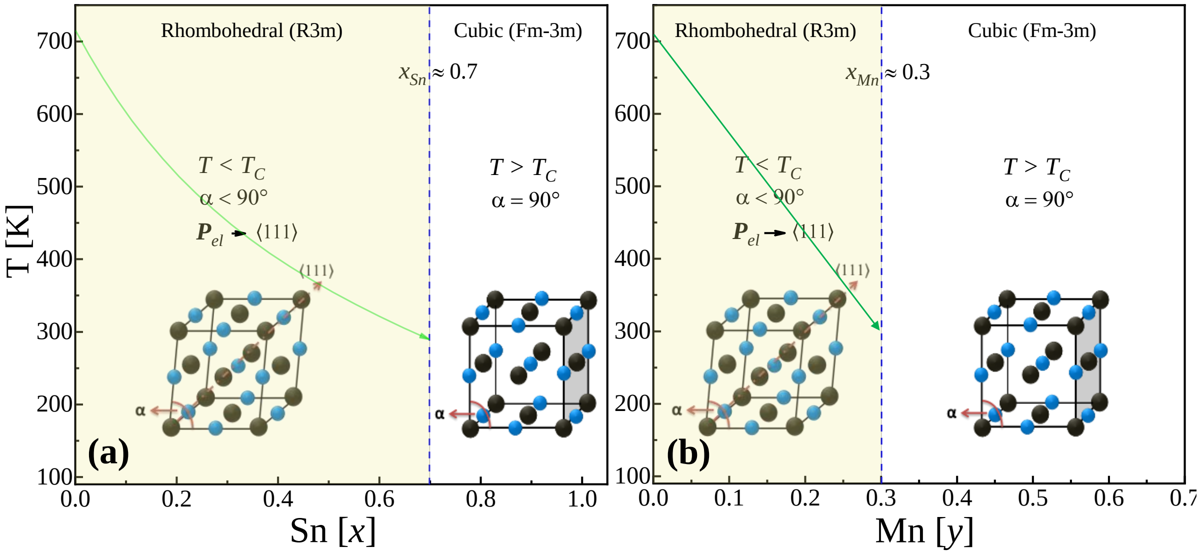

FIG. 2.2 Variations in crystal structure of (a) $Ge_{1-x}Sn_xTe$ [117], (b) $Ge_{1-y}Mn_yTe$ [103] as a function of Sn or Mn content, respectively. At $x < 0.7$ and $y < 0.3$, ferroelectric polarization is held inherited from host GeTe in $Ge_{1-x}Sn_xTe$ and $Ge_{1-y}Mn_yTe$, respectively. Here the electric dipole, $\boldsymbol{P}_{el}$ is produced along (111) direction due to the distortion of the unit cell whereas corner angle, α, remains less than 90˚. The y-axis shows approximate Curie temperature at each Sn or Mn content value in (a) and (b), respectively.

In the Mn rich regime, the crystal structure could be more complicated than a simple cubic symmetry. In the range of $0.2 < y < 0.5$ of Mn, the stable rocksalt structure is maintained whereas a mixed two phase regime is observed from $y = 0.5$ to $y = 0.92$. However; the rocksalt structure could be observed above $y = 0.5$ alloying content for the samples grown with the use of quenching process (rapid cooling of a material) when cooling from high temperatures. Above $y = 0.92$, a NiAs type of close packed hexagonal phase was observed [119]. Furthermore, the alloying of rock-salt SnTe [120] with Mn ions produces hexagonal NiAs type structure with B13 symmetry at $y \geq 0.12$ in coexistence with the rocksalt phase [121]. In the MnTe phase, both Mn and Te atoms are octhedrally coordinated in the NiAs-like symmetry. Based on the structural variation in both $Ge_{1-y}Mn_yTe$ – $Sn_{1-y}Mn_yTe$ mixed crystals, the R3m and Fm-3m symmetries will be observed in the majority of compositions except those close to $y = 0$ or 1. MnTe with NiAs type hexagonal symmetry is expected at very high Mn composition.

2.3 Recent advances in GeTe and other polar compounds

In addition to the presence of ferromagnetic and ferroelectric coupling, GeTe and its derivative mixed crystals have demonstrated a number of different intriguing features. Among these, giant Rashba spin-splitting [122–124], tuning of ferroelectric features and its control over magnetic texture [30,125], and entanglement of ferromagnetic and orbital degrees of freedom [31] have unveiled new research necessities. In this sense, ferroelectric Rashba semiconductors are of immense interest [126] due to the possibility of ferroelectrically-controlled Rashba spin orbit coupling [127], spin orbit coupled electron transport in inversion asymmetric systems [128], spin to charge conversion [129], and the presence of topological surface states in SnTe related crystals [26]. In addition to the room temperature ferroelectric order in GeTe, the discovery of ferroelectricity in SnTe has been reported both theoretically [125] and experimentally [26] even for the films with thickness as small as single lattice constant which suggests that the ferroelectric polarization can be tuned by growth engineering in narrow bandgap compounds such as $Ge_{1-x-y}Sn_xMn_yTe$. Interestingly, the in-plane ferroelectricity was shown previously to exist at room temperature in 2 to 4 lattice constant thick films of SnTe [26]. The remnant ferroelectric polarization vector breaks the inversion symmetry and determines a giant k-dependent bulk Rashba spin-splitting of the valence bands. The existence of more than one ferroic order in a single system, for example multiferroic Rashba semiconductors provide an intriguing path to develop novel semiconductor spintronic materials which could integrate room temperature memory and computing functionalities in a single device.

Since ferromagnetic transition temperature of IV-VI DMS is far below room temperature, the recently developed IV-VI ferroelectric Rashba SC like α-GeTe [24,122–124] present themselves as excellent competitors of magnetic semiconductors. The density functional theory (DFT) simulations predict the reversal of spin direction in each sub-band upon inversion of the ferroelectric polarization which allows to control in a non-volatile and reversible manner the bulk spin texture electrically and utilize these exceptional characteristics in spintronics devices [122,123]. Certain compounds such as SnTe based materials are at the forefront of current research in which the spin-dependent transport phenomena plays role as information processing whereas the ferroelectric or ferromagnetic order accounts for the information storage [26,129]. Besides the Rashba effect and reversible nonvolatile memory control, ferroelectric materials offer striking research possibilities like engineering of their domain walls [130] which are believed to be extremely thin and therefore behaving like two dimensional sheets. In context of applications, the idea of domain wall engineering is to generate, move and eliminate domain walls by applying an external field in order to control the functionality of devices. Previous works reveal that these domain wall structures could be engineered, and their parameters be switched by applying external magnetic/electric field or stress [131]. Among the categories of ferroic materials, ferroelectrics have extremely thin domain boundaries extending down to a single lattice constant. Compared to tens of nanometers wide magnetic domain walls, narrow domain walls in ferroelectrics make them truly two dimensional objects and favorable for atomic scale device engineering [132,133]. These two dimensional topological defects represent new exciting functionalities where polarization variations in the domain walls cause the appearance of quasi one dimensional topological defects different from the established polarization vortex and skyrmion textures [134,135]. Moreover, the two dimensional functionality of these domain walls can be manipulated due to the fact that domain walls could be created, eliminated or displaced under an external electric field. These characteristics are providing interesting possibilities to revolutionize the nano-electronics at even smaller scale, hence representing an electric alternative to domain walls based spintronic devices [136–138].

2.4 Origin of ferromagnetism in diluted magnetic semiconductors

The inception of ferromagnetism in compound II-VI/III-V or IV-VI SC stems its origin from randomly placed magnetic impurities distributed in the SC matrix. The introduced magnetic ions can be either isoelectric (for example $Cd_{1-y}Mn_yTe$, $Zn_{1-z}Co_zO$, and $Pb_{1-z}Eu_zS$) or not such as in III-V DMS [139,140], and randomly distributed with very minute fraction in the host lattice. Magnetic moments in SC come from the unfilled *d* or *f* shells of TM metals or rare earths. This can induce magnetic order in the material when the localized magnetic moments establish exchange interaction. In DMS systems, local magnetic moments are connected via spin-spin interaction which can be described quantum mechanically. The phenomenon which involves cooperation and alignment of individual magnetic moments related to magnetic ions in materials such as DMS is called a magnetic exchange interaction [141]. Magnetic exchange interaction can be direct or indirect in different materials. Direct exchange can occur between magnetic moments on neighboring ions without any intermediate ion between them. On the other hand, exchange interaction can be established indirectly e.g. in materials with high charge density. In one of these indirect interactions, free charge carriers can mediate exchange interaction between magnetic ions (this topic will be discussed in detail later in this chapter). Due to the space limitations of this thesis, readers are referred to comprehensive review of magnetic exchange interactions which explains the magnetic behavior in II-VI DMS systems in Ref. 13. The magnetic exchange interaction between Mn ions e.g. in IV-VI (GeTe) or II-VI (ZnTe) DMS is mediated by the free charge carriers. In III-V DMS, Zener exchange interaction can be responsible to couple local magnetic moments. As a consequence, the magnetic exchange interaction between local magnetic moments can lead to different magnetic orderings such as ferromagnetism, antiferromagnetism, spin-glass magnetic state etc. The types of exchange interactions and consequent magnetic orders will be presented in the following sections.

2.4.1 Magnetic exchange interaction in DMS

In order to understand spin–spin exchange interaction, two electrons are considered with spatial coordinates of r_1 and r_2, respectively from a reference point or origin. In quantum mechanical terms, the two charge carriers have wavefunctions associated with them where the product of the wavefunctions can be assumed which represents wavefunction of the joint state if the charges communicate with each other via any mechanism. If wavefunction of the first charge carrier is represented by $\Psi_a(r_1)$ and that of the second carrier by $\Psi_b(r_2)$, the product of the combined configuration can be written as $\Psi_a(r_1)\Psi_b(r_2)$. For the electrons involved in the exchange interaction, the product of individual wavefunctions must be anti-symmetric either in singlet (S = 0) or triplet (S = 1) case. The resultant singlet and triplet state wavefunctions can be written as follows:

$$\Psi_S = \frac{1}{\sqrt{2}}\,[\Psi_a(r_1)\Psi_b(r_2) + \Psi_a(r_2)\Psi_b(r_1)]\,\chi_S, \tag{2.1}$$

$$\Psi_T = \frac{1}{\sqrt{2}}\,[\Psi_a(r_1)\Psi_b(r_2) - \Psi_a(r_2)\Psi_b(r_1)]\,\chi_T. \tag{2.2}$$

Here Ψ_S and Ψ_T take into account both the spin and spatial components. Also, $\Psi_a(r_1)\Psi_b(r_2)$ is the spatial part whereas χ_S and χ_T are the spin components of the wavefunction. One can write the energies of the above singlet and triplet products as follows.

$$E_S = \int \Psi_S^{*}\widehat{\mathcal{H}}\Psi_S\, dr_1 dr_2, \tag{2.3}$$

$$E_T = \int \Psi_T^{*}\widehat{\mathcal{H}}\Psi_T\, dr_1 dr_2. \tag{2.4}$$

Also, when the spin components, χ_S and χ_T of the states are presumed to have normalized values, the energy difference is then given by

$$E_S - E_T = 2 \int \Psi_a^*(r_1)\, \Psi_b^*(r_2)\, \hat{\mathcal{H}}\, \Psi_a(r_2)\, \Psi_b(r_1)\, dr_1 dr_2. \tag{2.5}$$

Now before deducing the conclusion of energy difference when treating a singlet or a triplet state, it is obvious that by combining results of two particles each with spin equal to $\frac{1}{2}$, the final entity holds a spin quantum number of either $S = 0$ or 1. Whereas the eigenvalue of the total spin operator, $(\hat{S}^{\text{tot}})^2$ is written in the form of $S(S + 1)$ and in case of three components, the $(\hat{S}^{\text{tot}})^2 = \hat{S}_x^2 + \hat{S}_y^2 + \hat{S}_z^2$. Moreover, the eigenvalues of each of these three components are equal to $\frac{1}{4}$, then evaluating such a relation for any spin state yields the following outcome

$$\hat{S}^2 \,|\Psi\rangle = (\hat{S}_x^2 + \hat{S}_y^2 + \hat{S}_z^2)\, |\Psi\rangle, \tag{2.6}$$

$$\hat{S}^2 \,|\Psi\rangle = \left(\frac{1}{4} + \frac{1}{4} + \frac{1}{4}\right) |\Psi\rangle = \frac{3}{4}\, |\Psi\rangle. \tag{2.7}$$

In the context of eqs. 2.6 and 2.7, the energy difference relation takes the form of either $\boldsymbol{S}_1 \cdot \boldsymbol{S}_2 = -\frac{3}{4}$ or $\boldsymbol{S}_1 \cdot \boldsymbol{S}_2 = \frac{1}{4}$ for a singlet or triplet state, respectively. With these changes, the energy difference term is written in the form of an effective Hamiltonian:

$$\hat{H} = \frac{1}{4}\,(E_S + 3E_T) - (E_S - E_T) S_1 \cdot S_2. \tag{2.8}$$

Here the second term in eq. 2.8 is representing the exchange term related to spins of two charge carriers between which the interaction is taking place. This yields a final spin dependent term which interprets the exchange interaction between two spins [142], see eq. 2.9:

$$\hat{H}^{\text{spin}} = -2J \hat{S}_1 \cdot \hat{S}_2. \tag{2.9}$$

In eq. 2.9, the term J represents exchange integral originating from two electrons wavefunction whereas $\hat{S}_1$ and $\hat{S}_2$ are spin operators of charge carrier 1 and 2, respectively. Here the spins residing on two different impurities are represented by 1 and 2 whereas J denotes the exchange constant which is a consequence of overlap of wavefunctions participating in the interaction process. The magnetic exchange is thus quantum mechanical mechanism that fundamentally evolves from the interference of wavefunctions of the charge carriers. Moreover, it is strong in the closest overlap proximity while decays with increasing distance between the spin entities.

With the brief introduction of magnetic exchange interaction, an overview of several exchange mechanisms is provided in the following sections which explain the foundation of producing magnetic ordering in magnetic materials. The next topics are intended to cover particularly the

Zener's double-exchange model [143–145], Zener's *p–d* exchange theory [97,146–149], superexchange interaction [150,151] and RKKY mechanism [99–101].

2.4.2 Zener's double-exchange model

In this section, the concept of Zener's double exchange [143–145] and Zener's *p–d* exchange interactions [97,146–149] are described. This mechanism of exchange interaction between magnetic moments was put forward by Zener in 1951 which he named as "double exchange" [143]. Zener proposed the model which describes the inception of ferromagnetism driven by the exchange interaction between carriers and localized spins. Also, a similar model was proposed by H. Fröhlich and F. R. N. Nabarro in 1940 to explain nuclear ferromagnetism [152]. According to Zener's proposed theoretical model, a free charge carrier being localized by the potential of Mn ion can move backward or forward between two Mn ions in the system. The spin of the above mentioned electron couples with the magnetic moment of the impurity ion which leads to indirect exchange interaction between Mn ions. Zener assumed that this spin coupling which initiates the interaction between Mn ions is probably leading to ferromagnetic order in nature. In Fig. 2.3, a similar picture is shown with two Mn ions having different charge states which facilitate the double exchange mechanism via hopping of a free electron.

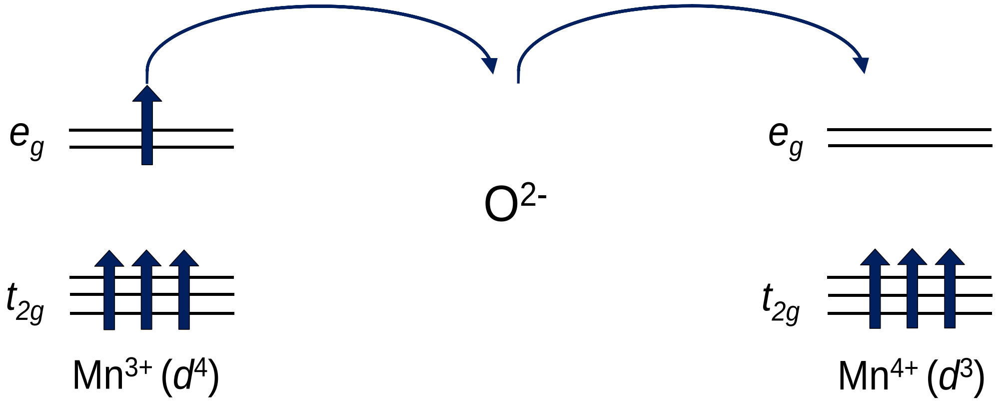

FIG. 2.3 Mechanism of double exchange interaction between Mn–Mn ions. This interaction occurs via hopping thorough an anion (O^{2-}) which reduces kinetic energy to obtain parallel orientation between Mn spins [153].

Such an exchange interaction favors the parallel spin alignment since the electron transfer between central and neighboring sites should have the same spin state. This leads to stabilization of high spin state and therefore results in the ferromagnetic order.

In this section, the Zener's double exchange model is applied particularly to DMS materials. In Fig. 2.4, the spin-polarized density of states (DOS) of a transition metal such as Mn is shown in which spin-up and spin-down electron pairs do not share the same spatial orbital [154]. The Fermi level is denoted by E_F which is presumed to be located in the partially occupied band of the transition metal ion. The Fermi level shown in Fig. 2.4 is considered at the center of the impurity band which means that occupied states come from bonding states only with the anti-bonding states being empty. The shaded area in Fig. 2.4(a,b) shows the band broadening of *d*–states as marked by red arrows and *p*–*d* mixing shown as light-blue arrows, respectively. This band broadening of the impurity bands results in an energy gain during the double exchange mechanism. In case of the coexistent Mn^{3+} and Mn^{4+} ions in $La_{1-z}Sr_zMnO_3$, P-G. de Gennes [155] was able to explain the origin of ferromagnetism in view of the band broadening and resulting energy gain. Near the partially filled bands, the band energy is larger for parallel than antiparallel configuration when the bandwidth is smaller than the exchange splitting [145]. Here two important dependencies can be described as follows:

(a) The bandwidth of magnetic ion is proportional to the square root of the doping concentration, $\sqrt{z}$.

(b) The bandwidth is also proportional to the hopping matrix element, t_h which quantifies the quantum-mechanical coupling between the orbitals on a pair of nearby impurities. The two dependencies can be presented mathematically in the form of eq. 2.10 [154]

$$\Delta E_{DX} \sim \sqrt{z}|t_h|, \tag{2.10}$$

where ΔE_{DX} is the energy gained during the double exchange. Such behavior holds true when band width of the transition metal varies as square root of the coordination number, $\sqrt{N_C}$, where N_C denotes coordination number. When DMS materials with high degree of disorder are considered, N_C varies linearly against concentration; z, of the magnetic impurity. In case of *p*–*d* exchange as shown in Fig. 2.4(b) for narrow gap SC such as GaSb, [146–149] the Mn majority and minority *d*–levels lie below the *p* level of Sb and above the Fermi level, E_F, respectively. This kind of physical situation indicates that the magnetic moment related to Mn is localized at its impurity site. As shown in Fig. 2.4(b), hybridization occurs between the *d* and *p* wavefunctions of the impurity and the *p*-element (e.g. As in case of $Ga_{1-y}Mn_yAs$), respectively which causes a shift in the *p*-band energies. As a result of such hybridization, the majority *p*-band is moved towards higher energy level whereas the one related to minority moves towards lower energy [147]. Consequently, spin-polarization initiates between the magnetic ions. The *p*–*d* exchange mechanism effectively induces ferromagnetic order between the magnetic impurities [149]. In addition to providing a playground for exchange mechanism, the hybridization between *p*–*d* levels also contribute towards carriers (holes) binding energy, E_b (in case of Cu-O, E_b was defined as the binding energy of a hole on each square potential well of O atoms bound to the central Cu^{2+} ion as a result of hybridization) [156].

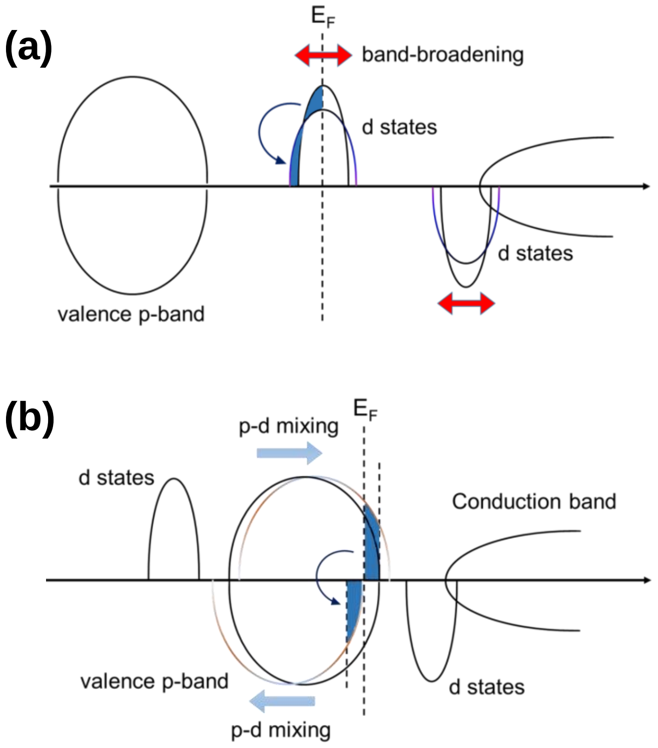

FIG. 2.4 (a) Schematic representation of spin-polarized density of states when a transition metal such as Mn is introduced in a wide gap semiconductor e.g. GaN. (b) Schematic illustration of the spin-polarized density of states demonstrating the *p*–*d* exchange in a narrow gap semiconductor such as GaSb [154].

In case of *p*–*d* exchange as shown in Fig. 2.4(b) for narrow gap SC such as GaSb, [146–149] the Mn majority and minority *d*–levels lie below the *p* level of Sb and above the Fermi level, E_F, respectively. This kind of physical situation indicates that the magnetic moment related to Mn is localized at its impurity site. As shown in Fig. 2.4(b), hybridization occurs between the *d* and *p* wavefunctions of the impurity and the *p*-element (e.g. As in case of $Ga_{1-y}Mn_yAs$), respectively which causes a shift in the *p*-band energies. As a result of such hybridization, the majority *p*-band is moved towards higher energy level whereas the one related to minority moves towards lower energy [147]. Consequently, spin-polarization initiates between the magnetic ions. The *p*–*d* exchange mechanism effectively induces ferromagnetic order between the magnetic impurities [149]. In addition to providing a playground for exchange mechanism, the hybridization between *p*–*d* levels also contribute towards carriers (holes) binding energy, E_b (in case of Cu-O, E_b was defined as the binding energy of a hole on each square potential well of O atoms bound to the central Cu^{2+} ion as a result of hybridization) [156]. The assessment of E_b is made by considering a spherical potential $V(r) = V_0\Theta(b-r)$ of a square potential well created by the magnetic ion [157]. The depth of this square well, V_0 can be then calculated by *p*–*d* hybridization using the following equation

$$V_0 = \frac{5}{8\pi}\frac{\beta N_0}{1.04}\left(1-\frac{\Delta_{\mathrm{eff}}}{U_{\mathrm{eff}}}\right)\left(\frac{a_0}{b}\right)^3. \tag{2.11}$$

Here β denotes exchange integral related to the *p–d* hybridization, N_0 represents cation concentration [158], Δ_{eff} means energy difference between d^4/d^5 level and valence band; U_{eff} shows correlation energy in case of 3d electrons and b/a_0 is the radius of the potential well which is expressed in the lattice constants' units. When the category of wide gap semiconductors is considered, the localized wavefunctions associated with deep levels of magnetic ion yield short ranged double exchange interaction. The consequence of such mechanism could be observed in the diluted impurity systems where ferromagnetic phase cannot penetrate across the host lattice and resulting Curie temperatures are small for instance less than 50 K for $Ga_{1-y}Mn_yN$ with ≈6 % of Mn [159,160]. In $Ga_{1-y}Mn_yAs$, the double exchange interaction is dominant due the fact that impurity bands form within the gap whereas T_C values vary linearly with $\sqrt{z}$. In contrast, in case of the localized *d*-states of the impurity, the *p–d* exchange mechanism governs the interaction e.g. in $Ga_{1-y}Mn_ySb$. Here the position of the impurity (Mn) *d*–states controls the likelihood of the dominant mechanism [148].

2.4.3 Superexchange mechanism

When magnetic impurities are added in small fractions into SC, the separation between these randomly distributed impurities is definitely large enough as compared to the diamagnetic atoms of the host lattice. First proposed by Kramers, the intermediate atom between the magnetic ions was assumed to have some degree of paramagnetism such as in the case of MnO [161]. According to Kramer's interpretation, one p-electron from the intermediate ion transfers to an s or d-level of Mn^{2+} and thus initiates magnetic exchange interaction. Such a situation leads to a type of short range interaction known as the superexchange which plays the role of a competitor to the long range interaction facilitated by carriers [83,150,162,163]. In superexchange coupling, the magnetic moments of magnetic ions are coupled together owing to the *p–d* hybridization in the absence of charge carriers. The superexchange is a short range kinetic (kinetic refers to the interaction between electrons at two different ionic sites) exchange interaction with antiparallel spin orientation being energetically favorable. This configuration results in minimum energy of the system which governs the magnetic properties of DMS such as Mn^{2+} based II-VI structures [164].

The interpretation of superexchange mechanism was then considered by J. B. Goodenough [163] to investigate the origin of perovskite type $La_{1-z}Sr_zCoO_{3-\lambda}$ mixed crystals. His work revealed that the magnetic interaction stems from the presence of excited states in the cation-anion-cation arrangement. In this configuration, either one or two of the excited electrons from 2p level of oxygen relocate to empty or nearly filled orbitals of the cation which then overlap the oxygen ions from both sides. This configuration deduces that when octahedral arrangement of cations is placed on either side of an anion, the exchange interaction results in an antiparallel spin configuration if the e_g orbital is partially filled e.g. Mn^{2+}, Co^{3+} etc. Moreover, the magnitude of superexchange interaction increases when exchange splitting energy, E_{ex} decreases [163]. The exchange splitting energy denotes magnitude of the *d*-level split by the intra-atomic exchange effect.

The underlying model of the superexchange could be understood in terms of a molecular model having two atomic states which are different in energy, assuming $E_1 < E_2$ where a hopping term is denoted by t_h. After hybridization, the energy related to molecular levels could be written as,

$$E_{\pm} = \frac{1}{2}(E_1 + E_2) \pm \sqrt{(\frac{1}{2} - (E_1 - E_2))^2 + |t_h|}. \tag{2.12}$$

In case the system has only lower level, E_1 occupied then the binding energy becomes,

$$\Delta E \cong \frac{|t_h|^2}{(E_1 - E_2)}. \tag{2.13}$$

Next, the above model can be described for impurity ions possessing opposite spins and concentration, z in the form of following relation,

$$\Delta E_{\mathrm{SX}} \cong z \frac{|t_h|^2}{(E^{\uparrow}_{t_{2\mathrm{g}}} - E^{\downarrow}_{t_{2\mathrm{g}}})}. \tag{2.14}$$

Eq. 2.14 gives the energy gained by each Mn impurity for antiparallel spin configuration resulting in the negative exchange constant value. The hopping term between t_{2g} states of the neighboring ions is denoted by t_h whereas the denominator represents the energy split of the t_{2g} states from majority and minority levels. The system usually reaches minimum total energy when antiparallel arrangement of neighboring localized spins is present. Accordingly, superexchange mechanism can be expected in magnetic dopants which have singly occupied hybridized d-orbital e.g. Mn^{2+}, Co^{2+} and Fe^{2+} ions. For such systems as mentioned above, a schematic picture of superexchange interaction leading to anti-ferromagnetic order in MnTe is shown in Fig. 2.5. Here a p-orbital from Te^{2-} is shown that mediates the magnetic exchange interaction between d–orbitals of the transition metal ions.

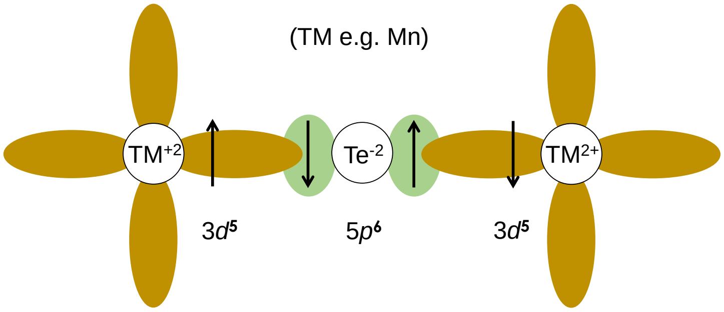

FIG. 2.5 (a) Schematic representation of an antiferromagnetic superexchange interaction where an example of MnTe is shown. The abbreviation TM denotes transition metal such as Mn.

The presence and role of the superexchange interaction in IV-VI DMS such as $Ge_{1-x}Mn_xTe$ and $Ge_{1-x-y}Sn_xMn_yTe$ can be of significance due to similar type of alloys studied in this thesis. In one such example, Fukuma *et al.*, worked on $Ge_{1-x}Mn_yTe$ films with $0.07 \leqslant y \leqslant 0.53$ [50] who interpreted the magnetic results based on competing Ruderman–Kittel–Kasuya–Yosida exchange and the antiferromagnetic superexchange interaction. The antiferromagnetic superexchange interaction was particularly detected for high Mn concentration with $y = 0.3$ and above. Similar impact of high Mn content was also reported for $(GeTe)_{1-y}(MnTe)_y$ alloys where significant inconsistency was detected between Curie temperature and its expected dependence on Mn content at $y > 0.2$ [19]. In the above studies, a part of Mn ions did not contribute to ferromagnetic order at high Mn concentrations due to the appearance of antiferromagnetic MnTe [19,50]. Similar influence of superexchange interaction might be anticipated in the quaternary $Ge_{1-x-y}Sn_xMn_yTe$ DMS.

Besides the antiferromagnetic nature of superexchange interaction reviewed above, this mechanism can also lead to ferromagnetic order in certain compounds e.g. Cr^{2+} doped ZnSe and ZnTe [98,160]. The parallel spin configuration resulting from superexchange depends upon the charge states of TM impurities and bond configurations, as interpreted by Anderson-Goodenough-Kanamori [150,162,163]. In case where Cr^{2+} ions are present in certain compounds having the tetrahedral arrangement, the superexchange leads to ferromagnetic order yielding $J_{\mathrm{ex}} > 0$. In case of the superexchange interaction resulting in ferromagnetic order, the energy difference of the superexchange pairing can be written as:

$$\Delta E_{\mathrm{SX}} \cong z\,\frac{|t_h|^2}{(E^{\uparrow}_{t_{2g}} - E^{\uparrow}_{e_g})}. \tag{2.15}$$

Here the hopping term, t_h is considered between $E^{\uparrow}_{e_g}$ and $E^{\uparrow}_{t_{2g}}$ states residing on the neighboring impurity ions. Furthermore, the superexchange mechanism can play a dominant role and overtake the double exchange interaction when the charge states associated with TM impurity have same state or its electrons are localized.

2.4.4 Ruderman-Kittel-Kasuya-Yosida (RKKY) mechanism

The Ruderman-Kittel-Kasuya-Yosida interaction best known as RKKY interaction [99–101] was originally suggested in particular to study the influence of a localized nuclear magnetic moment on the spins of an electron gas in metals. Due to high carrier concertation in DMS materials, the RKKY mechanism is therefore anticipated to operate in compounds in which substantial carrier concentration e.g. of the order of $\sim 10^{19} - 10^{20}\ \mathrm{cm}^{-3}$ was observed [166]. This exchange interaction occurs between localized moments of the magnetic ions which is mediated by the conduction charge carriers making RKKY an indirect magnetic interaction. This is an important exchange mechanism in DMS materials with high carrier concentration allowing the coupling between localized magnetic moments. One magnetic impurity causes an oscillatory perturbation in the wavefunctions of the conduction charge carriers that carries it to the next moment residing on a localized magnetic impurity. This oscillatory perturbation generated in the free charge carriers establishes a long range magnetic interaction among the randomly placed impurity ions. These types of oscillations carried by the charge carriers are termed as the Friedel oscillations [167]. This indirect exchange interaction originates from the superposition of the oscillatory perturbation of spin-up and spin-down carriers in the charge density. Moreover, different degree of potential is experienced by the spin-up and spin-down conduction carriers inside the periodic environment. Depending on the type and concentration of magnetic impurities in the lattice, the RKKY interaction can produce a ferromagnetic or antiferromagnetic order since the separation between impurities can have substantial influence on the coupling phenomena. However; the resulting magnetic order cannot be limited to these two spin configurations but can produce diverse forms of intriguing magnetic states. Fig. 2.6 which shows the behavior of RKKY exchange coupling as a function of distance between magnetic impurities.

The Coulomb potential associated with the localized magnetic moment of an impurity has a different effect on spin-up and spin-down charge carriers. The *s*–*d* Kondo Hamiltonian (Hamiltonian which represents the interaction between the spin of the conduction charge carriers and the spin of magnetic impurity) is used to describe the exchange interaction between static impurities and conduction charge carriers. The spin-dependent Hamiltonian based on Coulomb exchange was originally presented as in eq. 2.16.

$$\hat{H}_{\mathrm{ex}} = -2\sum_{i,j} J_{i,j}\, e^{i(\vec{i}-\vec{j})\vec{R}}\, \vec{S}_L \cdot \vec{S}_{k,k'} \qquad (2.16)$$

In eq. 2.16, the exchange constant is denoted by J_{ij}, the spin operator of state L is given by $\vec{S}_L$ whereas R denotes the position of the ion, and spin operator of the band carrier is denoted by $\vec{S}_{i,j}$.

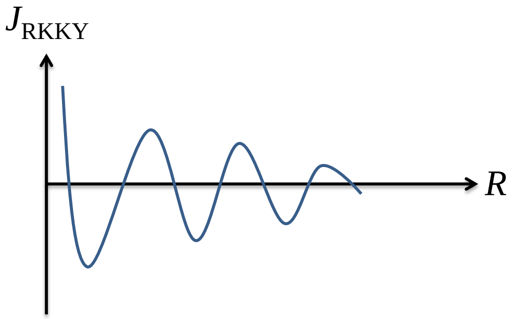

FIG. 2.6 Schematic representation of the exchange integral, J_{RKKY} plotted against distance, R between magnetic impurities which represents the indirect RKKY interaction. The magnitude of the exchange integral shows a damped decrease as a function of distance.

In order to proceed with the mathematical expression, an assumption needs to be made that the magnetic moments of two impurities are placed at positions R_i and R_j. The two-impurity *s*–*d* Kondo Hamiltonian can be described as below

$$\hat{H}_{s-d} = -\sum_{i,q} J_{i,i+q}\, e^{\mathrm{i}\vec{q}\vec{R}_i}\, \vec{S}_i \cdot \vec{S}_{i,i+q} - \sum_{i,q} J_{i+q,i}\, e^{-\mathrm{i}\vec{q}\vec{R}_{ji}}\, \vec{S}_j \cdot \vec{S}_{i+q,i} \tag{2.17}$$

Eq. 2.17 can be viewed in a similar way and described by the Heisenberg Hamiltonian, as discussed earlier in equation 2.9.

The term J term in eq. 2.17 shows energy associated with the exchange coupling which is influenced by the density of states the charge carriers have at the Fermi level, $\rho(\varepsilon_F)$ during the perturbation process. Additionally, J also depends upon the exchange integral denoted by $N_0\alpha$ which comes from the s-d exchange interaction. The term N_0 denotes concentration of the magnetic impurities whereas α is used to represent exchange constant for s-like electrons. The s–d interaction is written as following when considering the standard form of RKKY interaction in the original form presented by Ruderman and Kittel [99]

$$\hat{H}_{s-d} = -(N_0\alpha)\,\delta(\vec{r} - \vec{R}_i)\,(\vec{S}_i \cdot \vec{S}_2). \tag{2.18}$$

Then the exchange energy, J_{ij} takes the form;

$$J_{ij}(R) = \frac{\rho(\varepsilon_F) k_F^3 (N_0\alpha)^2}{2\pi} F(x)(2k_F R). \tag{2.19}$$

The distance between magnetic impurities is denoted by $R = R_j - R_i$, $F(x)(2k_F R)$ represents the oscillatory spatial function and the Fermi wave vector is represented by k_F. Eq. 2.19 defines conditions for the interaction to either lead to ferromagnetic or anti-ferromagnetic order. For example, the function denoted by $F(x) > 0$ when $R < \pi / 2k_F$ and in case when $x \rightarrow \infty$ or the distance is fairly large, $F(x) = -\cos(x) / x^3$. These limits lead to conclusions that the RKKY indirect interaction produces ferromagnetic phase when the distance is short whereas the oscillatory perturbation declines in amplitude at large distances. Moreover, the sign of the exchange constant α does not influence the exchange integral.

In view of the IV-VI DMSs such as $Pb_{1-x-y}Sn_yMn_xTe$ [18,116,168] and $Ge_{1-x}Mn_xTe$ [169] having high carrier density has played vital role in inducing ferromagnetism via carrier mediated magnetic interactions. The RKKY mechanism in such materials can be used to calculate the magnetic transition temperature, T_C, by the following equation

$$T_C = \frac{2yS(S+1)}{3k_B} J. \tag{2.20}$$

Here y is the magnetic ion concentration, k_B the Boltzmann constant, S denotes spin of the magnetic ions and J the total exchange integral that demonstrates the sum of all the exchange interactions between the magnetic ions and the conduction band carriers. Furthermore, the total RKKY exchange integral can also be deduced in terms of the band carriers' effective mass, m^*, lattice constant a_0 and Fermi wave vector k_F

$$J_{\mathrm{RRKY}} = \sum_n v_n I_n,$$

$$J_{\mathrm{RRKY}} = \sum_n v_n \left[(m^*) \left(\frac{a_0^2}{2^9 \pi^3 \hbar^2} \right) (2k_F a_0)^4 \right] J_{pd}^2 \sum_{ij} z_{ij} F(2k_F R_{ij}) \mathrm{e}^{-R_{ij}/\lambda}. \tag{2.21}$$

The Fermi wave vector in eq. 2.21 is defined as below taking into account the charge carrier concentration, n

$$k_F = \left(\frac{3\pi^2 n}{v_n}\right)^{1/3}.$$

The Fermi wave vector is assumed to represent a single valley in the band structure associated with a spherical surface that consists of a number of valleys denoted by v_n while $\boldsymbol{z}_{ij}$ defines the number of nearest neighbors.

2.5 Magnetic order in diluted magnetic semiconductors

The alignment of magnetic moments in DMS materials depends upon the type and sign of exchange interactions between magnetic moments. Three basic situations are possible: positive ($J > 0$), negative ($J < 0$) or a coexistence of both the types. Different sign of exchange constant leads to a range of magnetic orderings including complex magnetic states such as spin-glass, re-entrant spin-glass, cluster-glass etc. This section presents selected types of magnetic ordering and the underlying mechanisms that cause such spin configurations.

2.5.1 Ferromagnetism

In ferromagnetic (FM) phase, a material exhibits net spontaneous magnetization below Curie temperature, T_C, in the absence of the external magnetic field. The magnetic moments achieve alignment in the same direction however; the parallel alignment holds within magnetic domains whereas domains have different orientations across the material's volume. Within each domain, the magnetic moments precess around the same axis while macroscopic magnetic moment of magnetic domains is oriented so as to minimize the total energy of the ferromagnet. Within individual domains, the alignment of magnetic moments leading to spontaneous magnetization is attributed to internal magnetic field. The idea of interaction and alignment of magnetic moments in FM is described by the molecular field theory which was originally proposed by Pierre-Ernest Weiss. This theory explains that any individual magnetic moment in the FM experiences an effective field called a molecular field, B_M. Considering a magnetic moment having spin up (↑) state at a given site in SC lattice, this produces an effective field parallel to its direction which is carried to the neighboring site and influences the nearby magnetic moments. The molecular field aligns a large number of magnetic moments in the sample whereas the field is proportional to magnetization of the material. When a ferromagnet is subjected to an external magnetic field, the total magnetization is taken as sum of the external field and the internal molecular field produced by the medium itself, $\vec{B}_{\text{total}} = \vec{B} + \vec{B}_M$. The molecular field $\vec{B}_M$ is then proportional to magnetization which is written as; $\vec{B}_M = \lambda_M \vec{M}$. The term λ_M

is called the molecular field constant which defines the magnitude of the internal field. In case of FM, $\lambda_M > 0$ due to significant Coulomb energy involved in the magnetic exchange interaction. The magnitude of molecular field is usually very large (about 10^3 T) compared to magnetic field produced by a laboratory magnet [170] in FM compared to paramagnets where it could be omitted.

2.5.2 Anti-ferromagnetism

The anti-ferromagnetic (AFM) state dominates when exchange coupling constant between the magnetic moments is negative i.e. $J < 0$. In an AFM ordering, the (↑) and (↓) configurations take two adjacent sublattices both with opposite spin states. In order to describe the AFM state using Weiss molecular theory, it is assumed to consist of two interpenetrating sublattices. An initial assumption is made where molecular field associated with one lattice is proportional to the net magnetization of the second sublattice. The AFM sublattices could be named as “+” or “–” which represent the configurations with spin-up or spin-down, respectively. This way, the molecular field could be defined separately for the two sublattices as $B_+ = -|\lambda_M|\,\vec{M}_-$, and $B_- = -|\lambda_M|\,\vec{M}_+$. As presented in Fig. 2.7, these two mathematical expressions could be illustrated as each sublattice has an internal magnetic field which is experienced by the neighboring lattice with magnetic moments in opposite direction. In other words, the negative sign shows that the molecular field is antiparallel to the external magnetic field. Therefore, the sign of the molecular field constant is negative in this situation. These sublattices are identical however; the difference arises from the opposite directions of the magnetic moments. This could be interpreted as; $|M_+| = |M_-| = M$, where M shows magnetization in each sublattice. The molecular field for FM and AFM orders produces same quantitative expression which could be written as below

$$B_M = -\frac{2}{g\mu_B}\sum_j J_L \hat{S}_j \qquad (2.22)$$

Eq. 2.22 defines the effective molecular field produced by an ion at the *j*-th site and experienced by an ion at the *i*-th site of the lattice. Here $g\mu_B\,\hat{S}_j \cdot B_M$ is the Zeeman part where g denotes the g-factor also called Landé factor which describes the ratio of the magnetic moment μ total angular momentum J_L of a particle where μ_B representing the Bohr magneton. By introducing the molecular field term in the form of eq. 2.22, the exchange interaction could also be illustrated in terms of an effective molecular field when the magnetic moments have configuration similar to Fig. 2.7

$$\hat{H}^{\text{spin}} = g\mu_B \sum_i \hat{S}_i \cdot (B + B_M). \qquad (2.23)$$

This presents a form of Hamiltonian by introducing the molecular field term, B_M. Such a Hamiltonian could be expected to be valid for each sublattice which generalizes the presence of an equivalent effective field at each site of the system. The AFM materials are known to show magnetic transition at temperature which is called Néel temperature, T_N. In AFM phase, the difference of two sub lattices is considered to define a term called staggered magnetization which could be written as; $\vec{M}_+ - \vec{M}_-$.

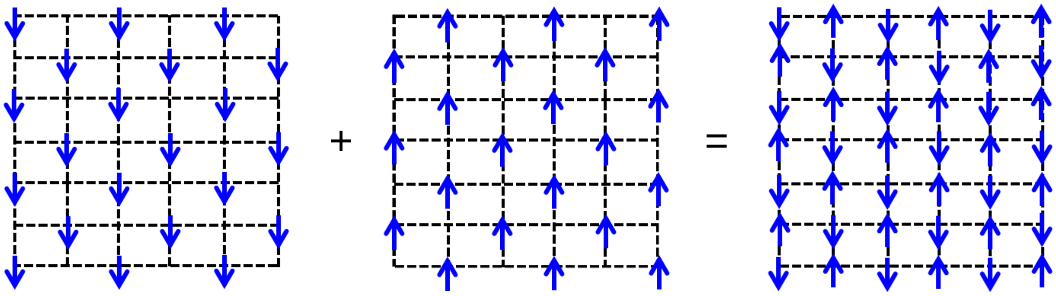

FIG. 2.7 Schematic representation of an antiferromagnetic ordering with antiparallel magnetic moments (right side image) which constitutes of two sublattices each with a particular spin direction (left side images).

The above mentioned magnetic orders can be differentiated based on the sign of J, which holds positive value for ferromagnetic however; remains negative for anti-ferromagnetic order.

- For FM order in which the magnetic moments align in the same direction, Fig 1.8, $J > 0$ and exchange energy achieves its minimum value as a result of $\hat{S}_1 \uparrow\uparrow \hat{S}_2$ configuration at $T < T_C$ where T_C is the Curie temperature at which magnetic transition occurs. The material manifests spontaneous magnetization below the Curie temperature.
- In case of AFM order, the exchange energy is similar as in FM phase but opposite in sign which results in $\hat{S}_1 \uparrow\downarrow \hat{S}_2$ configuration that is followed across the material. Here $J < 0$ and magnetic transition occurs at Neel temperature i.e. the system is AFM at $T < T_N$. This type of magnetic order does not result in net magnetization.
- The third type is FM phase in which the similar spin configuration of $\hat{S}_1 \uparrow\downarrow \hat{S}_2$ yields minimum exchange energy. The $J < 0$ situation remains the same when considering the magnetic ordering at $T < T_N$. This situation is different as the two sublattices have unequal and oppositely directed magnetic moments which produce net magnetization. Schematic representation of the types of magnetic order discussed above is shown in Fig. 2.8.

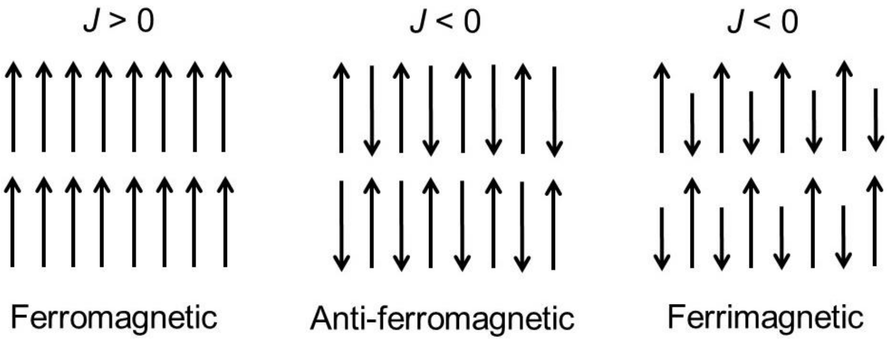

FIG. 2.8 Spin configuration and magnitude of exchange integral, J shown for three types of the magnetic order (a) ferromagnetic, (b) anti-ferromagnetic and (c) ferrimagnetic.

2.5.3 Glassy magnetic states

(a) Spin glass state

Besides the FM and AFM phases, the magnetic interactions between magnetic moments below the transition temperature could also give rise to a randomly oriented magnetic state called a spin-glass. This type of glassy magnetic state is an analogue of structurally disordered state by considering the disordered lattice sites in terms of randomly oriented spins. In spin glass systems, the magnetic moments are believed to be in frustration which originates from structural disorder in the lattice. In spin glasses, both positive ($J > 0$) and negative ($J < 0$) type exchange interactions are simultaneously present and compete against each other which results in randomness and magnetic frustration. The magnetically glassy state breaks the periodicity of spin orientations which remain in a frozen state, see Fig. 2.9(a). Spin glass state is different than e.g. helical magnetic state and a sinusoidal magnet [171]. Since spin glass systems have randomly oriented magnetic moments, it is imperative to make distinction between a spin-glass and a paramagnetic state. The primary difference between these two states lies in the fact that in a paramagnet, in contrast to a spin glass, thermal fluctuations of spatial spins are present. In paramagnets, the randomly oriented spins fluctuate whereas in a spin-glass they are frozen in space.

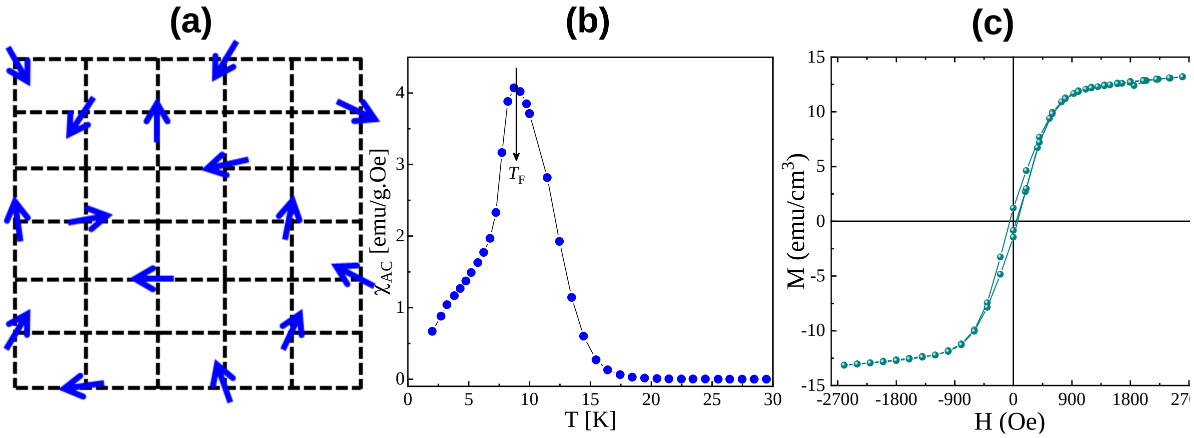

FIG. 2.9(a) Schematic representation of a spin glass (frustrated) state in which randomly oriented and spatially frozen magnetic moments from a diluted magnetic impurity are shown: (b) Typical example of temperature dependent magnetic susceptibility of a spin-glass system. (c) S-shaped magnetization curve representing a spin glass state.

Unlike a phase transition from high temperature disordered state to a low temperature ordered phase such as FM, spin glasses show a completely different behavior below transition temperature. While the spin glass state is highly disordered, it is very much different than the high temperature spin-disordered (paramagnetic) state. Typical example of a spin-glass state is CuMn alloy which constitutes few atomic percent of Mn concentration [172]. The Mn ions are present in the system with dilute amount where the magnetic exchange is carried by the RKKY interaction via conduction charge carriers. Such systems do not exhibit well defined ground state due to the fact that RKKY interaction oscillates in sign (oscillating between $J > 0$ and $J < 0$) which leads to either FM or AFM state. Consistently, the system has a large number of possible ground states with built-in frustration where magnetic moments get into a frozen state below a certain temperature called the freezing temperature, T_F. This system with mixed magnetic interactions is characterized by random though cooperative freezing of spins. Below T_F, the magnetic moments are in highly irreversible frozen state which lack long range geometrical order. Spin-glass state can either be detected in systems with site randomness e.g. random Mn ions in Cu matrix or bond randomness where nearest neighbors have variations of magnetic interactions with either $J > 0$ or $J < 0$.

Since order parameter in spin glass systems is time, these systems are studied with alternating magnetic field in which the most common approach is the ac magnetic susceptibility measurements at different magnetic field frequencies. In such studies, spin-glasses are characterized by a sharp cusp-like shape in the temperature dependent ac magnetic susceptibility curves, $\chi_{AC}(T)$, where the maximum is referred to the freezing temperature, T_F. Due to a number intriguing features, a large number of materials have been investigated which exhibit canonical spin-glass ordering for example metallic $(Fe_{1-y}Mn_y)_{75}P_{16}B_6A_{l3}$ [172], an insulating system, $Al_2Mn_5Si_4O_{16}$ [172], and diluted magnetic semiconductors such as $Zn_{1-y}Mn_yTe/Cd_{l-y}Mn_ySe$ [173]. In AuFe spin-glass system, Cannella and Mydosh had observed sharp cusps in temperature dependent ac-susceptibility results at different frequencies [174]. The cusp maximum moved towards higher temperature as the concentration of Fe increased [174]. Since the investigation of AuFe spin-glass system, the magnetic interactions and unusual features of spin glasses prompted extensive amount of published papers in this field in the following decades. Unlike ferromagnetic ordering which exhibits a stable and saturated plateau in magnetic susceptibility curves below T_C, the spin-glass systems show a drop in the $\chi_{AC}(T)$ curves below T_F as shown in Fig. 2.9(b). Moreover, the position of the cusp maximum on temperature scale in $\chi_{AC}(T)$ curves is sensitive to the frequency of the applied alternating magnetic field which is generally used to differentiate between different magnetic states [175]. Besides a cusp in the $\chi_{AC}(T)$ curves, the spin glass state also unveils its fingerprint in the magnetic field dependent magnetization results $M(H)$. As presented in Fig. 2.9(c), a characteristic s-shaped $M(H)$ curve is observed for a spin-glass [176]. Such a distinction could be safely made when comparing it to a square-like $M(H)$ hysteresis of ferromagnetic phase.

A spin-glass state involves mixed exchange interactions and therefore lacks dominant magnetic exchange type [177]. Due to limited space in this thesis, the readers are referred to a detailed discussion about spin-glasses with RKKY exchange interactions in Ref. 178. The random and unequal path lengths between the magnetic moments yield two important outcomes; microscopically same type of interaction between pairs of ions which result in parallel alignment whereas for others it is negative which favors an anti-parallel orientation. This leads to a frustrated and disordered state that is locked in time.

(b) Cluster glass state

As the concentration of magnetic ions is increased in the host material, the magnetic moments of the alloyed ions might be at first or second nearest lattice sites to a neighbour impurity. These neighboring magnetic ions can couple together via magnetic exchange interaction either parallel or antiparallel depending on the type of magnetic element and its charge state. Consequently, magnetic clusters can form across the host material as a result of the concentration fluctuation in the alloy [179]. The magnetically glassy state is not limited to only spin-glasses but can also lead to a cluster glass system. In contrast to spin-glasses in which individual spins are in a frustrated state, small sized clusters are formed in cluster glasses where spins have local preferable orientations within the clusters. Therefore, both intercluster and intracluster exchange interactions occur rather than only between individual magnetic moments. A schematic representation of a cluster-glass state with ferromagnetic type alignment in each cluster is shown in Fig. 2.10 which illustrates locked-in regions of a cluster glass state. The magnetic order in a cluster glass state is preserved in each cluster as shown by the circular regions in Fig. 2.10.

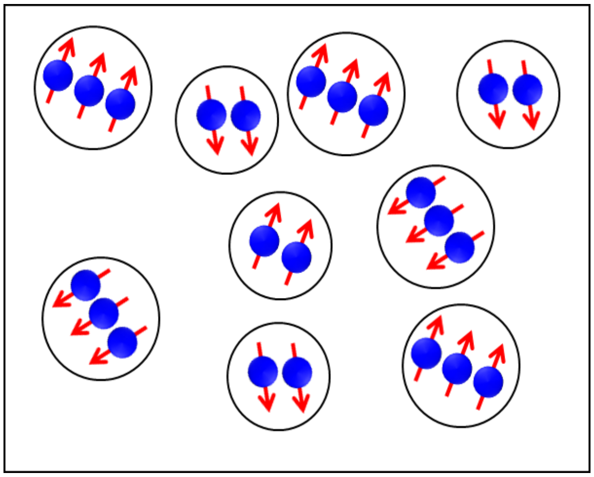

FIG. 2.10 Schematic representation of a cluster glass state which is visualized as small regions with similar spin orientation however; of different sizes.

Experimentally, the cusp-like shape in $\chi_{AC}(T)$ curves might represent transition to different magnetic states such as spin-glass, cluster-glass or a superparamagnetic state [180,181]. Therefore, for the above mentioned magnetic states, the observation of a maximum in $\chi_{AC}(T)$ might not be sufficient to make definitive assessment of the observed type of the magnetic order. For detailed investigation, several approaches are made in order to make a distinction magnetic cluster glass and other magnetic states. Shift in $\chi_{AC}(T)$ maximum at different frequencies is typically used in order to identify the exact magnetic state e.g. in previously studied cluster glass systems such as $LiZn_2V_3O_8$ [182], $La_{1-\delta}Mn_{0.7}Fe_{0.3}O_3$ [183], and $Cr_{0.5}Fe_{0.5}Ga$ [184]. In view of the $\chi_{AC}(T)$ results, the observed cusp looks similar for a spin glass and cluster glass state. The difference in the variation of cusp position in $\chi_{AC}(T)$ of spin glass and cluster glass allows differentiating between the two magnetic states. A scaling relation is used to estimate the scaling parameter describing the change of the temperature maximum, ΔT_F, per decade of frequency, see eq. 2.24 [179]

$$R = \frac{\Delta T_F}{T_F(\log \Delta f)}. \tag{2.24}$$

A quantitative measure of the shift in cusp position is obtained from $\Delta T_F/T_F$ per decade of frequency. The ΔT_F term represents difference in freezing temperature, T_F, which varies by changing frequency value over a decade i.e. from f_1 to f_2 and $\Delta f = f_2 - f_1$ is defined as the difference of two consecutive frequency values. The scaling parameter, R, is related to precession and order parameter of the magnetic state. The obtained value of the parameter, R then defines the presence of either a spin-glass, $0.005 < R < 0.05$, or a cluster-glass, $0.02 < R < 0.06$, ordering [179]. The cusp position in frequency dependent $\chi_{AC}(T)$ results moves towards higher temperature for spin glass and small size cluster glasses. In case of a cluster state with large size, cusp position remains stable and does not shift with changing frequency.

In order to identify the glassy magnetic state, spin dynamics of the system can provide better insight into the size of the clusters. The shift in freezing temperature, T_F as a function of frequency, f, of the applied magnetic field is analyzed to determine the spin relaxation time, τ, and potential barrier [179,180]. The spin relaxation time defines the single flip time of the magnetic moment whereas activation energy or potential barrier, E_a/k_B defines the barrier between two easy orientations [185]. The above two parameters determined from phenomenological laws can be used to differentiate canonical spin glass and cluster glass systems. For canonical spin glass systems, the spin relaxation time lies between 10^{-10} to 10^{-13} s [186] whereas large time values, $\tau > 10^{-10}$ s might characterize the presence of magnetic cluster glass. The clusters size influences the spin relaxation time, τ which is closer to the upper limit of 10^{-10} to 10^{-13} s for small size clusters. Substantially large values of $\tau \sim 10^{-5}$ to 10^{-7} s were reported to represent clusters of larger size [186].

In another approach, dc-magnetization studies can be used to identify the exact type of either spin glass or cluster glass state [187]. In this approach, zero-field-cooled (ZFC) and the field-cooled (FC) magnetization studies are typically performed at different magnetic field magnitudes. The magnetization curves obtained in the ZFC mode, $M_{\mathrm{ZFC}}(T)$ and FC mode, $M_{\mathrm{FC}}(T)$ are collected during heating the samples after cooling to the lowest temperatures was performed either without magnetic field or in the applied field, respectively. Primary distinction between the two states could be made by analyzing the bifurcation and irreversibility temperature of the ZFC and FC magnetization results. Particularly in the low temperature regime below the cusp's maximum, a drastic reduction in ZFC branch might give an insight into the presence of a spin-glass whereas a slow decline denotes the presence of a cluster glass [187]. In addition to the behavior of ZFC branch below maxima, the irreversibility temperature, T_{Irr}, is shifted to lower temperatures when magnitude of the applied magnetic field is increased. This shift in T_{Irr}, can be analyzed using the de Almeida-Thouless relation as presented in equation 2.25

$$H = H_0\left[1 - \left\{\frac{T_{\mathrm{Irr}}(H)}{T_{\mathrm{Irr}}(0)}\right\}\right]^{\Phi/2} \tag{2.25}$$

In eq. 2.25, the characteristic field amplitude is denoted by H_0, freezing temperature is represented by $T_{\mathrm{Irr}}(0)$ which can also be written as T_g at $H = 0$ is the spin-glass transition temperature whereas Φ denotes dynamic exponent related to shift in TIrr with changing magnetic field magnitude. The value of dynamic exponent for spin glass state remains $\Phi = 1.5$ whereas higher values in the range 1.7 – 1.9 define cluster glass state [188,189].

2.6 Selected magnetotransport phenomena in diluted magnetic semiconductors

This section is aimed to describe selected magnetotransport phenomena which occur in the DMS systems. The resistivity tensor with 9 components can be reduced to 3 independent components in the Hall effect configuration. In this thesis, Hall resistivity, $\rho_{xy}(H)$, and longitudinal resistivity/magnetoresistance, $\rho_{xx}(H)$, were studied. Hall resistivity component, $\rho_{xy}(H)$, can give rise to a number of intriguing effects such as anomalous Hall effect, quantum Hall effect, spin Hall effect etc. Additionally, $\rho_{xx}(H)$, can reveal various effects such as giant magnetoresistance, Shubnikov–de Haas oscillations and many others.

2.6.1 Ordinary Hall effect (OHE)

First discovered in 1879 [190], Edwin H. Hall detected that the charge carriers in a metal deflect in a direction perpendicular to the electric current and the applied magnetic field. Such sideways deflection of charge carriers that is caused by Lorentz force (eq. 2.26), generates an additional transverse voltage between the edges of the conductor

$$F = q\,[E + (v \times B)]. \tag{2.26}$$

The Lorentz force, F is normal to the plane of $v \times B$ which produces the Hall voltage. The phenomenon of deflecting the moving charge carriers towards the edges of the conductor when under an external magnetic field was termed as the Hall effect. Since the other categories of the Hall effect family were discovered later, this primary discovery was named as ordinary Hall effect. A typical Hall effect measurement setup used in this thesis is shown in Fig. 2.11. The conducting sample, named as Hall bar, is placed in the presence of an applied magnetic field directed normal to its surface. The Lorentz force deflects electrons and holes in opposite directions of the sample. This results into accumulation of electrons and holes on the opposite edges of the current carrying Hall bar.

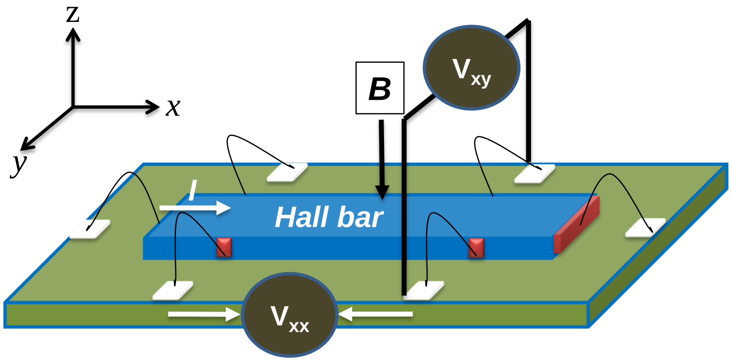

FIG. 2.11 Schematic representation of Hall effect measurement setup containing six-contacts attached to the sample. The two contacts at the ends are called the current contacts whereas the remaining four contacts at the edges are used to measure longitudinal and transverse voltages.

The deflection of charge carriers continues until a steady state is achieved as a consequence of the equilibrium between the electric and magnetic force. Under such an equilibrium condition, it is convenient to write the $E_y = v_x B_z$ where E_y represents electric field component in the y-direction and B_z is magnetic field along z direction. In the basic geometry used in this thesis, two components of the resistivity; the one parallel to the current referred to as magnetoresistance, ρ_{xx} whereas the second part arises from the transverse component which is referred to as Hall resistivity, ρ_{xy}. Under the most basic assumptions, ρ_{xy} can be described as $\rho_{xy} = R_0 H$. Here R_0 is known as the ordinary Hall coefficient which can be used in order to calculate the carrier density, n, as $R_0 = 1/ne$ where e is electronic charge. Experimentally, the sign of R_0 allows finding out the type of majority charge carriers (electrons or holes). The longitudinal and transverse (Hall) voltages are denoted as V_{xx} and V_{xy}, respectively.

2.6.2 Anomalous Hall effect (AHE)

Soon following the discovery of OHE in 1879, Edwin H. Hall observed a ten times larger effect in 1881while studying iron samples [191]. These two discoveries were fascinating since there was little available knowledge about the motion of charge carriers in conductors at the time of Hall's findings. The later effect which occurs in materials with broken time reversal symmetry is called the extraordinary or anomalous Hall effect (AHE). AHE is present in materials in which magnetic ions cause asymmetric scattering of charge carriers. The anomalous factor in the case of ferromagnetic materials arises from magnetic ordering and is proportional to magnetization term [192]. The in-depth understanding of AHE remained controversial due to the lack of modern day concepts in condensed matter theory such as Berry curvature which was termed as an anomalous velocity by Karplus and Luttinger [193]. Early experimentalists established an expression which illustrates the contributions of the normal and anomalous components of ρ_{xy}, see eq. 2.27

$$\rho_{xy} = R_0 H + \mu_0 R_s M. \tag{2.27}$$

The first term, $R_0 H$ represents the OHE component which is proportional to the external magnetic field. The second component, $R_s M_z$ represents the AHE contribution which is proportional to magnetization, M, accompanied by AHE constant, R_s. Unlike the R_0, which appeared to depend upon the charge carrier density of the material, R_s on the other hand varied with the type of material. Also R_s was found to vary with certain parameters of the ferromagnetic sample and with longitudinal resistivity, ρ_{xx} values [194]. The physical phenomenon of AHE can be understood tacking into account the presence of spin-orbit interaction (SOI) in the material. Later studies found that AHE could be caused by mainly two mechanisms, intrinsic and extrinsic scattering. A schematic picture in Fig. 2.12 presents a description of the intrinsic and extrinsic sources which cause AHE effect.

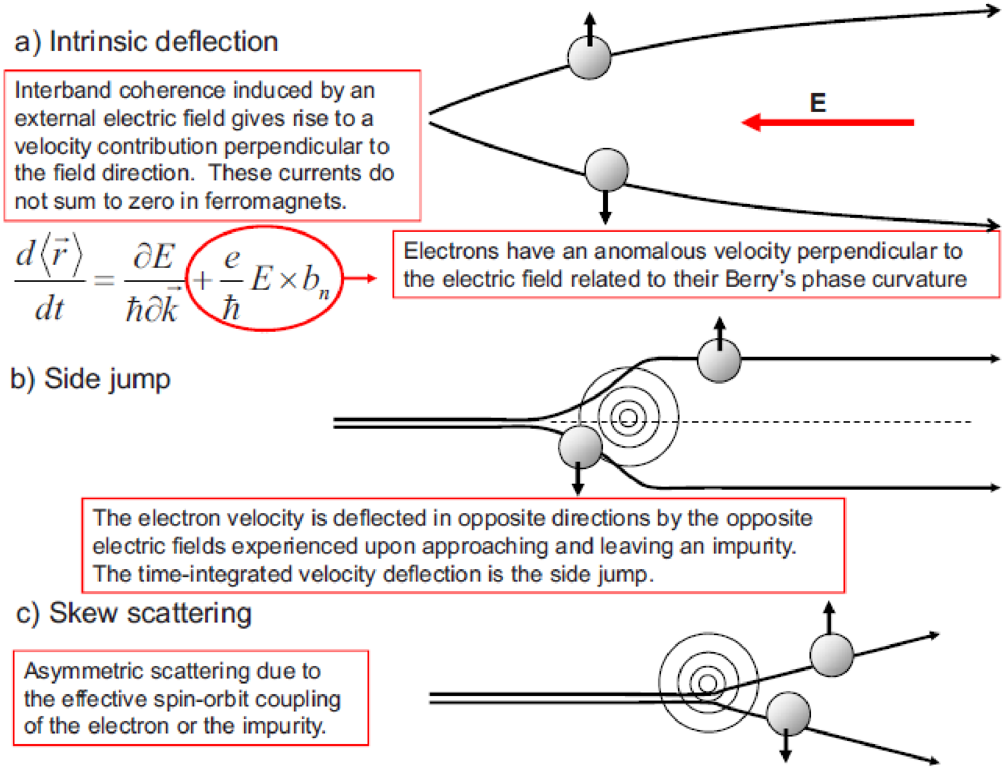

Interband coherence induced by an external electric field gives rise to a velocity contribution perpendicular to the field direction. These currents do not sum to zero in ferromagnets.

$$\frac{d\langle\vec{r}\rangle}{dt} = \frac{\partial E}{\hbar\partial\vec{k}} + \frac{e}{\hbar}E \times b_n$$

Electrons have an anomalous velocity perpendicular to the electric field related to their Berry's phase curvature

The electron velocity is deflected in opposite directions by the opposite electric fields experienced upon approaching and leaving an impurity. The time-integrated velocity deflection is the side jump.

Asymmetric scattering due to the effective spin-orbit coupling of the electron or the impurity.

FIG. 2.12 Illustration of the AHE phenomena originated by three mechanisms in ferromagnetic materials. The intrinsic source is shown in (a) whereas extrinsic mechanisms are given in (b) and (c) [192].

(a) Intrinsic mechanism is thought to be the simplest source causing AHE. The intrinsic source of AHE was first reported by Karplus and Luttinger (KL) [193] which was later interpreted in terms of Berry curvature. The KL interpretation was based on the spin-orbit coupling of the polarized conduction charge carriers. According to KL, the interband matrix components associated with the electric potential-energy cooperate with the spin-orbit coupling which as a result produces an electric current in direction perpendicular to both the external magnetic field and magnetization of the sample [193]. In other words, the spin splitting in the electronic bands can produce Hall conductivity, σ_{xy}, when the spin-orbit interaction is sufficiently strong. This contribution to AHE was identified as independent of scattering processes. The intrinsic mechanism which contributes to AHE conductivity depends only on material's band structure within a perfect crystal [192]. The intrinsic mechanism leads to $\rho_{xy} \propto \rho_{xx}^2$ dependence showing a similar relation as Berger's side jump mechanism.

(b) The extrinsic AHE source stems from the scattering of charge carries off the magnetic impurities in the system. The second part of Fig. 2.12 shows schematic representation of the so called side-jump (SJ) mechanism which was introduced by L. Berger in 1970 [194]. The SJ scattering is induced in the center of mass of the wave packet which undergoes a finite sideways displacement after scattering from an impurity potential. This transverse shift in the center of mass of the wave packet is also asymmetric for spin-up and spin-down configurations. The scattered charge carriers in this mechanism move parallel to their original directions but shifted perpendicular to it. The SJ mechanism is reflected in ρ_{xy} in a way that can be described as $\rho_{xy} \propto \rho_{xx}^2$ [192].

(c) The last scattering source presented in Fig. 2.12 is known as the skew scattering (SS). This contribution to extrinsic mechanism began with the controversy that was developed when Smit observed that the scattering of band carriers from impurities cannot be disregarded in a perfect periodic lattice [195]. This interpretation by Smit introduced an extrinsic source of the AHE which was named as skew scattering mechanism. As presented in Fig. 2.12, the SS contribution arises as a result of the asymmetric carrier scattering in which the up and down spins are impacted differently by the impurity potential. Considering the effective spin-orbit coupling phenomenon, a band carrier suffers scattering and moves at a certain angle with respect to its original path. Consequently, carriers having spin-up are scattered principally in one direction whereas those with spin-down are deflected in the other direction. The skew scattering mechanism depends on the details of the scattering center’s potential. This mechanism is proportional to longitudinal resistivity, ρ_{xx} as $\rho_{xy} \propto \rho_{xx}$ [192,196].

2.6.3 Spin Hall effect

The manipulation of spin related phenomena have opened new prospects in view of spintronics research. One of the important effects is the generation of direct and inverse type of transverse spin currents [198]. Spin Hall effect (SHE) which is generated by electrical currents is a consequence of relativistic spin orbit coupling. In 1971, the idea of generating pure spin current by SHE was proposed in nonmagnetic materials by Dyakonov and Perel [198]. Direct SHE is observed due when electrical current passes through a conducting sample, it generates a transverse spin current which is polarized in perpendicular direction to plane defined by charge and spin current. Following that, the extrinsic inverse SHE was predicted by J. E. Hirsch after nearly three decades in 1999 [199]. In case of the inverse SHE, a transverse charge current is produced by pure spin current. In order to generate both direct and inverse SHE, the system must exhibit spin orbit coupling. Also, proposal of intrinsic SHE was put forward by Murakami *et al*., [200] and Sinova *et al*., [201]. As a result of the charge carriers moving in a crystal in case of intrinsic SHE, a spin dependent velocity in transverse direction can be produced. This transverse velocity is generated as a result of the relativistic spin orbit field of the perfect crystal even if there is no scattering. The fundamental concept of SHE is based on the AHE phenomenon in which the spin direction plays vital role in the spin-orbit interactions induced by asymmetric deflection of the charge carriers [202]. A simple demonstration is presented in Fig. 2.13 that displays a group of six types of Hall effects. The first two types, OHE and AHE were discussed in previous sections which depend on the applied magnetic field and spontaneous magnetization, respectively. In Fig. 2.13(c,f), pure spin Hall effect and its cousin, the quantum spin Hall effect are drawn schematically. Those simplified pictures demonstrate that in a system which possess spin-orbit coupling, the charge carriers with up and down spin directions experience forces of different magnitude.

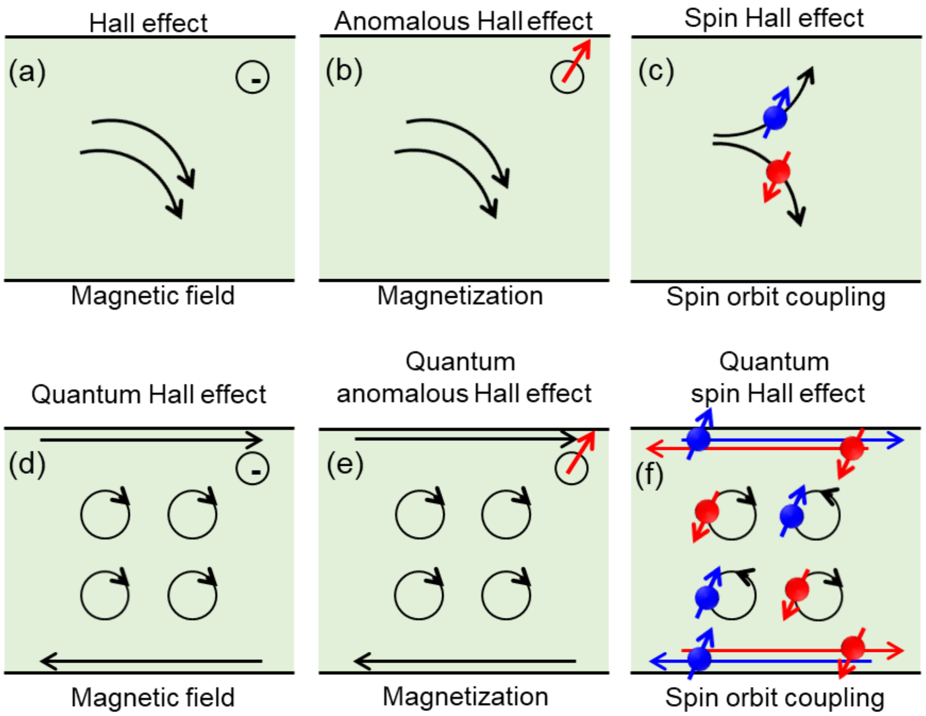

FIG. 2.13 Out of many phenomena related to Hall effect, six types of Hall effect (most common) which do not reflect all of them. The schematic illustrations represent (a) Hall effect (b) Anomalous Hal effect (c) Spin Hall effect (d) Quantum Hall effect (e) Quantum anomalous Hall effect, and (f) Quantum spin Hall effect [202].

As a consequence, the moving conduction carriers in the presence of an external electric field will follow different paths due to their different spin orientations and hence named as spin Hall effect [202]. The name spin Hall effect was coined due to the fact that there is only a net spin current however; there is no net charge current. In contrast to typical Hall effect of charge current, the prerequisite of the time reversal symmetry breaking is not necessary which means that SHE can be detected in standard semiconductors even without the external magnetic field [202].

2.6.4 Quantum Hall effect

The quantization of physical effects and quantities has revolutionized the advancement of condensed matter physics e.g. quantized nature of light, quanta of lattice vibrations and energy etc. In the context of Hall effect, T. Ando *et al.*, first predicted the quantized nature of the Hall conductance in 1975 [203] followed by the K. von Klitzing's work who made the discovery of quantum Hall effect (QHE) at low temperatures [204]. The QHE phenomenon was recorded as a sequence of quantized plateaus in the $\sigma_{xy}(B)$ results for a two-dimensional electron gas system. At the same time, the longitudinal conductivity, σ_{xx} dropped to zero whereas the $\sigma_{xy}(B)$ Hall plateaus were added to the curve with a constant stepwise increase of magnitude, $\sigma_{xy} = e^2/h$. The simultaneous drop of σ_{xx} to zero indicates that the sample behaves as an insulator when the quantized nature of Hall conductivity is occurred. The $\sigma_{xx} = 0$ case occurs because Landau levels split and there are no available free states for the carriers to move freely in the crystal. A simplified picture of QHE is shown in Fig. 2.13(d) which occurs when the conduction charge carriers in the sample achieve an incompressible state along with a strong unidirectional edge state also known as chiral edge state. As presented in Fig. 1.23(d), the propagation occurs only along the boundary whereas the remaining states become localized inside the sample's volume.

It is natural to expect an anomalous behavior of QHE in real condensed matter systems which should represent similar phenomenon as discovered for OHE and SHE. This pursuit led to the first model proposed by F. D. M. Haldane which illustrated the quantized form of Hall conductance in the absence of any magnetic field [205]. The quantization of AHE in tetradymite semiconductors Bi_2Te_3, Bi_2Se_3 and Sb_2Te_3 was proposed by Yu *et al.*, by making investigations via first- principle calculations [206]. These compounds were reported to form insulators having magnetic ordering when doped with Cr or Fe whereas quantized Hall conductance was noticed. This realization of anomalous QHE was made without the use of external magnetic field [207] in Bi_2Te_3, Bi_2Se_3 and Sb_2Te_3 which are three dimensional topological insulators [208,209]. Encouraged by the earlier theoretical predictions, the experimental observation of anomalous QHE was detected by Chang *et al.* in magnetic topological insulator, $(Bi,Sb)_2Te_3$ doped with Cr [209].

2.6.5 Charge localization phenomenon

The behavior of charge carriers in conducting materials is one of the intriguing phenomena in condensed matter physics. A specific physical effect which is known as the localization of charge carriers in disordered materials is presented in this section. The underlying mechanism which causes the charge localization is based on the electrons wave interference during their transport. The interference of wavefunctions occurs when charge carriers are scattered from imperfections in the system. In 1958, P. W. Anderson published his work based on the random potential produced by the lattice imperfections which caused the localization of charge carriers [210–212]. The degree of imperfections immensely affects the carrier transport which can lead to metal to insulator (MIT) transition at higher disorder. Anderson stated that high concentration of lattice disorder can lead to the localization of charge carriers irrespective of the system's size. Anderson localization suppresses the electrical conductivity due to restricting the motion of charges carriers as a result of disorder. Such an effect illustrates that the probability of a charge carrier to return to a particular location is high and wavefunctions overlap due to interference phenomenon. Contrary to this, a small degree of disorder insignificantly affects the transport process which results into decay of return probability.

The electron is initially assumed to possess a Gaussian wave-packet (Gaussian wave-packet can be obtained by the superposition of plane waves). In the presence of a certain disorder-induced potential, $V(z)$, the state of the carriers' motion can be described as wavefunction $\Psi(z, t)$ due to the influence of the disorder potential. When the magnitude of potential $V(z)$ is large and overcomes the kinetic energy of the charge carrier, it results in restricting the motion of charge carriers inside a potential well and hence initiates the charge localization phenomenon. In the presence of a large number of imperfections, the charge carrier suffers substantial scattering events rate that cause strong localization or Anderson localization.

2.6.6 Weak localization and weak anti-localization effect

After the discovery of Anderson's charge localization, a genuine theory was still missing until early 1980s which could interpret a three dimensional localization phenomenon. Particularly, the variation of conductance with the reduction in dimensionality of the systems was not well established on microscopic scale. After the Anderson's localization, another interesting effect was discovered known as the weak localization. Weak localization (WL) of charge which is based on the enhanced backscattering of the carriers wavefunction was developed. Formulated by Wolfgang Götze, Peter Wölfle and Dieter Vollhardt, the WL theory was considered as a precursor to the previously known Anderson localization [213]. In order to better understand the basic physics behind WL effect, the conduction charge carriers are considered as plane waves which propagate in all directions after scattering. The scattered waves have a possibility to interfere and superimpose coherently which cause backscattering of the charge carriers. The backscattering of the charge carriers leads to WL effect. WL arises from constructive interference between time-reversed scattered waves of the charge carriers [214]. At the same time, the spin dynamics of the carriers, which in systems with strong SOI is coupled to their orbital angular momentum, introduce interference of time-reversed paths. The distance travelled by charge carriers before they lose their phase coherence is known as the phase coherence length, l_{φ}. As the charge carrier experiences a sequence of scattering events along its path, the spin orientation is randomized on a characteristic length scale of spin–orbit scattering length l_{SO}. The stronger the SOI is, the smaller the l_{SO}. Here, the interference of time-reversed paths reduces the backscattering probability below its classical value at zero magnetic field. This is the weak anti-localization (WAL) effect, readily observable when $l_{SO} \ll l_{\varphi}$.

In Fig. 2.14, a schematic picture is shown to differentiate between ballistic, diffusive and quantum diffusive regimes of motion of charge carriers in solid state physics. Such a differentiation is made based on the length travelled by carriers before encountering a scattering event. In Fig. 2.14(a), the charge carriers are not scattered from the ions of the crystal.

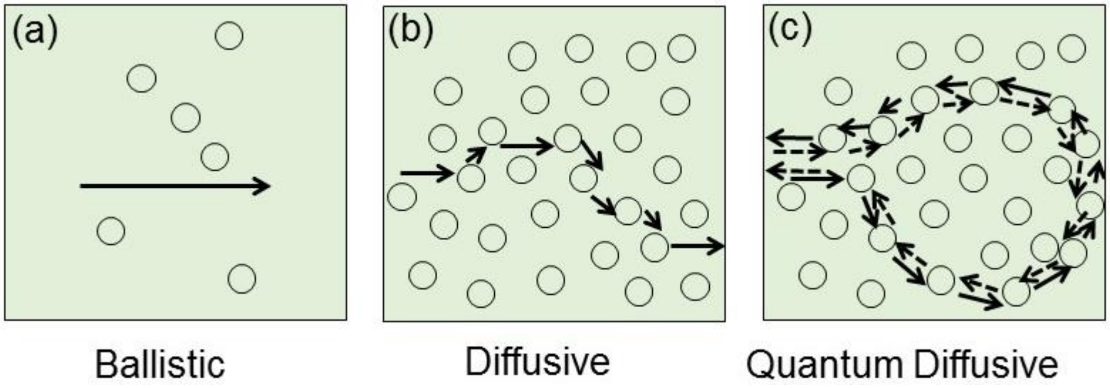

FIG. 2.14 Motion of charge carriers in solids depicting a (a) ballistic, (b) semiclassical diffusive, and (c) quantum diffusive transport regimes.

In Fig. 2.14(b), sufficient concentration of impurities is shown that results in an increased scattering rate which is called diffusive transport. In Fig. 2.14(c), impurities in the system can restrict the charge carriers to a region in which the carriers have probability to return to their initial position known as WL effect. In the WL effect, destructive interference of electrons can suppress their backscattering and hence conductivity is enhanced with decreasing temperature because of the suppressed decoherence mechanisms at low temperatures. A magnetic field can destroy the interference and as a consequence the enhanced conductivity, so the signature of the weak anti-localization is a negative magnetoconductivity, which has been observed in many materials [215–218]. If the carriers can travel for $l \gg L$ where L denotes the lateral dimension of the sample as shown in Fig. 2.14(a), the transport type is categorized as ballistic without the scattering events. The diffusive transport regime shown in Fig. 2.14(b) occurs due to the charge scatterings which sets the condition, $l \ll L$. The diffusive transport can be further categorized into classical and quantum diffusive regimes, see Fig. 2.14(b,c) in which the $l_{\varphi} \leq l$ and $l_{\varphi} \geq l$ demonstrate the classical and quantum boundaries in terms of scattering lengths [219]. The quantum diffusive regime, which prompts the WL and WAL effects arises from the quantum interference of the time reversed scattering paths of charge carriers. Such an effect due to WL or WAL describes correction to conductivity in the low temperature quantum diffusive regime. The above mentioned parameters show a set of conditions which allow either classical or quantum diffusive motion of charge carriers. The difference between WL and WAL effects is typically seen in the magnetoconductivity, $\Delta\sigma$ vs H results around the zero magnetic field. A cusp-like shape is observed in $\Delta\sigma$ that indicates the presence of WL or WAL phenomenon whereas sign of $\Delta\sigma$ distinguishes both effects.

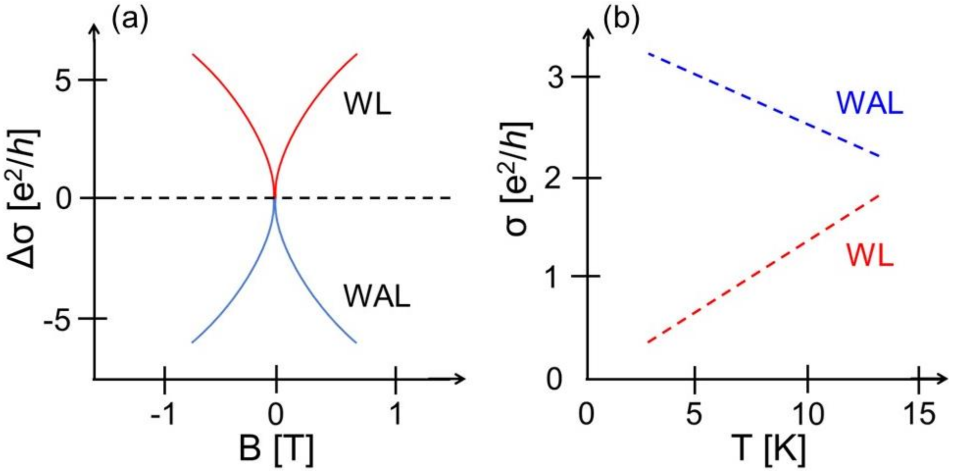

FIG. 2.15 Schematic representation of WL or WAL effects. (a) Negative or positive cusp in magnetoconductivity vs applied field signifies WAL and WL effect, respectively. (b) Magnetoconductivity dependence on temperature is shown. The scales on x and y-axis are arbitrary.

A generic distinction is shown in Fig. 2.15(a) where a positive or negative cusp-like shape in magnetoconductivity illustrates a WL or WAL effect, respectively. Similarly, these quantum interference effects show strong dependence on temperature as seen in Fig. 2.15(b). Important parameters that are associated with WL/WAL phenomena are defined below. During the charge carrier's motion, the average distance travelled by the electron or hole before elastic scattering by lattice imperfections is described as the mean free path, l. The phase coherence length of the carriers is illustrated as l_φ which is the distance it travels in a solid before it loses its phase coherence.

CHAPTER 3

Materials' preparation and experimental techniques

In this chapter, methods of sample preparation and measurement techniques are presented. The chapter begins with the description of modified Bridgman method used for the growth of $Ge_{1-x-y}Sn_xMn_yTe$ crystals studied in this thesis. The measurement section is aimed to present description about chemical composition and structural characterization e.g. energy dispersive x-ray fluorescence (EDXRF) and high resolution x–ray diffractometery (HRXRD). The most important and detailed studies were performed using two magnetometers; LakeShore 7229 magnetometer and Physical Property Measurement System platform (PPMS, Quantum Design) to study $Ge_{1-x-y}Sn_xMn_yTe$ multiferroics. For the electron transport investigations of $Ge_{1-x-y}Sn_xMn_yTe$ samples, two Hall effect measurement setups were used to perform magnetotransport measurements as a function of temperature and magnetic field.

3.1 Bridgman growth technique

The bulk samples of $Ge_{1-x-y}Sn_xMn_yTe$ multiferroics were grown via modified Bridgman technique. A simplified schematic illustration of the growth setup named after Percy Williams Bridgman is shown in Fig. 3.1.

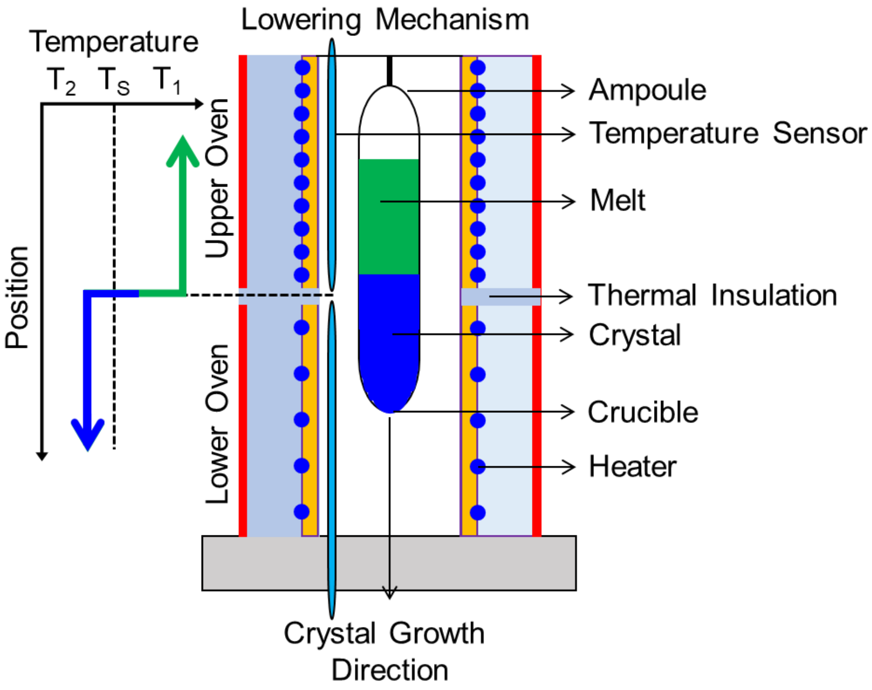

FIG. 3.1 Side view of the modified Bridgman technique used for the bulk crystal growth.

Bridgman method, in which the growth conditions can be precisely controlled, is used to grow crystals of various compositions. The basis of Bridgman method is focused on the control of the temperature gradient in the specific direction in which the crystal growth is desired [220,221]. In a modified Bridgman method which is known as the Bridgman–Stockbarger method, two well controlled temperature zones are achieved by using two separate furnaces with a baffle in-between [222]. Initially, the precursors are heated above their melting points in the melt (hot) zone which can be directed both in horizontal and vertical manner depending on the choice of the method. In Fig. 3.1, a vertical crystal growth arrangement is shown that was used to synthesize the samples to be studied in this thesis. The temperature gradient requires constant control throughout the growth process. From the hot zone, the melt is transferred through the temperature gradient to the cooling region after it is stirred. In contrast to a static system in which temperature is controlled in a single zone, the dynamic cooling mechanism consists of multiple zones. During the transfer of the melt, the crystallization process begins at the bottom of the crucible whereas the nucleation process occurs along the long axis of the cooling zone. This phase of the growth should be carefully controlled in a slow manner in order to achieve the aimed uniform crystallization. Moreover, the ampoules with sharp edges are used to prevent large volume of nucleation which could result in a number grains and therefore impact the quality of the crystallization. After the crystallized material is obtained through this mechanism, the samples are cooled down to room temperature.

3.1.1 Samples' growth via modified Bridgman technique

The bulk crystalline samples of $Ge_{1\text{-}x\text{-}y}Sn_xMn_yTe$ semiconductor multiferroics were prepared by modified vertical Bridgman growth-technique as explained in Refs. 55,220,222,223. In 1958 while working on obtaining metallic crystals from molten source materials, Aust and Chalmers introduced modifications to the previously used Bridgman setup [224]. These modifications suggested that the distance from bottom to the top of the crystal which is normal to the solid-liquid interface, can be made shorter which prevents the formation of lineage boundaries. The modified technique was used in order to reduce the misorientations caused by lineage and obtain crystalline aluminum with upgraded structural quality [224]. Using this improved technique, paramagnetic Mn impurities were introduced into $Ge_{1-x}Sn_xTe$ lattice which enriched the homogeneity of the $Ge_{1\text{-}x\text{-}y}Sn_xMn_yTe$ samples. Prior to the growth of $Ge_{1\text{-}x\text{-}y}Sn_xMn_yTe$ samples, the precursor materials were obtained by subjecting the ultra-pure materials to high temperature. In the next phase, the obtained binary compounds such as GeTe, SnTe, and $MnTe_2$ were used as source materials to synthesize the desired $Ge_{1\text{-}x\text{-}y}Sn_xMn_yTe$ crystals. Since a modified Bridgman technique was used for the growth of $Ge_{1\text{-}x\text{-}y}Sn_xMn_yTe$ samples, the appropriate modifications mentioned above were carefully supplemented to the system. Presynthesized $MnTe_2$ was preferred over the metallic manganese due to its relatively lower melting temperature of 941 ± 3 °C [225] compared to 1244 °C for Mn [226] which in turn improved the Mn ions dissolution into the melt. In this thesis, the growth of samples to be studied is based on the directional crystallization technique as shown in Fig. 3.1. For this reason, the inner surface of the ampoule was protected by semi-transparent graphite layer in order to minimize the interaction between the melt and the quartz ampoule at high temperatures. Furthermore, the graphite layer also prevents the adhesion of the grown ingot to the walls of the quartz ampoule. Before the initiation of the crystallization process, an additional heating source was installed around the crystal growth zone. The additional heater was aimed to provide a radial temperature gradient in addition to the existing longitudinal gradient. In this experiment of directional crystallization, the ampoule was drawn at a steady speed of 1.5 mm/hr along the furnace while simultaneously, the temperature gradient was about 30–40 °C at the front of the crystallization. The modifications stated above enabled us to move the angle of the solid-liquid interface by about 15° relative to the horizontal line. In addition to the control over interface angle, the movement resulted into better melt mixing and also reduced the crystalline block from a typical few down to a single as-grown ingot of cylindrical shape. Consequently, this technique introduced diamagnetic Sn and paramagnetic Mn ions into SC GeTe matrix along the axis of crystallization growth. The final crystals of $Ge_{1-x-y}Sn_xMn_yTe$ were obtained in a wide range of doping concentration with $0.2 \leq x \leq 0.8$ and $0.02 \leq y \leq 0.086$.

3.1.2 Samples' cutting and electrical contacts

After the crystal growth, the cylindrical ingot was cut into disc-shaped fragments of about 1.5 mm thick. Each disc-shaped sample represents chemical composition with particular stoichiometric values of the alloying elements, x and y, to be determined. The disc like samples were then further cut into small pieces for structural characterization and advanced magnetic and electronic transport studies. WS-32 wire-saw was used as cutting machine to prepare bar-shaped samples for magnetotransport and magnetometric measurements. The advantage of this cutting process is that it introduces very small defects as compared to other techniques. Bar shaped samples were obtained with high precession resulting into bars of width, $w \approx 1$ mm thickness, $t \approx 1.5$ mm and length of about 8 mm. Prior to making contacts, bar-shaped samples were cleaned in several stages in order to remove any adhesives and unnecessary materials which might have detrimental effects on the electrical and magnetic measurements.

- At first, the samples were treated in hot water for about 10 to 15 min. By putting the samples in hot water, certain unnecessary chemicals such as residual of grease, glue and paraffin can be removed. After the first phase of cleaning, the Hall bars still contain sufficient amount of residual substances which might influence the desired properties of the compounds. Therefore, the samples are further treated with the following cleaning agents

- GSMT bars were put in toluene-filled beaker for about 10 – 15 minutes. Toluene is a volatile and colorless organic solvent with a chemical formula, $C_6H_5CH_3$. Owing to its effective role as solvent, the 10 – 15 minutes cleaning treatment of the samples in toluene dissolves the vax remains and other adhesives from the surface of the bars.
- The toluene-cleaned samples were then transferred to next phase of acetone (C_3H_6O) treatment for 10 – 15 minutes. Acetone can clean oily stains and other organic residues that reside on the samples' surface. Unfortunately, after a 10 – 15 minutes' bath in acetone, the samples can inherit additional residues from acetone. For this reason, the samples are next transferred to an isopropanol treatment as a final cleansing agent.
- The samples are subjected to the final cleaning treatment in which an isopropanol (C_3H_8O) bath is given for the same 10 – 15 minutes' duration. Isopropanol possesses effective degreasing capabilities which efficiently remove any residue substances.

Subsequently, the samples were transferred to the soldering section where electrical contacts were attached to the samples. Soldering is a typical practice used for connecting metal wires to establish an electrical circuit between the sample and the cables in the sample holder used in the measuring equipment e.g. a cryostat. Gold (Au) wires about 8 mm long were connected to the samples via soldering-iron using indium as soldering element. Indium melts at a rather low temperature of T = 156.7 °C and remains ductile at as low as cryogenic temperatures. The two wires connected at the opposite ends of the sample work as electric current connections whereas the remaining contacts operate for measuring the longitudinal and Hall resistivity tensor components.

3.1.3 Experimental techniques used for characterization of samples

- Selected $Ge_{1-x-y}Sn_xMn_yTe$ samples were investigated using several different techniques for structural, magnetic and electrical studies. The chemical compositions of $Ge_{1-x-y}Sn_xMn_yTe$ samples were determined by using energy dispersive x-ray fluorescence (EDXRF). The crystal structure of these samples was analyzed via high resolution x-ray diffraction (HRXRD) with conventional tube x-ray source.
- In the second part of experimental work, detailed magnetometric measurements were performed using Lakeshore 7229 AC susceptometer and magnetometer equipped with a superconducting magnet. In this part, the temperature dependence of the AC magnetic susceptibility, $\chi_{AC}(T)$, and magnetic field dependent magnetization, $M(H)$, were studied. For the temperature dependent zero-field-cooled (ZFC) and field-cooled (FC) magnetization study, vibrating sample magnetometer

(VSM) was used which is as an option of a commercial Physical Property Measurement System platform (PPMS, Quantum Design).

- The magnetotransport studies were conducted using two different Hall effect measurement setups; the first setup has an iron yoke electromagnet equipped with a helium flow cryostat allowing magnetic field up to $B = 1.4$ T and temperature range from $T \approx 4.3$ K to 300 K. The second Hall effect measurement setup is equipped with a superconducting magnet which generates magnetic field up to $B = 13$ T equipped with variable temperature insert capable of stabilizing sample temperature in the range from $T \approx 1.6$ K to 300 K. Detailed description of the above measuring systems will be provided in the following sections.

3.2 Energy dispersive x-ray fluorescence

X-ray fluorescence spectroscopy is a well-recognized analytical method extensively used for investigating the elemental composition of compounds. This technique has the capability to determine chemical composition of several elements simultaneously. In this thesis, the chemical compositions of Sn and Mn alloyed GeTe crystals were determined using EDXRF spectrometer. For the samples' investigation in this thesis, Tracor Spectrace 5000 EDXRF spectrometer was used. In performing the EDXRF analysis, electrons in the atoms in the sample are excited from ground state with incident x–rays. The excited electrons fall to the ground states and emit characteristic x–rays in this process. Schematic representation of fluorescence phenomenon is shown in Fig. 3.2.

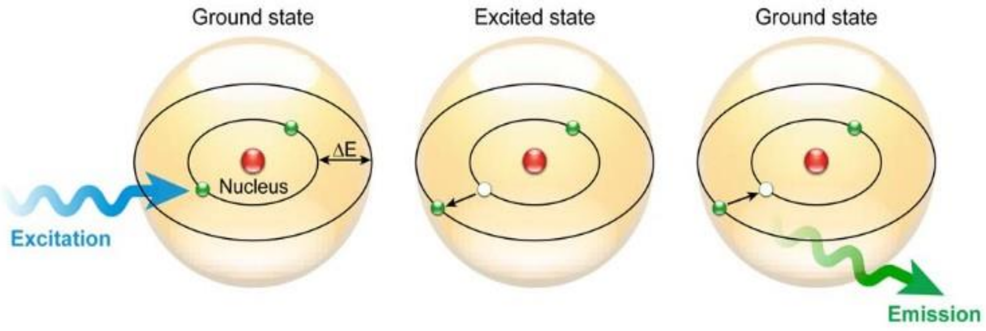

FIG. 3.2 Schematic representation of fluorescence phenomenon [227].

The emitted x-rays are analyzed in order to determine the chemical composition of the material. Typical EDXRF machines are equipped with an x-ray source in the form of an x-ray tube which emits high energy photons and incident on the target material. The incident photons with sufficient energy, $h\upsilon$ can excite the nucleus-bound electrons inside the sample. During this process of fluorescence, the emitted photons are known as characteristic x-rays. The emitted energy spectrum is characteristic of each element in the sample. The incident and emitted x-rays from x-ray tube and sample respectively, are labeled as x-ray beam in Fig. 3.3.

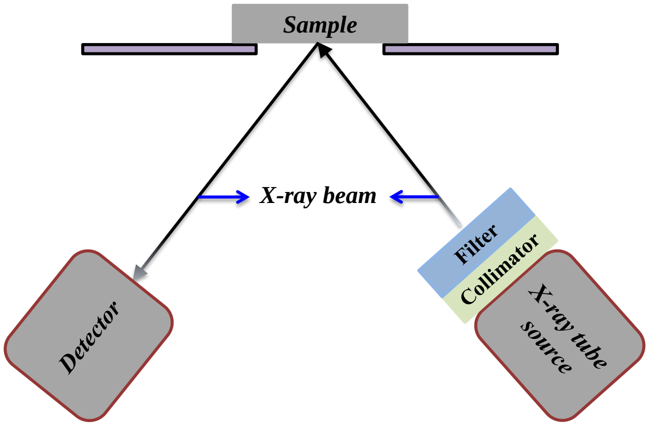

FIG. 3.3 Side view of the schematic representation of Tracor X-ray Spectrace 5000 fluorescence machine used in this thesis.

Simplified schematic view of the EDXRF machine used for samples' characterization in this thesis is shown in Fig. 3.3. The generated x-ray beam passes through a 0.005 inch thin Beryllium window and is then collimated and filtered before striking the sample. The characteristic X-rays emitted from the specimen are collected at a solid-state detector which then resolves the energies of the X-ray photons with appropriate precision. The relative intensities are analyzed against energy to perform the data analysis. The relative intensity of the elements in the sample can be determined for the known spectrometer geometry using eq. 3.1

$$I_L = I_0 \omega_A g_L \frac{r_A - 1}{r_A} \frac{d\Omega}{4\pi} \frac{C_A \mu_A(\lambda_{pri}) \csc(\varphi)}{\mu_M(\lambda_{pri}) \csc(\varphi) + \mu_M(\lambda_L) \csc(\Phi_f)} . \quad (3.1)$$

The quantities used in equation 3.1 are defined below: I_L is the line intensity of the composition to be measured, I_0 is the intensity of the primary beam with an effective wavelength, λ_{pri}, λ_{pri} denotes effective wavelength of the primary X-ray beam, λ_L represents wavelength of the measured line of the composition, g_L denotes fractional value of the measured line of the sample, r_A is the absorption edge jump ratio of the composition A, C_A is concentration of the composition A, $d\Omega/4\pi$ is the fractional value of the fluorescent X-ray which is directed towards the detector, $\mu_A(\lambda_{pri})$ is mass absorption coefficient of the composition A for λ_{pri}, $\mu_M(\lambda_{pri})$ is the mass absorption coefficient of the matrix for λ_{pri}, $\mu_M(\lambda_L)$ denotes mass absorption coefficient of the matrix for line, λ_L related to the composition, φ is incident angle of the primary x–ray beam, and Φ_f represents the angle of reflection of the fluorescent x–ray beam.

The elemental compositions of the $Ge_{1-x-y}Sn_xMn_yTe$ crystals in this thesis were obtained via EDXRF technique which yielded the results within ≈10% of the typical relative uncertainty. These samples showed slight inhomogeneity in the entire range of the alloyed concentrations. The inhomogeneity measured for $Ge_{1-x-y}Sn_xMn_yTe$ samples was about the relative uncertainty of the EDXRF technique which was smaller than ~10% of the estimated molar ratio.

3.3 X-ray diffraction

X-ray diffraction is a widely used technique to determine the crystal structure of materials. This method finds its uses in a broad range of materials which include mono and polycrystalline solids, amorphous materials and crystalline-amorphous mixtures. x-ray diffraction is also used to determine the size of crystallites and phase analysis of the materials. The principle of HRXRD technique is based on the concept of wave interference developed by two English physicists, Sir W. H. Bragg and (his son) Sir W. L. Bragg in 1913. They worked on the relationship between incident and reflected beams of x–rays to understand why the beams reflected from crystal surfaces make certain angles. In recognition of the Braggs' work focused on determining the crystal structure of NaCl, ZnS and diamond, they received the 1915's Nobel Prize in physics for this breakthrough work. The Braggs' relationship developed for diffraction of electromagnetic waves from periodic crystal lattices was formulated in the form of eq. 3.2.

$$n\lambda = 2d\sin\theta \qquad (3.2)$$

In eq. 3.2, n denotes an integer, λ represents wavelength of the incident x–ray beam, the parameter d shows distance between parallel atomic planes in the crystal which reflect the incident x–ray beam whereas θ is the angle between the incoming x–ray beam and the diffracting crystal planes. The x–ray beam is incident on the crystal surface which reflects a part of the beam from a shallow lattice plane. The remaining part of the x-ray beam penetrates into the material's surface. The x–ray beam that enters the crystal is subsequently reflected from the inner atomic planes as shown in Fig. 3.4. The reflected x–ray beams are being detected and histogram is made as a function of θ. In order to satisfy conditions in equation 2.1, the distance between the regular arrays of atoms should be of the order of the wavelength of incident beam, typical value is a few angstroms (Å), 1 Å = 10^{-10} m. Suitable wavelength range for studying the crystal structures of solids is around 0.1 Å – 100 Å. A family of planes in the sample produces a diffraction peak only when the conditions are set for constructive interference. The diffracted beams yield constructive interference only if the distance $2d\sin\theta$ is equal to $n\lambda$. For integer values of n, the distance $2d\sin\theta$ will always produce constructive interference at the detector for the beams diffracted from all parallel planes. The analysis of the interference pattern provides information about the crystal structure of the material.

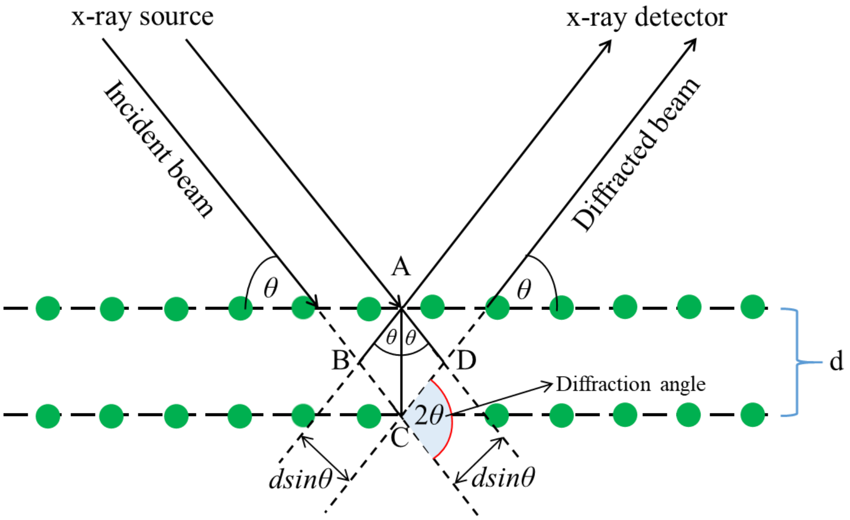

FIG. 3.4 X–ray diffraction by a crystalline material where regular atomic arrays are shown by horizontal lines with lattice points representing periodic arrangement of atoms. The incident beam diffracted from a deeper plane (point C in the figure) covers longer distance than the one from the shallow plane thus setting conditions for Bragg's law in terms of beam's wavelength. The distance BC+CD = 2*dsin*θ is the multiplicity of λ for constructive interference.

The HEXRD studies can also be used to determine the lattice constants and volume of the unit cell of the crystal. The lattice parameters along x, y and z axis are typically denoted by a, b and c whereas the angles formed by these axes are represented by α, β and γ. The information about the above mentioned lattice parameters can be used to determine the volume of the unit cell.

The crystal structure of the $Ge_{1-x-y}Sn_xMn_yTe$ samples studied in this thesis was investigated at room temperature only by means of high resolution multipurpose XPert Pro MPD x–ray diffractometer operated with a conventional $CuK_{\alpha1}$ tube x–ray source of wavelength, λ = 1.5406 Å. Detailed results of the crystal structure and lattice parameters of $Ge_{1-x-y}Sn_xMn_yTe$ samples will be presented in the next chapter.

3.4 Magnetometric measurement techniques

3.4.1 AC/DC magnetometer

The $Ge_{1-x-y}Sn_xMn_yTe$ crystals were investigated to understand their magnetic properties in the broad alloying range of $0.2 \leq x \leq 0.8$ and $0.02 \leq y \leq 0.086$. The LakeShore 7229 susceptometer/magnetometer system was used for the magnetometric studies in which the temperature was varied from T = 4.2 K to 120 K. The frequency dependent magnetic susceptibility, χ_{AC}, measurements were performed at an alternating magnetic field, H_{AC} = 10 Oe, and frequency up to f = 10 kHz. In addition, LakeShore 7229 magnetometer equipped with a superconducting magnet which generates a DC magnetic field up to H = 90 kOe was used to obtain the magnetic field dependent magnetization, $M(H)$, results. Schematic representation of the LakeShore 7229 susceptometer/magnetometer used for magnetometric studies in this thesis is shown in Fig. 3.5. The operating principle and specifications of the LakeShore 7229 magnetometer are provided below.

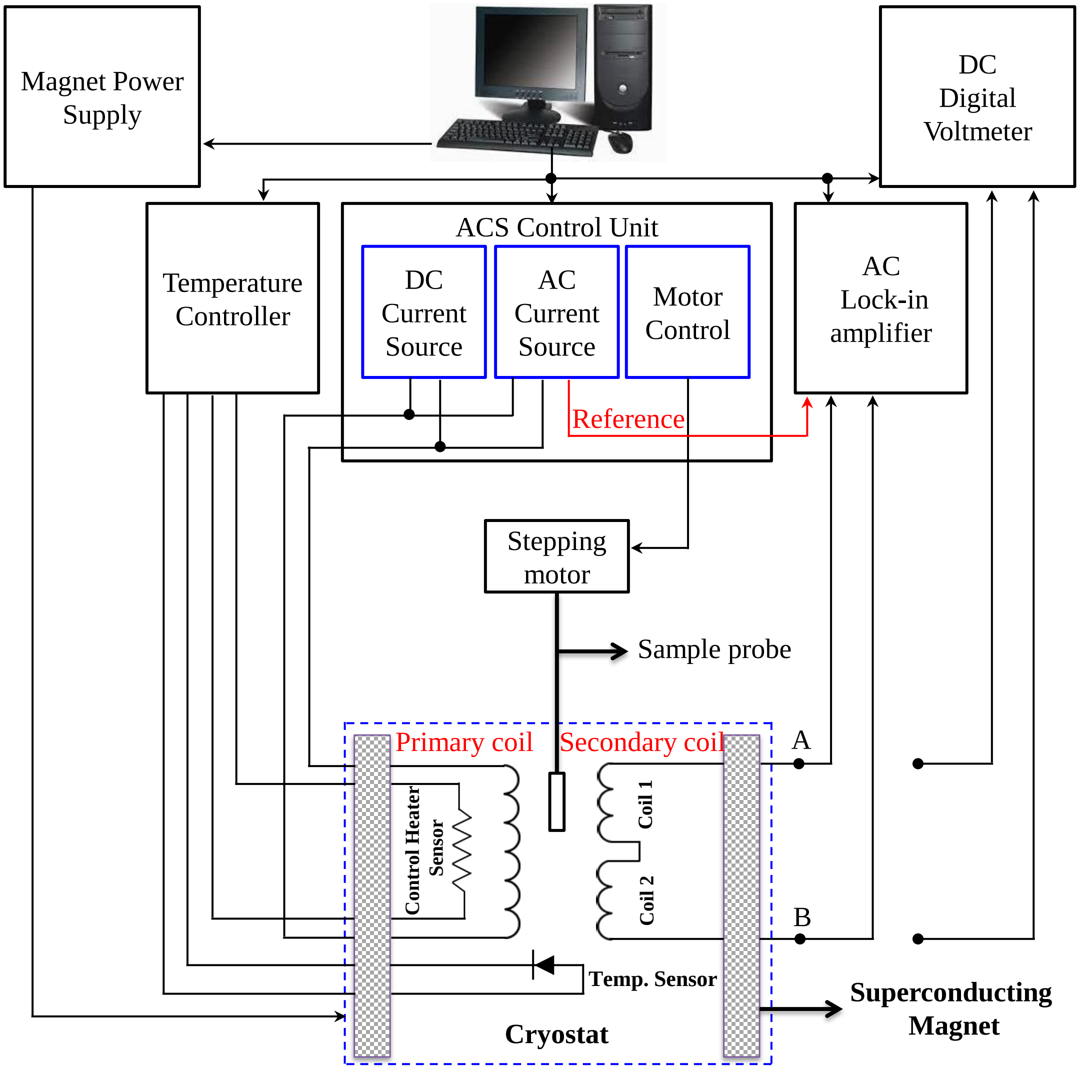

FIG. 3.5 Schematic representation of the experimental setup (LakeShore 7229 susceptometer/magnetometer) used for the AC and DC magnetic studies of $Ge_{1-x-y}Sn_xMn_yTe$ crystals.

3.4.2 Magnetic susceptibility measurements

During magnetic susceptibility measurements, the sample is held inside a sample-holder which is transferred inside the cryostat before performing the measurements. The sample chamber is cooled down to $T \approx 4.2$ K by filling the magnet with liquid helium. In order to stabilize the temperature during measurements, a heating source is installed near the sample where the temperature is monitored by a resistance thermometer. For the purpose of temperature stabilization, LakeShore DRC 91CA temperature controller is installed in the setup which monitors thermometer and controls heater power. A combination of rotary pump and a turbomolecular pump work together to control the helium gas pressure inside the operating chambers of the magnetometer. In the AC susceptometer, the sample that needs to be measured is exposed to a small alternating magnetic field. The magnetic flux variations caused by the sample are picked up by a sensing coil wound around the sample space. This flux variation induces voltage in the secondary coil and the voltage is detected via lock-in amplifier. The primary coil is connected to LakeShore 140, an AC current source which in turn generates an alternating magnetic field. The primary coil can generate magnetic from 0.00125 Oe to 30 Oe with high stability of about 0.05%. Two identical sensing coils (secondary coils) are placed inside the primary coil which are positioned symmetrical to each other and permit uniform magnitude of electric current. If the configuration of the sensing coils is such that they are perfectly symmetric and wound opposite to each other, the lock-In amplifier does not detect any voltage when the coil assembly is empty (sample is not placed inside). After the sample is placed inside, this causes imbalance of the voltage. The measured voltage is proportional to the magnetic susceptibility of the sample. Due to the possible imperfection in the secondary coils and external factors (temperature or pressure difference between secondary coils), the offset voltage introduced by the secondary coil system U_{off} should be eliminated. For this purpose, each measurement was carried out in two stages. In the first stage, the sample was located in the lower secondary coil. The voltage $U_1 = U_{\mathrm{sam}} + U_{\mathrm{off}}$ is read where U_{sam} is the voltage induced by the sample present in the coil space. Then the rest of the measurement is performed by placing the sample in the upper secondary coil, obtaining the voltage: $U_2 = -U_{\mathrm{sam}} + U_{\mathrm{off}}$. The voltage coming only from the sample can be calculated from the relationship $U_{\mathrm{sam}} = (U_1 - U_2) / 2$.

In case of the magnetic susceptibility measurements, the obtained values extract both in-phase or real part, $\mathrm{Re}(\chi_{\mathrm{AC}})$, and out of phase or imaginary, $\mathrm{Im}(\chi_{\mathrm{AC}})$, components of the total magnetic susceptibility. Such complex susceptibility response is obtained when the frequency of the oscillating magnetic field and the timescale of the magnetic relaxation of the sample are comparable. In this situation, there might be some phase lag resulting in dissipation when the external perturbation is slightly faster or slower than the natural frequency of the magnetic system. Thus, the $\chi_{\mathrm{AC}}(T)$ response is collected in two parts: the in-phase (real) and out-of-phase (imaginary) component respectively [228]. The AC magnetic susceptibility measured by the machine shown in Fig. 3.5 has a sensitivity up to 2×10^{-8} emu. In order to obtain accurate susceptibility result of the sample, the sample holder contribution is manually subtracted from the total (holder + sample) susceptibility data. In the rest of the thesis, the real and imaginary components of the magnetic susceptibility will be denoted by χ'_{AC}

and χ''_{AC}, respectively. The magnetic susceptibility obtained measurement procedure discussed above can be described as following

$$\chi = \frac{\alpha_k U_{sam}}{V f H_{\mathrm{AC}}} \tag{3.3}$$

Eq. 3.3 describes factors upon which the result of the AC magnetic susceptibility of the sample depends. Here α_k is interpreted as the calibration constant of the instrument which is associated with the system's geometry. The amplitude of the alternating magnetic field is denoted by H_{AC} and its frequency by f whereas V_{sam} shows the volume of the sample which is being investigated.

3.4.3 Magnetic hysteresis, *M*(*H*) measurements

Measurements of the magnetization of the $\mathrm{Ge}_{1-x-y}\mathrm{Sn}_x\mathrm{Mn}_y\mathrm{Te}$ samples were performed using the Weiss extraction method. The superconducting magnet used for these measurements produces a magnetic field of magnitude, $-90 \leq H \leq 90$ kOe with an accuracy of about 1 Oe by the use of a LakeShore 610 bipolar power supply. The term Weiss extraction method can generally be used to refer to methods which rely on detection of a change in flux when the sample is slowly removed/extracted with a constant speed from a sensing coil. This change in flux is directly proportional to the magnetization of the sample. In order to perform DC magnetization measurements, the AC current source shown in Fig. 3.5 is disabled. The lock-In current amplifier is replaced with high-speed integrating digital voltmeter (DVM). In this method, the purpose of DVM is to integrate over time the voltage induced in the secondary coils of the magnetometer. In order to move the sample between the two secondary coils, stepping motor is used, refer to Fig. 3.5. Due to the fact that the voltage sampling capabilities by the Keithley 182 voltmeter are many times faster than the sample movement time between the secondary coils, therefore the voltage vs time curve with a few hundred points can be measured. This voltage can be integrated over time and this integral is directly proportional to the magnetic moment of the sample, M, that can be described by the following relationship

$$\mathrm{M} = k_{\mathrm{m}} \cdot \frac{1}{2}\int_0^2 \boldsymbol{U}_{\mathrm{sam}}(t)dt. \tag{3.4}$$

The accuracy of measurement is carefully handled by executing two measurement cycles in which the voltage is measured when lifting and lowering the sample. This procedure eliminates the additional contribution to the voltage which arises from the asymmetry of the coils. Also, voltage value before the measurement process is subtracted from the result, which allows for the elimination of background noise. The obtained magnetization results are additionally revised by making corrections related to the demagnetization effects (magnetic field inside the sample may have a different value than the field induced by the magnet) and the DC calibration constant, k_{m}, which is related to geometry of the device. By introducing a number of these corrections, it is possible to measure the magnetic moment of the sample with an accuracy of 9×10^{-5} emu using the above mentioned Weiss extraction magnetometer. The DC calibration constant, k_m, is also related to the coefficient of AC susceptibility calibration, α. This relation can be described by the simplified equation $k_\mathrm{m} = \pi\alpha$. The two coefficients k_m and α in eq. 3.5 relate the magnetic flux coupled between a sensing coil and magnetized sample. Using the experimental setup shown above, the magnetization hysteresis, $M(H)$ curves of $\mathrm{Ge}_{1\text{-}x\text{-}y}\mathrm{Sn}_x\mathrm{Mn}_y\mathrm{Te}$ samples were determined by dividing the measured magnetic moment by the mass of the sample.

3.5 Electron transport techniques

Electron transport measurements of the $\mathrm{Ge}_{1\text{-}x\text{-}y}\mathrm{Sn}_x\mathrm{Mn}_y\mathrm{Te}$ crystals were made using two experimental setups. The first Hall effect measurement setup was used to study $\mathrm{Ge}_{1\text{-}x\text{-}y}\mathrm{Sn}_x\mathrm{Mn}_y\mathrm{Te}$ crystals over a wide temperature range between $T \approx 4.3$ K and 300 K which generates magnetic field induction not exceeding $H = 14$ kOe. In this setup, electrical conductivity and the Hall effect measurements were performed in a system equipped with an electromagnet. In the second experimental setup, transverse magnetoresistance and the Hall effect measurements were made using a measurement system equipped with a superconducting coil enabling the generation of a magnetic field with maximum induction not exceeding 130 kOe. Using this system, $\mathrm{Ge}_{1\text{-}x\text{-}y}\mathrm{Sn}_x\mathrm{Mn}_y\mathrm{Te}$ crystals were studied in the temperature range from $T \approx 1.6$ K up to about 30 K. Preparation of the samples for electron transport measurements and the above mentioned experimental setups are presented in the following sections.

3.5.1 Preparation of $\mathrm{Ge}_{1\text{-}x\text{-}y}\mathrm{Sn}_x\mathrm{Mn}_y\mathrm{Te}$ crystals for magnetotransport measurements

The electron transport measurements of the $\mathrm{Ge}_{1\text{-}x\text{-}y}\mathrm{Sn}_x\mathrm{Mn}_y\mathrm{Te}$ crystals were made using a standard six-contact technique using direct current. The Hall bars obtained after cutting were chemically cleaned in few stages as mentioned earlier in section 3.1.2. A small amount of gold chloride was applied on selected areas on which electrical contacts were to be connected. After that, gold (Au) wires were soldered to the samples' surfaces using indium (In) as soldering paste. The dimensions of the samples and electrical contacts were determined using a microscope equipped with a movable stage which is moved using micrometer screws. The uncertainties during the determination of samples' dimensions were about 0.01 mm. All six contacts attached to each sample were about 8 mm long. The crystals with contacts were then soldered in the sample holders for the electron transport measurements. Prior to starting the measurements, current-voltage linearity characteristics were checked for each sample. Typical schematic representation of a Hall bar with six contacts is shown in

Fig. 3.6. In Fig. 3.6, Hall bar is shown which represents the geometry used for electron transport measurements in this thesis. Six gold wires are shown which connect sample to the holder via horizontal pads using indium as soldering element. The surfaces of the pads were covered with indium paste and hence labeled as In pads in the Fig. 3.6. The direct current is denoted by *I*, and applied magnetic field is shown directed normal to the sample's surface. The contacts which measure longitudinal conductivity and Hall voltage are denoted by V_{xx} and V_{xy}, respectively.

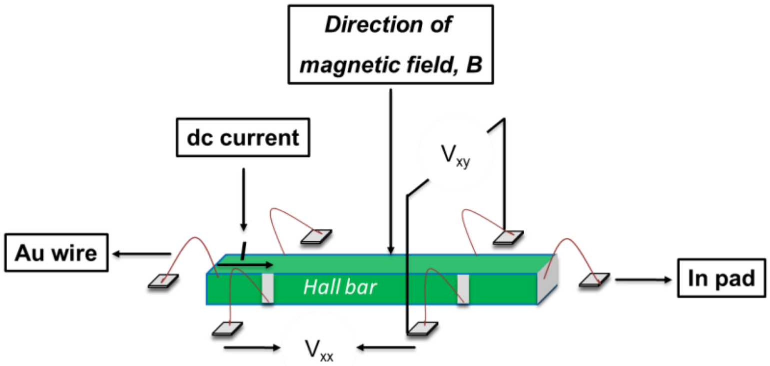

FIG. 3.6 A schematic sketch of the bar-shaped sample prepared for the electron transport measurements. The sample is connected to the Hall setup by six contacts dc current method.

3.5.2 Low field magnetotransport setup

The electrical properties of the $Ge_{1-x-y}Sn_xMn_yTe$ crystals were measured using low field Hall effect measurement system with a direct current of I = 100 mA, see schematic representation in Fig. 3.7. This setup can perform measurements over a wide temperature range between $T \approx 4.3$ and 300 K and generates magnetic field induction not exceeding H = 14 kOe. The electron transport studies of $Ge_{1-x-y}Sn_xMn_yTe$ crystals were focused on variable temperature charge carrier concentration, $n_h(T)$, carrier mobility, $\mu(T)$, and temperature dependent resistivity, $\rho_{xx}(T)$, measured from $T \approx 4.3$ to 300 K. Additionally, transverse magnetoresistance and, $\rho_{xx}(H)$ and Hall resistivity, $\rho_{xy}(H)$ components were investigated up to H = 14 kOe. The experimental setup shown schematically in Fig. 3.7 consists of a cryostat with forced helium flow that works as sample cooling medium. The cryostat enabled temperature stabilization over a wide range between 4.3 K and 360 K with an accuracy of approximately $T \approx 0.05$ K. Liquid helium flow from the tank labeled as [1] in Fig. 3.7 through the cryostat [2] was achieved by generating a negative pressure by a set of two vacuum pumps and the amount of helium flowing through the cryostat was controlled by a needle valve [10]. Helium cooled the sample denoted as [5] through heat exchanger labeled as [9]. In the upper part of heat exchanger is a resistance coil [8] which makes it possible to precisely stabilize the temperature. Temperature stabilization was performed using a four-probe measurement method [6]. The temperature readings were constantly checked and stabilized by connecting LakeShore 332 temperature controller to the system. Additionally, [3] represents electrical connections between the sample holder and the measurement system and [11] shows schematic diagram of sample holder.

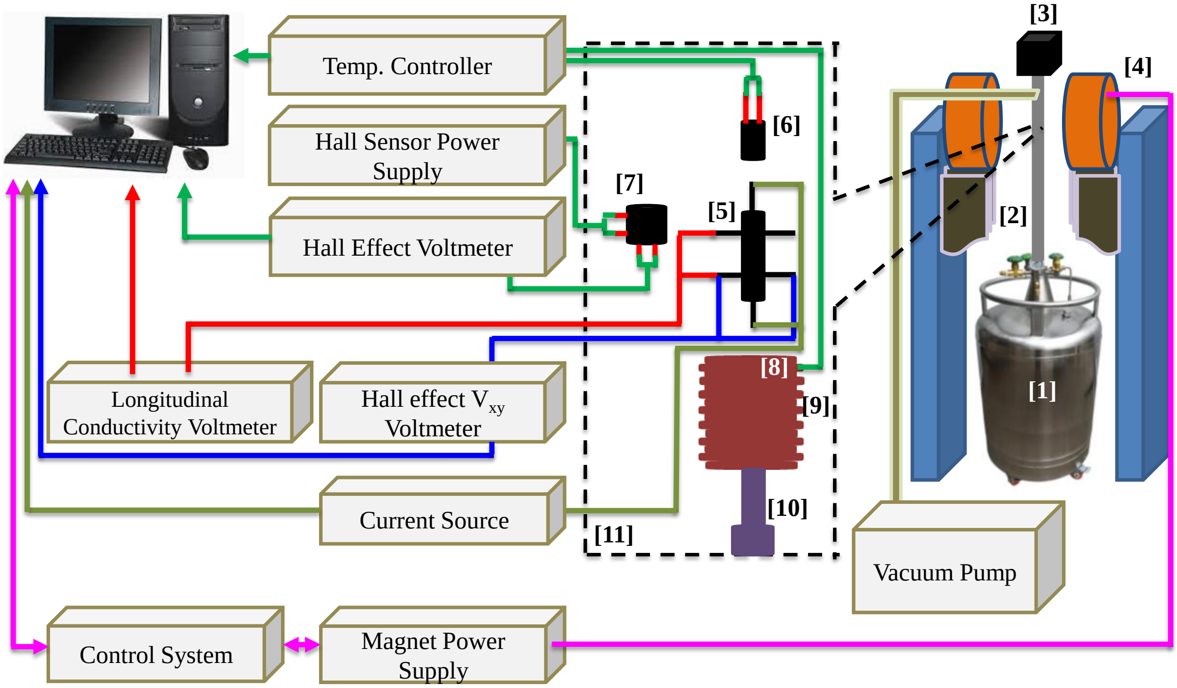

FIG. 3.7 Schematic representation showing the experimental measurement setup used for electron transport studies of $Ge_{1-x-y}Sn_xMn_yTe$ crystals. This is a low magnetic field setup which generates maximum magnetic field up to $H = 14$ kOe.

Magnetic field used during the Hall effect measurements was generated by an electromagnet [4] enabling magnetic induction in the range $-14 \leq H \leq 14$ kOe. The coil was powered by a bipolar power supply LakeShore 612 generating direct current in the range, $-25 \leq I \leq 25$ A and voltage $-25 \leq V \leq 25$ V. The power supply was controlled by a computer and LakeShore 601 controller. The value of the magnetic field induction near the sample was measured using a Hall effect sensor [7] powered by a DC power supply. The error in determining the value of external magnetic field that penetrates the sample was $\Delta H = 10$ Oe. The voltages related to resistivity components, V_{xx}, and V_{xy}, are recorded using Keithley 2182 nano voltmeters.

3.5.3 High field magnetotransport setup

Studies of the electrical properties of $Ge_{1-x-y}Sn_xMn_yTe$ crystals were investigated using high field magnetotransport setup shown in Fig. 3.8. In this thesis, two components, magnetoresistance and the

Hall resistivity were studied as a function of the applied magnetic field. The magnetotransport setup shown in Fig. 3.8 is equipped with a superconducting coil (Cryogenic Consultants Ltd) generating a magnetic field with a maximum induction of $-130 \leq H \leq 130$ kOe.

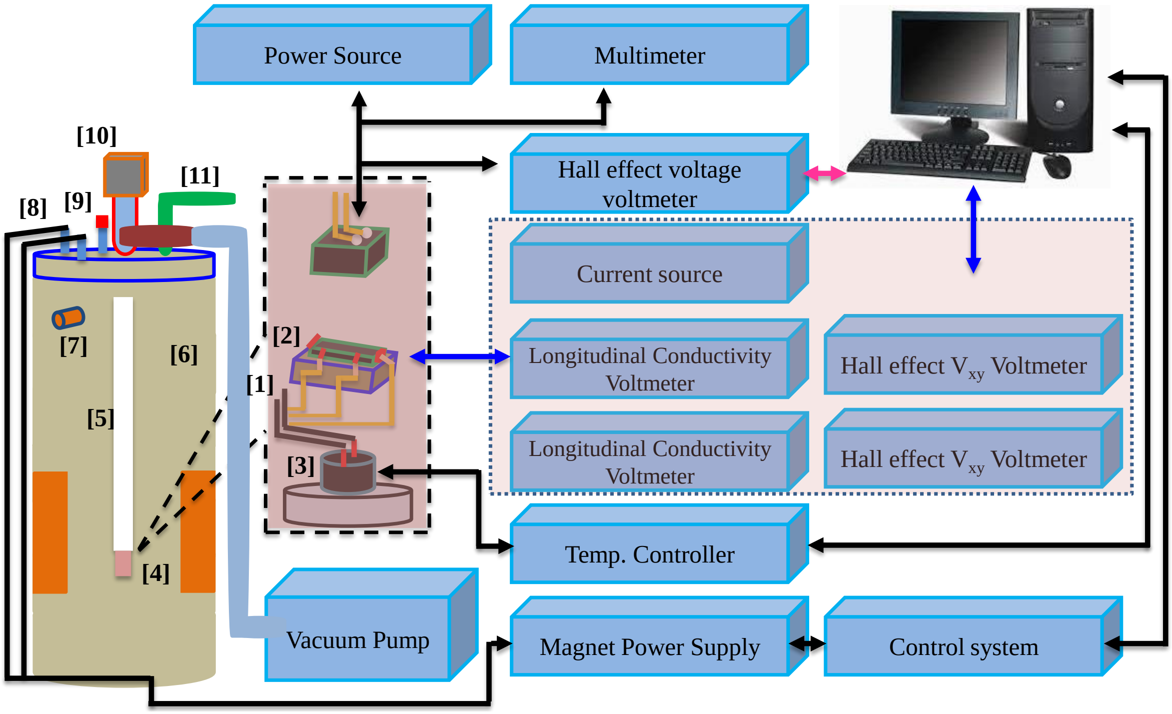

FIG. 3.8 Schematic representation showing high field experimental measurement setup used for magnetotransport studies of $Ge_{1-x-y}Sn_xMn_yTe$ crystals. This measurement setup can generate magnetic field up to $H = 130$ kOe.

Using high field superconducting magnet, the voltage measurements along and perpendicular to the DC current were performed as a function of the applied magnetic field normal to the surface of the sample. The superconducting magnet is operated when immersed in liquid helium and is powered by a computer controlled Oxford 612 bipolar generating power supply with direct current between $-94 \leq I \leq 94$ A and voltage $-5 \leq V \leq 5$ V. The magnitude of the magnetic field induction was measured using a Hall effect sensor in order to maintain accurate value of the applied field near the sample. The magnetic field sensor was powered by a stabilized current source operated with a current of 75 mA. The Hall effect voltage (proportional to the applied magnetic field) was measured using a voltmeter which was then recorded using a computer.

In Fig. 3.8, part of the system labeled as [1] shows magnified view of the sample holder, [2] denotes Hall bar of $Ge_{1-x-y}Sn_xMn_yTe$ crystals whereas [3] represents resistance thermometer. Superconducting coil is shown as [4], sample holder is labeled as [5], label [6] shows helium cryostat (not visible in the figure), [7] shows the valve that enables pumping of the space around the cryostat. Two cables which supply power to the superconducting coil are shown as [8] and the label [9] shows the valve that is used to fill the cryostat with liquid helium. The label [10] points to the electrical connections which connect sample holder to the system whereas [11] labels the exit part which lets the gaseous liquid out of the cryostat.

For high field electron transport measurements, the samples with same electrical contacts and dimensions as used in the low field Hall setup were connected to the sample holder and transferred down in the chamber. The experimental setup used to study $\mathrm{Ge}_{1-x-y}\mathrm{Sn}_x\mathrm{Mn}_y\mathrm{Te}$ crystals was equipped with a helium cryostat that enables magnetotransport measurements in a wide temperature range between $1.6 \leq T \leq 300$ K. The cryostat cools down the sample by means of pressure driven helium flow via vacuum pump which results in controlled helium flow. The helium flow rate is controlled by the needle valve and is adjusted according to the requirements of the measurements. The sample temperature (measured by the temperature stabilizer) was recorded during the measurements by computer. The samples were carefully investigated with the same values of DC current ($I = 100$ mA) as provided in the low field setup. The magnetoresistance and Hall the resistivity measurements were performed from $T \approx 1.6$ K up to 30 K. During the measurements, four voltages were recorded: two conduction voltages V_{xx} and two Hall voltages V_{xy}. This made it possible to check the electrical uniformity of the samples and enhanced the accuracy of the measured resistivity values. The longitudinal voltage values were recorded using Keithley voltmeters whereas the Hall voltages were measured using Keithley nano-voltmeters. All measured electrical voltages were then recorded using a computer connected to the measurement system.

CHAPTER 4

Structural characterizations of $Ge_{1\text{-}x\text{-}y}Sn_xMn_yTe$ multiferroics

This chapter presents the chemical compositions and crystal structure studies of $Ge_{1\text{-}x\text{-}y}Sn_xMn_yTe$ crystals at room temperature. The influence of alloying Sn and Mn on the polar crystal structure of α–GeTe was investigated up to the alloying contents, $x = 0.79$ and $y = 0.086$.

4.1 Chemical composition analysis

The bulk samples of $Ge_{1\text{-}x\text{-}y}Sn_xMn_yTe$ crystals studied in this thesis were grown via modified Bridgman method as described in detail in section 3.1. Four ingots were grown for the studies in this thesis in order to obtain $Ge_{1\text{-}x\text{-}y}Sn_xMn_yTe$ crystals with desired stoichiometric proportions. Out of a number of disc-shaped samples, four slices with thickness about 1 mm were selected from each ingot. The elemental compositions of the samples obtained from $Ge_{1\text{-}x\text{-}y}Sn_xMn_yTe$ ingots were determined using EDXRF technique; see section 3.2 for detailed description of the equipment and its working principle. The EDXRF technique used in this thesis allows for determination of elemental composition of the crystals with an uncertainty of about 10%. In terms of the chemical composition using EDXRF, the measurements showed homogeneous distribution of individual elements in the studied crystals. The measurement results showed that the chemical composition of $Ge_{1\text{-}x\text{-}y}Sn_xMn_yTe$ crystals changed as a function of ingot length along the crystal-growth axis. Among the crystals characterized for investigations in this thesis, four series of $Ge_{1\text{-}x\text{-}y}Sn_xMn_yTe$ crystals with the lowest relative inhomogeneity were selected. The first series of $Ge_{1\text{-}x\text{-}y}Sn_xMn_yTe$ samples included crystals in which Sn content showed very slight variation and remained relatively constant with $x \approx 0.183\pm0.001$, while the concentration of Mn ions changed within wide range of $0.027 \leq y \leq 0.06$. The second series included samples in which Sn content showed slightly larger variation in the range $x \approx 0.4\pm0.01$, while Mn content varied within broad range of $0.027 \leq y \leq 0.06$. For the third and fourth series, the concentration of Sn was close to $x \approx 0.59\pm0.05$ and $x \approx 0.75\pm0.04$, and Mn proportions were obtained in the range $0.030 \leq y \leq 0.086$ and $0.040 \leq y \leq 0.072$, respectively. The obtained results in the form of molar fractions of alloying elements Sn and Mn, i.e. x, and y, together with the measurement uncertainties in their determination are listed in Table I.

4.2 Crystal structure of Ge-rich $Ge_{1-x-y}Sn_xMn_yTe$ crystals

The $Ge_{1\text{-}x\text{-}y}Sn_xMn_yTe$ bulk crystals were investigated in the range, $2\theta = 20 - 145°$ in order to study the influence of the alloying elements, Sn and Mn on the room temperature crystal symmetry of α–GeTe. In Fig. 4.1(a–d), the HRXRD patterns of the samples with different Sn and Mn concentrations are shown.

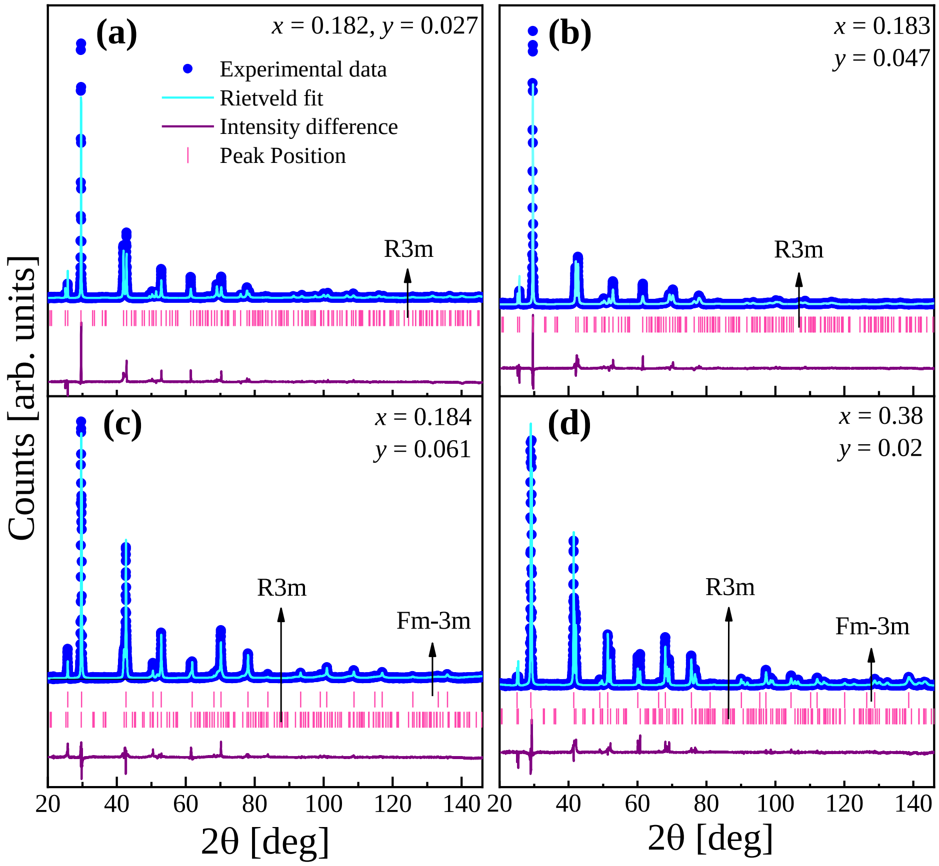

FIG. 4.1 X-Ray diffraction results of $Ge_{1-x-y}Sn_xMn_yTe$ multiferroic samples with (a) $x = 0.182$, $y = 0.027$, (b) $x = 0.183$, $y = 0.047$ (c) $x = 0.184$, $y = 0.061$ and (d) $x = 0.38$, $y = 0.02$. In (c,d), the two phase coexistent symmetry is shown by R3m and Fm-3m peak positions.

In Fig. 4.1, the experimental diffraction patterns are shown as blue points for all samples whereas the light-blue lines represent the obtained fits to the data using Rietveld refinement method. Rietveld analysis is generally used for refinement of the crystal structures based on powder x-ray diffraction [229]. The method of Rietveld refinement was initially developed for the analysis of crystal structures investigated with neutron-diffraction [229,230] which subsequently expanded to refinement of diffraction results with synchrotron radiation and x-ray powder diffraction [231–234]. As shown in Fig. 4.1, good fits were obtained where the Bragg peaks were successfully indexed to R3m and Fm-3m symmetries. The crystal structure is refined by comparing the calculated diffraction pattern with the measured pattern where the reliability index measures the difference between the two patterns. For $Ge_{1-x-y}Sn_xMn_yTe$ samples, the intensity difference between the measured Bragg peaks and Rietveld fits is denoted by the purple lines at the bottom of each panel whereas the Bragg peaks are represented by vertical ticks.

The samples with low Sn content $x = 0.182$, 0.183 and $y = 0.027$, 0.047 exhibited low symmetry rhombohedral crystal structure (space group R3m) at room temperature (JCPDS, no.47–1079) [235] which is inherited from the parent polar GeTe crystal demonstrating a spontaneous ferroelectric polarization due to distortion in the [111] direction [30,31,103]. Furthermore, the samples with $x =$ 0.184, 0.38 and $y = 0.061$, 0.02 crystallize in mixed phase in which the R3m and cubic (space group Fm-3m with JCPDS, no.54–0498) symmetries coexist [236]. The HRXRD patterns of R3m and mixed phase R3m/Fm-3m crystal structures are presented in Fig. 4.1(a,b) and (c,d), respectively. Thus, in the Sn and Mn content range $x = 0.182 – 0.38$ and $y = 0.02 – 0.061$, the $Ge_{1\text{-}x\text{-}y}Sn_xMn_yTe$ HRXRD patterns reveal two crystal symmetries with R3m and Fm-3m space groups.

Comparing the present crystal structural results to the previous work on $Ge_{1\text{-}x\text{-}y}Sn_xMn_yTe$ crystals [220,222] which exhibited pure rhombohedral symmetry, this work shows that the R3m symmetry in the low Sn regime is consistent with the previous results. As the concentrations of Sn and Mn ions are increased from $x = 0.183$ and $y = 0.047$ to $x = 0.184$ and $y = 0.061$, the crystal structure manifests a phase transition from rhombohedral to cubic symmetry. In case of ternary alloys, Kriener *et al.*, claimed that heat treated $Ge_{1–x}Mn_xTe$ switches from polar to non-polar structure at about 12% Mn [237] whereas Przybylińska *et al.*, [103] reported structural transition at Mn content close to 30%. The ferroelectric to paraelectric structural phase transition occurs at $x = 0.4$, $y = 0.052$ for the samples studied in this thesis which is compositionally more complicated than the ternary compounds studied in [103,237] due to alloying GeTe with two elements. The coexistence of R3m and Fm-3m phases for $Ge_{1\text{-}x\text{-}y}Sn_xMn_yTe$ with $x = 0.184$ and $y = 0.061$ might indicate a phase-boundary at which the polar crystal symmetry of $Ge_{1\text{-}x\text{-}y}Sn_xMn_yTe$ samples switches to a non-polar cubic structure typical of SnTe at room temperature [238]. Therefore, compositions with low contents of Sn and Mn are promising materials to study the room temperature multiferroic features due to the spatially broken crystal symmetry. Further incorporation of Sn and Mn ions beyond $x = 0.184$, 0.38 and $y = 0.02$, 0.061 in the host α–GeTe, is projected to convert the crystal symmetry from rhombohedral type to cubic rock salt Fm-3m phase.

4.3 Crystal structure of Sn-rich $Ge_{1–x–y}Sn_xMn_yTe$ crystals

Due to the high solubility of Sn and Mn ions in *α*–GeTe lattice, the proportions of Sn and Mn ions were further boosted beyond the alloying concentrations shown in Fig. 4.2. The persistent two-phase symmetry in Fig. 4.2(c,d) over such a wide chemical composition range (from $x = 0.184$ to 0.38 and $y = 0.02$ to 0.061) show that the transition from polar to pure non-polar symmetry is rather slow and ferroelectric features can be studied up to $x + y \approx 0.45$ in $Ge_{1-x-y}Sn_xMn_yTe$. With further increase in Mn content up to $y = 0.052$ with nearly the same Sn amount, the boundary consisting of R3m and Fm-3m phases switches into a single phase rock salt symmetry for the entire series of Sn-rich crystals, Fig. 4.2(a-f).

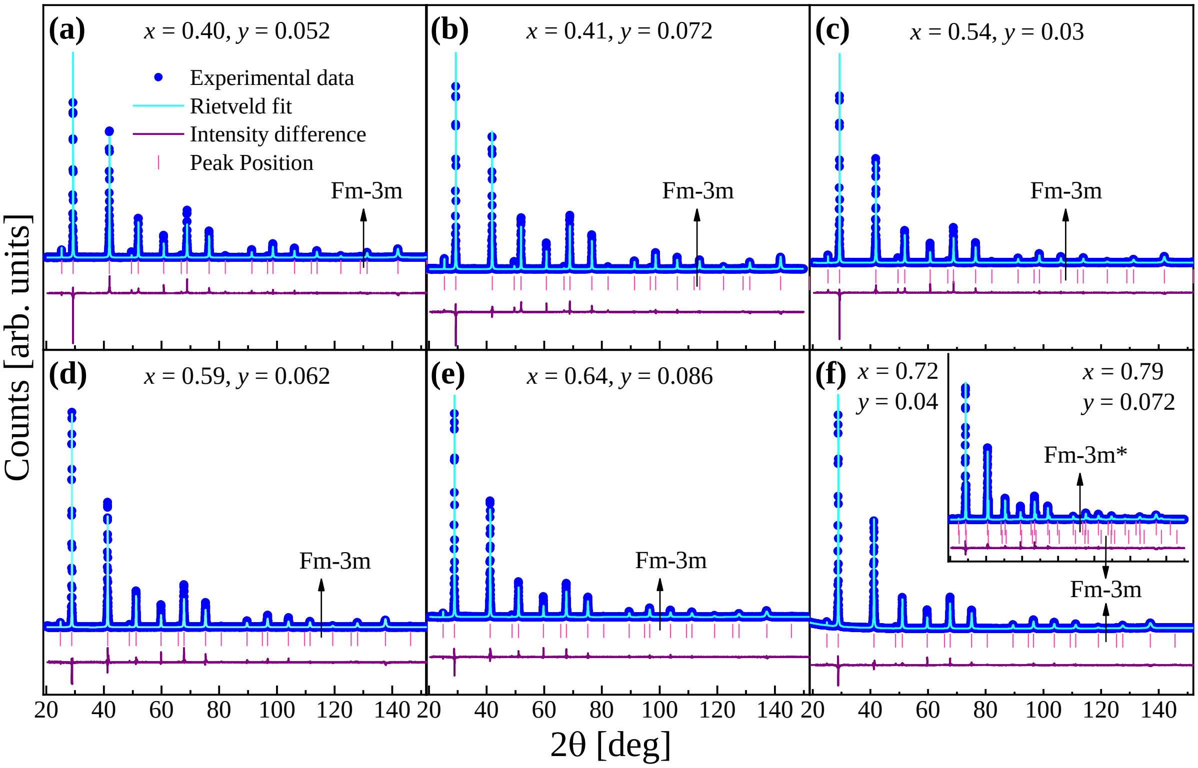

FIG. 4.2 X-ray diffraction results of $Ge_{1-x-y}Sn_xMn_yTe$ crystals with (a) $x = 0.4$, $y = 0.052$, (b) $x = 0.41$, $y = 0.072$ (c) $x = 0.54$, $y = 0.03$ (d) $x = 0.59$, $y = 0.062$ (e) $x = 0.64$, $y = 0.086$ (f) $x = 0.72$, $y = 0.04$ whereas the inset of (f) shows sample with $x = 0.79$, $y = 0.072$ which manifests two cubic symmetries with different lattice parameters.

However, the crystal with the highest Sn and Mn concentrations, $x = 0.79$ and $y = 0.072$ exhibits two rocksalt phases with different lattice parameters indicated in Fig. 4.3 by Fm-3m and Fm-3m* labels. In the Sn-rich crystals, the R3m phase of α–GeTe slowly disappears and SnTe Fm-3m cubic phase dominates at room temperature. Ferroelectric order in rhombohedral $Ge_{1-x-y}Sn_xMn_yTe$ arises due to the average relative displacement of Te sublattice from the centrosymmetric position within the unit cell and subsequently produces a permanent electric dipole; see R3m symmetry in Fig. 4.3. In the presence of an electric dipole, the elongation of the unit cell along the c-axis and therefore the deviation of c/a ratio (where a and c are lattice constants) from unity are used as a signature of the ferroelectric phase. In case of $Ge_{1-x-y}Sn_xMn_yTe$ samples, the c/a ratio and corner angle, α, become unity and 90 degree, respectively at $x + y \approx 0.45$ which results in the vanishing of the electric dipole.

The phase transition at room temperature of $Ge_{1-x-y}Sn_xMn_yTe$ samples as a function of Sn and Mn concentrations is shown in Fig. 4.3. In the low alloying regime with $x \leq 0.4$ and $y \leq 0.047$, rhombohedral symmetry was observed as shown by the schematic R3m unit cell. The R3m unit cell shows slightly distorted structure in the [111] direction where the angle $\alpha < 90°$. In this alloying regime, the lattice constants, a, and c, are shown which exhibit very small variation as the alloying contents are increased. In the alloying regime, $0.4 \leq x \leq 0.8$, the crystal structure of $Ge_{1-x-y}Sn_xMn_yTe$ samples switched to high symmetry Fm-3m phase. Within this alloying regime, the lattice constant, a, showed slight increase between $x = 0.6$ and 0.8. For the sample with the highest alloying concentration $x = 0.79$ and $y = 0.072$, the crystal showed Fm-3m phase with different lattice parameter values where the second cubic phase is shown as Fm-3m*. It should be noted that the two coexistent cubic phases with different lattice constants were observed only for $x = 0.79$ and $y = 0.072$.

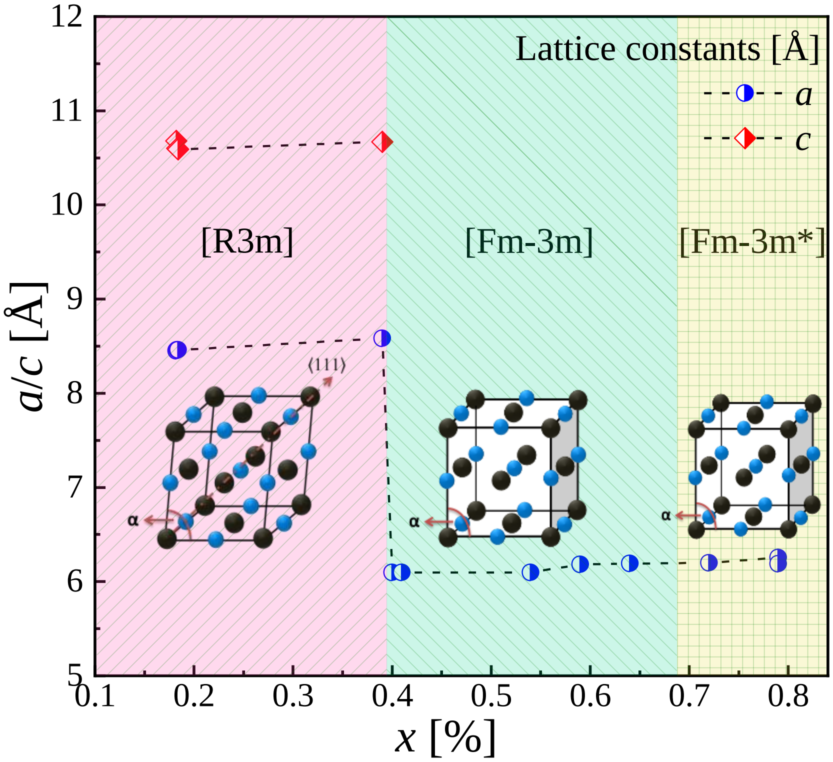

FIG. 4.3 Lattice parameter values, a and c as a function of alloying concentrations, x and y, here x-axis represents Sn only. The corner sites of the unit cells (black) represent Ge, Sn, Mn whereas the blue symbols represent Te ions.

For the $Ge_{1-x-y}Sn_xMn_yTe$ crystals discussed above, the chemical composition results and lattice constants (obtained from Rietveld refinement method) are summarized in Table I.

TABLE I: Chemical compositions of the alloying elements extracted from the EDXRF measurements and crystallographic parameters obtained from the HRXRD studies of $Ge_{1-x-y}Sn_xMn_yTe$ crystals are presented in the following table. Here x and y denote the molar contents of Sn and Mn ions, a and c represent the unit-cell parameters, the crystal structure type and specific space groups deduced from the HRXRD measurements are also provided.

$x \pm \Delta x$	$y \pm \Delta y$	$a \pm a$ [Å]	$c \pm c$ [Å]	crystal structure	space group
0.182 ± 0.01	0.027 ± 0.006	8.450 ± 0.002	10.68 ± 0.002	rhombohedral	R3m
0.183 ± 0.01	0.047 ± 0.006	8.460 ± 0.002	10.6 ± 0.002	rhombohedral	R3m
0.184 ± 0.01	0.060 ± 0.006	8.460 ± 0.002 5.994 ± 0.002	10.59 ± 0.02 –	rhombohedral /cubic	R3m Fm-3m
0.39 ± 0.03	0.020 ± 0.002	8.581 ± 0.002 6.161 ± 0.002	10.67 ± 0.02 –	rhombohedral /cubic	R3m Fm-3m
0.40 ± 0.04	0.052 ± 0.005	6.097 ± 0.002	–	cubic	Fm-3m
0.41 ± 0.04	0.072 ± 0.007	6.097 ± 0.002	–	cubic	Fm-3m
0.54 ± 0.05	0.030 ± 0.003	6.098 ± 0.002	–	cubic	Fm-3m
0.59 ± 0.06	0.062 ± 0.006	6.182 ± 0.002	–	cubic	Fm-3m
0.64 ± 0.06	0.086 ± 0.009	6.192 ± 0.002	–	cubic	Fm-3m
0.72 ± 0.07	0.040 ± 0.004	6.198 ± 0.002	–	cubic	Fm-3m
0.79 ± 0.08	0.072 ± 0.007	6.254 ± 0.002	–	cubic	Fm-3m
		6.19 ± 0.002	–	cubic*	Fm-3m*

CHAPTER 5

Magnetic interactions in $Ge_{1-x-y}Sn_xMn_yTe$ multiferroics

This chapter of the thesis presents detailed studies of the magnetic interactions in $Ge_{1-x-y}Sn_xMn_yTe$ bulk multiferroics in the broad alloying range. The possibilities of tuning magnetic interactions are studied as a function of both Sn and Mn concentrations. The presence of locked-in spin glass, cluster glass and ferromagnetic order depending on the alloying compositions is also studied. In addition, magnetic phase diagram of $Ge_{1-x-y}Sn_xMn_yTe$ will be constructed based on the findings deduced from both the AC and DC magnetometric measurements.

5.1 Introduction

Tuning of materials' functional properties based on the randomly distributed magnetic ions in a standard semiconductor has met plentiful efforts both on experimental and theoretical parts [83]. Contrary to existing semiconducting materials which utilize electronic charge only, the integration of spin with tunable semiconducting characteristics in a single system can lead to new efficient and miniaturized designs [46,83,239]. For the purpose of developing functionally efficient materials, diluted magnetic semiconductors (DMS) from group II–VI [84–89], III–V [108,109] and IV–VI [18–22,31] are widely investigated compounds. Until now, several DMS materials have shown pronounced achievements in moving the magnetic transition temperature, T_C, higher for instance $Ga_{1-y}Mn_yAs$ epitaxial layers with about 11% – 13% of Mn content reached $T_C = 185$ K as reported by Olejník *et al*., [240] and 200 K by Chen *et al*., in nano-engineered $Ga_{1-y}Mn_yAs$ films [21].

Among a large number of materials, IV–VI DMS have several advantages e.g. high solubility of magnetic ions [241], tuning of ferroelectric order and its connection to spin-texture [30], entanglement phenomenon resulting from spin orbit interaction and magnetic order [31], and spin-light conversion owing to the higher-order Dresselhaus SOI in materials having broken symmetry e.g. α–GeTe [24]. Owing to the broken symmetry along with small band gap of α–GeTe, this system and its alloys provide an appropriate foundation to tune spin-texture by ferroelectric polarization for device applications [30,122,123]. In the context of FM order, α–GeTe alloyed with Mn has demonstrated appreciable enhancement of FM phase up to 200 K [22] since the pioneering work on $Ge_{1-x}Mn_xTe$ in 1966 [242]. The Curie temperature and magnetotransport properties of DMSs can be manipulated by altering the charge density as a consequence of varying magnetic ions' content [52].

In that context, linear relationship between T_C and Mn content in $Mn_{1-x}Ge_x$ was shown to change between 25 K and 116 K by varying doping concentration [243].

It is imperative to understand the origin of magnetic interactions in alloys with Mn; e.g. $In_{1-x}Mn_xAs$ was studied in which the magnetic, electrical and optical properties were demonstrated as a function of Mn content [244]. Other example is the fully charge carrier compensating $Ga_{1-y}Mn_yAs$ [245] which displayed antiferromagnetic order between Mn impurities. The magnetic order in IV–VI crystals e.g. $Sn_{1-y}Mn_yTe$ and $Ge_{1-y}Mn_yTe$ with $n \sim 10^{19}$ cm^{-3} is believed to be due to the indirect RKKY exchange interaction mediated by conduction charge carriers [18,22,31,103,168]. As an example, $Pb_{1-y}Mn_yTe$ with low charge carrier density exhibited a paramagnetic (PM) state [246], a SG state was detected for Mn content, $y \leq 0.2$ [247] below $T = 1$ K, and FM order was shown when the charge carrier density was about 7×10^{20} cm^{-3} [248]. These findings hinted towards diverse range of magnetic interactions which lead to understanding the complexity of magnetic interactions in IV-VI DMS and tuning the functional temperature limits up towards room temperature.

In this chapter of the thesis, the quaternary $Ge_{1-x-y}Sn_xMn_yTe$ crystals with diamagnetic Sn, $x = 0.182$–0.79 and paramagnetic Mn, $y = 0.02$–0.086 ions, respectively were studied. The alloying concentrations of Sn and Mn ions are significantly varied to investigate the compositional influence on magnetic interactions in $Ge_{1-x-y}Sn_xMn_yTe$. Specifically, the influence of alloying on magnetic exchange constant and magnetic order in $Ge_{1-x-y}Sn_xMn_yTe$ was studied. Since compositions with wide Mn content have already been studied, the studies of these alloys with high Sn content are unexplored and offer prospects to alter the type of magnetic interactions in $Ge_{1-x-y}Sn_xMn_yTe$ multiferroics. $Ge_{1-x-y}Sn_xMn_yTe$ alloys with large variation in Sn content demonstrate substantial variation in magnetic ordering. Specifically, the influence of Sn-rich regime on the locked-in spin-disordered state is presented. Prior to the current results, previous work on $Ge_{1-x-y}Sn_xMn_yTe$ bulk crystals revealed several different magnetic states e.g. conventional SG [220] and FM characteristics for doping contents of Sn = 0.09 and Mn = 0.039 [222]. This thesis extends far beyond Refs. 220,222 by aiming to examine the whole series of Sn from $x = 0.2$ to 0.8. In this sense, $Ge_{1-x-y}Sn_xMn_yTe$ samples with wide compositional variation were studied to convey an inclusive description of the magnetic interactions induced in $Ge_{1-y}Mn_yTe$-$Sn_{1-y}Mn_yTe$ mixed crystals.

5.2 Magnetic Interactions in $Ge_{1-x-y}Sn_xMn_yTe$ Alloys

5.2.1 AC Magnetic Susceptibility

The detailed studies of magnetic phenomena in $Ge_{1-x-y}Sn_xMn_yTe$ multiferroics begin with the temperature dependent AC magnetic susceptibility, $\chi_{AC}(T)$, results obtained with the Lakeshore 7229 AC susceptometer. Magnetic field with amplitude, $H_{AC} = 10$ Oe and frequency, $f = 625$ Hz were fixed during the measurement performed between $T \approx 4.5$ to 120 K. For the crystals with $x \approx 0.2$, and $0.027 \leq y \leq 0.061$, both real, χ'_{AC}, and imaginary, χ''_{AC}, components of the AC susceptibility and the inverse of χ'_{AC} against temperature are shown in Fig. 5.1(a) and (b), respectively.

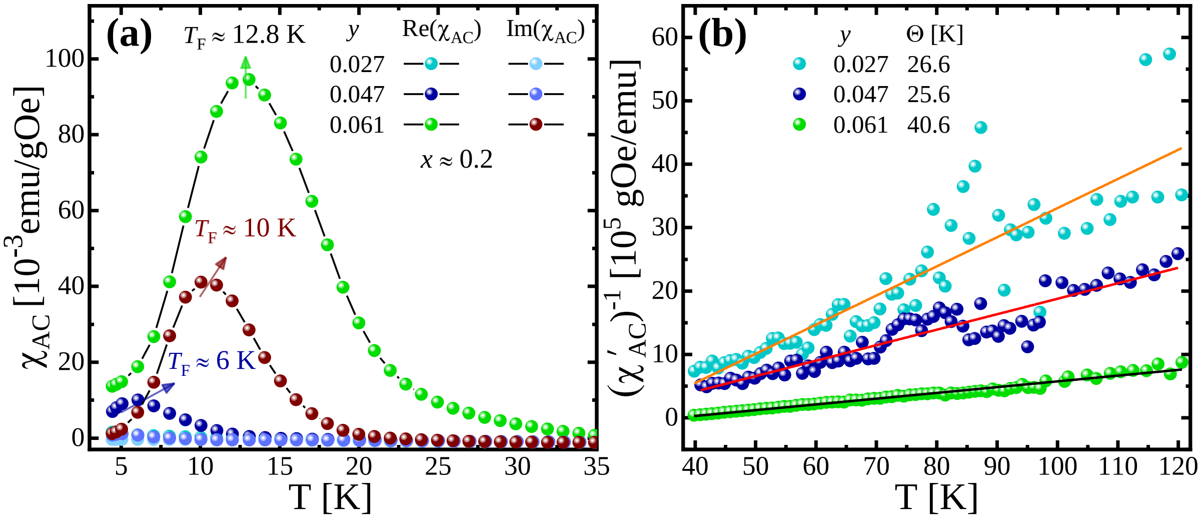

FIG. 5.1 (a) Real and imaginary components of the AC magnetic susceptibility, $\chi_{\mathrm{AC}}(T)$, as a function of temperature, T, for the samples with $x \approx 0.2$, and $0.027 \leq y \leq 0.061$. (b) The inverse of χ'_{AC} vs. T results where solid lines represent fits to the modified Curie-Weiss law in the high temperature PM regime.

In case of the crystals with $x \approx 0.2$ and $y = 0.047$, 0.061 as shown in Fig. 5.1(a), the χ'_{AC} results display nearly symmetric cusps at $T \approx 6$ K and $T \approx 12.8$ K, respectively which might be indicating transition from one of several magnetic orderings e.g. ferromagnetic, super paramagnetic, antiferromagnetic, spin glass or magnetic cluster glass to paramagnetic state. Such maxima in the $\chi'_{\mathrm{AC}}(T)$ curves of semimagnetic materials have been previously associated with either a spin glass or superparamagnetic state, though it might also indicate a transition from PM to FM phase [180,181]. For the crystal with $y = 0.061$, the imaginary part also manifests a clear cusp shape though at a slightly lower temperature, $T_{\mathrm{F}} \approx 10$ K. However, for $x \approx 0.2$ and $y = 0.027$ which has the smallest content of Mn ions, the χ'_{AC} vs. T curve shows small susceptibility value near $T \approx 4.5$ K. This might represent a transition to an ordered or glassy state below $T \approx 4.5$ K.

Since the alloying amount of Sn ions in these compositions is nearly constant, $x \approx 0.2$, therefore the crystals will be differentiated by the Mn content only in the following parts. The transition displayed by the maxima of the χ'_{AC} vs T curves moves towards higher temperature as the Mn concentration increases in Fig. 5.1. Furthermore, the magnitude of susceptibility maxima also shows a significant increase of about an order of magnitude as the Mn concentration is increased from $y = 0.047$ to 0.061. In addition to the shape of the cusps in the $\chi'_{\mathrm{AC}}(T)$ dependence, the behavior of these curves below maxima might also signify different magnetic states. In that context, the susceptibility curve for y = 0.047 shows slow decrease below the cusp maximum also called the freezing temperature; T_F, indicates a behavior similar to frustrated magnetic state. Unlike a cusp shaped $\chi'_{AC}(T)$ curve, a PM-FM transition is typically characterized by a fast decrease in the susceptibility curve near the transition temperature. In the current crystals, the appearance of the round and nearly symmetric cusp particularly displayed by the sample with y = 0.047 reflects that the magnetic state could represent either a SG or another similar magnetically frustrated state [181]. In order to determine the exact magnetic state from $\chi_{AC}(T)$ curves in Fig. 5.1, detailed magnetic studies and data analysis are required which will be later presented in the frequency dependent $\chi'_{AC}(T)$ and magnetic field dependent magnetization studies.

In addition to the anatomy of susceptibility curves, the magnetic $\chi_{AC}(T)$ results are further evaluated by assessing the inverse of χ'_{AC} dependences with the modified Curie-Weiss (CW) law. The modified CW law is of great significance to understand the behavior of the magnetic materials utilizing the temperature range above the transition point. In that context, the $(\chi'_{AC})^{-1}$ results fitted to modified CW law (eq. 5.1) are shown in Fig. 5.1(b) which yield good fits for all samples

$$\chi'_{AC} = \frac{C}{T - \Theta} + \chi_{dia}. \tag{5.1}$$

Eq. 5.1 was used to analyze the inverse of χ'_{AC} vs T results of $Ge_{1-x-y}Sn_xMn_yTe$ samples by appropriate fitting to the modified CW law, see Fig. 5.1(b). The CW constant, C, diamagnetic term χ_{dia} of the host lattice GeTe and the CW temperature, Θ, were used as fitting parameters. It is apparent from the fitted lines that the samples follow modified CW law in the PM regime for all compositions presented in Fig. 5.1. Since the host material GeTe belongs to group IV-VI and is diamagnetic semiconductor, it adds its diamagnetic term; $\chi_{dia} = -3 \times 10^{-7}$ emu/g [220] which is independent of temperature. By fitting the results to eq. 5.1, the values of the free parameters; CW constant, and CW temperature, Θ, were obtained. Since the samples show PM state at high temperatures e.g. $T \geq 40$ K, the CW fitting was attempted from T = 40 K to T = 120 K for all samples, refer to Fig. 5.1(b). Furthermore, eq. 5.1 demonstrates that if the inverse of the real part of the susceptibility could be interpreted by CW law then Curie constant, C, is written in the following form

$$C = \frac{N_0 g^2 \mu_B^2 J(J+1) y_\theta}{3k_B}. \tag{5.2}$$

In eq. 5.2, N_0 denotes the number of cations per gram, g shows the Lande spin-splitting g-factor and has a value of 2 for Mn^{2+} ions, μ_B represents Bohr magneton, k_B denotes Boltzmann constant whereas y_θ represents the effective Mn content. The fitting yielded Θ values for samples with y = 0.027 and 0.047 equal to 26.6 and 25.6 K, respectively however; it increased to Θ = 40.6 K for the sample having Mn content, y = 0.061. These results unveil that Θ has positive values which characterize that the Mn impurities have magnetic interactions with positive sign of exchange constant. In addition, the relationship between Mn content and the CW temperature is not linear for these samples which suggest that the dependence of Θ can also be attributed to the variation in electrical properties changing Sn content in $Ge_{1-x-y}Sn_xMn_yTe$.

The magnetic susceptibility investigations are further extended to $Ge_{1-x-y}Sn_xMn_yTe$ samples with comparatively higher Sn concentrations, $x \approx 0.4$. In Fig. 5.2(a,b), the $\chi_{AC}(T)$ results of the samples with Sn and Mn contents $x \approx 0.4$ and $0.02 \leq y \leq 0.072$ are presented. The $\chi_{AC}(T)$ curves of these samples have noticeable cusp-shaped AC susceptibility exhibited by both real and imaginary components of $\chi_{AC}(T)$, see Fig. 5.2(a). Since a maximum in the χ_{AC} results requires further investigations to find out the underlying magnetic order, the value of freezing temperature, T_F, for each χ'_{AC} curve was estimated by obtaining best fits to the curves using polynomial function. The appropriate fits yielded peak values as T_F = 7 K and 10.2 K which in the case of glassy magnetic state represent freezing temperature, T_F, for samples with y = 0.052 and 0.072, respectively. These T_F values will be analyzed as a function of frequency, f, of the applied magnetic field in the next section in order to identify the exact magnetic order of the samples displaying cusps in $\chi'_{AC}(T)$ curves.

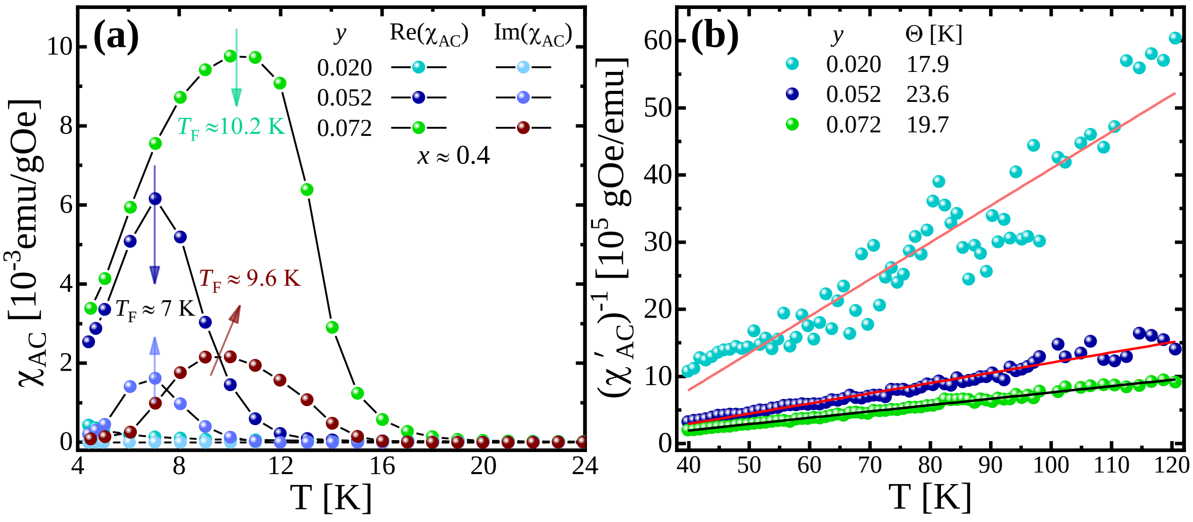

FIG. 5.2(a) Temperature dependence of the real and imaginary parts of magnetic susceptibility for the samples with $x \approx 0.4$, and $0.02 \leq y \leq 0.072$. (b) The $(\chi'_{AC})^{-1}$ results (scatters) fitted to the modified CW law (lines).

As obvious from the curves in Fig. 5.2(a), the maxima of cusps related to both χ'_{AC} and χ''_{AC} components for y = 0.052 are positioned at nearly the same temperatures. Such correlation between the real and imaginary components has been previously shown for $Eu_{0.4}Sr_{0.6}S$ SG system [249], molecular magnets [250], and SG state of URh_2Ge_2 [251]. On the other hand, the difference in T_F

values of real and imaginary parts for the sample with $y = 0.072$ demonstrate similar trend as cluster SG, $Mn_{0.73}Fe_{0.27}NiGe$ [252], FM cluster glass U_2IrSi_3 [253], and SG with short-range FM order [254]. Thus, it is assumed that the shifting of T_F values in χ''_{AC} away from those in χ'_{AC} curves might be an indication of the presence of magnetic clusters in the material. The cusps in $\chi_{AC}(T)$ curves observed in Fig. 5.1 and Fig. 5.2 are likely clues of complex magnetic systems which undergo strong irreversibility processes below the maxima in χ'_{AC}(T) dependencies. The occurrence of maxima in these systems signifies the onset of freezing process of magnetic moments which might lead to either SG or magnetic CG among several others. However; the interpretation of the exact type of magnetic order will be further probed by the frequency dependent susceptibility measurements for selected samples displaying maxima in $\chi_{AC}(T)$ curves.

Nevertheless, the profile of χ_{AC} cusp is different for each sample, for instance a broad maximum is observed for $y = 0.072$, whereas a relatively sharp peak for $y = 0.052$. Also, the magnitude and width of the cusps increase for the samples with higher Mn concentration. Cusps in $\chi_{AC}(T)$ curves are suggestive of different kinds of magnetic states which might change as a function of magnetic impurities in the samples. However, the samples with $x \approx 0.4$ and $y = 0.052$ and 0.072 in Fig. 5.2(a) showing faster decrease in the $\chi'_{AC}(T)$ results at temperature below the cusps rather proposes the presence of SG or CG state (detailed investigation of the source of the $\chi'_{AC}(T)$ maxima will be shown in the following sections). In comparison, the $\chi_{AC}(T)$ curves of the sample with $x \approx 0.4$ and $y = 0.02$ shows rather small $\chi'_{AC} \approx 4\times10^{-4}$ emu/gOe near $T \approx 4.5$ K in which no obvious transition to an ordered magnetic phase could be detected in the available temperature range. Such a magnetic response is predictable in compositions with low Mn content and random Mn distribution. When the molar concentration of magnetic ions is very small and are significantly separated in the sample's volume, the system might behave as a PM.

In concluding remarks related to Figs. 5.1 and 5.2, the $Ge_{1-x-y}Sn_xMn_yTe$ crystals with $x \approx 0.2$, $y = 0.047$, 0.060 and $x \approx 0.4$, $y = 0.052$, 0.072 manifest cusps in the $\chi_{AC}(T)$ curves. The occurrence of such maxima in $\chi_{AC}(T)$ might suggest the onset of freezing process of magnetic moments which can lead to irreversible glassy magnetic state. Supporting arguments and explanation of these cusps in $\chi_{AC}(T)$ will be provided in detail below using both static and dynamic magnetization approaches.

This section presents AC magnetic susceptibility results of the samples with comparatively higher Sn content. These measurements were made at applied magnetic field, $H_{AC} = 10$ Oe of frequency, $f = 625$ Hz. As shown in Fig. 5.3(a–d), $\chi_{AC}(T)$ results for the samples with Sn contents, $x \approx 0.6$ and $x \approx 0.8$ are shown. These samples demonstrate susceptibility of a plateau-like shape at low temperatures ($4.5 \leq T \leq 7$ K) e.g. samples with $y = 0.062$, 0.086 in Fig. 5.3(a) and $y = 0.077$ in Fig. 5.3(c). The curves manifest sharp transition from an ordered to PM state as compared to $\chi_{AC}(T)$

results in Fig. 5.1 and Fig. 5.2. As the cusps in $\chi_{AC}(T)$ curves disappear for these samples which might be an indication of the presence of FM phase rather than glassy magnetic state. Therefore, the transition temperature in these samples is characterized by the Curie temperature, T_C, rather than T_F. The T_C values were determined by taking double derivative of χ'_{AC} with temperature, $\partial^2\mathrm{Re}(\chi_{AC})/\partial T^2 = 0$. For the compositions with $x \approx 0.6$ and $y = 0.062$, 0.086, the obtained T_C values are equal to 7 K and 12 K, respectively. Moreover, the χ''_{AC} component is substantially smaller for the crystals presenting plateau-like χ'_{AC} in Fig. 5.3 in comparison with those displaying cusps. For instance, for $y = 0.086$, the highest value of χ''_{AC} component is ~11% of the χ'_{AC} which was about 29% of χ'_{AC} in case of $x \approx 0.4$ and $y = 0.05$. This comparison might suggest that the out-of-phase component, χ''_{AC} of magnetic susceptibility is larger in samples with glassy magnetic state than those indicating other ordered phases.

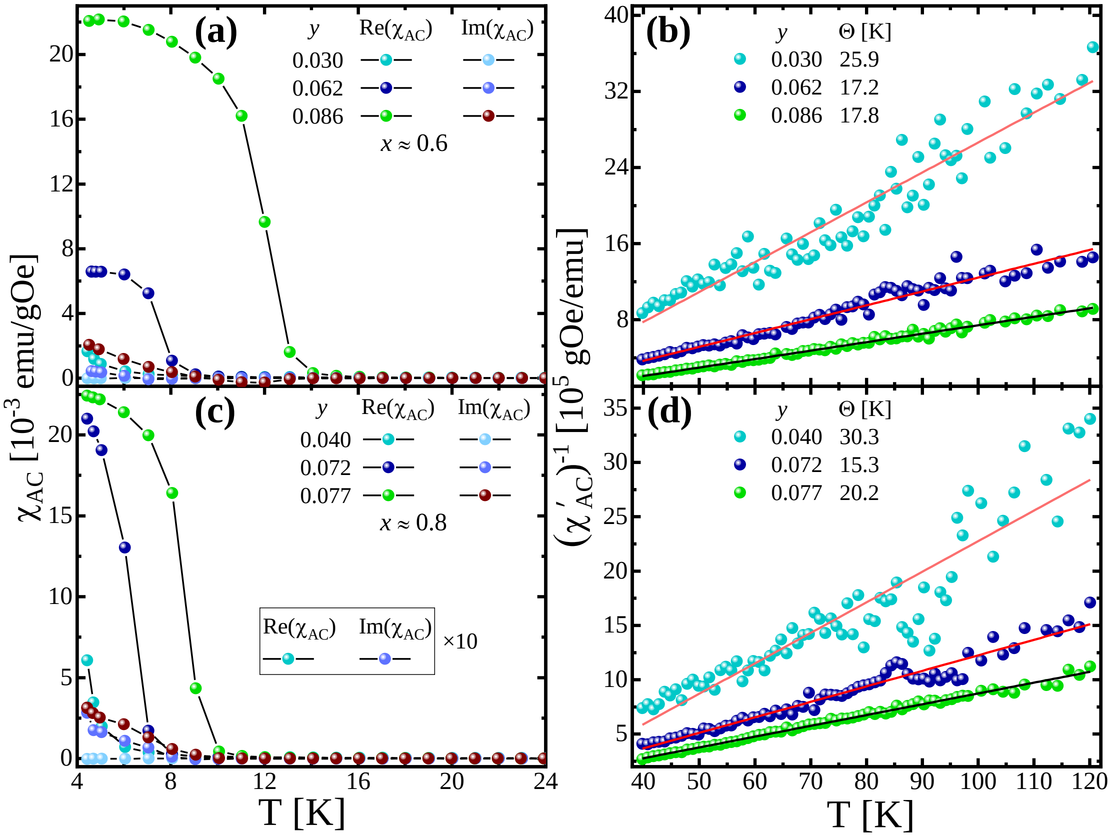

FIG. 5.3 Variable temperature χ'_{AC} and χ''_{AC} parts of magnetic susceptibility for $\mathrm{Ge}_{1\text{-}x\text{-}y}\mathrm{Sn}_x\mathrm{Mn}_y\mathrm{Te}$ samples with (a) $x \approx 0.6$, $0.03 \leq y \leq 0.086$ (c) $x \approx 0.8$, $0.04 \leq y \leq 0.077$. The modified CW law fits are presented in (b) and (d) for the samples in (a) and (c), respectively.

On further extending the alloying content of Sn from $x \approx 0.6$ to $x \approx 0.8$, refer to Fig. 5.3(d), $\chi_{AC}(T)$ results reveal similar transition behavior as seen for $x \approx 0.6$. These crystals manifest features similar to transition to FM-like state which can be characterized by fast decrease in χ'_{AC} near the transition temperature from an ordered phase to a PM state [255]. The plateau like $\chi_{\mathrm{AC}}(T)$ regime below T_C, also implies magnetic order similar to FM as the curves nearly saturate without any sign of magnetic frustration as observed in Figs. 5.1 and 5.2. In order to understand the behavior of both susceptibility components in various magnetic systems, detailed investigations are required prior to drawing any reasonable conclusions [256]. In addition to the variation in magnetic order as a function of Sn and Mn contents, the transition temperature from PM to an ordered phase decreases as Sn content increases, see for example Figs. 5.1 to 5.3. Such reduction in T_{C} might also be correlated to the magnetic exchange constant, J_{pd}, decreases when concentration of Sn is increased into GeTe. The J_{pd} value in $\mathrm{Ge}_{1\text{-}x\text{-}y}\mathrm{Sn}_x\mathrm{Mn}_y\mathrm{Te}$ alloys should in principle vary between the established values for GeTe close to $J_{\mathrm{pd}} \approx 0.8$ eV [19] and $J_{\mathrm{pd}} \approx 0.2$ eV [181]. Previous results have also showed that an increase in the lattice constant and hence bond length between magnetic ions might reduce the T_{C} values, see for example van der Waals bonded $\mathrm{Fe}_{3-x}\mathrm{GeTe}_2$ ferromagnet for details [257].

Based on the above data analysis, the determined values of Curie-Weiss temperature Θ, Curie-Weiss temperature C, Curie temperature, T_C, freezing temperature, T_{F}, and effective magnetic moment, μ_{eff} for all $\mathrm{Ge}_{1\text{-}x\text{-}y}\mathrm{Sn}_x\mathrm{Mn}_y\mathrm{Te}$ crystals are provided in Table II.

TABLE II: The Sn content x, Mn content y, Curie temperature T_C, Curie Weiss−temperature Θ, Curie−Weiss constant C, spin or cluster-glass freezing temperature T_{F}, and $\boldsymbol{\mu}_{\mathrm{eff}}$ is the effective magnetic moment in the units of Bohr magneton, $\boldsymbol{\mu}_B$.

x	y	T_{C} [K]	Θ [K]	C (10^{-4}) [emu.K/g]	T_{F} [K]	μ_{eff} [μ_B]
0.182 ± 0.01	0.027 ± 0.006	---	26.6 ± 3.16	2.35 ± 0.80	---	2.08 ± 0.03
0.183 ± 0.01	0.047 ± 0.006	---	25.6 ± 2.90	3.65 ± 1.83	5.3 ± 0.22	3.1 ± 0.03
0.184 ± 0.01	0.060 ± 0.006	---	40.6 ± 3. 60	10 ± 1.55	21.5 ± 0.59	7.69 ± 0.05
0.39 ± 0.03	0.020 ± 0.002	---	17.9 ± 1.41	2.54 ± 0.68	---	1.95 ± 0.02
0.40 ± 0.04	0.052 ± 0.005	---	23.6 ± 3.06	6.8 ± 1.15	7.1 ± 0.48	5.23 ± 0.06
0.41 ± 0.04	0.072 ± 0.007	---	19.7 ± 2.11	10.5 ± 1.3	10.5 ± 0.51	8.08 ± 0.06
0.54 ± 0.05	0.030 ± 0.003	---	25.9 ± 2.97	2.85 ± 0.61	---	2.19 ± 0.02
0.59 ± 0.06	0.062 ± 0.006	7 ± 0.40	17.2 ± 1.56	6.57 ± 1.55	---	5.05 ± 0.03
0.64 ± 0.06	0.086 ± 0.009	12 ± 1.13	17.8 ± 1.72	11.1 ± 1.25	---	8.54 ± 0.04
0.72 ± 0.07	0.040 ± 0.004	4.3 ± 0.64	30.3 ± 3.19	3.2 ± 0.46	---	2.46 ± 0.03
0.79 ± 0.08	0.072 ± 0.007	6 ± 0.66	15.3 ± 1.46	7.26 ± 2.08	---	5.58 ± 0.04
0.84 ± 0.07	0.077 ± 0.006	9 ± 0.93	20.2 ± 1.93	10.8 ± 3.11	---	8.31 ± 0.06

Furthermore, Curie Weiss constant, C, obtained from fitting $(\chi'_{\mathrm{AC}})^{-1}(T)$ curves to the modified CW law can be used to calculate the magnitude of the effective magnetic moment of Mn ions, μ_{eff} in each composition. For $Ge_{1-x-y}Sn_xMn_yTe$ crystals, μ_{eff} values were determined using equation 5.3 as presented below

$$\mu_{\mathrm{eff}} = \sqrt{\frac{3k_B C}{N_{\mathrm{A}}}}\,. \tag{5.3}$$

Here k_B is the Boltzmann constant and N_{A} denotes the Avogadro's constant. The values of effective magnetic moment were determined in the units of Bohr magneton, μ_B, as presented in detail in Table II. The dependency of μ_{eff} on Mn concentration demonstrates an increasing relationship for the whole series of $Ge_{1-x-y}Sn_xMn_yTe$ samples except two compositions; $x = 0.59$, $y = 0.062$ and $x = 0.79$, $y = 0.072$ which show a slight deviation, see Fig. 5.4. For Mn concentration $y \leq 0.047$, the effective magnetic moment remains less than $\mu_{\mathrm{eff}} \approx 3.1\ \mu_{\mathrm{B}}$ which then increases to about $5.2\ \mu_{\mathrm{B}}$ for the sample with $y = 0.052$. As presented in Figs. 5.1 to 5.3, the obtained values of C, yielded large uncertainties for several samples due to rather challenging fitting process of $(\chi'_{\mathrm{AC}})^{-1}$ results to modified CW law. The decrease in the μ_{eff} values for the samples with $x = 0.59$, $y = 0.062$ and $x = 0.79$, $y = 0.072$ can possibly occur due to uncertainties in the determination of Curie-Weiss constant. The overall dependence of $\mu_{\mathrm{eff}}(y)$ manifests an increasing trend for the entire Mn concentration. Additionally, high Sn content in the Sn-rich regime of $Ge_{1-x-y}Sn_xMn_yTe$ samples can lead to unequal lattice parameters and therefore inter-Mn distances are altered. This might also influence the magnitude of effective magnetic moment in our samples. In several other alloys with magnetic impurities, readers are referred to Refs. 258–260 in which the authors demonstrate the influence of alloying content on the magnitude of effective magnetic moment.

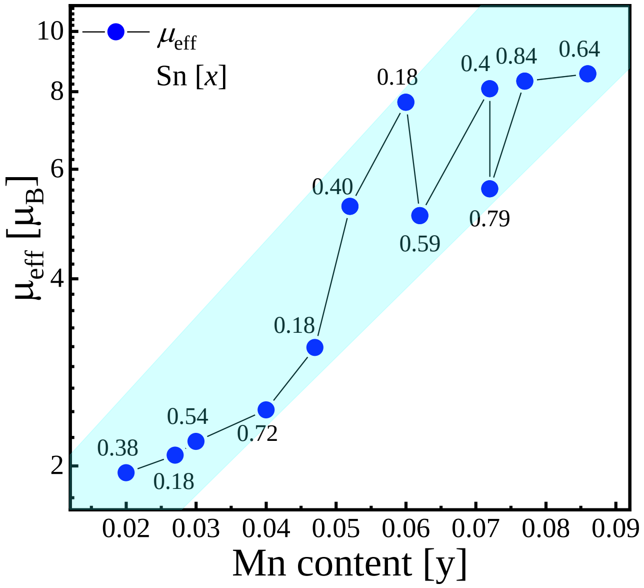

FIG. 5.4 Effective magnetic moment, μ_{eff} plotted vs Mn concentration in the $Ge_{1-x-y}Sn_xMn_yTe$ samples. Except two compositions at $y = 0.062$ and 0.072, μ_{eff} values generally increase as a function of the Mn content.

It is important to further understand the magnetic state responsible for the presence of cusps in $\chi'_{\mathrm{AC}}(T)$ curves and spin dynamics in $\mathrm{Ge}_{1-x-y}\mathrm{Sn}_x\mathrm{Mn}_y\mathrm{Te}$ samples. As stated earlier, the symmetric cusp-like shapes in the susceptibility curves indicate the presence of either super-paramagnetic or glassy magnetic state. In order to identify exact magnetic state, typical approach is applied to study the $\chi'_{\mathrm{AC}}(T)$ curves at different frequencies of the alternating magnetic field. The frequency dependent $\chi_{\mathrm{AC}}(T)$ measurements were made for selected samples at magnetic field magnitude, $H_{\mathrm{AC}} = 10$ Oe and in the frequency range, $7 \leq f \leq 10$ kHz. The magnitude of the applied magnetic field was decreased to $H_{\mathrm{AC}} = 0.5$ Oe at the highest $f = 9970$ Hz owing to the working limitations of the instrument. In Fig. 5.5(a), the frequency dependent $\chi'_{\mathrm{AC}}(T)$ results for the sample with low Sn content $x \approx 0.2$ and $y = 0.047$ is presented. The T_{F} values were determined from the frequency dependent $\chi'_{\mathrm{AC}}(T)$ curves by applying polynomial function and extracting the maximum position of the fitted function. The T_{F} value at the lowest frequency of 7 Hz was estimated as $T_{\mathrm{F}} = 5.3$ K which moved up to $T_{\mathrm{F}} = 6$ K at the highest value of $f = 9970$ Hz. The determined T_{F} values are shown in Fig. 5.5(a) for each frequency between 7 Hz and 9970 Hz. The shift in AC susceptibility cusp is clearly noticeable by comparing the T_{F} values as the frequency of the applied oscillating field increases. This might indicate the onset of frustrated magnetic state at the freezing temperature, T_{F}. In addition to the $\chi'_{\mathrm{AC}}(T)$ curves, the frequency dependent results of the imaginary component, $\chi''_{\mathrm{AC}}(T)$, of this crystal are presented in Fig. 5.5(b). The χ''_{AC} response to variation in frequency of alternating magnetic field is consistent with χ'_{AC} however; with slightly lower T_{F} values. The $\chi''_{\mathrm{AC}}(T)$ component at $f = 7$ Hz however; does not show clear maximum which might occur in the low temperature regime.

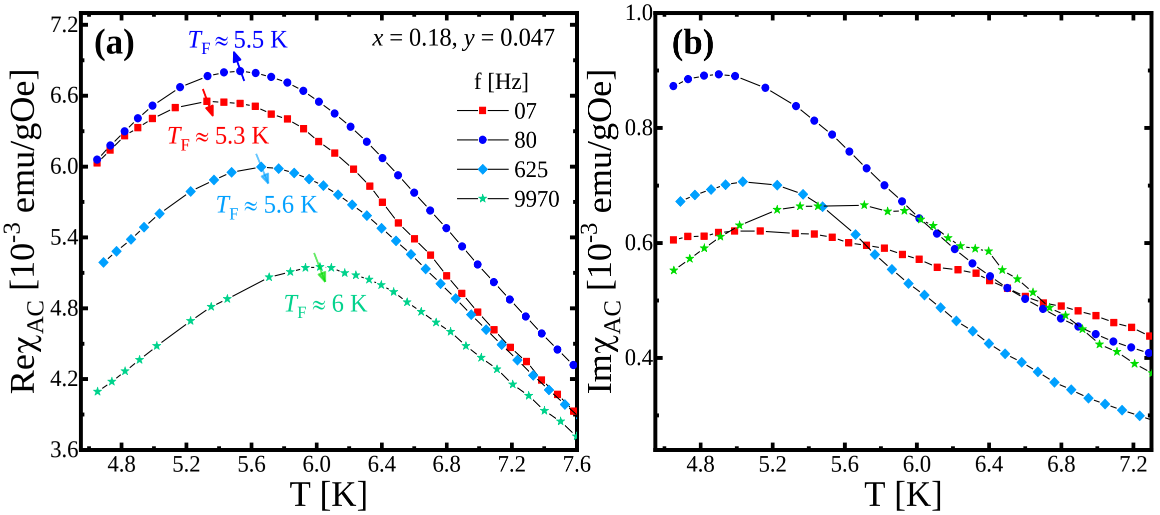

FIG. 5.5 Temperature dependence of both (a) real, $\chi'_{\mathrm{AC}}(T)$, and (b) imaginary, $\chi''_{\mathrm{AC}}(T)$ results of the sample with $y = 0.047$ obtained at selected frequency $f = 7, 80, 625, 9970$ Hz. The maximum of χ'_{AC} moves to higher temperatures with inceasing frequency of the oscillating magnetic field.

The frequency dependent χ'_{AC} and χ''_{AC} results for the other selected samples are presented in Fig. 5.6. The composition with $x \approx 0.2$ and $y = 0.06$ shows double maxima at $T_{F1} \approx 10.5$ K and $T_{F2} \approx 21.5$ K which are also visible in its imaginary part though at slightly different temperatures, see Fig. 3.8(a,b). Similarly, the sample with $x = 0.4$ and $y = 0.052$ reveals a single sharp maximum in both χ'_{AC} and χ''_{AC} at $T \approx 8.7$ K and $T \approx 8.3$ K, respectively. Insets to Fig. 5.6(c,d) showing results for the sample with $x \approx 0.4$ and $y = 0.052$ illustrate that such a large variation in frequency does not reveal any shift in the maxima in both χ'_{AC} and χ''_{AC} parts. The first maximum present in the sample with $x \approx 0.2$ and $y = 0.06$ seems to be static as the frequency is increased whereas T_{F2} moves towards higher temperatures continuously up to $f = 10$ kHz. Similar to T_{F1}, the maximum shown by the sample with $x = 0.4$ and $y = 0.052$ is also independent of frequency of the oscillating magnetic field between $f = 40$ Hz and 10 kHz. The frequency dependent results will be further analyzed in the following paragraph in order to conclude the type of magnetic order in each sample.

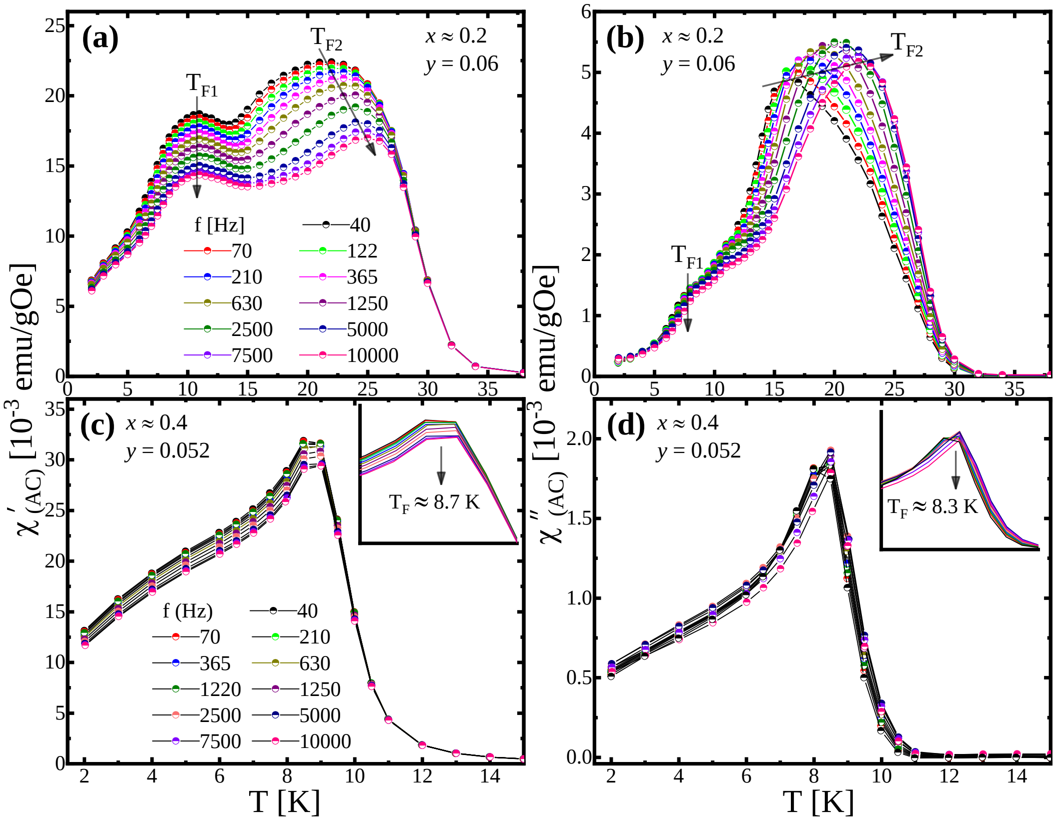

FIG. 5.6 Temperature dependencies of the magnetic susceptibility components, χ'_{AC} and χ''_{AC} for the samples with (a,b) $x \approx 0.2$ and $y = 0.06$ and (c,d) $x \approx 0.4$ and $y = 0.052$ measured at $40 \leq f \leq 10{,}000$ Hz. Insets to (c) and (d) show the magnified view of the maxima observed for χ'_{AC} and χ''_{AC}, respectively.

As shown in Figs. 5.5 and 5.6, there are several indications of frustrated or glassy magnetic states in these samples which could either be typical of SG or CG. For this reason, the $\chi_{AC}(T)$ results are discussed which can identify the exact type of the magnetic order in these samples. The discussion part begins with first considering the samples which showed frequency dependent cusps in $\chi_{AC}(T)$, a typical signature of transition to various magnetic states e.g. SG, CG or superparamagnetic state [180,181]. For SG type magnetic state, it has been extensively investigated that the anomalies in the form of cusps in the magnetic susceptibility which signify a freezing temperature, T_F, of the system, moves up [182–186] on the temperature scale as the frequency of AC magnetic field increases. The double maxima in both χ'_{AC} and χ''_{AC} for the sample with $x \approx 0.2$, $y = 0.06$ is similar to the results obtained by Eftimova *et al.* [261] who had observed shoulder–like maximum in the χ''_{AC} and its dependence on the applied frequency for $Pd_8Co_{50}A_{142}$ SG alloy. Also, Koyano *et al.*, has reported the presence of a shoulder in both χ'_{AC} and χ''_{AC} components in $Fe_{1/4}TiS_2$ CG alloy which diminished at higher excitation frequency [262]. This manifestation of a shoulder-shape in $\chi_{AC}(T)$ was credited to the possible existence of small size magnetic clusters in the alloys [262]. Similar to these previous works, the emergence of double maxima in the χ'_{AC} curves might also initiate due to the presence of magnetic clusters of varying sizes. Since T_{F1} observed in both the χ'_{AC} and χ''_{AC} (see Fig. 5.6(a,b)) are independent of frequency variation, it possibly represents magnetic clusters with small size FM like order at low temperatures. The T_F vs f results defined for the sample with $x \approx 0.4$ and $y = 0.052$ (see Fig. 5.6(c,d)) however; do not show any frequency dependence in the whole range of frequency values which could also originate due to clustering effect of Mn ions. The nature of magnetic order in $Ge_{1-x-y}Sn_xMn_yTe$ samples will be further discussed in the following sections.

For the sample with $y = 0.047$ and 0.06, the T_{F2} values continuously rise as a function frequency in the range $f = 7$ Hz – 10 kHz. The scaling parameter, R, for the crystal with $y = 0.047$ and 0.06 was assessed by using eq. 2.24 taking into account $f = 7$ Hz and 10 kHz.

The estimated value of scaling parameter, R, characterizes a particular type of magnetic ordering based on the χ'_{AC} analysis. For the sample with $x \approx 0.2$ and $y = 0.047$ shown in Fig. 5.5, the scaling parameter value was calculated as 0.017 ± 0.002. Based on the established values in the previous works [179,182–186], the glassy magnetic ordering in this crystal is recognized as spin-glass since value of R is around 0.01 [179]. Similarly, the R value determined for the sample with $x \approx 0.2$ and $y = 0.06$ equals $R = 0.033$ which indicates the formation of magnetic clusters in the sample. Typically, the values of R for CG systems are ranked in the range, $R \approx 0.02 - 0.06$ though it is limited to $R \approx 0.005 - 0.01$ for conventional SG state [179,263]. In case of super-paramagnetic state, the scaling parameter, R yields values $R > 0.13$ [263]. After this first indication of Mn clusters, the type of magnetic state and formation of Mn clusters in this sample will be further discussed below in detail with the aid of analysis based on different phenomenological laws.

Further analyses are made in this section based on the relationship between T_F vs f response obtained from χ_{AC} results. The spin dynamics of the disordered and frustrated magnetic state is investigated which provides a comprehensive knowledge to understand the nature of magnetic interactions. Thus, the response of freezing temperature, T_F, to the variable frequency is first analyzed using Arrhenius law (AL) which is written as eq. 5.5 [264]

$$f = f_0 \exp\left(-\frac{E_a}{k_B T_F}\right), \tag{5.5}$$

where f is the driving frequency in $\chi_{AC}(T)$ results, and $\tau_0 = 1/f$ denotes the dynamic fluctuation time. The experimental results plotted in the form of log(f) vs $1/T_F$ dependencies are shown in Fig. 5.7 together with lines indicating fits to eq. 5.5 for the samples with $x \approx 0.2$ and $y = 0.047$ and 0.06.

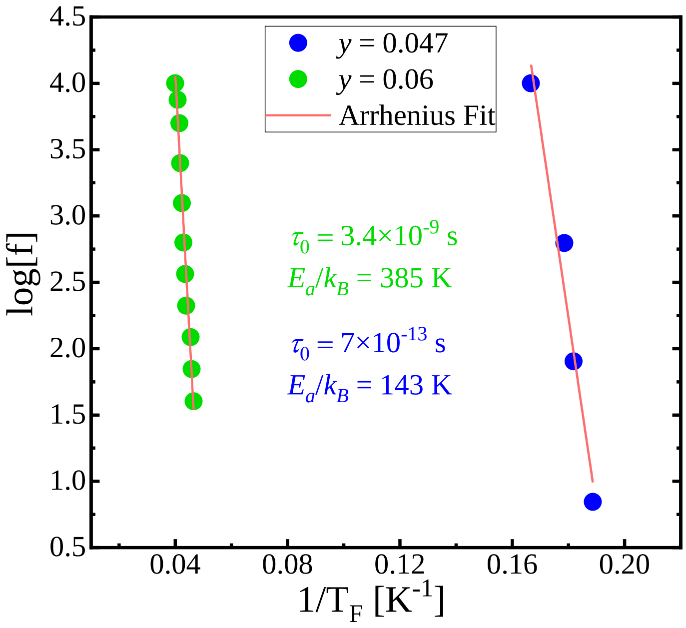

FIG. 5.7 The log(f) vs $1/T_F$ dependence for the crystals with $x \approx 0.2$ and $y = 0.047$, 0.06. The scatters denote experimental results whereas solid lines represent fits obtained from Arrhenius law, see eq. 5.5.

The activation energy or potential barrier written as E_a/k_B defines a blockade between the two easy orientations of magnetic moments [185]. During the fitting process, E_a/k_B was taken as a free parameter. The values obtained from AL fitting are provided in Fig. 5.7. The values of E_a/k_B were estimated as 143 K and 385 K for $x \approx 0.2$, $y = 0.047$ and $x \approx 0.2$, 0.06. The E_a/k_B values should be typically in the range 1–2T_F [264,265] in conventional SG systems. These values obtained for the samples with $x \approx 0.2$ and $y = 0.047$, 0.06 using AL fitting are substantially high. For other disordered magnetic systems, large values of barrier potential, $E_a/k_B \approx 719$ K were reported for $La_{0.5}Sr_{0.5}CoO_3$ [266], $E_a/k_B \approx 568$ K for $CaBaFe_{4-x}Li_xO_7$ [267], and $E_a/k_B \approx 800$ K for U_2CuSi_3 [268]. Similarly, the dynamic fluctuation time that defines the shortest relaxation time present in the system, τ_0, [265] values were obtained for the current samples as 7×10^{-13} s and 3.4×10^{-9} s for $x \approx 0.2$, $y = 0.047$ and $x \approx 0.2$, $y = 0.06$, respectively. The range of characteristic τ values in SG state generally occurs from 10^{-10} to 10^{-13} s [184], which means that SG state is present in the sample with $x \approx 0.2$ and $y = 0.047$. The $\tau_0 = 3.4\times10^{-9}$ s obtained for the sample with $x \approx 0.2$, $y = 0.06$ yields slightly larger value of spin relaxation time than the conventional SG systems.

Next, the T_F dependency on varying frequency was analyzed to study the nature of the magnetic disorder using critical slowing down or power law (PL) given by eq. 5.6 [264]

$$\tau = \tau_0\left(\frac{T_F - T_g}{T_g}\right)^{-z\nu}. \tag{5.6}$$

To build an appropriate fitting equation, eq. 5.6 was rearranged in the form of eq. 5.7

$$\ln(\tau) = \ln(\tau_0) - z\nu\ln\left(\frac{T_F - T_g}{T_g}\right). \tag{5.7}$$

In the above equations, the $\ln(\tau_0)$ term characterizes the intercept of the fitted line and $z\nu$ signifies the slope deduced from the fitting function using eq. 5.7. The SG temperature, T_g, used in this relation was determined by extrapolating the T_F fitted line to $T_F(f \rightarrow 0)$, see Fig. 5.8. The spin relaxation time diverges when the system approaches transition temperature, T_g. The determined τ_0 values shown in Fig. 5.8 are equal to 4.9×10^{-4} s and 7.9×10^{-4} s for the sample with $y = 0.047$ and 0.06, respectively. This indicates that the single dynamic fluctuation time is significantly larger than the typical range for SG systems [184]. The large τ_0 values determined from eq. 5.7 also indicate the slowing down of spin relaxation near the transition temperature, T_g.

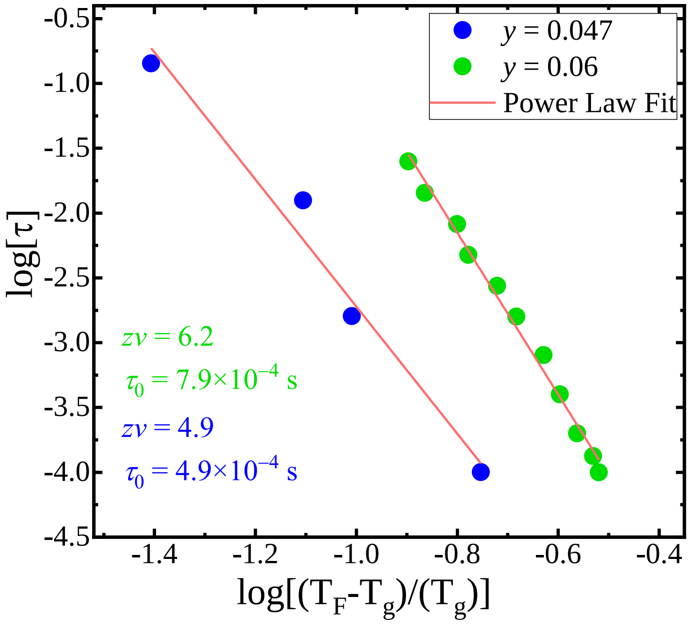

FIG. 5.8 The $\log(\tau)$ vs $\log((T_F–T_g)/T_g))$ results where x–axis denotes reduced temperature and τ is spin-relaxation time; the results are fitted to the law of critical slowing down denoted by lines, refer to eq. 5.7.

Large τ_0 values in $x \approx 0.2$, $y = 0.047$ and $x \approx 0.2$, $y = 0.06$ might indicate a possible presence of the FM-like clusters in the samples [269–271]. The next important fitting parameter used in the PL fitting is dynamic critical exponent, $z\nu$, which illustrates the type of magnetic state. The $z\nu$ values deduced from PL fits are equal to as $z\nu = 4.9$ and 6.2 which are in the range of pure SG systems i.e. $z\nu = 4 - 12$ [176]. Since the PL fitting results into very large τ_0 value compared to SG systems whereas $z\nu$ values falls in the range defined for SG, therefore, it is assumed that the PL fitting yields unconvincing results to describe $T_F(f)$ dependency in the present samples. For this reason, the analysis is further extended in order to obtain more definite conclusions.

The nature of a magnetic glassy state was further analyzed by using Vogel-Fulcher (VF) law which is written in the following form [264]

$$f = f_0 \exp\left(-\frac{E_a}{k_B(T_F - T_0)}\right). \tag{5.8}$$

In order to obtain a proper fitting to determine the Vogel-Fulcher temperature, T_0, eq. 5.8 was rearranged as below in the form of empirical VF law

$$T_F = \frac{E_a/k_B}{\ln(f_0/f)} + T_0. \tag{5.9}$$

T_0 denotes VF temperature in eqs. 4.8 and 5.9. The experimental results are plotted in the form of T_F vs $1/\ln(f_0/f)$ and fitted to eq. 5.9 as shown in Fig. 5.9(a).

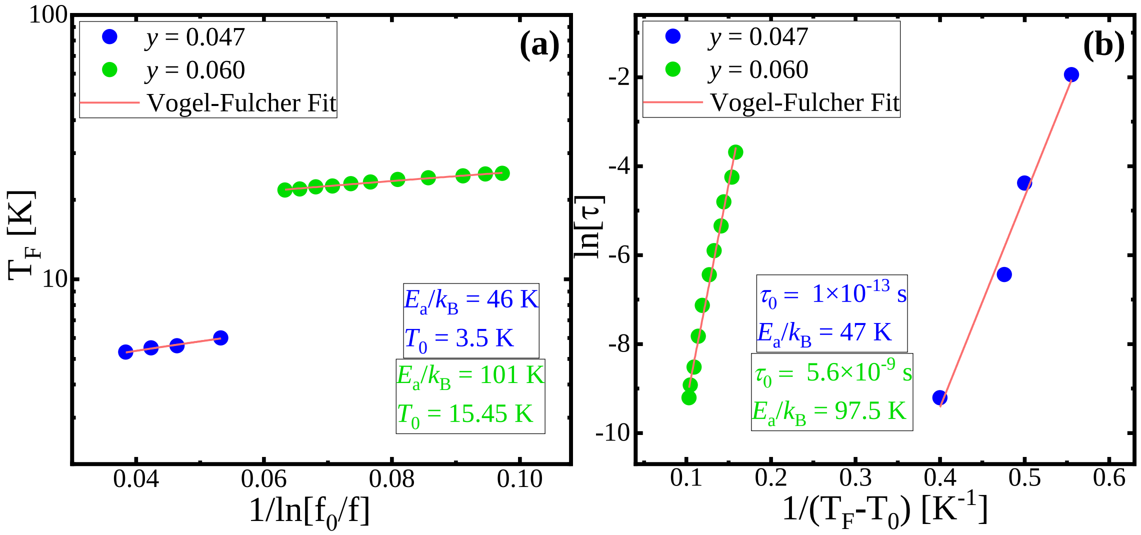

FIG. 5.9(a) T_F vs $1/\log(f_0/f)$, here the points represent experimental results whereas solid line characterizes fits obtained from empirical Vogel–Fulcher law. (b) The experimental results fitted to Vogel–Fulcher law where T_0 is Vogel-Fulcher temperature.

The value of the attempt frequency $f_0 = 1/\tau_0$ was held fixed during the fitting (f_0 was determined from AL equation). The potential barrier, E_a/k_B, and Vogel-Fulcher temperature, T_0, were chosen as free parameters. After the determination of T_0, the VF law was extended to equation 4.10 to estimate the values of dynamic fluctuation time, τ_0 presented in Fig. 5.9(b). For this purpose, the VF law was rearranged in the form of eq. 5.10 to allow appropriate fit

$$\ln(f) = \ln(f_0) - \frac{E_a/k_B}{(T_F\text{-}T_0)}. \tag{5.10}$$

The results plotted as $\ln(\tau)$ vs $1/(T_F - T_0)$ were fitted to eq. 5.10 with f_0 and E_a/k_B as free parameters. By comparing the fitting parameters with other fitting laws shown in Fig. 5.7 and Fig. 5.8, the τ_0 values were obtained as 5.6×10^{-9} s and 1×10^{-13} s for the crystals having $x \approx 0.2$, $y = 0.047$ and $x \approx 0.2$, 0.06, respectively. The outcomes indicate that the crystal with $x \approx 0.2$, $y = 0.047$ yields τ_0 value similar to CG systems whereas the sample with $y = 0.06$ results in slightly smaller value than re-entrant spin glasses [182,272,273] though similar to CG systems [176,184,186,274]. Unlike conventional SG systems, re-entrant spin glasses manifest ferromagnetic phase below Curie temperature, T_C however; they show transition to a frozen state at $T_g < T_C$. Likewise, the $E_a/k_B \approx 46$ K for $y = 0.047$ determined from both fitting equations are similar whereas for $y = 0.06$, $E_a/k_B = 97 - 101$ K were obtained. For canonical SG, the E_a/k_B value remains ~$2T_F$ as previously reported for different systems [264,265]. These values for both samples are about 5 – 6 times the T_F which are similar to CG like behavior [266,267,274].

Additionally, the Vogel-Fulcher temperature, T_0, determined in Fig. 5.9(a) yielded positive value which indicates the development of magnetic clusters [186]. Previous studies suggest that T_0 should yield values between 0 K and T_F [275], this indicates that the empirical VF law calculates a convincing value of $T_0 = 3.5$ K ($T_F = 6$ K) and 15.45 K ($T_F = 21.5$ K) for the crystal $x \approx 0.2$, $y = 0.047$ and $x \approx 0.2$, 0.06, respectively. The existence of magnetic clusters could also be identified by using a criterion introduced by Tholence which is described as $T^* = (T_F - T_0)/T_F$, where T^* is called the figure of merit of magnetic clustering [186,275]. Tholence criterion has been considered to analyze several systems and is regarded as an approach determining the degree of magnetic clustering in a system [186,275]. Applying this relation to our samples which shows signatures of magnetic clusters, the T^* value for the sample with $x \approx 0.2$, $y = 0.06$ equals 0.28 ± 0.02 which yields value an order of magnitude larger than those for SGs [275], this supports our earlier interpretation of the presence of magnetic clusters in the sample with $x \approx 0.2$, 0.06, as obtained in the preceding sections [186,275]. In addition to the distinction between frustrated magnetic states, T_0 values can be related to the type of exchange interactions among the magnetic moments [275]. Also, as the spin relaxation time τ_0 for $x \approx 0.2$, $y = 0.06$ is slightly larger than the upper limit for canonical SG state; this suggests that the interactions between magnetic moments are mostly related to the Mn clusters rather than classical SG state. Similarly, the values of potential barrier, $E_a/k_B \approx 5T_F$ also indicate the existence of magnetic CG state in this sample. Concluding the above discussion, the spin relaxation time, τ_0, activation energy,

E_a/k_B, and Tholence criterion validate the presence of Mn clusters for the sample with $x \approx 0.2$, $y = 0.06$. Consequently, the disordered magnetic state in this crystal is suggested to arise from the appearance of magnetic clusters.

Finally, a comparison between the spin-relaxation times determined for the current $Ge_{1-x-y}Sn_xMn_yTe$ samples and previous literature data is presented in Fig. 5.10. The parameters deduced using eq. 5.5 – 5.10 were analyzed to draw comparison with previously reported works. In Fig. 5.10, the τ_0 values for the samples with $x \approx 0.2$, $y = 0.047$ and $x \approx 0.2$, $y = 0.06$ are marked which represent a SG and CG state, respectively.

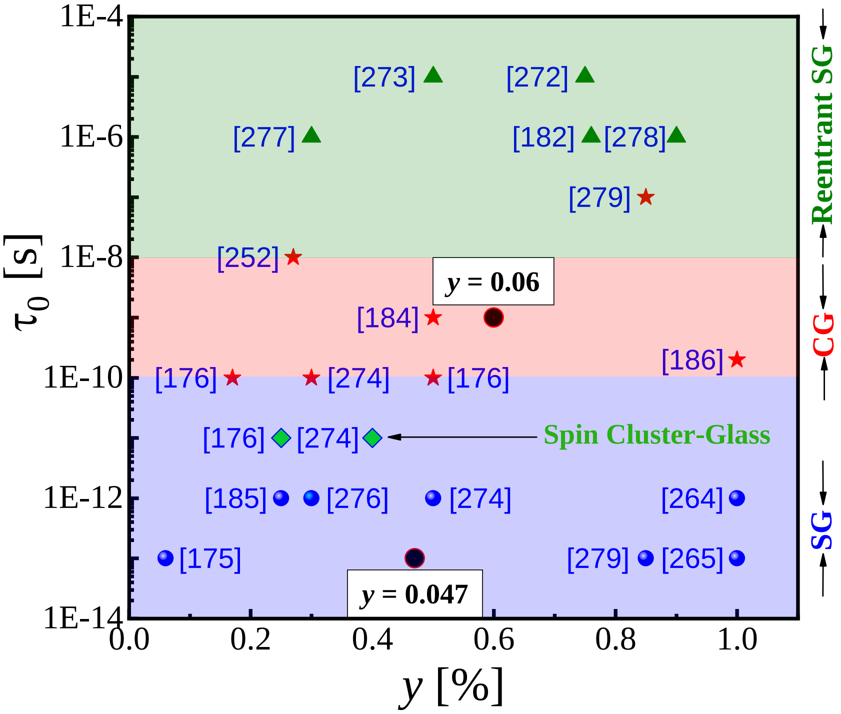

FIG. 5.10 Comparison of calculated values of spin relaxation time, τ_0 for different disordered magnetic systems. τ_0 values reported in several previous works [175,176,182,184–186,252,264,265,272–275,276–279] are shown whereas the current samples with $x \approx 0.2$, $y = 0.047$ and $x \approx 0.2$, $y = 0.06$ represent either a spin-glass or a cluster-glass state, respectively. Note that the horizontal axis denotes arbitrary scale for several references.

Low τ_0 values were reported for reentrant spin-glasses with different compositions that holds the upper part in Fig. 5.10. The sample $y = 0.06$ with $\tau_0 \sim 10^{-9}$ s might represent magnetic clusters of small size as the obtained τ_0 value is slightly larger than those observed for typical SG state. Since the acceptable values of τ_0 slightly vary in literature, therefore the boundaries separating different magnetic states might not seem as sharp as presented in Fig. 5.10. For example, the spin cluster-glass with $\tau_0 \sim 10^{-11}$ s in Ref. 188 is illustrated as SG state in other materials systems [184].

5.2.2 Magnetic coercivity and analysis of magnetic anisotropy

In this section, the analysis of the high field magnetization, $M(H)$, is presented measured at an applied magnetic field up to $H \leq 90$ kOe and at several temperatures from $T \approx 4.5$ K to $T \approx 20$ K. The $M(H)$ investigations of the $Ge_{1-x-y}Sn_xMn_yTe$ samples were made up to high magnetic field in order to assess the temperature dependence of the coercive field, H_C, remanent magnetization, M_R, and saturation magnetization, M_S. In Fig. 5.11(a,b), the $M(H)$ curves measured at $T \approx 4.5$ K are presented for the $Ge_{1-x-y}Sn_xMn_yTe$ samples with relatively low Sn content, $x \approx 0.2$ and $x \approx 0.4$, respectively. The inset of each panel shows hysteresis curve obtained at $T \approx 4.5$ K for the sample with highest Mn content.

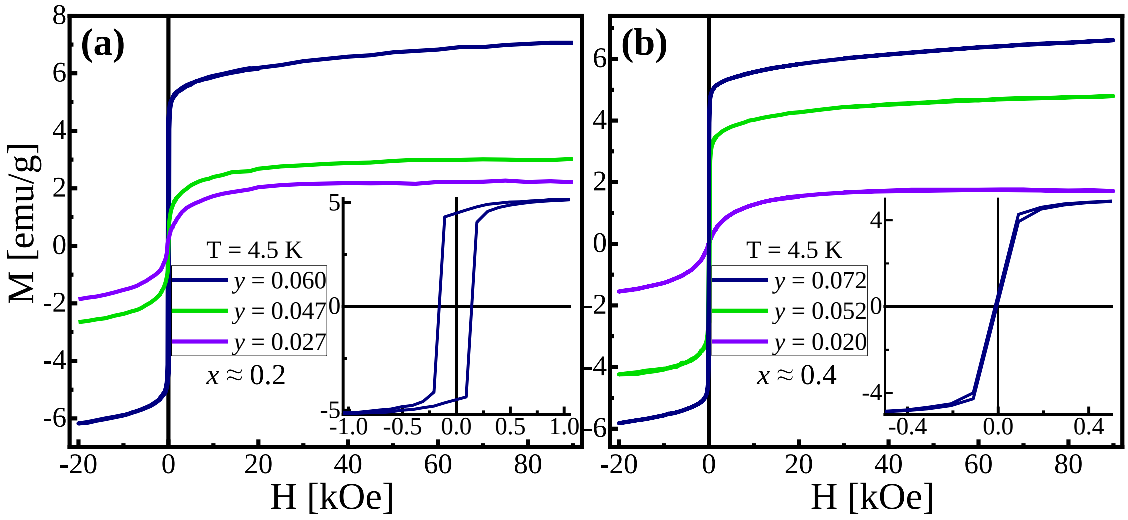

FIG. 5.11 Magnetization hysteresis, $M(H)$ results for $Ge_{1-x-y}Sn_xMn_yTe$ crystals with Sn and Mn concentrations (a) $x \approx 0.2$, $0.027 \leq y \leq 0.060$, (b) $x \approx 0.4$, $0.02 \leq y \leq 0.072$. The insets represent $M(H)$ hysteresis curves for the compositions with highest Mn content in each panel.

For all $Ge_{1-x-y}Sn_xMn_yTe$ compositions, the saturation magnetization increases depending on the Mn concentration. The crystals with low Mn content show saturation at $H \approx 30 - 40$ kOe however; the compositions with highest Mn contents do not manifest saturation even up to $H \approx 90$ kOe. Also, the irreversibility of the curves seems to remain below $H \leq 0.2$ kOe. In Fig. 5.11(b), the $M(H)$ curve does not show obvious hysteresis as compared to the square-like hysteresis for the sample with $x \approx 0.2$, $y = 0.06$. In order to further analyze the magnetic hysteresis and the obtained parameters, detailed values of $H_C(T)$, and $M_R(T)$, are given in Fig. 5.12(a–d). The values of $H_C(T)$, and $M_R(T)$ were calculated by fitting appropriate parts of the $M(H)$ curves to a polynomial function. The obtained values of $H_C(T)$, and $M_R(T)$ for all $Ge_{1-x-y}Sn_xMn_yTe$ samples were determined with less than 10% uncertainty. In addition, the saturation magnetization, M_S, values were calculated using the law of approach to saturation, see eq. 5.11

$$M = M_S\left(1 - \frac{A}{H} - \frac{B}{H^2}\right). \tag{5.11}$$

The A/H term in eq. 5.11 is called magnetic hardness which comes from local crystalline defects or leakage field from ferromagnetic materials. The term B/H^2 arises from magnetocrystalline anisotropy and is called the anisotropy constant. In order to determine the M_S values, the quantities A, B, and M_S were taken as fitting parameters.

The sample with $x \approx 0.4$, $y = 0.072$ has smaller value of magnetization remanence, $M_R = 0.5$ emu/g compared to the sample with $x \approx 0.2$, $y = 0.06$ with $M_R = 4.5$ emu/g. The narrow magnetic hysteresis of the crystal having $x \approx 0.4$, $y = 0.072$ might represent typical behavior of a SG state. The coercivity values for entire series of $Ge_{1-x-y}Sn_xMn_yTe$ crystals remain in the range $H_C \leq 160$ Oe. These values are small in comparison with the previous work on $Ge_{1-y}Mn_yTe$ epitaxial films e.g. $H_C \approx 450$ Oe at $T = 4.2$ K with $y = 0.78$ [52], $H_C \approx 400$ Oe at $T = 4.2$ K with $y = 0.44$ [50], and $H_C \approx 500$ Oe at $T = 5$ K with $y = 0.98$ [280]. On the other hand, the $H_C \approx 160$ Oe for the crystal with $x \approx 0.2$, $y = 0.06$ in Fig. 5.12(a) is similar to H_C values of $Ge_{1-x-y}Sn_xMn_yTe$ results obtained by Grochot *et al.*, with $y \approx 0.1$ [281]. The above comparison reveals that the smaller H_C values of $Ge_{1-x-y}Sn_xMn_yTe$ crystals than those obtained in Ref. 46, 47 might be ascribed to the SG/CG state in the samples shown in Fig. 5.11.

The temperature dependencies of H_C and M_R are presented in Fig. 5.12(a–d) for the samples with $x \approx 0.2$, $0.027 \leq y \leq 0.060$ and $x \approx 0.4$, $0.020 \leq y \leq 0.072$. In the left panel, compositions with $x \approx 0.2$ are shown in which the sample with $y = 0.061$ manifests monotonic reduction in both H_C and M_R up to $T \approx 20$ K. This sample exhibited a square shaped magnetic hysteresis at $T \approx 4.5$ K.

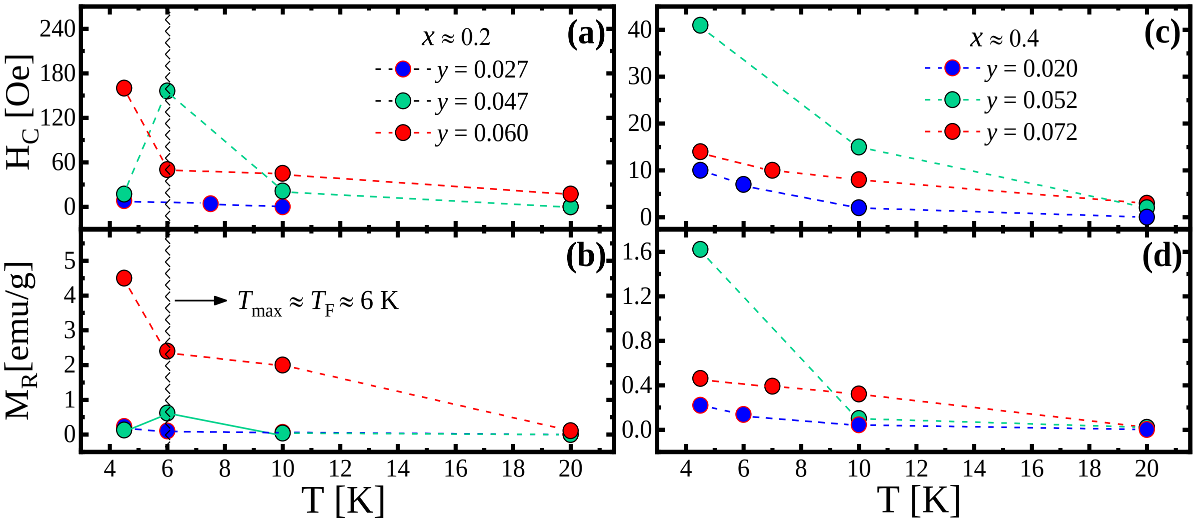

FIG. 5.12 Temperature dependence of coercivity, H_C and remanent magnetization, M_R, for the crystals with (a,b) $x \approx 0.2$, $0.027 \leq y \leq 0.061$, (c,d) $x \approx 0.4$, $0.02 \leq y \leq 0.072$. The hatched line show anomaly in H_C and M_R for $y = 0.047$.

The composition with the lowest Mn content, $y = 0.027$ in Fig. 5.12(a,b) exhibits nearly zero value of M_R at all temperatures owing to its paramagnetic type magnetic state in this temperature range. The crystals with Mn contents, $x \approx 0.2$, $y = 0.06$ and $x \approx 0.4$, $y = 0.052$ manifest narrowing of $M(H)$ loops with increasing temperature. For all other $Ge_{1-x-y}Sn_xMn_yTe$ samples in Fig. 5.11, the variation in H_C and M_R is slow excluding the sample with $x \approx 0.2$, $y = 0.047$ which shows peaks in $H_C(T)$, and $M_R(T)$, results at $T \approx 6$ K. At $T \approx 20$ K, the $Ge_{1-x-y}Sn_xMn_yTe$ samples behave similar to paramagnetic materials with almost reversible $M(H)$ curves which can also be seen from nearly zero M_R and H_C values in Fig. 5.12(a–d). The loss of irreversible behavior of $M(H)$ curves at high temperatures is typical mechanism arising from increasing thermal energy of the crystal with increasing temperature [282]. For the crystals with $y = 0.052$ and 0.06, the non-linear decrease in $M_R(T)$ and $H_C(T)$ curves around $T = 10$ K and 6 K, respectively is to a certain degree, similar to an exponential decrease reported for FeTb random magnets [283], random anisotropy system [284], Fe-Zr amorphous alloy [285], amorphous magnetic films like Dy-Cu/Dy-Al [286] among several other systems [287–289]. Such $H_C(T)$ behavior in these systems has been interpreted to magnetic system in which magnetic moments have correlation of a ferromagnetic type on a small scale, though the magnetization, M rotates stochastically when considered on a large scale the [283]. Although the temperature scale is limited to a few points in Fig. 5.13, the mechanism describing $H_C(T)$ might be similar as interpreted in the above systems. Besides the above two samples which demonstrate typical trend of reduction in $M_R(T)$ and $H_C(T)$, the crystal with $x \approx 0.2$, $y = 0.047$ shows interesting M_R and H_C outcomes due to the SG type magnetic state. As discussed earlier, the frequency dependent susceptibility deduced that the sample holds a SG state below the freezing temperature, $T_F = 5.3$ K. Peaks in $M_R(T)$ results occur at $T = 6$ K which is close to value of the $T_F = 5.3$ K for this sample. Such anomaly in $M_R(T)$ has been previously observed for SG state [290]. Likewise, the temperature dependent coercivity of the crystal with, $x \approx 0.2$, $y = 0.047$ demonstrates similar anomaly as presented in Fig. 5.12(a). The maximum around T_F showed by the crystal with, $x \approx 0.2$, $y = 0.047$ is similar to anomalous coercivity near the magnetic transition temperature observed by Mannan *et al.*, in CuMn spin-glass system [291]. The maximum in coercive field reflects fluctuations in the spin-disorder previously testified at the interfaces of ferromagnetic-antiferromagnetic configurations [292] which presumably has similar origin in the spin-glass state for our crystal with $y = 0.047$.

In this part, the $M(H)$ curves in the Sn-rich regime with $x \approx 0.6$, $0.030 \leq y \leq 0.086$ and $x \approx 0.8$, $0.040 \leq y \leq 0.077$ are shown in Fig. 5.13. The $M(H)$ curves obtained at $T \sim 4.5$ K, exhibit similar trend as shown in Fig. 5.11 for the samples with lower Sn concentration. Increase in Sn+Mn content beyond $x \approx 0.4$ produces clear square-like hysteresis loops as presented in the insets to Fig. 5.13. The sample with $x \approx 0.6$, $y = 0.086$ manifests highest values of magnetic saturation, $M_R \approx 5.5$ emu/g among all $Ge_{1-x-y}Sn_xMn_yTe$ compositions whereas the magnitude of $H_C \approx 160$ Oe is comparable to other samples with $x \approx 0.8$, $y = 0.077$ in Fig. 5.13(b) and $x \approx 0.2$, $y = 0.06$ in Fig. 5.12(a).

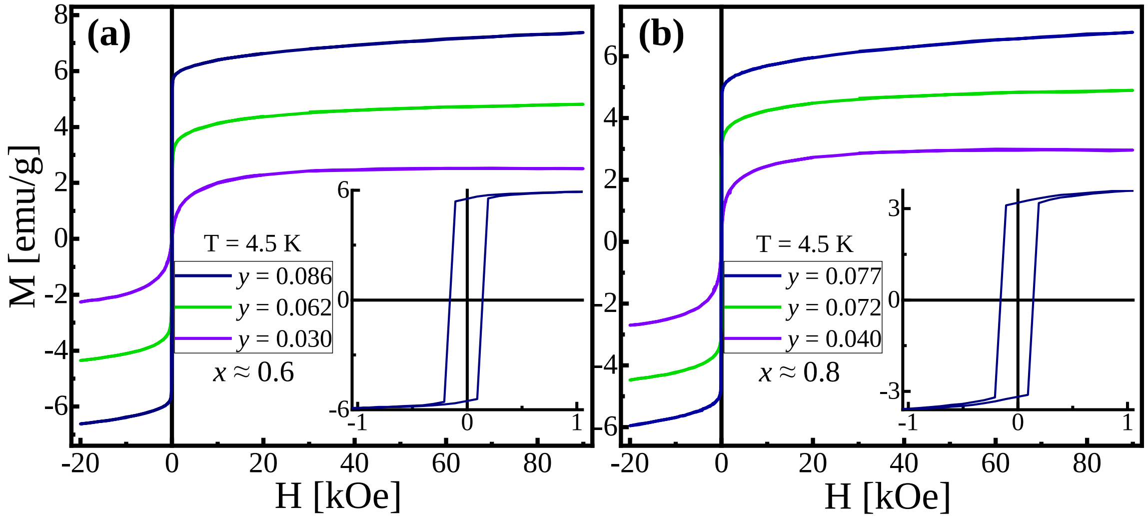

FIG. 5.13 Magnetization vs magnetic field dependence of the crystals with (a) $x \approx 0.6$, $0.03 \leq y \leq 0.086$, (b) $x \approx 0.8$, $0.04 \leq y \leq 0.077$. The insets in (a) and (b) represent enlarged $M(H)$ curves for the samples with $y = 0.086$ and $y = 0.077$, respectively.

Besides the $M(H)$ characteristics presented above, the temperature dependent magnetization remanence, $M_R(T)$, and coercive field, $H_C(T)$, are presented for the Sn-rich samples in Fig. 5.14(a–d). At $T \approx 4.5$ K, the compositions with $x \approx 0.6$, $y = 0.086$ and, $x \approx 0.8$, $y = 0.077$ reached $M_R \approx 5.5$ emu/g and 3.9 emu/g, respectively, although the magnitude of H_C was determined to have similar values for both samples, see Fig. 5.14(a,c). Moreover, the crystals with $x \approx 0.6$, $y = 0.086$ and $x \approx 0.8$, $y = 0.077$ maintain their irreversible behavior even at comparatively higher temperatures of $T = 15$ K and 10 K, respectively.

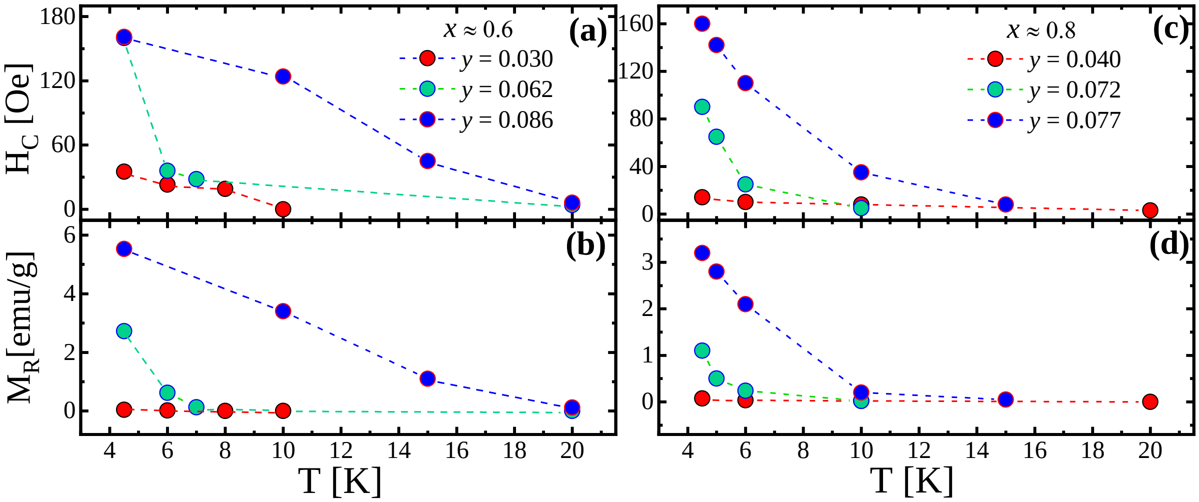

FIG. 5.14 Temperature dependent coercivity, H_C and remanent magnetization, M_R, for the crystals with (a,b) $x \approx 0.6$, $0.030 \leq y \leq 0.086$, (c,d) $x \approx 0.8$, $0.04 \leq y \leq 0.077$.

Since thermal variation of coercivity seems to follow approximately an exponential decrease for the samples with $x \approx 0.4$, $y = 0.052$, $x \approx 0.6$, $y = 0.062$, $x \approx 0.8$, 0.072 and $x \approx 0.8$, 0.077, therefore, this temperature dependence is further discussed based on the exponential law to identify the mechanism responsible for such behavior. Such an exponential dependence of coercivity on temperature has been previously attributed to the possible effects of local random anisotropy in magnetic systems such as amorphous FeY [293] and in amorphous alloys of iron incorporated with several rare earth metals [287]. The temperature dependent coercivity presented in above sections is analyzed as shown in Fig. 5.15 which shows an abrupt decrease below $T = 10$ K except for the sample with $x \approx 0.4$, $y = 0.052$ which manifests slow decrease. The exponential behavior of $H_C(T)$ of these $Ge_{1-x-y}Sn_xMn_yTe$ samples can be successfully described with eq. 5.11 where the lines represent fits to the equation [287]

$$H_C(T) = H_{C0}\exp(-\omega T), \qquad (5.11)$$

where H_{C0} represents the coercivity values at $T = 0$ K, and ω is a constant which were both taken as fitting parameters. This relation yielded good fits to the $H_C(T)$ curves presented, see Fig. 5.15. The estimated values of H_{C0} and ω, are provided in Fig. 5.15 where ω remains between 0.2 – 0.9 K^{-1}. The zero field coercivity, H_{C0}, obtained for the four samples shows large variation from $H_{C0} \approx 8100$ Oe for $y = 0.062$ to $H_{C0} \approx 600$ Oe for $y = 0.077$. This sharp variation suggests that the H_C values might achieve significantly large magnitude near zero temperature regimes. However; it is difficult to explain such large variation on the basis of anisotropy only. Such changes might also arise from compositional and magnetic exchange fluctuations in the magnetic system [285]. Besides the zero field coercivity, the determined values of ω for $Ge_{1-x-y}Sn_xMn_yTe$ alloys are similar to those calculated for random anisotropic systems [284], though, bigger than for instance for $Hf_{57}Fe_{43}$ alloy [282].

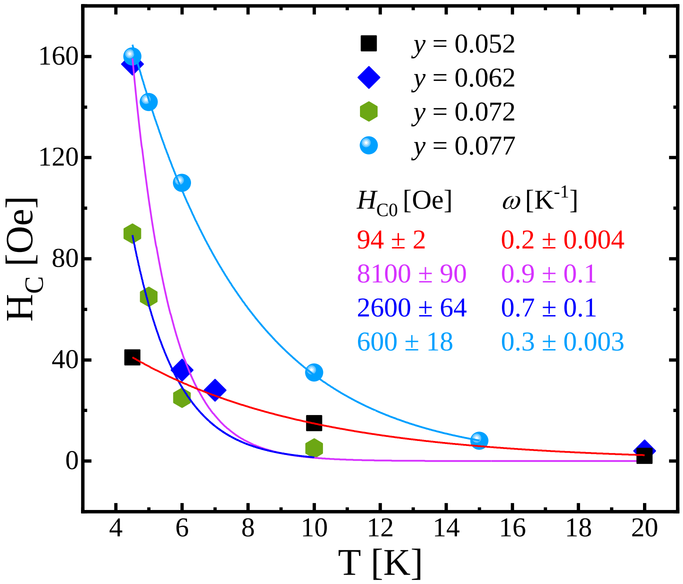

FIG. 5.15 Temperature dependence of coercivity, H_C, of the selected samples which display exponential decrease. The solid lines are fits to exponential law, see eq. 5.11.

The small values of ω obtained in [282] were ascribed to the weak exchange interaction in $Hf_{57}Fe_{43}$ alloys. In comparison to the ω values in Ref. 282, the magnitude of ω for $Ge_{1-x-y}Sn_xMn_yTe$ alloys is bigger by a factor of two to six which might be indicating relatively strong exchange interaction in the present compositions. Further, the values of ω do not demonstrate a clear trend as a function of Mn content which suggests assuming that random anisotropy in different $Ge_{1-x-y}Sn_xMn_yTe$ compositions could also influence the exponential decay of coercivity.

Thus far, the influence of temperature on the magnetization remanence and coercivity in $Ge_{1-x-y}Sn_xMn_yTe$ alloys were presented. It is also important to analyze the impact of Mn concentration on the saturation magnetization values, M_S, for the whole $Ge_{1-x-y}Sn_xMn_yTe$ series presented above. For all samples with Mn content in the range $0.02 \leq y \leq 0.086$, the $M_S = f(y)$ results obtained at $T \approx 4.5$ K are shown on a logarithmic scale, see Fig. 5.16(a). With few exceptions, all M_S values demonstrate a general as a function of Mn proportion. Furthermore, the deviation in $M_S(y)$ dependence from linear trend is comparatively small (this can be seen by comparing the deviation of the M_S values from the linear fit shown as dashed line). In Fig. 5.16(b), the experimental M_S(exp) values are plotted against theoretical, M_S(th) values for all samples. All $Ge_{1-x-y}Sn_xMn_yTe$ samples demonstrate a general increase between M_S(exp) and M_S(th) values. The M_S(th) values were calculated taking into account Mn concentration and spin, $S = 5/2$ for Mn ions using the relation $M_S = g\mu_B N_0 S$. The calculated M_S(th) values are about two times larger than M_S(exp) values which illustrate experimental values are lower than the expected values; see Fig. 5.16(b). The low values for $Ge_{1-x-y}Sn_xMn_yTe$ can arise due to probable presence of AFM MnTe which night suppress the M_S(exp) values. Another explanation can be related to a fraction of Mn ions in a charge state different than 2+ resulting in lower total magnetic moment per Mn ion.

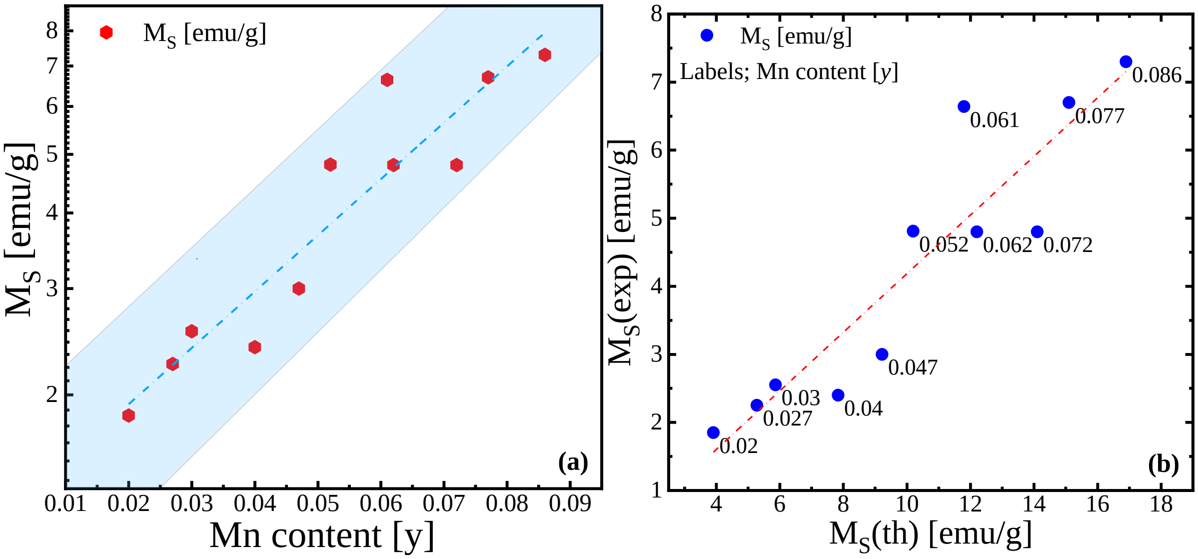

FIG. 5.16(a) Variation of saturation magnetization, M_S, as a function of Mn concentration (b) comparison of the experimental and theoretical values of saturation magnetization. Labels in (b) denote Mn concentration.

The magnetic quantities extracted from the field dependent magnetization results are presented in Table III.

TABLE III: Magnetic properties H_C, M_R, and M_S obtained at $T = 4.5$ K for $Ge_{1-x-y}Sn_xMn_yTe$ samples as a function of Sn and Mn contents.

x	y	M_R[emu/g] $T = 4.5$ K	H_C [Oe] $T = 4.5$ K	M_S [emu/g]
0.182 ± 0.01	0.027 ± 0.006	0.23 ± 0.02	15 ± 2	2±0.05
0.183 ± 0.01	0.047 ± 0.006	0.16 ± 0.02	10 ± 1	2.2±0.04
0.184 ± 0.01	0.060 ± 0.006	4.6 ± 0.1	160 ± 7	5±0.03
0.39 ± 0.03	0.020 ± 0.002	---	---	1.85±0.03
0.40 ± 0.04	0.052 ± 0.005	0.5 ± 0.01	14 ± 1	4.95±0.04
0.41 ± 0.04	0.072 ± 0.007	1.4 ± 0.04	70 ± 3	4.81±0.04
0.54 ± 0.05	0.030 ± 0.003	---	---	2.64±0.04
0.59 ± 0.06	0.062 ± 0.006	1.3 ± 0.04	30 ± 2	4.8±0.05
0.64 ± 0.06	0.086 ± 0.009	3.9 ± 0.1	160 ± 6	7.3±0.05
0.72 ± 0.07	0.040 ± 0.004	0.1 ± 0.03	23 ± 2	3.11±0.03
0.79 ± 0.08	0.072 ± 0.007	2.7 ± 0.1	55 ± 2	4.8±0.04
0.84 ± 0.07	0.077 ± 0.007	5.5 ± 0.3	160 ± 6	6.7±0.05

5.2.3 Scaling of irreversibility temperatures

In order to complement the $\chi_{AC}(T)$ results, the temperature dependent static magnetization, $M(T)$, measurements were performed at several constant magnetic field amplitudes to further evaluate the types of magnetic order identified in $Ge_{1-x-y}Sn_xMn_yTe$ crystals. Measurements of the zero-field-cooled $M_{ZFC}(T)$ and field-cooled $M_{FC}(T)$ curves were performed over a wide range of magnetic field 10 Oe ≤ H_{DC} ≤ 200 Oe. The $M_{ZFC}(T)$ and $M_{FC}(T)$ results were collected during the sample heating after cooling the samples from temperatures well above the magnetic transition temperature observed in the $\chi_{AC}(T)$ results down to 2 K either in the absence of the external magnetic field or in the presence of applied field, respectively. In all M_{ZFC}-$M_{FC}(T)$ dependencies (Fig. 5.17(b–d)) except for the ample with $x \approx 0.2$, $y = 0.047$, sharp increase of the magnetization value with decreasing the temperature is clearly visible. However, below the magnetic transition temperatures, the samples with different Sn and Mn concentrations reveal different magnetic behavior. The ZFC branches for the crystals having $x \approx 0.2$, 0.4 and $y = 0.047$, 0.052 show cusps and broad maxima, at $H = 15$ Oe as shown in Fig. 5.17(a,b), sequentially. The approximate temperature values of the peak's maxima in the ZFC curves were determined to be equal to $T \approx 5.4$ K and $T \approx 8$ K at $H = 15$ Oe for these crystals. The largest magnitude of the splitting/bifurcation between the ZFC and the FC curves is visible for the crystal, $x \approx 0.2$, $y = 0.047$ among all of the results presented in Fig. 5.17 whereas the bifurcation gradually decreases for the samples with $x \approx 0.4$, 0.59, $y = 0.052$, 0.062 and disappears for $x \approx 0.79$, $y = 0.072$. Such maxima along with significant bifurcation of the M_{ZFC} and M_{FC} curves observed for the samples with $x \approx 0.2$, 0.4, $y = 0.047$, 0.052 have been previously discussed for different systems to

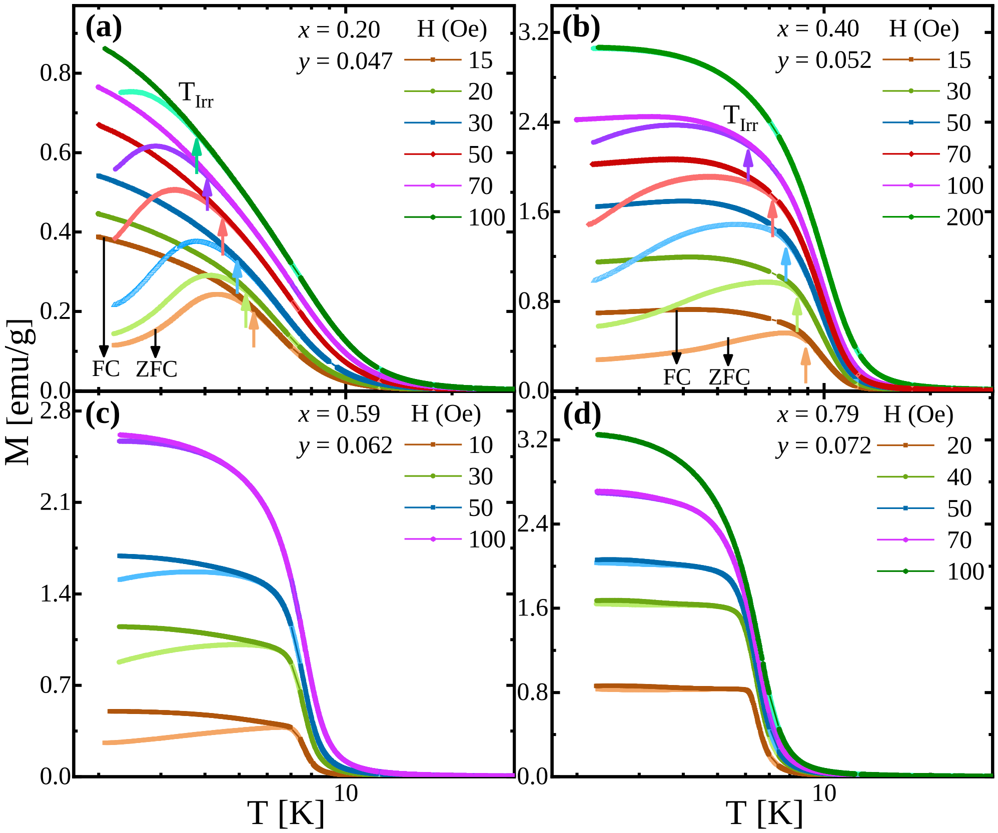

FIG. 5.17(a–d) Temperature dependent zero-field-cooled and field-cooled branches of DC magnetization for selected samples with (a) $x \approx 0.2$, $y = 0.047$ (b) $x \approx 0.4$, $y = 0.052$ (c) $x \approx 0.6$, $y = 0.062$ and (d) $x \approx 0.8$, $y =$

Also, the temperature at which the splitting between ZFC and FC curves initiates, i.e. $\Delta M = M_{\mathrm{FC}}(T) - M_{\mathrm{ZFC}}(T) \neq 0$, called T_{Irr}, illustrates an irreversible magnetization process [262,294], which was determined as $T_{\mathrm{Irr}} \approx 5$ K (for $x \approx 0.2$, $y = 0.047$) and 10 K (for $x \approx 0.4$, $y = 0.052$) for results obtained at 15 Oe. The ΔM (at the lowest temperature) and T_{Irr} values for the two crystals in Fig. 5.17(a,b) reduce with the increase in magnitude of the external magnetic field. The presence of ΔM parameter and its relationship with the freezing process or frustration might lead a magnetic transition to either SG or CG state [295]. These will be analyzed in detail in the following section.

In Fig. 5.17(c), the $M_{\mathrm{ZFC-FC}}(T)$ results obtained for the $Ge_{1-x-y}Sn_xMn_yTe$ alloy with intermediate composition, $x \approx 0.6$, $y = 0.062$ are shown. The ZFC results of this sample exhibit nearly flat curves as compared to the samples in Fig. 5.17(a,b) with a rather slow M_{ZFC} decrease when cooling towards low temperatures. This difference might suggest a magnetic state different than those shown by the samples with $x \approx 0.2$, 0.4 and $y = 0.047$, 0.052. This tendency in $M_{\mathrm{ZFC-FC}}(T)$ results is very similar to the magnetic properties reported in $La_{1-x}Sr_xCoO_3$ system [187]. In these results, two processes; the magnetic field driven shift of irreversibility temperature towards low values and squeezing of bifurcation between $M_{\mathrm{FC}}(T)$ and $M_{\mathrm{ZFC}}(T)$ indicate that frustration exists among magnetic moments that may lead to SG-like state. It is also essential to note that the irreversibility temperature in these curves is less than maxima temperature, $T_{\mathrm{max}} \lesssim T_{\mathrm{Irr}}$, which is not true in case of conventional SG systems therefore; it might signify the existence of magnetic clusters in the $Ge_{1-x-y}Sn_xMn_yTe$ samples [176,296]. In Fig. 5.17(d), the $M_{\mathrm{ZFC-FC}}(T)$ results for the Sn-rich crystal with $x \sim 0.8$ and $y = 0.072$ are presented. As the sample is cooled down, both ZFC and FC branches reveal identical magnetization paths down to $T = 2$ K with insignificant signatures of irreversibility.

In comparison with the results in Fig. 5.17(a–c) with the samples with $x \approx 0.2$, $y = 0.047$, $x \approx 0.4$, $y = 0.052$ and $x \approx 0.6$, $y = 0.062$, the ZFC and FC results Fig. 5.17(d) show clearly flat plateaus where the maxima and bifurcation disappear at all measured field values. The behavior of ZFC and FC curves in Fig. 5.17(d) reveal ferromagnetic type ordering which is also obvious from the saturated magnetization curves. Unlike the results in Fig. 5.17(a,b) which probably present mixed magnetic interactions owing to the presence of magnetically glassy state, the results in Fig. 5.17(c) show typical characteristics of FM phase. Until this part, the tuning of magnetic states in $Ge_{1-x-y}Sn_xMn_yTe$ crystals was presented in terms of Mn content. However; the glassy magnetic regime suggests that in addition to Mn content, the involvement of Sn ions cannot be disregarded. For instance, the crystal with $x \approx 0.4$, $y = 0.072$ as shown earlier in Fig. 5.2(a) shows a frustrated magnetic state whereas $x \approx 0.8$, $y = 0.072$ in Fig. 5.3(c) displays an FM-like order with the same Mn level. These outcomes propose that the variation of magnetic states in GSMT samples is clearly influenced by the presence of Sn ions. The impact of Sn ions was also discussed in previous sections in the context of crystal structure which affects the magnetic interactions between Mn ions. The complex nature of magnetic interactions at 5 – 7 % of Mn content is credited to the possible development of varying size magnetic clusters that could also be predicted by comparing the width of $\chi_{\mathrm{AC}}(T)$ dependencies. Unlike the conventional SG state, these samples establish magnetic clusters which consist of frozen FM-like order that were not detected previously in $Ge_{1-x-y}Sn_xMn_yTe$ alloys [220,222]. The results of DC magnetization signifying Mn clusters will be further analyzed by interpreting the shift in T_{Irr} as a function of magnitude of magnetic field.

In Fig. 5.17 as presented above, an impurity dependent clear transition is obviously observed from a large irreversibility to relatively small magnitude of bifurcation and subsequently a long range FM phase. This showed an obvious trend of variation in the relative level of freezing and clustering as a function of alloying concentration. Likewise, selected samples from the remaining compositions are presented in Fig. 5.18 in sequence of increasing Mn content. The $M(T)$ results for the sample having $x \approx 0.4$, $y = 0.02$ show small magnetization value around 0.4 emu/g at $H = 15$ Oe at $T \approx 2$ K that increases to about 0.17 emu/g at $H = 100$ Oe. This sample does not reveal any particular indication of transition to an ordered magnetic state even at low temperatures.

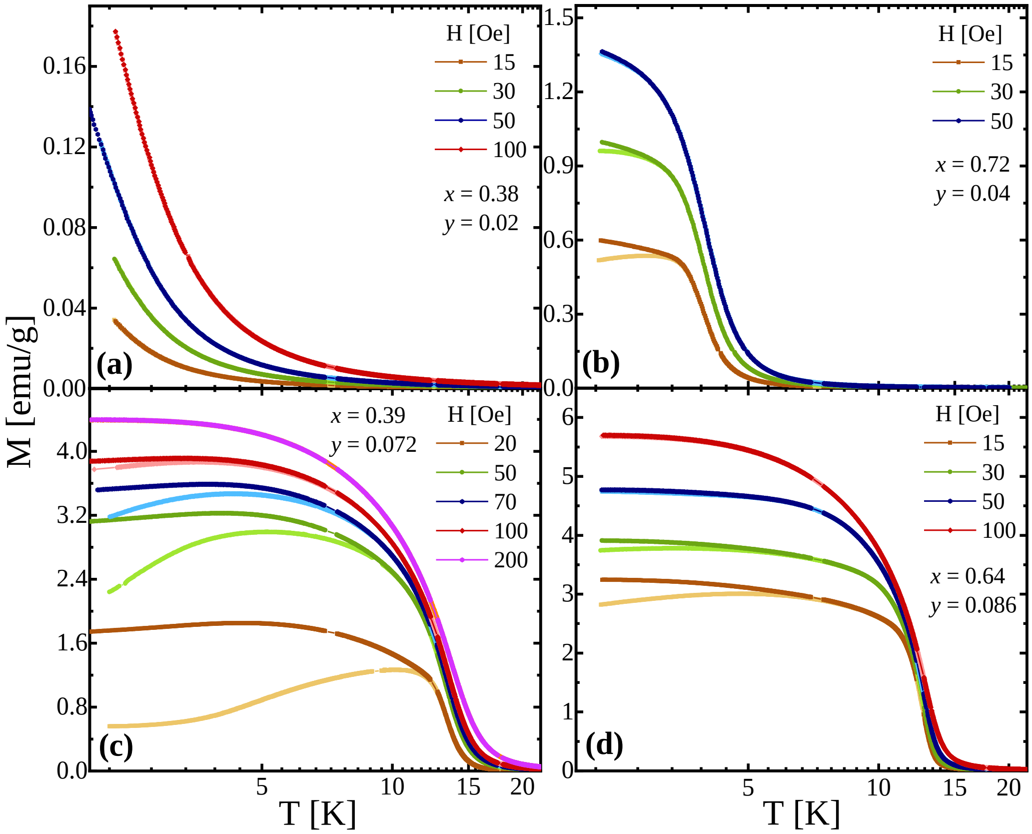

FIG. 5.18 The zero–field–cooled and field–cooled $M(T)$ dependence for GSMT crystals with (a) $x = 0.38$, $y = 0.02$ demonstrating features of a paramagnetic state, (b,c) samples with $x = 0.64$, $y = 0.086$ and $x = 0.72$, $y = 0.04$ displaying weak splitting in the ZFC–FC curves, and (d) $x = 0.79$, $y = 0.072$ shows negligible splitting in the ZFC–FC branches from $H = 20$ Oe to $H = 100$ Oe. The saturated FC curves indicate the FM type of magnetic order.

As presented earlier in Fig. 5.2(a), this sample with the lowermost Mn impurity content behaves as a PM down to the lowest temperature achieved in that experiment. The results in Fig. 5.18(b) and (c) exhibit a transition to an ordered state at $T \approx 4$ K and ≈ 14 K, respectively. Likewise, the crystal with the highest Mn amount $x \approx 0.6$, $y = 0.086$ manifest ferromagnetic type behavior with nearly flat $M(T)$ curves below the transition temperature. Besides a small splitting between ZFC and FC curves, the results suggest FM-like transition where the splitting between ZFC and FC curves might occur due to the fact that the anisotropy of the system overcomes the external magnetic field. The final results for the sample with $x \approx 0.6$, $y = 0.086$ in Fig. 5.18(d) demonstrate convincing curves of an FM phase which show very small irreversibility and achieve $M(H)$ curve at $T \approx 4.5$ K which are typical features of FM type magnetic order.

Since the $M(T)$ results in Fig. 5.17(c,d) for the samples with $x \approx 0.6$, 0.8 and $y = 0.062$, 0.072 showed different FC-ZFC behavior than the samples in Fig. 5.17(a,b), therefore, the magnetization hysteresis results of these crystals are presented in order to further support the $M(T)$ results. The isothermal $M(H)$ curve for the sample with $x \approx 0.6$ and $y = 0.062$ measured at $T \approx 4.5$ K is shown in Fig. 5.19(a). The $M(H)$ loop for this sample is different from the square–like hysteresis depicting FM phase in Fig. 5.19(b) and also differs from a characteristic S–shaped curve of a SG state shown in Ref. 176. The $M(H)$ loop in Fig. 5.19(a) manifests somewhat an intermediate magnetic state between a typical S–shaped curve of SG systems and a square–like loop typical of FM order.

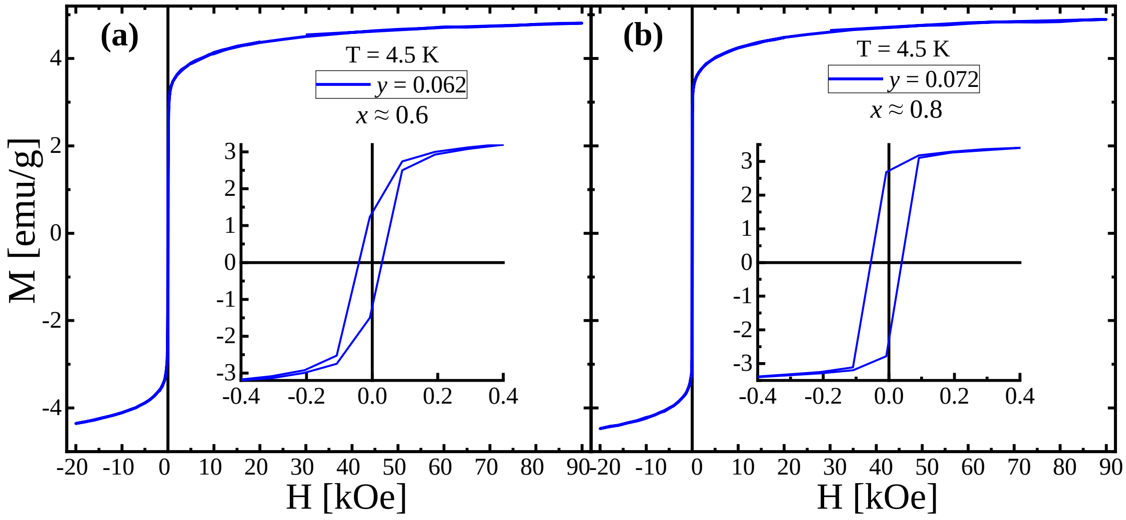

FIG. 5.19(a,b) Magnetization hysteresis, $M(H)$ curves of the compositions $x \approx 0.6$, 0.8 and $y = 0.062$, 0.072, respectively. The insets present hysteresis cuts between $-0.4 \leq H \leq 0.4$ kOe where (b) reveals a square–like hysteresis loop indicating a long range ferromagnetic order.

This might represent the existence of FM-like magnetic clusters in the sample which can also be anticipated from the broad maxima and slow decrease in ZFC curves below the transition temperature, see Fig. 5.19(c). Also, the plateau like shape in $\chi'_{AC}(T)$ results of $x \approx 0.6$, $y = 0.062$ earlier shown in Fig. 5.3(a) indicates similar FM type phase. Though; the $M_R(T)$ and $H_C(T)$ values show a drastic decline above $T \approx 4.5$ K which is probably due to the fact that the FM-like phase declines faster at $T \geq 4.5$ K. Furthermore, comparing the magnetic behavior of two samples with same Mn content $y = 0.072$ though different Sn content $x \approx 0.4$ in Fig. 5.18(c) and $x \approx 0.8$ in Fig. 5.17(d) reveals the impact of Sn ions on the magnetic ordering of $Ge_{1-x-y}Sn_xMn_yTe$ crystals. The sample with $x \approx 0.8$, $y = 0.072$ shows ferromagnetic like $M(T)$ curves with negligible bifurcation, see

Fig. 5.17(d). This can also be complemented by the square-like $M(H)$ curve shown in Fig. 5.19(b). However; the crystal with $x \approx 0.4$, $y = 0.072$ manifests large bifurcation as shown in Fig. 5.18(c) which demonstrates similar behavior as SG or CG. Particularly, the $M_R(T)$ and $H_C(T)$ results for $x \approx 0.4$ show negligibly small values of both parameters even at the lowest measured temperature which disregards the presence of the FM order. These observations in $M(T)$ and $M(H)$ results for the samples with $x \approx 0.4$, $y = 0.072$ and $x \approx 0.8$, $y = 0.072$ can also be supported by taking into account the $\chi'_{\mathrm{AC}}(T)$ results. In Fig. 5.2(a), the sample with $x \approx 0.4$, $y = 0.072$ showed nearly symmetric cusp with freezing temperature value, $T_{\mathrm{F}} \approx 10.2$ K which was discussed and stated to show glassy magnetic state. This interpretation is consistent with the $M(T)$ and $M_R(T)/H_C(T)$ results for this sample with $x \approx 0.4$, $y = 0.072$ discussed above. Moreover, the $\chi'_{\mathrm{AC}}(T)$ results for the sample with $x \approx 0.8$, $y = 0.072$ showed sharp transition from PM to an ordered state possibly representing an ordered state different than SG or CG state, see Fig. 5.3(c). Comparing the $\chi'_{\mathrm{AC}}(T)$ curves with the flat $M(T)$ curves in Fig. 5.17(d) square-like $M(H)$ hysteresis in Fig. 5.19(b), this sample can be illustrated to represent FM type magnetic phase.

As mentioned earlier in both AC and DC magnetometric analysis, there are several indications of frustrated or glassy magnetic states which could either be typical of SG or CG systems. Particularly, the $\chi_{\mathrm{AC}}(T)$ curves which anticipated frustrated magnetic state for $x \approx 0.4$, $y = 0.052$ however; obvious conclusions could not be deduced from the frequency dependent magnetic susceptibility results. Further analysis is attempted for this crystal by considering the evolution of the ZFC maxima observed in the results of the $M_{\mathrm{ZFC}}(T)$ measurements as presented in Fig. 5.17(b). The maxima in ZFC branches shifted towards lower temperatures along with the T_{Irr} values as magnitude of DC magnetic field was increased from 15 Oe to 200 Oe. The estimated values of the irreversibility temperature based on the $M(T)$ results shown in Fig. 5.17(b) are marked by arrows of the same colors as the $M(T)$ curves. In similar studies performed on the SG systems, the shift in T_{Irr} to lower temperature as H increases is shown to follow a power law, the De Almeida-Thouless (AT) line [188,189] which follows the relation, $\delta T_{\mathrm{Irr}} \propto H^{2/3}$. Here, δT_{Irr} represents a shift in irreversibility temperature. Eq. 5.12 was used to analyze the δT_{Irr} vs H dependence for the samples with $x \approx 0.2$, $y = 0.047$, $x \approx 0.2$, $y = 0.060$, $x \approx 0.4$, $y = 0.052$, and $x \approx 0.4$, $y = 0.072$

$$H = H_0\left[1 - \left\{\frac{T_{\mathrm{Irr}}(H)}{T_{\mathrm{Irr}}(H{=}0)}\right\}\right]^{\Phi/2}. \tag{5.12}$$

In eq. 5.12, the magnetic field amplitude H_0, irreversibility temperature, $T_{\mathrm{Irr}}(H{=}0)$, and crossover exponent Φ were used as fitting parameters. The parameter $T_{\mathrm{Irr}}(H)$ represents the value of irreversibility temperature at a certain magnetic field whereas $T_{\mathrm{Irr}}(H{=}0)$ denoted the irreversibility temperature at $H = 0$. The parameter $T_{\mathrm{Irr}}(0)$ represents the SG transition temperature, T_g, at zero magnetic field. The critical AT lines in Fig. 5.20(a) which conventionally separate a SG state from a PM state, were determined for the samples by fitting the experimental data to eq. 5.12. The best fits to the experimental results are shown in Fig. 5.20(a) demonstrate that the results follow the AT equation in an $H^{2/3}$-T_{Irr} plane.

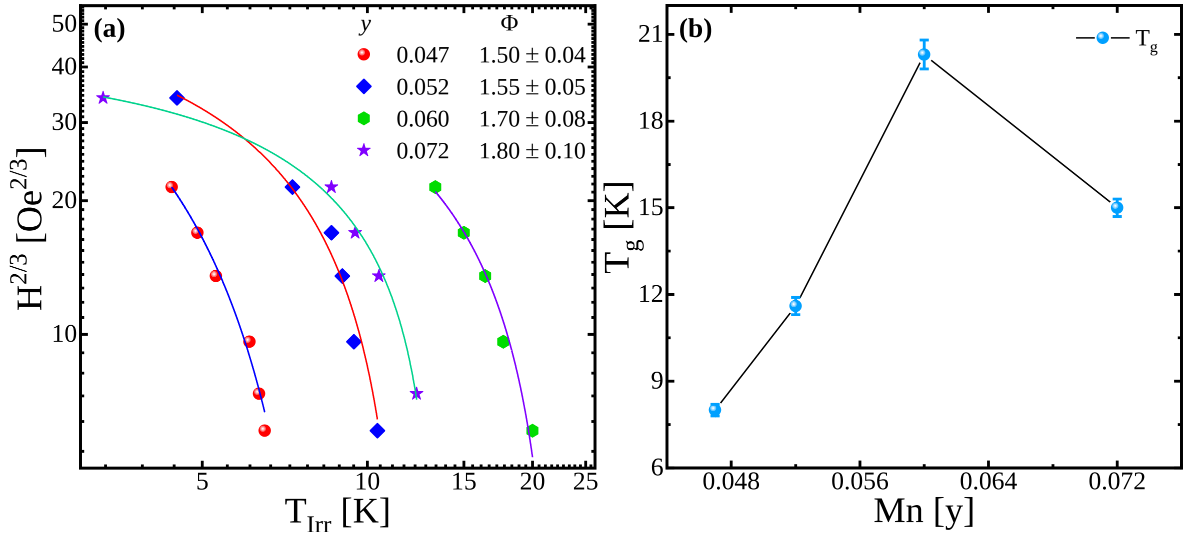

FIG. 5.20(a) The T_{Irr} vs $H^{2/3}$ values for $x \approx 0.2$, $y = 0.047$, $x \approx 0.2$, $y = 0.060$, $x \approx 0.4$, $y = 0.052$, and $x \approx 0.4$, $y = 0.072$ compositions extracted from static $M(T)$ results. Data points (scatters) were fitted to De Almeida-Thouless equation (solid lines). (b) T_{g} values for the samples shown in (a) as a function of Mn contents.

Except for the sample with $y = 0.047$, these values extracted from the fitted lines show slight deviation from the standard value, $\Phi = 1.5$ accepted for canonical SG systems [188,189]. The obtained value for the sample with $x \approx 0.2$, $y = 0.047$ validates the presence of SG state as observed earlier in the $\chi_{\mathrm{AC}}(T)$ and $M_R(T)/H_C(T)$ results. For the sample with $x \approx 0.4$, $y = 0.052$, $\Phi = 1.55$ shows slight deviation from the values typical of SG system. In addition, the two samples with $y = 0.06$ and 0.072 yield $\Phi = 1.7$ and 1.8, respectively, which are approximately in the range of CG systems agreeing well with the earlier work by Pallab *et al.*, [184]. However; the deviation for the crystals having $x \approx 0.2$, $y = 0.060$ and $x \approx 0.4$, $y = 0.072$ might also indicate that the glassy magnetic state either belongs to a non-mean-field universality class or arises due to strong anisotropy as discussed in earlier works [184,297]. The fitted AT lines presented here could be extrapolated towards crossover with temperature scale which would define the estimated SG/CG temperature, T_g values at $H = 0$. The T_g values for the samples in Fig. 5.20(a) determined during AT fitting process are shown in Fig. 5.20(b).

As a final note on the $M(T)$ results and AT fitting, the ΔM term for the crystals having $x \approx 0.4$, $y = 0.052$, $x \approx 0.6$, $y = 0.062$ in Fig. Fig. 5.17(b,c) and $x \approx 0.4$, $y = 0.072$ in Fig. 5.18(c) persistently shows non-zero values up to an external magnetic field equal to 100 Oe. This signifies that the inception point of irreversibility i.e. $\Delta M = M_{\mathrm{FC}}(T) - M_{\mathrm{ZFC}}(T) \neq 0$ is still present even at $H = 100$ Oe. On further increase in the magnitude of magnetic field to $H = 200$ Oe in Fig. 5.17 and Fig. 5.18, the ZFC and FC branches start to follow the same path up to the lowest measured temperature where $\Delta M = M_{\mathrm{FC}}(T) - M_{\mathrm{ZFC}}(T) = 0$. The decline in T_{Irr} with increasing magnetic field could also be explained by analyzing the AT lines in Fig. 5.20 which shows that the irreversibility disappears in the high field regime. Based on the analysis of data gathered in Fig. 5.17 and Fig. 5.18, the magnetic order in these samples vary from a frozen locked-in state to a long range FM ordering as the x and y contents increase. It is imperative to mention that the ZFC curves which show bifurcation in Fig. 5.17 and Fig. 5.18 do not drop at temperatures below each maximum unlike conventional SG magnetic state. Such a disagreement might occur in the presence of Mn clusters in these samples. A similar non-zero ZFC branch was shown by Phan *et al.*, for polycrystalline perovskite $(\mathrm{Nd}_{0.65}\mathrm{Y}_{0.35})_{0.7}\mathrm{Sr}_{0.3}\mathrm{MnO}_3$ and was initiated by the coexistence of both FM and SG states [298]. The obvious magnetic hysteresis and irreversible processes in $M(T)$ results are signatures of FM-like magnetic clusters in the crystals having $x \approx 0.4$, $y = 0.052$ and $x \approx 0.6$, $y = 0.062$. For the sample with $x \approx 0.8$, $y = 0.072$, sharp transition to an ordered phase and nearly indistinguishable/constant magnetization is generally attributed to the presence of FM phase [299].

The studies of isothermal magnetization vs magnetic field are important in order to understand magnetic order and magnetic exchange. In this context, Brillouin function (BF) is a widely used model that is attempted to describe the isothermal magnetization; $M(H)$ curves [300,301]. As $M(H)$ curves do not manifest linear behavior vs magnetic field, these results can be described using BF which has been previously used for several DMS compounds [300,302,303]. The obtained magnetization curves of $\mathrm{Ge}_{1-x-y}\mathrm{Sn}_x\mathrm{Mn}_y\mathrm{Te}$ samples were analyzed using the Weiss model for ferromagnets. Therefore, slight modifications were introduced in BF by adding molecular field term and diamagnetic term in order to obtain better description of $M(H)$ results. The $M(H)$ results were fitted to eq. 5.13 as presented below [300,302,303]

$$M = M_S + \chi_{\mathrm{dia}} B. \tag{5.13}$$

Here, $M_S = g\mu_B N_0 S B_S(\zeta)$ in which $B_S(\zeta)$ denotes Brillouin function which is written as,

$$B_S(\zeta) = \frac{2S+1}{2S}\coth\left(\frac{2S+1}{2S}\zeta\right) - \frac{1}{2S}\coth\left(\frac{\zeta}{2S}\right) \tag{5.14}$$

$$\zeta = \frac{Sg\mu_B(B+\lambda_M M)}{k_B T} \tag{5.15}$$

The best fits to the experimental $M(H)$ curves were obtained for the low Mn samples only as displayed in Fig 5.21. Since appropriate fits were not obtained with the simple BF, therefore, modified BF was applied with an additional $\lambda_M M$ term as for the $M(H)$ curves obtained at $T \approx 4.5$ K.

The additional $\lambda_M M$ introduced in eq. 3.15 is a representation of the molecular field present in the system [170]. The product of λ_M and M means the coefficient of the Weiss molecular field. In case of the BF interpretation in the PM regime, the product $\lambda_M M$ in eq. 5.15 is omitted from the function. Additionally, the fitting process was performed taking into account the diamagnetic susceptibility term, $\chi_{\text{dia}} = -3\times10^{-7}$ emu·g^{-1}Oe^{-1} of the host lattice GeTe. The fits shown in Fig 5.21 also determined the values of fitting parameter, M_S, equal to 1.91 emu/g, 2.7 emu/g and 3.04 emu/g for the samples with $x \approx 0.4$, 0.6, 0.8 and $y = 0.02$, 0.03, 0.04, respectively. The comparison of M_S values determined from BF fitting with those obtained earlier using law of approach to saturation yielded less than 3% deviation. The M_S values obtained from BF fitting can be used to calculate the effective magnetic moment considering the relation $\mu_{\text{eff}} = M_S\{[(J+1)/J]\}^{1/2}$ [304]. Taking $J = S = 5/2$ for Mn ions in $\text{Ge}_{1-x-y}\text{Sn}_x\text{Mn}_y\text{Te}$ samples, μ_{eff} values were obtained equal to 2.67 μ_B, 3.78 μ_B, and 4.26 μ_B, for the samples with $y = 0.02$, 0.03, and 0.04, respectively. The μ_{eff} values obtained at $T = 4.5$ K are larger than μ_{eff} values obtained from high temperature CW analysis and in good agreement with the literature [304].

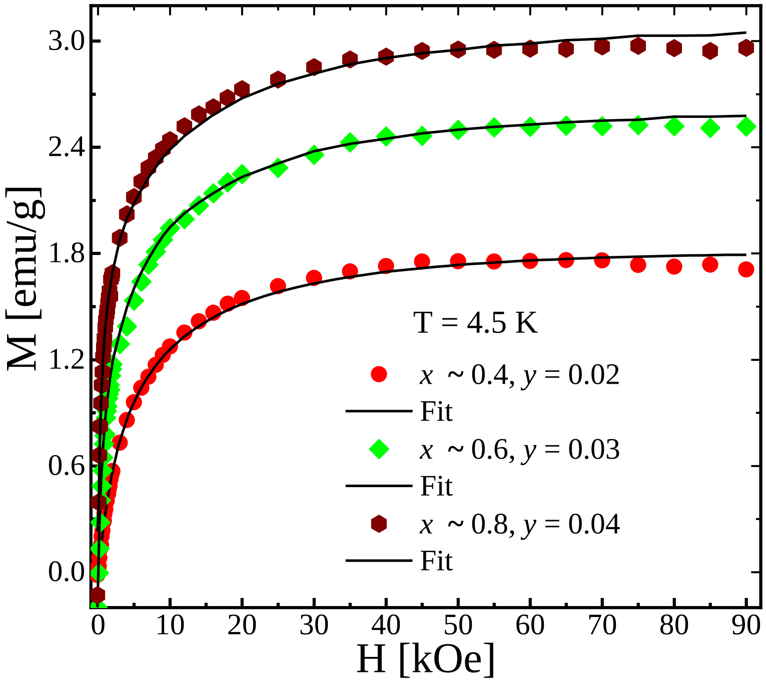

FIG. 5.21 Magnetization, $M(H)$ curves of three selected compositions fitted to the modified Brillouin function in the low temperature regime, $T \approx 4.5$ K. The samples with $x \approx 0.4$, 0.6, 0.8, $y = 0.02$, 0.03, 0.04 are denoted by scatters whereas solid lines show fits Brillouin function.

As presented in Fig 5.21, the fits were obtained after introducing $\lambda_M M$ term which made reasonable interpretation of the low temperature $M(H)$ results. Here, M_S evidently depends upon the concentration of Mn proportion in the alloys which have similar trend as discussed earlier for $M(H)$ results. Furthermore, the second free parameter, λ_M is essential part of the Weiss model which tells us about the nature of the spin alignment and exchange interaction among the magnetic moments. From these fits, the positive values of Weiss constant, $\lambda_M = 1.28$, 1.04 and 0.95 (g·Oe)/emu calculated for $y = 0.02$, 0.03 and 0.04, respectively indicate that the magnetic interaction is positive at $T \approx 4.5$ K. It is therefore assumed that the appropriate fitting of the $Ge_{1-x-y}Sn_xMn_yTe$ compositions is obtainable with the Weiss model of BF and consequently reveals that the dominant exchange interactions between the Mn^{2+} ions are positive.

5.3 Magnetic phase diagram of $Ge_{1-x-y}Sn_xMn_yTe$ crystals

The in-depth magnetometric studies of $Ge_{1-x-y}Sn_xMn_yTe$ crystals demonstrated variation in the nature of magnetic state at different alloying compositions. Based on the above magnetometric results discussed so far, this section presents magnetic phase diagram to show the types of magnetic states observed in the $Ge_{1-x-y}Sn_xMn_yTe$ alloys. In the low Mn alloying regime for $0.2 \leq x \leq 0.8$ and $y \leq 0.04$, small $\chi_{AC}(T)$ response was recorded and transition to an ordered magnetic phase was not observed down to $T \approx 4.5$ K; see $\chi'_{AC}(T)$ curves for the PM samples in Figs. 5.1, 5.2 and 5.3, respectively. Therefore, for low Mn content $y \leq 0.04$, the results clearly show PM state (marked as PM in Fig. 5.22).

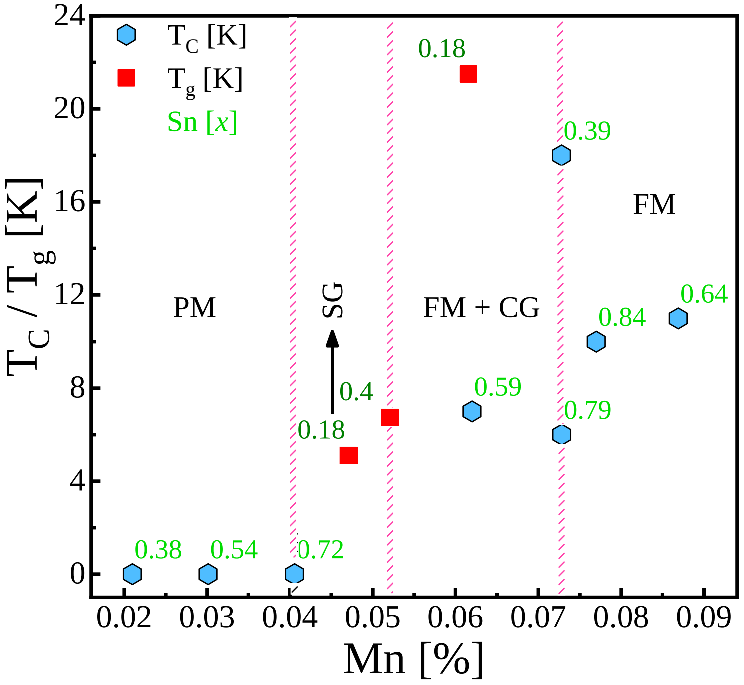

FIG. 5.22 Magnetic phase diagram of bulk $Ge_{1-x-y}Sn_xMn_yTe$ crystals as a function of Mn concentration.

The PM behavior of these low impurity compositions obviously signifies that the exchange interaction is too weak for the magnetic order to be detected at $T \approx 4.5$ K. As the Mn content is increased to about $0.04 \leq y \leq 0.047$ as discussed earlier in section 5.1, this sample demonstrated a SG state (see Fig. 5.22) with a scaling parameter, $R = 0.017$ [223]. The vertical hatched lines in Fig. 5.22 denote approximate boundaries separating different magnetic states. The $M_{\mathrm{ZFC}}(T)$–$M_{\mathrm{FC}}(T)$ results of this composition showed also a shift in irreversibility temperature, T_{Irr}, as the DC magnetic field was increased, Fig. 5.17. Moreover, the calculated values of τ_0 ~10^{-13} s and zv = 4.9 are in typical range of canonical SG systems. For the $\mathrm{Ge}_{1-x-y}\mathrm{Sn}_x\mathrm{Mn}_y\mathrm{Te}$ alloys with Mn content about 5%, the magnetic moments freeze in a SG state below the freezing temperature. This crystal with $x \approx 0.2$, $y = 0.047$ shows magnetic state which is different from conventional long range ferromagnetic or antiferromagnetic phases as a consequence of mixed magnetic interactions. The spin-disordered frozen state of SG system rather arises from frustration between FM and AFM type interactions [177]. Moreover, the calculated values of τ_0 and zv also indicate that the Mn^{2+} impurity ions freeze as a result of magnetic frustration though there is no indication of magnetic clusters in this sample. Increasing Mn concentration further to $0.052 \leq y \leq 0.02$, the T_{F} vs f results showed characteristics of Mn clustering effect. This alloying regime also manifests that magnetic moments are in a frustrated state with the presence of Mn clusters. Moreover, the CG composition also presents magnetic well defined hysteresis, therefore, these Mn clusters are assumed to constitute FM like ordering. As earlier reported by De *et al*., [305] and Chen *et al*., [306], the coexistence of disordered magnetic state and FM phase originates from frozen clusters constituting FM order. Therefore, in the Mn range, $0.52 \leq y \leq 0.72$, the $\mathrm{Ge}_{1-x-y}\mathrm{Sn}_x\mathrm{Mn}_y\mathrm{Te}$ alloys exhibit coexistence of Mn clusters and FM phase.

Finally, the compositions with the highest Mn concentration, $0.072 \leq y \leq 0.086$ are presented in the right part of Fig 5.22. The χ'_{AC} and $M(T)$ curves showed typical results of a long range FM phase in these samples. The FM order in this alloying range was also confirmed by the $M(H)$ results as presented in Fig 5.13. The square-like magnetic hysteresis observed for the crystals having $x \approx 0.6$, $y = 0.086$ and $x \approx 0.8$, $y = 0.077$ further support the presence of FM order in $\mathrm{Ge}_{1-x-y}\mathrm{Sn}_x\mathrm{Mn}_y\mathrm{Te}$ alloys with the highest Mn concentration studied in this thesis.

5.4 Determination of magnetic exchange constant

Finally, the discussion of the calculated critical temperature values in terms of the strength of the RKKY interactions is presented. In order to appropriately take into account, the magnetic exchange in IV-VI DMS such as $\mathrm{Ge}_{1-x-y}\mathrm{Sn}_x\mathrm{Mn}_y\mathrm{T}$ alloys, modified Sherrington – Southern model is used that was applied earlier for the same alloys as well as for other DMS alloys [181,222]. For complete explanation of the Sherrington – Southern model, refer to its description in Ref. 307 and also results obtained for $Ge_{1-x-y}Sn_xMn_yTe$ compositions with $x < 0.15$ are discussed in Ref. 222. These calculations were made with the exponential damping factor, $\lambda_d = 10$ nm, the crystal lattice parameters, $a = 5.98$ Å and $\alpha = 88.8°$.

As a result of these calculations, the Curie temperature vs. Mn content dependence was obtained for several material parameters, such as Sn content, x, carrier concentration, n_h, and Mn-hole exchange constant, J_{pd}. Experimental results together with theoretical lines are presented in Fig 5.23.

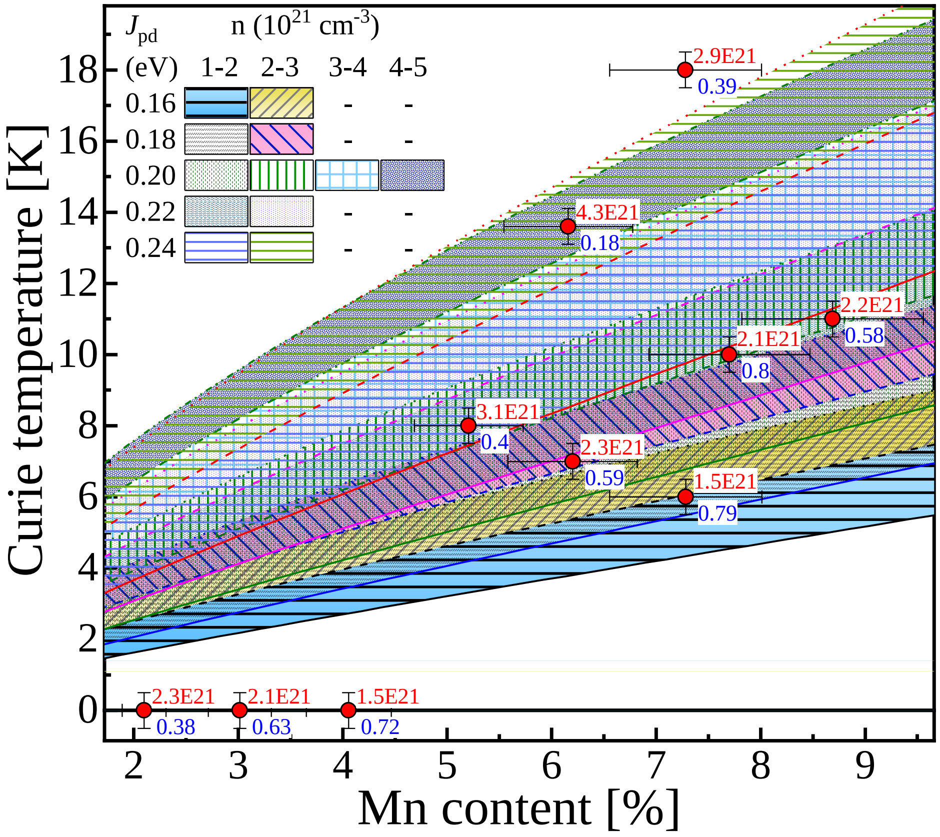

FIG. 5.23 The results illustrate relationship between calculated Curie temperature, T_C, against the Mn concentration, y, for the $Ge_{1-x-y}Sn_xMn_yTe$ compositions having different Sn concentration, x (marked as blue labels), and charge (hole) carrier density, n (marked as red labels). The lines denote results obtained from the modified Sherrington-Southern model for different magnetic exchange constant, J_{pd}, and charge carrier concentration, n_h values.

This analysis reproduced the experimental results very well yielding rather low J_{pd} values which did not exceed 0.24 eV. It is also clear that the values of J_{pd} are presenting a general decline with the increasing Sn content. For instance, for the compositions with $x \approx 0.2$, the J_{pd} value is about 0.24 eV which reduced to 0.16 eV for the compositions with the highest Sn, $x \approx 0.8$. The calculated values are smaller than $J_{\text{pd}} \sim 0.45$ eV determined previously in Ref. 222 for $Ge_{1-x-y}Sn_xMn_yTe$ alloys with $x \approx$

0.12 which follow the general trend of decrease in J_{pd} vs Sn concentration. However, the Mn-hole exchange parameter for these compositions is not showing monotonic dependence with Sn content, x, from the values reported for $Ge_{1-y}Mn_yTe$ equal to about 0.7 eV for bulk crystals [308] down to the value reported for $Sn_{1-y}Mn_yTe$ with $y > 0.1$ close to 0.1 eV [181]. The most important conclusion is related to the fact that the J_{pd} vs x dependence obtained in the present work is satisfying compared with the results presented in Ref. 222 and together these results show clearly that the J_{pd} is not a linear function of the Sn content in IV-VI DMS alloys. The J_{pd} values calculated for $Ge_{1-x-y}Sn_xMn_yTe$ crystals studied in this thesis together with the results from literature are presented in Fig 5.24. In the Sn concentration range from $x = 0.2$ to $x = 0.8$, the decline in J_{pd} value is rather slow as compared to the compositional range with $x \leq 0.2$ The overall J_{pd} values decline from about 0.8 eV for GeTe to about 0.1 eV for $x = 0.9$.

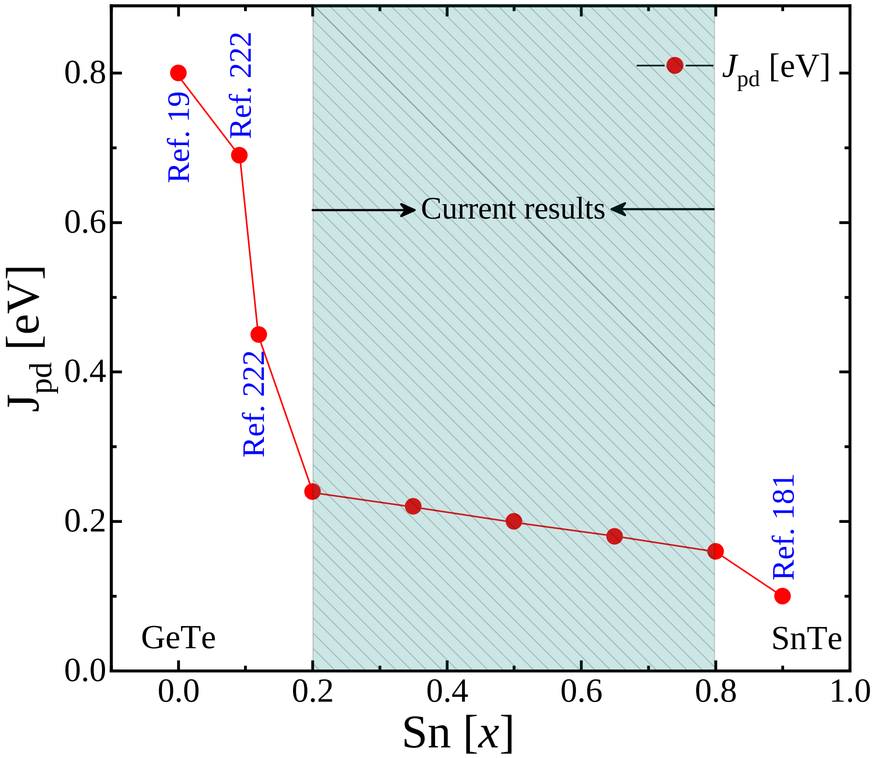

FIG. 5.24 J_{pd} values as a function of Sn content, x calculated for $Ge_{1-x-y}Sn_xMn_yTe$ compositions studied in this thesis are shown as shaded region. J_{pd} results obtained in previous works are marked with corresponding references [19,181,222].

CHAPTER 6

Magnetotransport Phenomena in G$_{1-x-y}$Sn$_x$Mn$_y$Te Multiferroics

6.1 Introduction

After the discovery of OHE and AHE, these phenomena have led to substantial theoretical and experimental discoveries over the years. Unlike the OHE phenomenon which occurs due to the Lorentz force on moving charge carriers, AHE arises as a consequence of spontaneous magnetization in the materials [309]. Pugh and Lippert then developed a relation with two different contributions to ρ_{xy} as; $\rho_{xy} = R_0H_z + \mu_0R_sM_z$, the first R_0H_z term shows contribution from ordinary Hall effect whereas $\mu_0R_sM_z$ represents anomalous Hall component [310–312]. Since the detection of AHE by E. H. Hall, both theoreticians and experimentalists have studied to find the true origin of AHE for more than a century due to the absence of concepts such as topological nature of electronic states and Berry curvature [192,313]. For this reason, the concept of AHE has been partially understood owing to the controversial mechanisms and insufficient knowledge. Nevertheless; several known mechanisms which cause AHE are the presence of FM phase, spin orbit coupling and disorder present in the system [202].

In order to better understand the origin of AHE, Karplus and Luttinger developed the first theoretical approach in which they considered the spin-orbit coupling of polarized electrons in conduction band and interband mixing which cause AHE [193]. The concept of Berry curvature that plays an important role in understanding the origin of AHE, was named by Luttinger as anomalous velocity that yielded quadratic relationship between anomalous and longitudinal resistivity, $\rho_{xy} \propto \rho_{xx}^2$ [193,314]. The KL theory was developed on the basis of intrinsic mechanism of AHE rather than extrinsic mechanism such as scattering from impurities. Following the Karplus and Luttinger theory, Smit suggested an extrinsic scattering mechanism accountable for AHE. This mechanism was considered on the basis of asymmetric or skew scattering (SS) mechanism of the spin-polarized electrons which is induced by SOI [195,315]. The Smit's proposed SS mechanism could be described by considering classical Boltzmann equation, refer to explanation by E. A. Stern [316]. Another extrinsic source of AHE was later proposed by L. Berger in 1970 which is called the SJ scattering mechanism of charge carriers from impurities in the samples [194]. In order to find the exact mechanism responsible for AHE, several scaling relations were presented in terms of ρ_{xx} e.g. $\rho_{xy}^{AH} \propto a\rho_{xx}+b\rho_{xx}^2$ [317] $\rho_{xy}^{AH} \propto b\rho_{xx}^2$ [196,318] $\rho_{xy}^{AH} \propto a\rho_{xx}$ [319] and $\rho_{xy}^{AH} \propto b\rho_{xx}^{\eta}$, here η yields either 1 or 2 for SS or SJ mechanism, respectively [320]. Since previous studies have suggested AHE to be proportional to the magnetization in the FM system, Nakatsuji *et al.*, claimed large AHE manifested by antiferromagnetic Mn_3Sn at room temperature [321]. This suggested that the AHE phenomenon is surprisingly wide-ranging than previously thought in ferromagnets only. Furthermore, large AHE was observed in half-metallic ferromagnet $Co_3Sn_2S_2$ that arises due to the presence of magnetic Weyl fermions [322], planar Hall effect was observed in $Co_3Sn_2S_2$ nanoflakes [323], and thickness dependent AHE was detected in topological semimetal Co_2MnGa thin films [324].

6.2 Temperature dependent resistivity and charge scattering

The temperature dependent longitudinal resistivity, $\rho_{xx}(T)$, results obtained for our $Ge_{1-x-y}Sn_xMn_yTe$ samples between $4.3 \leq T$ (K) ≤ 300 are shown in Fig. 6.1(a–c). All $Ge_{1-x-y}Sn_xMn_yTe$ samples show similar increasing trend in $\rho_{xx}(T)$ curves except two samples with $x \approx 0.2$, $y = 0.027$, 0.047. The sample with $x \approx 0.2$, $y = 0.047$ exhibit very weak temperature dependence up to $T \approx 125$ K above which the $\rho_{xx}(T)$ curve shows accelerated increase up to $T = 300$ K.

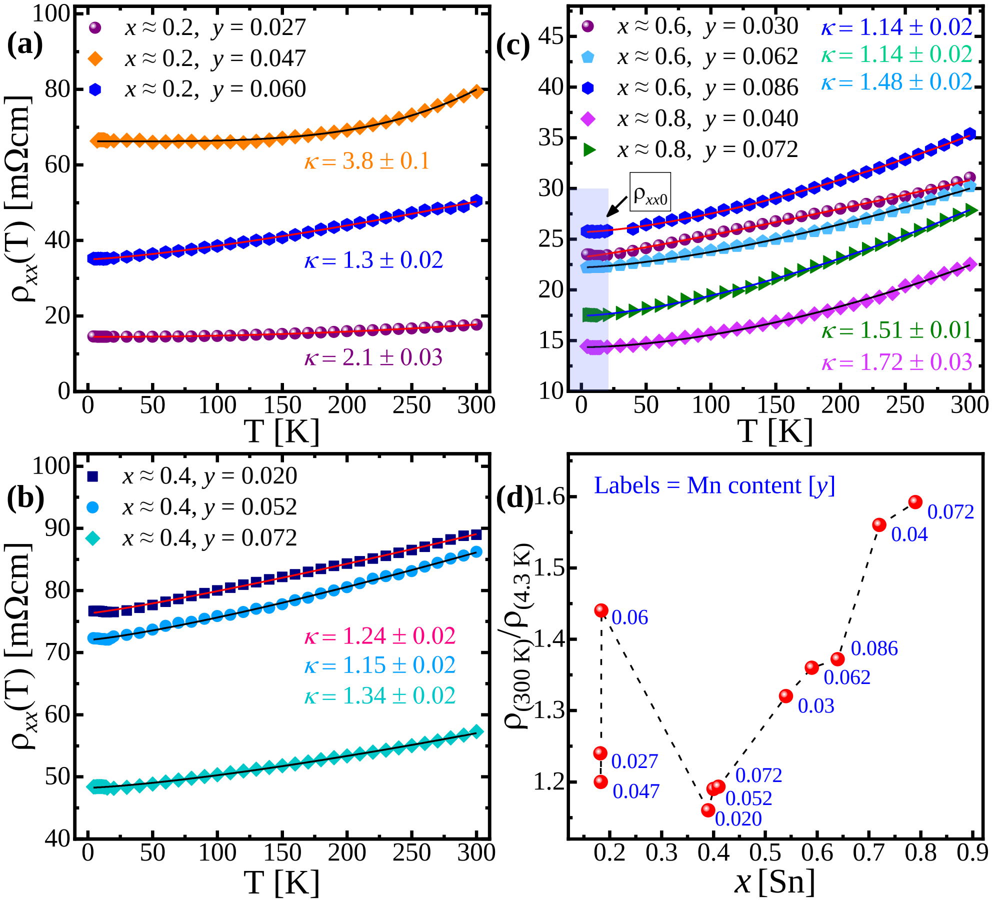

FIG. 6.1 Longitudinal resistivity, $\rho_{xx}(T)$ of $Ge_{1-x-y}Sn_xMn_yTe$ samples with (a) $x \approx 0.2$, $0.027 \leq y \leq 0.060$, (b) $x \approx 0.4$, $0.020 \leq y \leq 0.072$, and (c) $x \approx 0.6$, 0.8, $0.030 \leq y \leq 0.086$ from $T \approx 4.3$ K to $T = 300$ K. Solid lines denote fits to power law (eq. 6.1). (d) Residual resistivity ratio, $\rho_{xx(300\ K)}/\rho_{xx(4.3\ K)}$ vs. Sn content.

The resistivity results for all $Ge_{1-x-y}Sn_xMn_yTe$ samples show two regimes in $\rho_{xx}(T)$ curves; the temperature independent part below $T \approx 20$ K which is shown as shaded region in Fig. 6.1(c) and temperature dependent part that manifests nearly linear increase from $T \approx 20$ K up to $T = 300$ K. The temperature independent resistivity regime for the samples shown in Fig. 6.1(a–c) is discussed first. The flat parts in the $\rho_{xx}(T)$ curves of $Ge_{1-x-y}Sn_xMn_yTe$ samples are generally related to the charge scattering from impurities in the system. The dominant scattering centers of charge carriers are residual impurities in systems such as $Ge_{1-x-y}Sn_xMn_yTe$. The important aspect of impurities and other static defects such as grain boundaries and dislocations is that they disrupt the periodicity of the lattice which results in the temperature independent part called the residual resistivity, ρ_{xx0}. The magnitude of ρ_{xx0} should be proportional to the concentration of alloying element such as Sn and Mn in $G_{1-x-y}Sn_xMn_yTe$ samples. The $G_{1-x-y}Sn_xMn_yTe$ samples in Fig. 6.1(b) show an inverse trend where ρ_{xx0} decreases as the concentration of Mn increases which is opposite to the tendency in concentrated metallic alloys [325]. The results in Fig. 6.1(a,c) do not manifest a clear trend between ρ_{xx0} and Mn concentration. Such lack of relationship between ρ_{xx0} and concentration of alloying element was previously observed in several DMS systems [325–327]. The above lack of relationship between ρ_{xx0} and Mn concentration can be explained by taking into account two possible mechanisms. First, the increase in ρ_{xx0} with increasing Mn concentration arises due to enhanced scattering of charge carriers from alloying ions which is not true for the results in Fig. 6.1(a–c). The second mechanism explains that increase in Mn concentration introduces significant number of charge carriers (increase in conductivity) in the valence band which leads to reduction in ρ_{xx0}. The second mechanism might explain the decreasing ρ_{xx0} magnitude with increasing Mn content. For the results in Fig. 6.1(a–c), above two mechanisms in these samples cause the lack of proportionality between the residual resistivity and the Mn content. In the low temperature region, the residual resistivity, $\rho_{xx0}(4.3\text{ K})$, decreases from $\rho_{xx0}(4.3\text{ K}) \approx 77$ mΩcm for $x = 0.38$, $y = 0.02$ to $\rho_{xx0}(4.3\text{ K}) \approx 14$ mΩcm for $x = 0.8$, $y = 0.04$. These ρ_{xx0} values are large compared to other DMS systems [325,326] indicating substantial degree of disorder in $Ge_{1-x-y}Sn_xMn_yTe$ alloys. Considerable variation in ρ_{xx0} signifies that the low temperature resistivity originates due to scattering of charge carriers by the impurity sites in the alloys. Further, the residual resistivity ratio (RRR), $\rho_{xx}(300\text{ K})/\rho_{xx}(4.3\text{ K})$ rises in heavily alloyed samples from 1.11 to 1.59 for $x \approx 0.4$ to 0.8, respectively, as presented in Fig. 6.1(d). The large ρ_{xx0} values and extremely low RRR values are similar to previous studies of GeTe based alloys [328], however; quite large compared to other compounds e.g. Co_2MnSi, NiMnSb Heusler alloys [329], MgB_2 single crystals [330] and $Sr_2Cr_3As_2O_2$ layers [331]. The large $\rho_{xx0}(T)$ and low RRR of $Ge_{1-x-y}Sn_xMn_yTe$ samples are assumed to originate due to alloyed impurities [328].

In this part, the second regime in $\rho_{xx}(T)$ curves which shows temperature dependence is discussed. All $\rho_{xx}(T)$ curves except the one with $x \approx 0.2$, $y = 0.047$, show an increase between $T = 20$ – 300 K that represents a metallic-like behavior which likely occurs in degenerate semiconductors. At high temperatures, the charge carriers are scattered by phonons (quantized lattice vibrations) that leads to an increasing $\rho_{xx}(T)$ dependence, see the $\rho_{xx}(T)$ regime at $T \geq 20$ K in Figs. 6.1(a–c). Though there can be contributions from other mechanisms such as electro–electron scattering as well but their importance seems to be smaller than phonon scattering. In order to further analyze the exact mechanism causing this $\rho_{xx}(T)$ behavior, power law was used given by eq. 6.1 to analyze the experimental results

$$\rho_{xx}(T) = \rho_{xx0} + PT^{\kappa}. \tag{6.1}$$

As presented in Fig. 6.1(a–c), the experimental $\rho_{xx}(T)$ curves were fitted to eq. 6.1 in the entire temperature range which are shown as solid lines. For fitting procedure, ρ_{xx0}, P and κ were set as free parameters where P is coefficient of temperature and exponent κ denotes the slope of $\rho_{xx}(T)$ curves. Here ρ_{xx0} shows the residual resistivity which stems from impurities in $\mathrm{Ge}_{1-x-y}\mathrm{Sn}_x\mathrm{Mn}_y\mathrm{Te}$ samples while PT^{κ} comes from electron-electron collision or the phonon induced part that arises due to lattice vibrations (dynamic disorder). In addition to the impurity dominant regime discussed above, the electron-phonon scattering is one the most important mechanisms (among several others) in understanding the high temperature $\rho_{xx}(T)$ regime. The ρ_{xx0} values obtained during fitting are very close to the values evaluated from experimental results with less than 3% deviation. The values of κ obtained during fitting were equal to $\kappa = 2.1 \pm 0.03$, 3.8 ± 0.1 and 1.3 ± 0.02 for the crystals having $x \approx 0.2$, $y = 0.027$, 0.047, and 0.061, respectively. The obtained $\kappa = 2.1 \pm 0.03$ for the sample with $x \approx 0.2$, $y = 0.027$ shows nearly quadratic dependence, which represents Fermi liquid contribution (electron–electron scattering) in metals, semimetals and alloys [332–335]. The interpretation of $\rho_{xx}(T)$ curves with $\kappa = 2.1 \pm 0.03$ suggests that the scattering mechanism arising from electron–electron interaction is dominant as compared to other scattering sources for the sample with $x \approx 0.2$, $y = 0.027$ at $T \geq 20$ K. The electron–electron or electron–hole interaction was first predicted by Landau, Pomeranchuk and Baber for metals at low temperatures [332]. Later, Lawrence and Wilkins commented on the exponent related to electron–electron interaction who observed possible slight deviations from a $\sim T^2$ form [336]. As the Sn content is increased above $x \approx 0.2$, the values of κ remain in the range of $\kappa = 1.14 – 1.72$, see Fig. 6.1(b,c) for exact values of each sample. The $\rho_{xx}(T)$ behavior can be categorized in different sets depending on the determined values of κ. For the two crystals $x \approx 0.6$, 0.8, $y = 0.062$, 0.072, the exponent, κ yielded values very close to 1.5(0.02). The obtained $\kappa = 1.5$ values for these two samples are very similar to the results reported by Takagi *et al.* [337]. As obtained in several other calculations performed for nondegenerate cases, a $\kappa = 1.5$ term in the temperature dependent resistivity can arise from either interband electron-electron scattering [338,339] or intraband electron-phonon scattering [338,339]. Due to the above conflicting descriptions of the $\kappa = 1.5$ dependence, the true origin of such a temperature dependence of resistivity lack adequate interpretation for the $\rho_{xx}(T)$ curves of the crystals $x \approx 0.6$, 0.8, $y = 0.062$, 0.072. The lowest values of κ were determined for the three samples with $x \approx 0.4$, $y = 0.052$, and $x \approx 0.6$, $y = 0.03$, 0.062 which yielded $\kappa \approx 1.15 \pm 0.02$. The $\rho_{xx}(T)$ curves of these crystals display large deviation from $T^{1.5}$ and vary as $\rho_{xx}=f(T^{1.14\text{–}1.15})$. These values are to some extent close to pure phonon ($\kappa = 1$) scattering with a slightly higher κ value. It might be assumed that the $\rho_{xx}=f(T^{1.14\text{–}1.15})$ values indicate the presence of dominant electron–phonon scattering for the above three samples. The highest exponent was obtained for the sample with $x \approx 0.2$, $y = 0.047$ with $\kappa = 3.8 \pm 0.1$. The $\rho_{xx}(T)$ behavior of this sample excludes the contribution from either electron-phonon or electron-electron scattering mechanisms which can be described by either $\kappa = 1$ or $\kappa = 2$ dependencies, respectively. From literature it is known that the analysis of $\rho_{xx}(T)$ curves of V_3Si single crystal were scaled by Milewits *et al*. with $\kappa = 3$ which largely deviated in the both low and high temperature regimes [338]. Similarly, for Co_2MnSi Heusler alloys, $\kappa = 3.3$ was obtained for $\rho_{xx}(T)$ scaling at $T \leq 65$ K [340] whereas Jiang *et al*., also determined $\kappa = 3.3$ for polycrystalline $Sr_2Cr_3As_2O_2$ [341]. These results are closer to the $\kappa = 3.8$ dependency obtained for the crystal having $x \approx 0.2$, $y = 0.047$ presented in Fig. 6.1(a). The $\kappa > 3.3$ was suggested to come from either leading $s-d$ scattering or electron-magnon interaction [341–343]. In case of dominant $s-d$ scattering, the magnitude of scattering is proportional to the density of states of the materials.

6.3 Scaling of negative magnetoresistance

In this section, the isothermal magnetoresistance (MR) as a function of magnetic field, $\rho_{xx}(H)$, curves obtained at $-130 \leq H \leq 130$ kOe are presented, see Figs. 6.2 and 6.3. These curves were obtained after data were averaged for both the positive and negative current values equal to ± 100 mA during the measurement. The final normalized MR results were calculated with the relation, $\Delta\rho_{xx}/\rho_{xx}(0) = (\rho_{xx}(H) - \rho_{xx}(H{=}0))/\rho_{xx}(H{=}0)$. All $Ge_{1-x-y}Sn_xMn_yTe$ alloys manifest negative MR at temperatures below $T_C / T_g / T_{cg}$. Depending upon the alloying elements content, these MR isotherms show two distinct classes, samples for which the magnitude of MR value decreases as temperatures rises and those for which the MR magnitude increases with increasing temperature i.e. $x \approx 0.6$, $y = 0.062$, $x \approx 0.6$, $y = 0.086$, and $x \approx 0.8$, $y = 0.072$, see Fig. 6.3(b,c,e). The temperature dependence of MR is presented in Fig. 6.3(f,g) for all samples which depicts two different trends in the variation of MR vs T determined at $H = 130$ kOe. At the lowest measured temperature, $T \approx 1.6$ K, MR curves for all samples saturate at rather intermediate fields in the range $|H| \approx 40 - 80$ kOe except for the samples presented in Fig. 6.2(b,c,e,f).

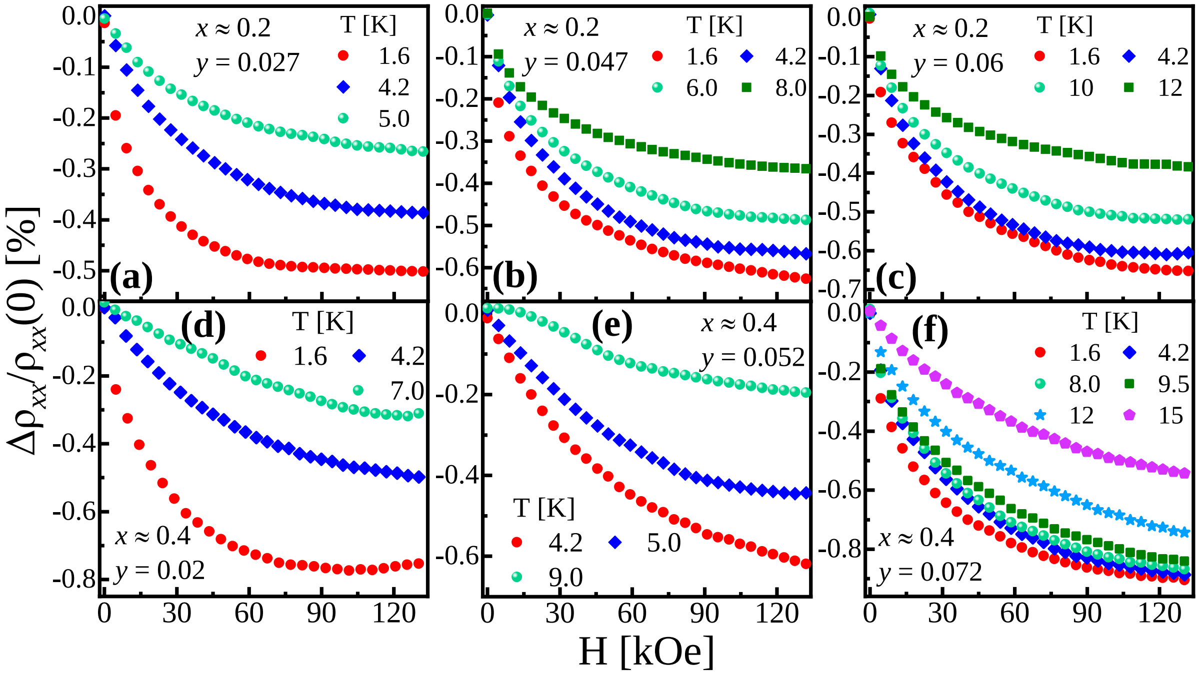

FIG. 6.2(a – f) $\Delta\rho_{xx}/\rho_{xx}(0)$ results below the magnetic transition temperatures for the crystals having $x \approx 0.2$, 0.4 and $0.02 \leq y \leq 0.072$. All samples exhibit decrease in the magnitude of MR as a function of temperature.

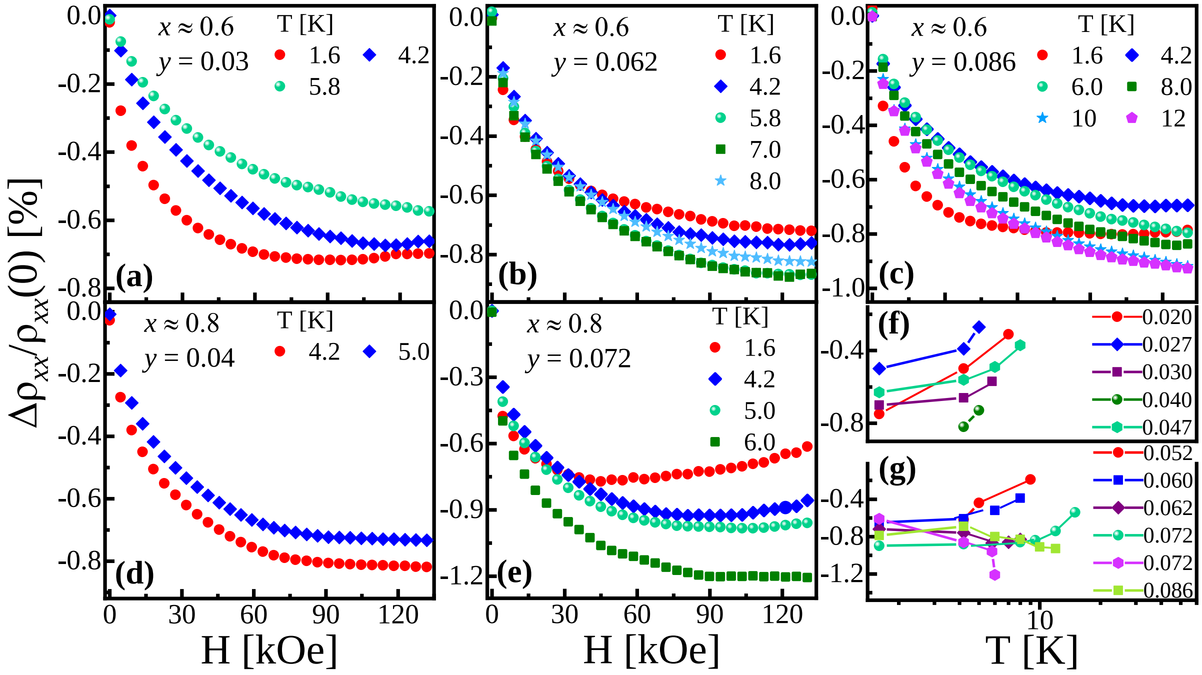

FIG. 6.3(a – e) $\Delta\rho_{xx}/\rho_{xx}(0)$ results below the magnetic transition temperature for the Sn-rich samples with $x \approx 0.6$, 0.8 and $0.03 \leq y \leq 0.086$. (g) Magnitude of MR values determined at $H = 130$ kOe for all samples is presented as a function of temperature.

Among all $Ge_{1-x-y}Sn_xMn_yTe$ samples, the crystal with $x \approx 0.8$, $y = 0.072$ shows even a positive upturn in the slope (see Fig. 6.3(e) for comparison) at $T \approx 1.6$ K. This could also be interpreted as a broad minimum in MR around 50 kOe. At magnetic field above 50 kOe, the MR magnitude for this sample starts to decrease and drops constantly up to 130 kOe. The maximum value of MR for each alloy is relatively small since the present $Ge_{1-x-y}Sn_xMn_yTe$ samples have low carrier mobility, (carrier mobility results will be presented later in Fig. 6.13) [344]. Besides the temperature dependencies, the magnitude of MR curves increases with Mn concentration in the low field regime e.g. $|H| \leq 60$ kOe. The MR results obtained at relatively low magnetic field values $H \leq 42$ kOe and $T \approx 4.2$ K for selected samples with different Mn content are shown in Fig 6.4(a,b). For the first three samples with $x \approx 0.2$ and $y = 0.027$, 0.047 and 0.060, the magnitude of *MR* increases with increasing Mn content. In the second set of samples presented in Fig 6.4(b), the magnitude of *MR* increases for three samples with $y = 0.020$, 0.072 and 0.072 which then drops for the highest Mn content of $y = 0.086$. This type of correlation between Mn content and *MR* suggests that the probability of spin scattering process decreases with increasing Mn content which is in good agreement with the previous results [345]. The drop in *MR* of the sample with $y = 0.086$ however; could not be justified without detailed investigation of the low field regime. One possible explanation might be the charge scattering due to localization effect for this particular sample which produces a drastic variation near zero-field regime. As shown in Fig 6.4(c), enlarged view of the MR curve for $y = 0.086$ (shown as shaded region) illustrates a cusp-like shape at $|H| \leq 2$ kOe which might indicate weak-localization effect at low temperatures.

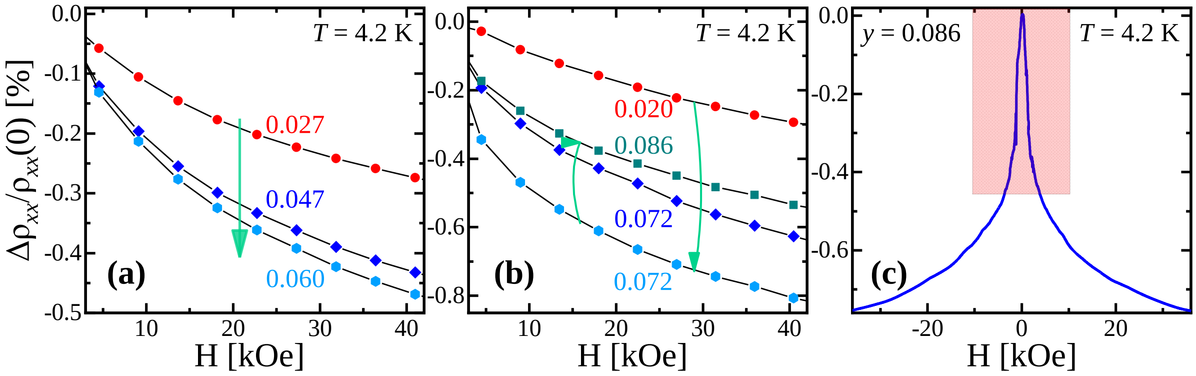

FIG. 6.4(a) $\Delta\rho_{xx}/\rho_{xx}(0)$ results at $T \approx 4.2$ K for the samples with $x \approx 0.2$, $y = 0.027$, 0.047, 0.060 (b) $x \approx 0.4$, $y = 0.020$, 0.072, $x \approx 0.6$, $y = 0.086$ and $x \approx 0.8$, $y = 0.072$ (c) low field MR curve for the sample with $x \approx 0.6$, $y = 0.086$ is shown at $T \approx 4.2$ K.

In addition, the above results also signify that negative magnetoresistance stems from the presence of the magnetic ions in $Ge_{1-x-y}Sn_xMn_yTe$ samples [345]. A generally argued source of negative MR is the low temperature weak localization effect though it appears prominent in the low field regime

[210]. For all $\rho_{xx}(H)$ isotherms obtained for $Ge_{1-x-y}Sn_xMn_yTe$ crystals, the *MR* variation is large around zero-field regime which might be due the weak localization effect, see Fig. 6.2 and Fig. 6.3. Also, the weak localization like behavior shown in Fig. 6.4(c) at low temperature is assumed to cause negative magnetoresistance in these alloys. The weak-localization effect is typically dominant around zero field and decays when the magnitude of magnetic field increases [220]. Additionally, negative MR can also be investigated with the third order *s-d* exchange Hamiltonian during spin scattering process in disordered states [346,347] in situations similar to Figs. 6.2 and 6.3. Furthermore, in the context of nature of scattering, the MR results are presented at $T \leq 15$ K which is within the residual resistivity limit of $T < 20$ K. This indicates that the role of phonons is smaller than ρ_{xx0} at temperatures at which MR results were obtained (detailed comparison of scattering from phonons and impurities will be presented in AHE section). Also the ρ_{xx0} contribution is presumed to be independent of the external magnetic field [348]. The scattering of conducting charge carriers is assumed to occur mostly due to random magnetic ions which cause negative MR in $Ge_{1-x-y}Sn_xMn_yTe$ samples.

The value and magnetic dependence of MR primarily depends upon the orientation of magnetic moments in the alloy. The present samples have a carrier mediated (RKKY) magnetic interactions as presented in previous chapter. These magnetometric results showed that $Ge_{1-x-y}Sn_xMn_yTe$ alloys manifest frustrated magnetic states coexistent with small ferromagnetic-like clusters [55]. In similar diluted magnetic alloys such as CuMn, Monod had discussed that over a wide range of temperatures and magnetic field values, the amplitude of negative MR varied as a quadratic function of magnetization [349]. However; deviations from the above quadratic behavior were also reported in case of concentrated alloys which were induced by the local magnetic field [349]. For Mn based canonical spin-glasses, Majumdar previously presented a general scaling between $\Delta\rho_{xx}/\rho_{xx}(0)$ and magnetization [350]

$$\Delta\rho_{xx}/\rho_{xx}(0) = -\beta M^2. \qquad (6.2)$$

The variation of negative *MR* with the square of the magnetization yielded a universal linear dependence for spin-glass systems. Here *M* denotes magnetization of the alloys and β is constant of proportionality. The variation of β with Mn ions was shown to be unique as it has revealed both concentration dependent and independent behavior for different alloys [351,352]. In Fig. 6.5, the above mentioned correlation between $\Delta\rho_{xx}/\rho_{xx}(0)$ and magnetization is attempted for the current samples at $T \approx 4.2$ K and magnetic field up to $|H| = 90$ kOe.

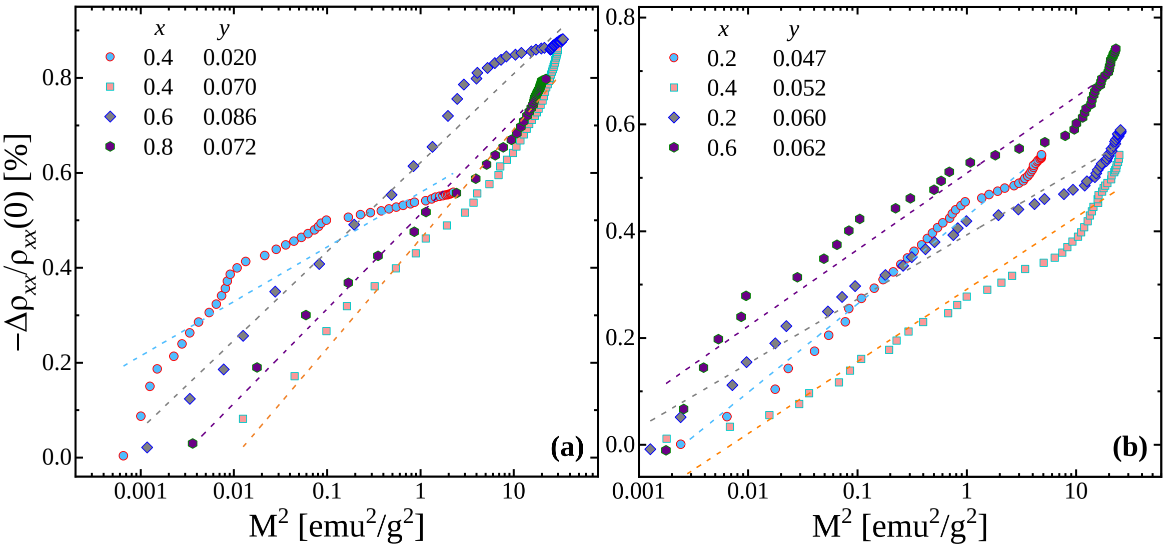

FIG. 6.5 *MR* results for selected samples plotted against the square of magnetization. The results do not demonstrate a straight line between *MR* and square of magnetization which can be expected for canonical spin-glass systems. Points represent experimental data whereas dashed lines denote linear fits.

In the low field regime, the $Ge_{1-x-y}Sn_xMn_yTe$ samples show nearly linear $\Delta\rho_{xx}/\rho_{xx}(0)$ vs M^2curves except for two crystals $x \approx 0.4$, 0.6 and $y = 0.02$, 0.062, see Fig. 6.5. Though the deviation from straight line is significantly large for all samples in the high magnetic field regime. In Ref. 350, the scaling between MR and M^2 showed a straight line having slope equal to 2 over a wide temperature range. In view of the above scaling relation, the $Ge_{1-x-y}Sn_xMn_yTe$ samples do not demonstrate such a universal scaling (straight line) between MR and M as presented in Fig. 6.5. All the samples show similar behavior except for the sample with $x \approx 0.2$, $y = 0.047$ which has a SG state as discussed in the previous chapter. Though this sample does not manifest a straight line between MR and M^2 similar to the results in Ref. 350, the different behavior shown in Fig. 6.5(b) might represent tendency towards similar scaling. The lack of relationship following eq. 6.2 might be indicative of a magnetic state different than conventional spin-glasses in which the magnetization M does not represent an order parameter. The sample with $x \approx 0.2$, $y = 0.047$ was categorized as a SG which also exhibited magnetic hysteresis further supports that the magnetic state is not a canonical SG. The absence of any obvious correlation between MR and M suggests a different interpretation for the current results. As this simplified scaling relation was formulated for canonical spin-glasses, therefore, such an interpretation holds inappropriate and deviates due to the presence of small ferromagnetic clusters in the $Ge_{1-x-y}Sn_xMn_yTe$ alloys.

Negative MR in magnetic alloys could also be interpreted in the context of reduction of the spin dependent scattering as a consequence of spin alignment in the presence of external magnetic field

[54]. Thus, a spin-disorder model by Gennes and Fisher et al., [353,354] is attempted to describe the negative MR in $Ge_{1-x-y}Sn_xMn_yTe$ alloys with the aid of the following equation

$$\rho_{sd} = 2\pi^2 \frac{k_F m^2 \Gamma^2 n_s}{n e^2 h^3} [S(S+1) - \langle S \rangle^2_{H,T}], \tag{6.3}$$

where ρ_{sd} represents the resistivity term in the spin disorder scattering, e is the electronic charge, k_F is wave vector associated with Fermi level, m is mass of electron, h is Planck's constant, n_S is density of electrons, S is the spin quantum number of paramagnetic Mn ions and Γ defines an effective factor extracted from the exchange integral associated with the charge carriers and magnetic ions. As discussed by Van Esch *et al*. the spin disorder scattering manifests a constant behavior in the paramagnetic region at $H = 0$, however; it gradually drops below T_C until the alignment of the magnetic moments [355]. In the paramagnetic regime, magnetic moments of Mn ions can be treated as a system with effective spin S =5/2 with g factor as a fitting parameter. Taking into account these assumptions, eq. 6.3 can be written in a modified form as given below

$$\rho_{sd} = 2\pi^2 \frac{k_F m^2 \Gamma^2 n_s}{n e^2 h^3} \times \left[\frac{1}{2} + \left\{\exp\left(\frac{-g_s \mu_B \mu_0 B}{2 k_B T}\right) + \exp\left(\frac{g_s \mu_B \mu_0 B}{2 k_B T}\right)\right\}^{-2}\right] + dB^2. \tag{6.4}$$

The fits to negative MR in Fig. 6.6 were obtained using eq. 6.4 in the spin-only ground state. In eq. 6.4, g_S is known as effective factor which is associated with the average value of the effective magnetic moment contributed by a Mn ion. The accurate interpretation of $\Delta\rho_{xx}/\rho_{xx}(0)$ isotherms require addition of quadratic term in eq. 6.4. This quadratic contribution stems from the orbital motion of charge carriers in the presence of the external magnetic field [356]. The quadratic term consistently contributed to the fitting process for all samples. Finally, the free parameter, g_S values were estimated during the fitting process. The results of the obtained fits along with the experimental results are shown for all samples in Fig. 6.6(a–k). The obtained values of g_S vs temperature are shown in Fig. 6.6(l). The smallest values of g_S were obtained for the crystals $x \approx 0.2$, 0.4, $y = 0.027$, 0.020 which yielded $g_S \approx 2 \pm 0.4$ whereas the sample with $x \approx 0.8$, $y = 0.072$ showed the highest value, $g_S \approx 8 \pm 0.4$. The obtained values of the effective factor, g_S, can be compared with effective magnetic moment calculated in the previous chapter for the same $Ge_{1-x-y}Sn_xMn_yTe$ alloys. For the crystals $x \approx 0.2$, $y = 0.027$, 0.047, $x \approx 0.4$, $y = 0.020$, $x \approx 0.6$, $y = 0.03$, 0.062 the deviation in the values of magnetic moment determined in chapter 3 and Fig. 6.6(a–k) is less than 5% though this deviation is large for the remaining samples. Additionally, the g_S values (see Fig. 6.6(l)) determined for all crystals manifest almost constant values at all measured temperatures.

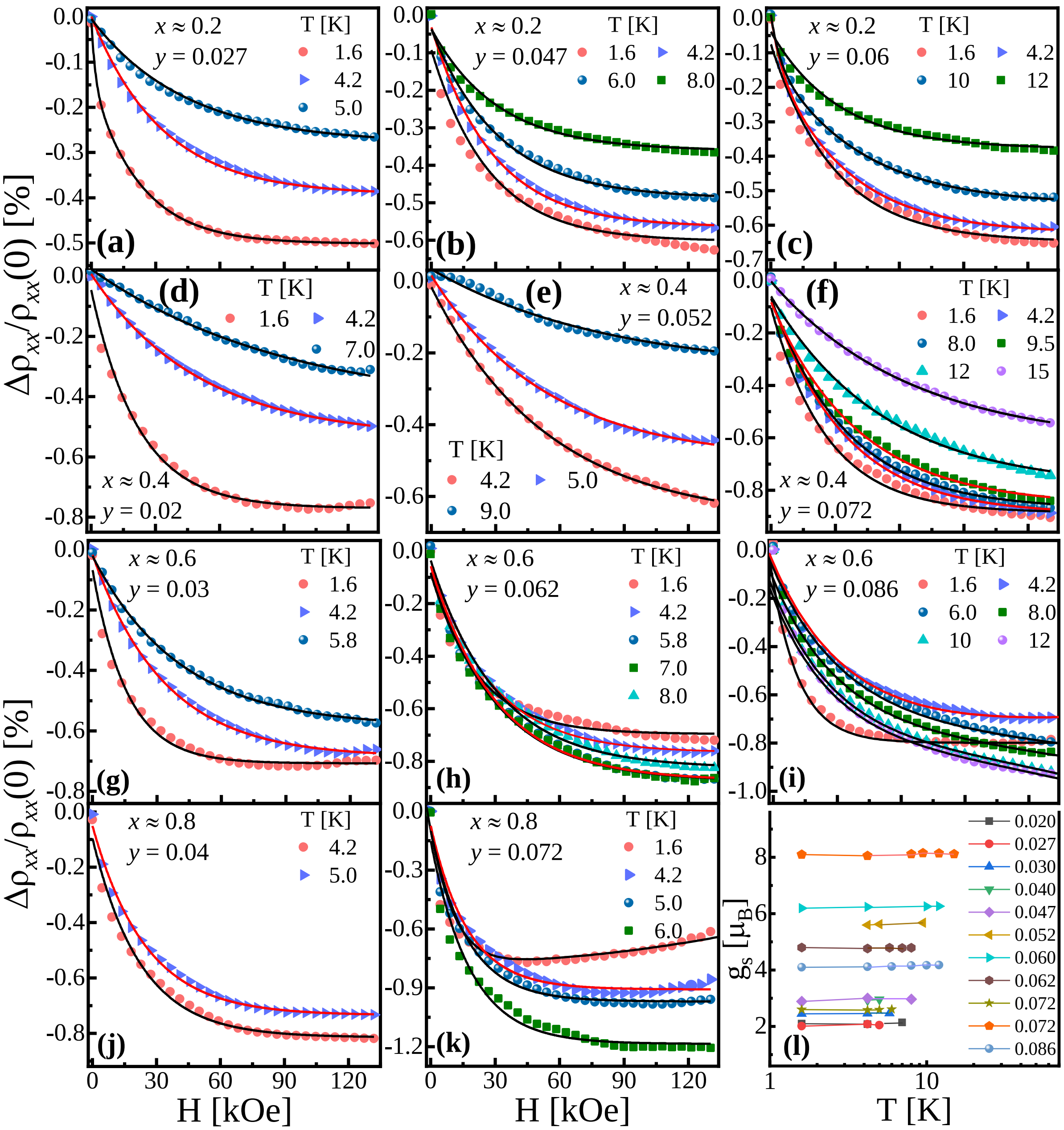

FIG. 6.6(a–k) Isotherms of the negative magnetoresistance, *MR* measured below the magnetic transition temperatures. The experimental data shown as scatter-points is fitted (solid lines) to the spin-disordered model given by eq. 6.4. (l) Temperature dependence of g_s values for all samples obtained from fitting of the *MR* curves.

The temperature dependence of the effective factor determined for $Ge_{1-x-y}Sn_xMn_yTe$ samples demonstrates similar trend as the temperature dependence of magnetic moment previously studied for different systems such as $CaFe_2As_2$ family of materials [357], magnetic moment distribution around impurities in iron [358], temperature dependence of local magnetic moments in paramagnetic metals [359], and temperature and thickness dependent results of magnetic moments in NiO epitaxial layers [360]. In case of $CaFe_2As_2$, the magnetic moments showed temperature dependence whereas the behavior became independent of temperature after sufficiently cooling the system. This temperature independent behavior was observed in the magnetically ordered phase of $CaFe_2As_2$ family of materials [357]. For paramagnetic metals, it was observed that the magnitude of magnetic moment decreases with increasing temperature [359]. The results obtained for the $Ge_{1-x-y}Sn_xMn_yTe$ alloys show similar temperature independent behavior below the magnetic transition temperatures.

6.4 Anomalous Hall effect

In this section, the Hall resistivity component, ρ_{xy}, of the magnetotransport results measured up to $|H|$ = 130 kOe is discussed. Several $\rho_{xy}(H)$ results are presented in Fig. 6.7 measured at selected stabilized temperatures for the samples with $0.2 \leq x \leq 0.8$ and $0.02 \leq y \leq 0.086$. All our samples demonstrate two positively sloped components; AHE at $|H| \leq 4$ kOe and OHE at $|H| \geq 4$ kOe. For the samples with low Mn contents $y \approx 0.02$, 0.027, 0.03, 0.04, a small AHE effect could only be seen at $T \approx 1.6$ K and $T = 4.2$ K whereas only OHE is observed at higher temperatures. In comparison, the alloys with comparatively higher Mn content manifest large AHE effect. Large magnitude of anomalous ρ_{xy} in the low field region is limited to $|H| \leq 4$ kOe which then develops into ordinary linear dependence up to $H = 130$ kOe. The two components of $\rho_{xy}(H)$ are generally interpreted by the equation 2.29 as the field dependent OHE and magnetization dependent AHE parts, respectively. As interpreted by Smith and Sears who explained the relation between magnetization and AHE [361], the AHE components in Fig. 6.7 show similar relation to the $M(H)$ curves for the same samples as presented earlier in Figs. 5.11 and 5.13.

In the inset of Fig. 6.8(a), a low field cut of the $\rho_{xy}(H)$ isotherm for the sample with $x \approx 0.4$, $y = 0.072$ at $T \approx 1.6$ K is presented. This shows $\rho_{xy}(H)$ with two components, AHE at $|H| \leq 4$ kOe and OHE at $|H| \geq 4$ kOe. The black solid lines indicate extrapolated lines to AHE and OHE parts of $\rho_{xy}(H)$ where y-intercept estimates spontaneous Hall coefficient, R_S, that is characteristic of magnetic materials. The solid red lines drawn through the extrapolated lines determine saturation magnetization, $4\pi M_S$, and total Hall resistivity, $4\pi(R_0+R_S)$ at x and y-intercepts, respectively [362]. The $\rho_{xy}(H)$ isotherms for the crystal having $x \approx 0.6$, $y = 0.086$ are shown in Fig. 6.8(b). Constant decrease in the magnitude of the ρ_{xy} curves is shown up to $T = 12$ K. As shown in the inset of Fig. 6.8(b), linear fits were applied to the high field OHE component which demonstrates determination of the magnitude of ρ_{AH} at different temperatures. The dashed lines represent the estimated values of ρ_{AH} at each temperature. The temperature dependence of ρ_{AH} values for all samples is shown in Fig. 6.7(l).

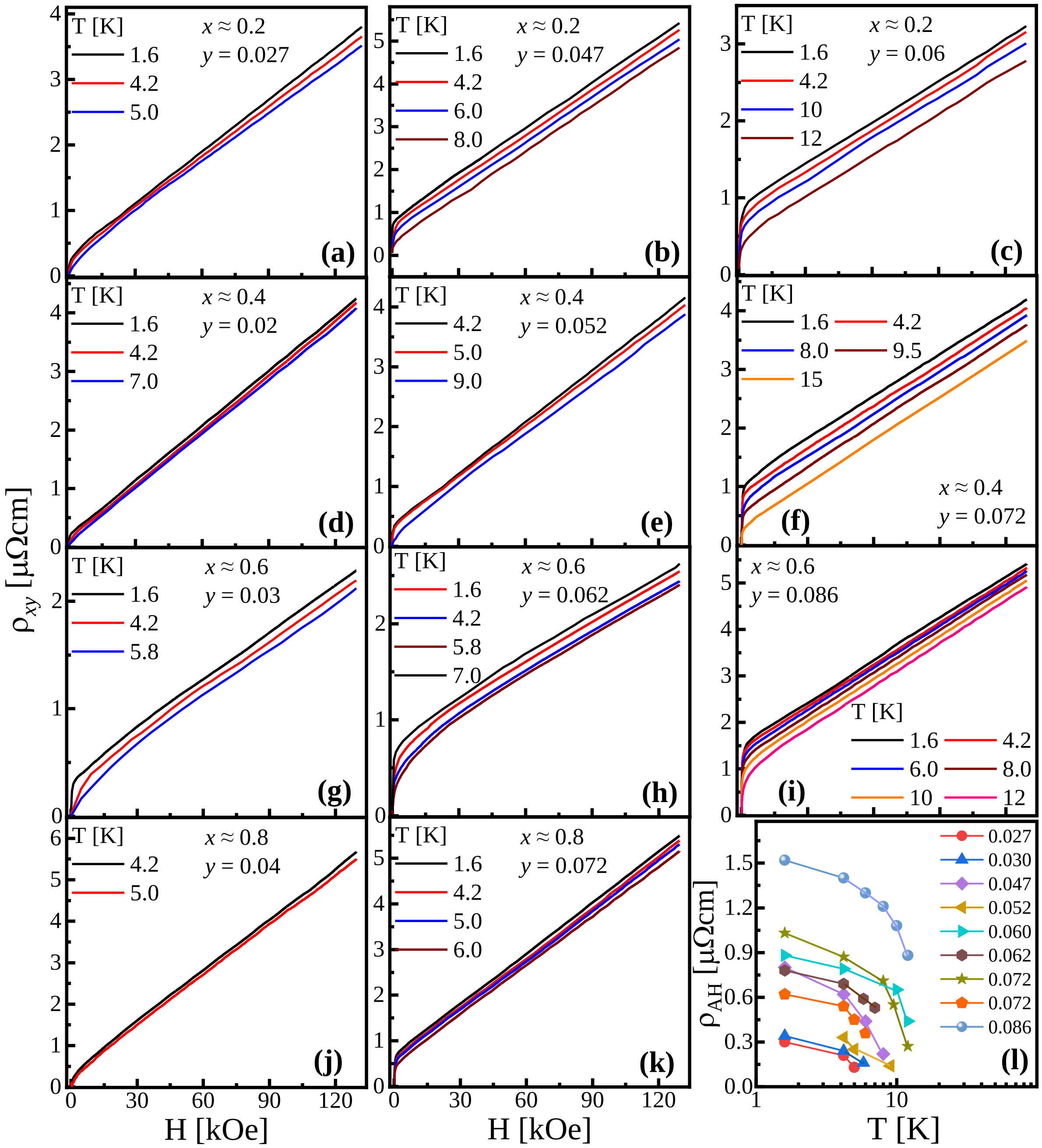

FIG. 6.7(a–k) Isotherms of the Hall resistivity, $\rho_{xy}(H)$ for the samples with $0.2 \le x \le 0.8$ and $0.02 \le y \le 0.086$. (l) Temperature dependence of anomalous Hall resistivity, ρ_{AH}.

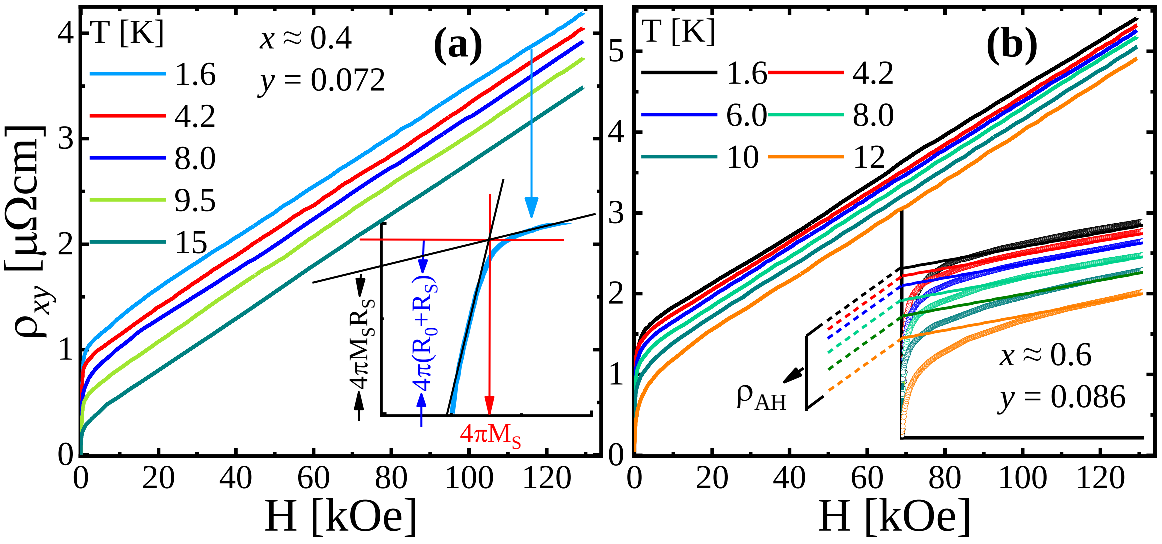

FIG. 6.8(a) Magnetic field dependence of Hall resistivity, $\rho_{xy}(H)$, results for $Ge_{1-x-y}Sn_xMn_yTe$ alloys for different concentrations Sn and Mn ions. Inset of (a) depicts the estimation of OHE, AHE components, inset of (b) demonstrates the determination of anomalous Hall resistivity, ρ_{AH} for different isotherms.

6.5 Parsing of the anomalous Hall resistivity

In order to identify the dominant scattering sources that cause AHE in $Ge_{1-x-y}Sn_xMn_yTe$ samples, it is fundamentally essential to correlate the transverse Hall resistivity to the longitudinal resistivity [192,196,363]. The values of anomalous Hall resistivity, ρ_{AH}, presented in Fig. 6.7(l) will be scaled against longitudinal resistivity, ρ_{xx} using several relations. A simplified approach starts with basic linear and quadratic correlations $\rho_{AH} \propto \rho_{xx}$ and $\rho_{AH} \propto \rho_{xx}^2$, respectively. These two relations are usually used to identify either SS or SJ mechanism after appropriate fitting of the experimental data. For the $Ge_{1-x-y}Sn_xMn_yTe$ alloys, the above two relations were used though convincing fits were not obtained. This probably means that the origin of AHE in the present alloys is rather complex that could not be deduced from a single scattering mechanism. For this reason, the scaling between ρ_{AH} vs ρ_{xx} was extended to scaling relations which takes into account contributions from both SS and SJ mechanisms. In the second attempt, the scaling analysis was performed using correlations which include contributions from both SS and SJ mechanisms. The first convincing results of ρ_{AH} vs ρ_{xx} for $Ge_{1-x-y}Sn_xMn_yTe$ alloys were obtained using $\rho_{AH} \propto b\rho_{xx}^{\eta}$. The scaling results of ρ_{AH} in terms of ρ_{xx} are presented in Fig. 6.9 to parse the major source of AHE in this material.

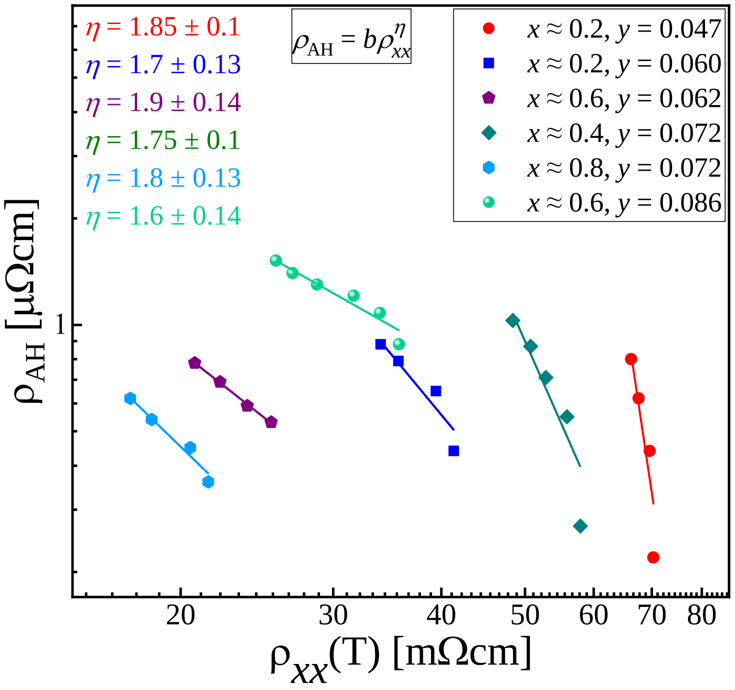

FIG. 6.9 Scaling of anomalous Hall resistivity, ρ_{AH} vs longitudinal resistivity, ρ_{xx} with the simplified relation provided at the top center of the figure. Fitting results of $\rho_{\text{AH}} = f(\rho_{xx})$ to the experimental data (scatters) are denoted by solid lines.

In Fig. 6.9, ρ_{AH} as a function of ρ_{xx} was fitted to a simplified relation, $b\rho_{xx}^{\eta}$ where the exponent $\eta = 1$ denotes SS and $\eta = 2$ means contribution from scattering dependent SJ and scattering independent intrinsic process induced by SOI [193,194]. This simple model could either separate contributions to AHE from SS, SJ or identifies superposition of scattering processes depending on the outcome of parameter η. The values of free parameter, η, obtained from scaling experimental results are presented in Fig. 6.9. Clearly, η yielded intermediate values in the range, $|\eta| = 1.6 – 1.9$ for the investigated $\text{Ge}_{1-x-y}\text{Sn}_x\text{Mn}_y\text{Te}$ alloys. Since η yields values from 1 – 2 for these results, it suggests an intermediate range where contributions are assumed to come from superposition of SS and SJ scattering processes [364]. These intermediate values might not sort out the true contribution proportion of each mechanism however; it could be interpreted that the SJ scattering is dominant here as deviation of η is large from the value accepted for SS scattering ($\eta = 1$). It is worth mentioning that these values do not always hold the narrow range of $\eta = 1 – 2$ and could exceed beyond 2 [364,365]. In the regime $\eta > 2$, the non-validity of this scattering relation was argued to come from larger mean free path compared to layers' thickness [365]. In another example, $\eta = 3.9$ was obtained for granular alloys resulting due to scattering rate at the interface [366] or due to residual resistivity, ρ_{xx0}, in γ′-Fe_4N films where the SJ and intrinsic mechanisms are governing [367]. These cases with $\eta > 2$ suggest that the exponent η does not hold universal values but fluctuates with geometry of the system e.g. thickness or granule's size. Besides the distinction of scattering mechanism on the basis of η, in general, asymmetric SS shows dominance at low temperature whereas SJ takes over in the high temperature range [348]. The AHE behavior exhibited by the current samples exists in the low temperature regime which on the basis of the above initial scaling does not originate from a unique and clearly dominant scattering mechanism. This outcome will be further justified using different scaling laws in the following section.

In the above section, the scaling with simplified relation indicates that SJ mechanism is dominant with contribution from SS source as well. However; the parsing of AHE requires more in-depth analysis so that to support the results obtained in Fig. 6.9. For this reason, the scaling process is further extended to relations which combine the SS and SJ terms. In this section, two additive relations were used which allow to determine the magnitude of coefficients of both SS and SJ mechanisms, and identify the dominant contribution to AHE. In that context, a two component additive relation of SS and SJ terms, $\rho_{\mathrm{AH}} = a_{sk}\rho_{xx} + b_{sj}\rho_{xx}^{2}$ is used to further evaluate whether the outcome in previous section holds correct, see Fig. 6.10(a). The SS parameter is denoted by a_{sk}, whereas b_{sj} contains contributions from both SJ and intrinsic mechanism. The obtained fits of the experimental results using the second scaling relation are shown in Fig. 6.10(a) by taking into account both scattering mechanisms. However; this equation does not uniquely separate the SS and SJ components, e.g. Kondorskii *et al*. and Crepieux *et al*. have shown that the SS component also contributes to the quadratic part [368,369].

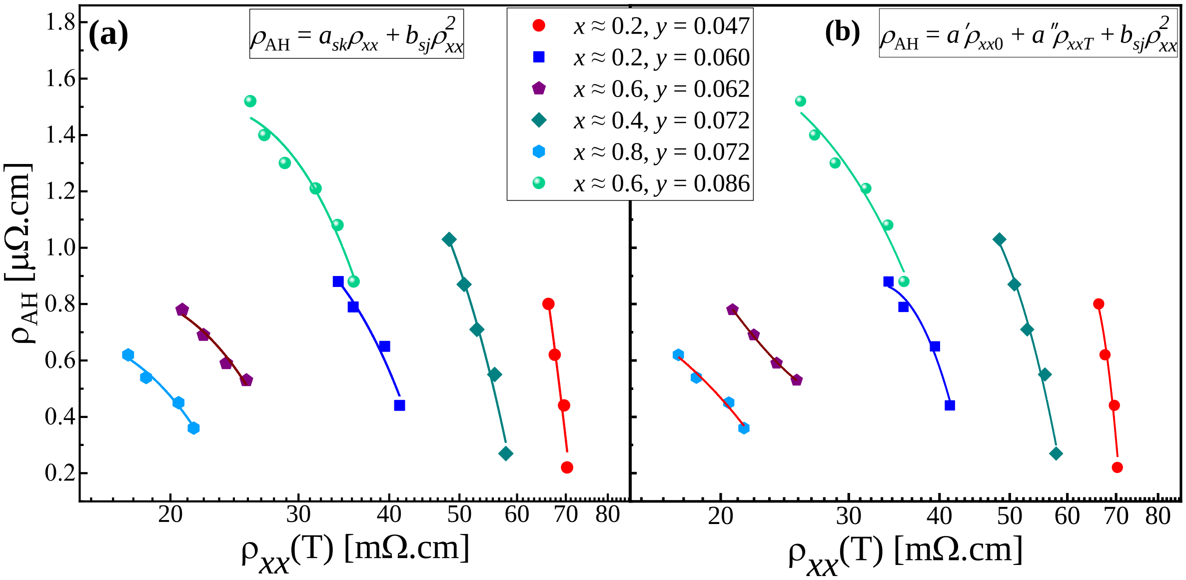

FIG. 6.10 Scaling of anomalous Hall resistivity, ρ_{AH}, vs longitudinal resistivity, ρ_{xx} with the (a) additive two-term relation and (b) modified scaling law. The fits are shown as solid lines while scatters represent experimental data.

The above generalized equation was recently modified by Tian *et al.*, who proposed the SS term as a sum of the residual resistivity, $a'\rho_{xx0}$, which is defect dependent and caused by impurities and the temperature dependent part, $a''\rho_{xx\mathrm{T}}$ (here $\rho_{xx\mathrm{T}} = \rho_{xx} - \rho_{xx0}$), that is proportional to temperature dependent part related to scattering induced by lattice vibrations [196,363]. The splitting of the total resistivity into residual and phonon induced parts originally comes from the Matthiessen's rule, $\rho_{xx} = \sum_i(\rho_i)$ in which ρ_i represents the resistivity component by the ith kind of scattering type [370,371]. The fits which are shown as solid lines in Fig. 6.10(b) were obtained with the modified scaling law, $\rho_{\mathrm{AH}} = a'\rho_{xx0} + a''\rho_{xx\mathrm{T}} + b_{sj}\rho_{xx}^2$, which treats the SS part as two independent scattering sources. Besides the outcome of different scattering parameters, the fitting results of the modified scaling law are compared to those obtained with the previous generalized model in Fig. 6.10(a). In several cases, the modified model clearly yields superior fits compared to both the previous models presented in Figs. 6.9 and 6.10(a). Free parameters values a', and a'', were estimated to make a distinction between the defect dependent and the phonon induced components of ρ_{xx} whereas the magnitude of b_{sj} is indicative of the role of SJ or intrinsic mechanism [194]. Moreover, the separation of intrinsic and SJ mechanisms is challenging as both of them correlate in a quadratic way to ρ_{xx}. The role of phonon scattering is generally very small in the case of SS mechanism. The modified scaling law also allows separating the roles of residual and temperature dependent resistivity, ρ_{xx0} and $\rho_{xx\mathrm{T}}$, respectively. However; the key outcome is expected to allow the comparison of the parameter b_{sj} with the earlier scaling results shown in Fig. 6.9 and hence validate whether the contribution of SJ scattering is still dominant.

The obtained results of coefficients a', a'', and b_{sj} are presented for all samples in Fig. 6.11. First important outcome of the scaling reveals that the coefficient of phonon related part, $a''\rho_{xx\mathrm{T}}$, is smaller than that of $a'\rho_{xx0}$ component. This agrees with the general notion that the phonon induced contribution is indeed smaller than the residual part of SS mechanism [196]. However; the non-negligible values of a'' compared to a' means the overall role of SS part comes from mixed sources of both phonon-induced and residual resistivity. In cases where phonon scattering role is trivial, the $\rho_{xx\mathrm{T}} \simeq 0$ approximation could be made in the zero temperature limits in which the total resistivity becomes $\rho_{xx} \simeq \rho_{xx0}$ [370]. The second central result is the comparison of SS and SJ contributions to ρ_{AH} obtained from the modified scaling model in Fig. 6.10(b). Here the SJ parameter, b_{sj} yields an order of magnitude larger values compared to the SS parameter, a', that satisfies the earlier discussion of dominant SJ contribution. On the other hand, the SS parameter reveals smaller but non-zero values which could be interpreted as the SJ source being dominant however; the role of SS cannot be ruled out. Based on the fitting results for $\mathrm{Ge}_{1-x-y}\mathrm{Sn}_x\mathrm{Mn}_y\mathrm{Te}$ samples, the interpretation of ρ_{AH} with the new scaling law and the one in Fig. 6.9 both find that SJ source is dominant with only minor contribution to the AHE coming from SS mechanism. In case of the SJ scattering, as described by L. Berger [194], the wavefunction of the charge carrier suffers a lateral displacement, Δl with respect to the scattering center. The scattering centers in samples such as $Ge_{1-x-y}Sn_xMn_yTe$ act as central potential sites.

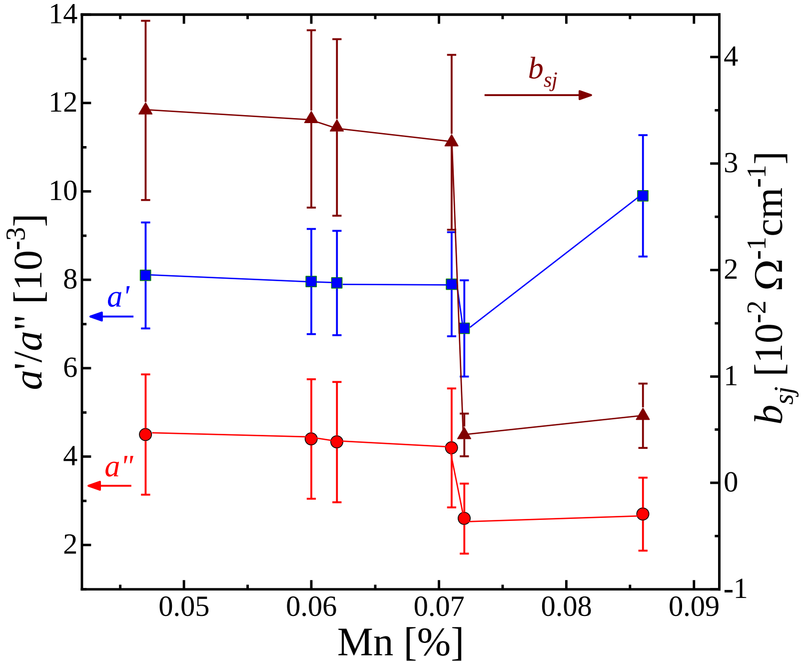

FIG. 6.11 Scaling results of a', a'', and b_{sj} obtained from the additive scaling relations: $\rho_{\mathrm{AH}} = a_{sk}\rho_{xx} + b_{sj}\rho_{xx}^2$, and $\rho_{\mathrm{AH}} = a'\rho_{xx0} + a''\rho_{xx\mathrm{T}} + b_{sj}\rho_{xx}^2$.

TABLE IV: Fitting parameters a', a'', b and η extracted after scaling the results with the relations $\rho_{xy}^{\mathrm{AH}} \propto b\rho_{xx}^{\eta}$, $\rho_{\mathrm{AH}} = a_{sk}\rho_{xx} + b_{sj}\rho_{xx}^2$, and $\rho_{\mathrm{AH}} = a'\rho_{xx0} + a''\rho_{xx\mathrm{T}} + b_{sj}\rho_{xx}^2$.

Mn	$a'(10^{-3})\pm\Delta a'(10^{-3})$	$a''(10^{-3})\pm\Delta a''(10^{-3})$	$b(10^{-2})\pm\Delta b(10^{-2})$	$\eta\pm\Delta\eta$
0.047	8.1±1.18	4.5±1.40	3.5±1.10	1.85±0.10
0.060	8±1.16	4.4±1.37	3.4±1.10	1.70±0.13
0.062	7.9±1.15	4.3±1.34	3.3±1.07	1.90±0.14
0.072	7.9±1.16	4.2±1.32	3.2±1.05	1.75±0.10
0.072	6.9±1.09	2.6±0.79	0.45±0.20	1.80±0.13
0.086	9.9±1.40	2.7±0.82	0.63±0.31	1.60±0.14

The ordinary and anomalous Hall coefficient, R_0 and R_S results obtained from the above data analysis are presented in this section. In the paramagnetic state, R_H coefficient can be generally considered to be equal to the normal Hall constant R_0 since the anomalous part vanishes. In Fig. 6.12, the temperature dependence of anomalous and ordinary Hall coefficient, R_S and R_H are shown which were obtained using the relation $\rho_{xy} = R_0H + \mu_0R_\mathrm{s}M$. Here, R_H arises from the Lorentz force while on the contrary R_S stems from magnetization in the crystals. Such a large Hall current arises due to left-right asymmetric scattering induced by spin-orbit coupling between the charge carriers and the lattice [372]. Apparently, AHE contribution is dominant over OHE since $R_S(T)$ is two orders of magnitude larger than $R_H(T)$ at $T \leq 15$ K.

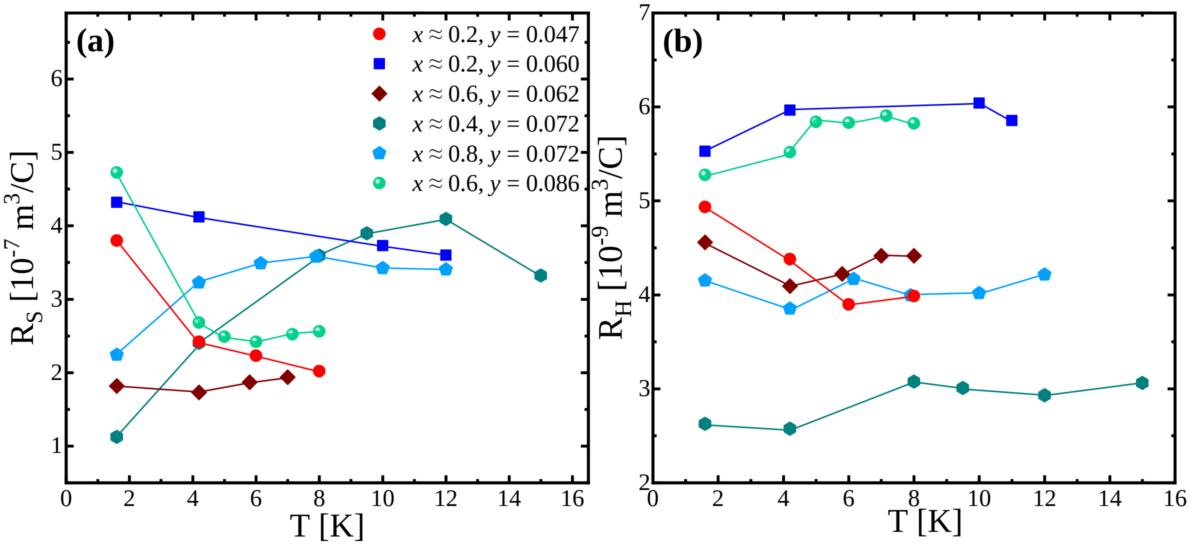

FIG. 6.12(a) Temperature dependent anomalous Hall coefficient, R_S and (b) ordinary Hall coefficient, R_H, at temperatures lower than $T \approx 16$ K.

The magnitude of $R_S(T)$ and $R_H(T)$ determined for our samples is consistent with previous work on $Ge_{1-x-y}Sn_xMn_yTe$ and $Ge_{1-x-y}Mn_xEu_yTe$ bulk alloys [356,373]. An interesting outcome here is nearly temperature independent behavior of R_S and R_H below the magnetic transition temperatures in each $Ge_{1-x-y}Sn_xMn_yTe$ sample. This profile is similar to results of other IV-VI narrow gap SC e.g. Mn and rare earth ions incorporated into SnTe alloys [374]. However, the temperature dependence and transition to negative R_S values were earlier recorded for $Sn_{1-x-y}Eu_xMn_yTe$ alloy [375]. In addition to IV-VI SC, a weakly T-dependent nature of R_S and R_H was also obtained in $Ga_{1-y}Mn_yAs$, selected samples of Fe and Mn based silicides and the ferromagnetic van der Waals semimetal Fe_3GeTe_2 [376,377]. It is also seen that the variation of R_S and R_H with concentration of Sn and Mn ions is not demonstrating any obvious dependence. This might happen due to the fact that different content of diamagnetic Sn probably influences the magnetic interactions among Mn ions. Such an explanation could be justified based on the tuning of magnetic interaction by Sn observed for the same alloys

[363]. However, the true mechanism behind the complex R_S and R_H dependence might arise from other parameters and could not be attributed to alloying compositions only.

The scaling and parsing of AHE in the previous section concluded that both SS and SJ mechanisms contribute to AHE whereas the latter being the dominant source. Since the quadratic term also represents intrinsic mechanism, such resistivity scaling cannot tell whether the dominant contribution comes from intrinsic or extrinsic mechanism. This section is continuation of the AHE analysis in order to separate the mechanisms responsible for AHE in $Ge_{1-x-y}Sn_xMn_yTe$ alloys. In order to separate the intrinsic from the extrinsic AHE source, the scaling relation between longitudinal and anomalous Hall conductivity tensor components, σ_{xx}, and σ_{AH}, is discussed. Both quantities were estimated using the equations $\sigma_{xx} = \rho_{xx}/(\rho_{xx}^2+\rho_{\mathrm{AH}}^2)$ and $\sigma_{\mathrm{AH}} = \rho_{\mathrm{AH}}/(\rho_{xx}^2+\rho_{\mathrm{AH}}^2)$ which might be reduced to $\sigma_{xx} = \rho_{xx}/\rho_{xx}^2$ and $\sigma_{\mathrm{AH}} = \rho_{\mathrm{AH}}/\rho_{xx}^2$ when $\rho_{xx} \gg \rho_{\mathrm{AH}}$ [378]. For the conductivity scaling, a comprehensive theory was recently proposed by Onoda *et al.*, that assesses both intrinsic and extrinsic AHE in multiband doped ferromagnets [379]. Here the conductivity scaling is generally categorized into three broad regions, (a) superclean metal regime $\sigma_{xx} > 10^6\ \Omega^{-1}\mathrm{cm}^{-1}$ where linear dependence in the form $\sigma_{\mathrm{AH}} \sim \sigma_{xx}$ is observed which represents dominant SS source (b) moderately dirty regime $\sigma_{xx} > 10^4 - 10^6\ \Omega^{-1}\mathrm{cm}^{-1}$ which is independent of scattering and dominated by intrinsic mechanism and (c) dirty metal regime $\sigma_{xx} < 10^4\ \Omega^{-1}\mathrm{cm}^{-1}$ in which the scaling relation follows $\sigma_{\mathrm{AH}} \sim \sigma_{xx}^{1.6}$. The scaling relation between $\rho_{\mathrm{AH}} \sim \rho_{xx}$ and $\rho_{\mathrm{AH}} \sim \rho_{xx}^2$ is assumed to yield nearly similar outcome as $\sigma_{\mathrm{AH}} \sim \sigma_{xx}$ and $\sigma_{\mathrm{AH}} \sim \sigma_{xx}^2$ [380]. The obtained results of the $\sigma_{\mathrm{AH}} = f(\sigma_{xx})$ scaling are presented in Fig. 6.13 at the same temperatures as presented above. It is obvious that the σ_{xx} results are within the bad metal hopping regime ($\sigma_{xx} < 10^4\ \Omega^{-1}\mathrm{cm}^{-1}$) which allows the interpretation of the form $\sigma_{\mathrm{AH}} = \sigma_{xx}^{\varepsilon}$ with $\varepsilon = 1.6$ [196,381].

The scaling presented in Fig. 6.13 to $\sigma_{\mathrm{AH}} \sim \sigma_{xx}^{\varepsilon}$ where ε denoted the universal scaling exponent shows good fits shown by solid lines over the entire range of $\sigma_{\mathrm{AH}} = f(\sigma_{xx})$ results. Though deviation can be seen from universal line $\varepsilon \sim 1.6$ which is shown as dashed lines. The estimated values, $\varepsilon = 1.72$, 1.76 and 1.8 are within the previously established limit of universal scaling, $\varepsilon = 1.33 - 1.8$ for majority of experimental results [196,382] whereas $\varepsilon \approx 1.5$ is close to the lower boundary. This non-trivial exponent, $\varepsilon \approx 1.6$, has been experimentally achieved in the poorly conducting regime for many systems such as itinerant ferromagnets [378], nanogranular films [383], ferromagnetic van der Waals semimetal [377], ε-Fe_3N nanocrystalline films [384] and several other systems [378]. The fact that $\sigma_{\mathrm{AH}} \sim \sigma_{xx}^{\varepsilon}$ scaling did not follow a constant line or $\sigma_{\mathrm{AH}} \sim$ constant further supports the low conductivity hopping regime in $Ge_{1-x-y}Sn_xMn_yTe$ alloys that is consistent with theoretically predicted value of $\varepsilon = 1.6$.

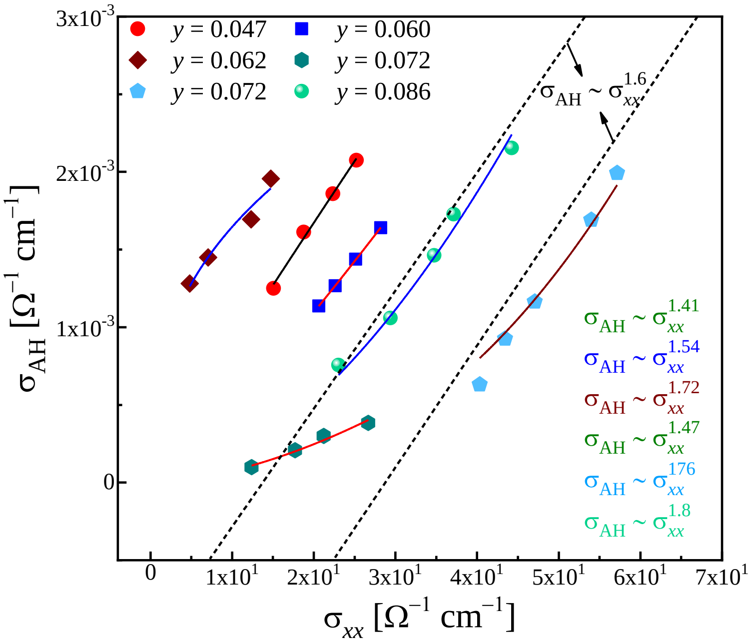

FIG. 6.13 Scaling between magnitude of anomalous Hall conductivity, σ_{AH} and longitudinal conductivity, σ_{xx}. The scaling relation, $\sigma_{\mathrm{AH}} \sim \sigma_{xx}^{\varepsilon}$ yielded fits shown as solid-blue lines whereas dashed-black lines denote reference fits for two alloys with $\varepsilon = 1.6$.

Previously, the parsing of AHE sources in these regimes has been discussed mainly in terms of intrinsic and extrinsic mechanisms. As the crossover occurs from linear to constant regime of σ_{xy}, the SS source decays whereas intrinsic and SJ mechanisms act as major AHE sources [379,385]. Typically, the intrinsic deflection mechanism is induced in systems when the multiband SOI system is linked to momentum space Berry phase [382]. But the SJ contribution is much smaller than the intrinsic source in the plateau region which could be ignored as argued theoretically by Miyasato *el al*., [385]. Since σ_{AH} = constant and $\varepsilon = 1$ regimes cannot be seen in Fig 6.13, it is safe to disregard the dominant role of both Berry curvature and asymmetric SS sources in the present $\mathrm{Ge}_{1-x-y}\mathrm{Sn}_x\mathrm{Mn}_y\mathrm{Te}$ alloys. Here in the bad metal hopping regime, the intrinsic part initiates a damped decay due to impurities which follows universal $\sim\sigma_{xx}^{1.6}$ dependence [378]. Furthermore, σ_{AH} is significantly suppressed in the bad metal regime compared to σ_{xx} due to damping or resonating condition [377]. This universal scaling dependence in hopping regime is remarkable as it yields same correlation irrespective of temperature, pressure and impurity content though depends on magnitude of σ_{xx} and impurity potential [379]. It appears that the scattering from lattice vibrations and impurities do not substantially influence the charge-carrier dynamics and therefore the relation $\sigma_{\mathrm{AH}} \sim \sigma_{xx}^{\varepsilon}$ yields universal scaling [380]. Thus, the control of $\sim\sigma_{xx}^{1.6}$ scaling reveals that spin-polarized charge carriers play vital role in inducing ferromagnetism that lead to AHE in these alloys. Also, in terms of nature of hopping, this scaling maintains its universality within $\varepsilon = 1.33 - 1.76$ limits whether the system is in Mott variable-range hopping, interactions-dependent or nearest-neighbor hopping [382].

6.6 Two scattering regimes in carrier mobility

In this section, the hole-carrier mobility, $\mu_h(T)$ and carrier concentration, $n_h(T)$ as a function of temperature are presented. The $\mu_h(T)$ and $n_h(T)$ results were obtained using the following relations. For the determination of $n_h(T)$, the relation $n_h = 1/R_H e$ was used. The Hall coefficient, R_H includes contributions from both ordinary and anomalous Hall constants, R_0 and R_S, respectively. The carrier mobility results were calculated by using the relation $\mu = \sigma_{xx} R_H$. Furthermore, the carrier mobility results in the low temperature regime were corrected to the results obtained from high field electron transport measurements. Based on the above relations and corrections to high field results, the $\mu_h(T)$ and $n_h(T)$ curves are presented in Fig. 6.14 which are being discussed in detail in the following paragraphs.

Drastic increase in $\mu_h(T)$ curves shows significant temperature dependence below $T \approx 50$ K while exhibit rather small variation between $T \approx 50 - 300$ K. The samples with alloying contents; $y = 0.030, 0.040, 0.062, 0.072$ and 0.086 show increase in $\mu_h(T)$ results from $T \approx 4.3$ K up to $T_{\max} \approx 6$ K, 7 K, 9 K and 13 K, respectively, at which maxima were recorded. Above the maxima, all the mentioned samples manifest decline in $\mu_h(T)$ up to $T \approx 300$ K. The temperatures at which maxima occur for these crystals are marked as $T_{\max}$, see Fig. 6.14(a,b). On the contrary, the remaining samples with $y = 0.020, 0.027, 0.047, 0.052, 0.06$ and 0.072 do not show any peaks. The maxima in $\mu_h(T)$ curves separate two different charge scattering regimes. At temperatures below $T_{\max}$, scattering from ionized impurities have dominant contribution whereas scattering from lattice vibrations dominate at $T > T_{\max}$ [386,387]. For the phonon induced part in the range $T > T_{\max}$, detailed analysis is presented below. The analysis of possible scattering sources responsible for the mobility behavior is presented in Fig. 6.14(a) by fitting the experimental data to $T^{-\gamma}$. Since μ_h in such materials is suppressed by phonon scattering, the results could be fitted to $\mu_h \sim T^{-\gamma}$ where the exponent γ is phonon related parameter and also it strongly depends upon the alloying content, see the dependency of obtained exponent with variation in alloying content presented in Fig. 6.14(a,b). The values of the parameter, γ, for all samples in Fig. 6.14(a,b) were determined which remain in the range $\gamma \approx 0.19 - 0.47$. Here, $\gamma < 1$ for $Ge_{1-x-y}Sn_xMn_yTe$ alloys is significantly smaller compared to $\gamma = 2.1 - 2.6$ obtained for different materials such as GaSe, $MoSe_2$ and MoS_2 and $\gamma = 1.2 - 1.7$ for $MoSe_2$ layers [388]. As discussed in detail by Fivaz *et. al.*, several scattering sources could be responsible depending on the outcome of γ. The $\gamma = 1$ regime was assigned to the dominant role by acoustic phonon modes whereas the variable values of γ were ascribed to interaction with either homopolar or polar optical phonon modes.

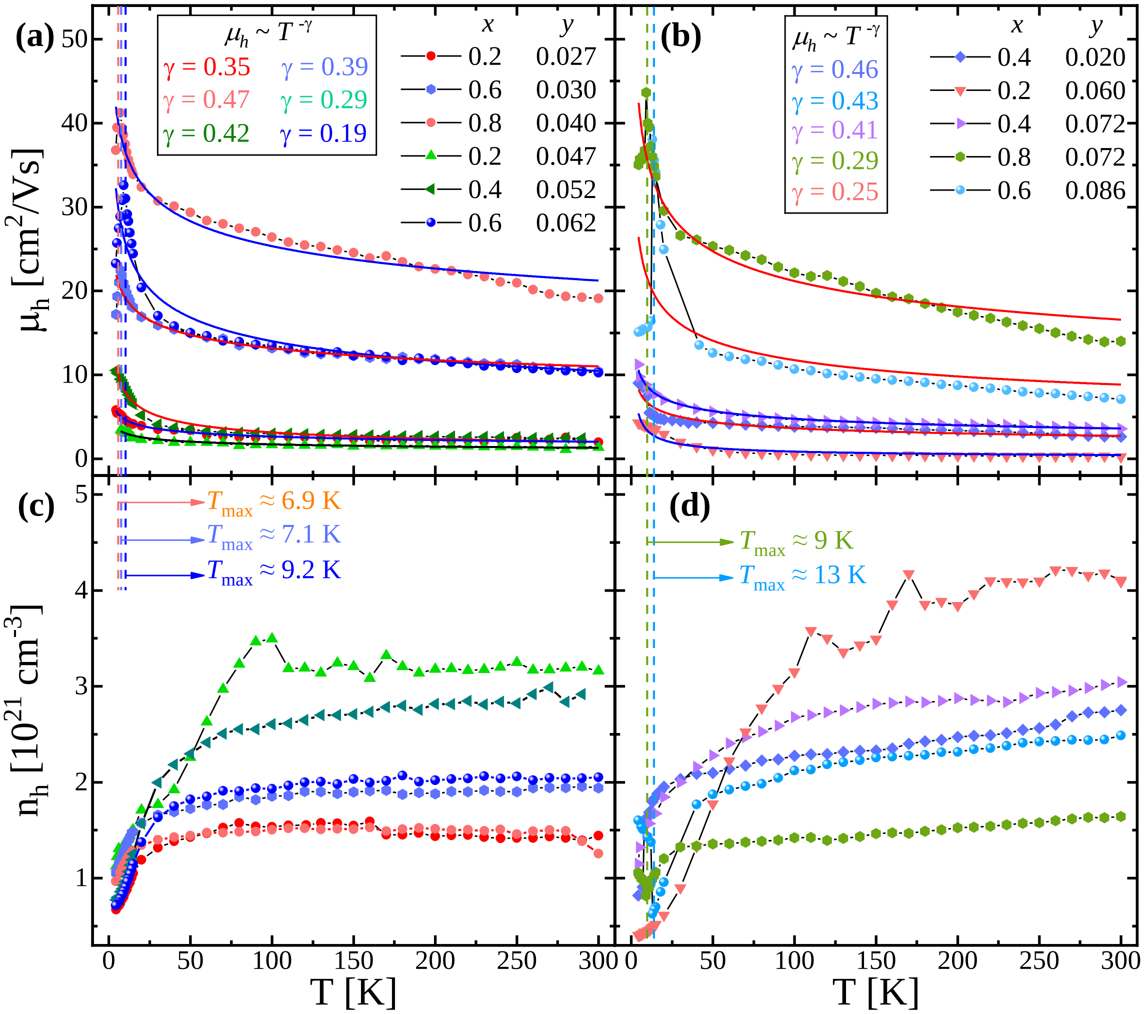

FIG. 6.14(a,b) Mobility, $\mu_h(T)$ results between $T \approx 4.3$ K – 300 K where solid lines denote fits to $\mu_h \sim T^{-\gamma}$. (c,d) Charge carrier concentration, $n_h(T)$ for the same samples.

In situation in which the center of mass of an atom and its mirror point remain unaffected and creates no first-order dipoles, such modes were categorized as homopolar whereas the opposite scenario produces polar phonon modes. The mobility calculations by Fivaz *et. al*., showed that γ shifted to lower than 1 regime for semiconductors like GaAs and InSb in the case of scattering of mobility carriers off the polar phonon optical modes of the lattice [389]. In low dimensional systems like $MoSe_2$, the decline in γ was attributed to the confinement of charge carriers in the layered structure [388]. However; the confinement of charge carriers could not be justified in the present bulk alloys which indicate that the small γ values presumably originate from interactions with polar phonon optical modes. In the low temperature regime where mobility drops faster from $T \approx 15$ K to 35 K, the outcome of γ still remains lower than 1 which means that the acoustic phonon scattering could be safely disregarded in the present results. According to previous explanations of carrier mobility in SCs materials, the $T^{-1.5}$ dependence is believed to indicate acoustic phonons as the dominant scattering center [390] which indicates that for the acoustic phonon scattering, γ can take values between 1 [389] and 1.5 [390]. While analyzing the current results, a very similar temperature dependence of $T^{-0.19}$ to $T^{-0.5}$ was reported by Irvine *et al.*, for lead halide perovskites [390] which is similar to the small exponent values obtained for our samples. Although the exact origin is ambiguous, this unusual $T^{-0.5}$ dependence was proposed to arise due to the possible formation of large polarons [391,392]. As a final note, the significant drop in $\mu_h(T)$ and its negative temperature dependence indicates that the dominant phonon scattering takes over at higher temperatures [393]. Consequently, in view of previous similar interpretations, it is assumed that the scattering from lattice vibrations arising from higher level of optically excited phonons or the presence of polarons could be the possible scattering sources [390–392]. The $\mu_h(T)$ results also show a large difference at $T \approx 4.3$ K for alloys of same material but different alloying contents. This is assumed to arise from substantial differences in the degree of impurities in the system [344].

Finally, variable temperature carrier concentration, $n_h(T)$ results are presented in Fig. 6.14(c,d). All samples present high concentration of charge carriers of the order of $n_h \approx 1.5–4\times10^{21}$ cm^{-3} at room temperature. The $n_h(T)$ results indicated that all studied samples were p-type semiconductors in which the carrier density strongly depends on the chemical composition of the alloy. The p-type carrier density in $Ge_{1-x-y}Sn_xMn_yTe$ is the consequence of significant concentration of defects in the crystals in the form of vacancies on the cation sites [394]. The temperature dependence of $n_h(T)$ curves is reasonably strong below $T \approx 50$ K which then switches to a weakly dependent regime up to $T \approx 100$ K except for two samples with $y = 0.047$, 0.06. These two samples with $y = 0.047$, 0.06 (which were concluded as spin glass and cluster glass in the previous chapter) manifest continuous increase in $n_h(T)$ curves up to about $T \approx 100 – 120$ K. The overall fluctuation in $n_h(T)$ results between $T \approx 4.3 – 300$ K does not illustrate particular trend as a function of Mn concentrations in the alloys. In the strong temperature dependent regime $T \leq 50$ K, the ratio $n_h(50\text{ K})/n_h(4.3\text{ K})$ remains between 2 and 3 which indicates the fluctuation is similar for all samples with slight differences. The weak temperature dependence of $n_h(T)$ at $T \geq 100$ K demonstrates typical degenerate semiconductors behavior [220]. At $T \approx 9$ K and 13 K, minima (shown as T_{min}) were recorded which are closely related to the T_{max} values in mobility curves, Fig. 6.14(b). For the crystals having $y = 0.027$, 0.030, 0.040, 0.047 and 0.062, the $n_h(T)$ curves show negligible fluctuation between $T \approx 50 – 300$ K. For the remaining crystals, the $n_h(50\text{ K})/n_h(4.3\text{ K})$ values range from 1.1 to 1.5 at $T \approx 50 – 300$ K which signifies metallic like conductivity behavior.

CHAPTER 7

SUMMARY

7.1 Structural and magnetometric part

In chapters 4 and 5, extensive investigations were performed related to elemental composition, crystal symmetry and magnetic order in $Ge_{1-x-y}Sn_xMn_yTe$ alloys. The following conclusions were made based on the detailed studies in this thesis.

- The EDXRF measurements determined the alloying concentrations of Sn and Mn ions into GeTe semiconductor. Sn and Mn contents were obtained in the range $0.2 \leq x \leq 0.8$ and $0.02 \leq y \leq 0.086$, respectively. The $Ge_{1-x-y}Sn_xMn_yTe$ alloys with correct stoichiometry suggesting that the incorporation of high alloying contents was successfully executed in order to obtain broad range of Sn and Mn alloyed GeTe compositions.
- Room temperature x–ray diffraction studies showed variation in the crystal symmetry of $Ge_{1-x-y}Sn_xMn_yTe$ as a function of alloying concentrations. Two important transitions related to crystal symmetry were observed; in the compositions with aggregate alloying content $x + y \leq 0.45$, low symmetry rhombohedral phase was obtained which is inherited from the parent compound, GeTe. The rhombohedral phase exhibited distortion along [111] direction whereas the corner angle $\alpha \approx 88.8°$. This broken inversion symmetry is related to the ferroelectric polarization along [111] direction similar to the widely studied host material, GeTe.
- At the alloying content $x + y \geq 0.45$, the crystal structure of $Ge_{1-x-y}Sn_xMn_yTe$ showed transition to high symmetry cubic phase. The cubic phase arises as substantial amount of Ge is replaced with Sn which results in crystal symmetry similar to that of SnTe at room temperature. Second phase transition occurred at the highest alloying concentration $x = 0.79$, $y = 0.072$ which illustrated cubic symmetry with two different lattice constants i.e. $a = 6.254 \pm 0.002$ Å and $a = 6.19 \pm 0.002$ Å. The disappearance of the rhombohedral symmetry signifies that the ferroelectric features move below room temperature in the Sn-rich GeTe crystals.
- In-depth investigations were made to understand the magnetic ordering in $Ge_{1-x-y}Sn_xMn_yTe$ alloys. In the low alloying content range, $0.2 \leq x \leq 0.4$ and $0.02 \leq y \leq 0.04$, the AC susceptibility, $\chi_{AC}(T)$ results did not manifest transition to an ordered state down to $T \approx 4.5$

K. As the Mn concentration was increased to $0.047 \leq y \leq 0.072$, cusp-like AC susceptibility, $\chi_{\mathrm{AC}}(T)$ results were obtained. The AC susceptibility of the selected samples with $x \approx 0.2$, $y = 0.047$, 0.06 and $x = 0.4$, $y = 0.052$ was further studied as a function frequency ($7 \leq f \leq 10$ kHz) as a means to identify the type of magnetic order. For the crystals $x \approx 0.2$, $y = 0.047$, 0.06, the frequency dependent shift in freezing temperature yielded scaling parameter values, $R = 0.017$ and 0.033 which indicated the presence of a spin glass and cluster glass state, respectively. Particularly for the sample with $x \approx 0.2$, $y = 0.06$, first maxima at $T \approx 10.5$ K remained independent of frequency which was attributed to ferromagnetic type of clusters.

- Furthermore, spin relaxation time and energy barrier values were also determined for the two samples using phenomenological scaling laws. The obtained values of spin relaxation time; $\tau \approx 10^{-9}$ s and $\approx 10^{-13}$ s for the samples with $y = 0.047$ and 0.06, respectively, are typical of spin glass and cluster glass states. The energy barrier values determined for the sample with $x \approx 0.2$, $y = 0.06$ were obtained with values up to $E_a/k_B \approx 385$ K which is about $20 \times T_{\mathrm{F}} \approx 21$ K. These large values were accredited to the Mn clustering effect in this sample.
- For the samples with highest alloying concentrations $0.6 \leq x \leq 0.8$ and $0.062 \leq y \leq 0.086$, the appearance of AC susceptibility, $\chi_{\mathrm{AC}}(T)$ curves changed from cusps to plateau-like shape. The saturated $\chi_{\mathrm{AC}}(T)$ curves indicated the presence of ferromagnetic order in these alloys. Ferromagnetic order in these samples was also supported by the square-like magnetization hysteresis.
- All $\mathrm{Ge}_{1-x-y}\mathrm{Sn}_x\mathrm{Mn}_y\mathrm{Te}$ crystals with $0.2 \leq x \leq 0.8$ and $0.02 \leq y \leq 0.086$ were properly analyzed with the modified Curie-Weiss law in the high temperature paramagnetic regime. Consequently, the obtained values of Curie-Weiss constant, C, were used in order to determine the effective magnetic moment, μ_{eff} for all $\mathrm{Ge}_{1-x-y}\mathrm{Sn}_x\mathrm{Mn}_y\mathrm{Te}$ samples.
- Based on the magnetization hysteresis, $M(H)$, curves, the remnant magnetization, M_R, and coercivity, H_C, values were determined. For the crystals having $x \approx 0.2$ and $y = 0.047$, both M_R and H_C values demonstrated maxima at $T \approx 6$ K which is close to its freezing temperature, $T_{\mathrm{F}} \approx 5.3$ K. Such maxima in $M_R(T)$ and $H_C(T)$ dependencies indicate the presence of spin glass state which is consistent with the $\chi_{\mathrm{AC}}(T)$ and $M(H)$ results. The $H_C(T)$ dependence for the samples with $y = 0.052$, 0.062, 0.072, 0.077 exhibited exponential decrease. Further analysis of these samples yielded ω equal to 0.2 – 0.9 K^{-1}. The obtained values of ω indicate the presence of random anisotropy in these samples.

- Further investigations were made by studying zero-field-cooled and field-cooled magnetization branches at $10 \leq H \leq 200$ Oe. For two samples with $x \approx 0.2$, $y = 0.047$, 0.06, the presence of frustrated magnetic state was confirmed by obtaining large bifurcation in the ZFC and FC magnetization curves. Furthermore, the exact type of magnetic ordering was further validated by using De-Almeida Thouless law. The crossover exponent values $\Phi \approx 1.5 - 1.8$ for the samples with $x \approx 0.2$, $y = 0.047$, 0.06 and $x \approx 0.4$, $y = 0.052$ also validated spin glass and cluster glass system in the above crystals.
- Bifurcation in ZFC and FC $M(T)$ results for crystals with $0.6 \leq x \leq 0.8$ and $0.072 \leq y \leq 0.086$ disappeared with respect to samples with $0.2 \leq x \leq 0.4$. These ZFC and FC results with negligible irreversibility further support the ferromagnetic order as mentioned above based on the AC susceptibility, $\chi_{\mathrm{AC}}(T)$, and magnetization hysteresis, $M(H)$ curves. Within the intermediate alloying range with $0.05 \leq y \leq 0.07$, the Mn ions accumulated in the form of small size FM like clusters.
- Finally, the J_{pd} calculations were made by using modified SS model in order to understand the interdependence of the magnetic transition temperatures, T_C / T_g to the carrier mediated RKKY interactions in the $\mathrm{Ge}_{1-x-y}\mathrm{Sn}_x\mathrm{Mn}_y\mathrm{Te}$ compositions. The obtained results of J_{pd} exchange constant which range from 0.16 to 0.24 eV indicated a decrease for the higher Sn concentration, which agree well with the earlier results.
- Based on the above magnetometric results, magnetic phase diagram was constructed for bulk $\mathrm{Ge}_{1-x-y}\mathrm{Sn}_x\mathrm{Mn}_y\mathrm{Te}$ samples with Sn and Mn concentrations $0.2 \leq x \leq 0.8$ and $0.02 \leq y \leq 0.086$, respectively. The samples with $y \leq 0.04$ did not show transition to an ordered state and demonstrated paramagnetic behavior. For the crystals having $x \approx 0.2$, $y = 0.047$, the AC susceptibility and DC magnetization results confirmed the presence of spin glass state. In the intermediate range with $0.052 \leq y \leq 0.072$, the samples indicated cluster glass state with ferromagnetic like Mn-clusters. Finally, the samples with highest Mn content $0.072 \leq y \leq 0.086$ manifested ferromagnetic order which showed plateau shape susceptibility curves and negligible irreversibility in the ZFC and FC curves.

7.2 Magnetotransport part

The investigations of electron transport phenomena in $Ge_{1-x-y}Sn_xMn_yTe$ multiferroics were made in the temperature range from $T \approx 1.6$ K to $T = 300$ K and magnetic field up $H = 130$ kOe. Important conclusions were made related the physical mechanism responsible for the observed electron transport phenomena as presented below.

- The behavior of the temperature dependent resistivity, $\rho_{xx}(T)$ of $Ge_{1-x-y}Sn_xMn_yTe$ crystals showed two broad regimes; the temperature independent part at $T \leq 20$ K (except for the spin glass sample with $y = 0.047$) and temperature dependent part between $20 \leq T \leq 300$ K. The temperature independent part of ρ_{xx0} takes major contribution from impurities in the system. Though the lack of relationship between the magnitude of $\rho_{xx0(4.3\ K)}$ and alloying concentration was attributed to two mechanisms. First, the increase trend of ρ_{xx0} with increasing Mn content occurred as a result enhanced scattering process of charge carriers from the ions of alloying elements. The second mechanism caused decrease in ρ_{xx0} values as the concentration of Sn and Mn is increased. The effect is responsible for increase in charge density in the valence band. Both these mechanisms are assumed to contribute to the behavior of ρ_{xx0} at $T \leq 20$ K.
- Furthermore, the values of residual resistivity ratio, RRR determined as $\rho_{xx(300\ K)}/\rho_{xx(4.3\ K)}$ remained in the range 1.11 – 1.59 for the crystals having $x \approx 0.4 - 0.8$. The large ρ_{xx0} and small RRR values illustrate the influence of alloying content on the charge scattering in the $Ge_{1-x-y}Sn_xMn_yTe$ samples.
- The temperature dependent resistivity, $\rho_{xx}(T)$ part of $Ge_{1-x-y}Sn_xMn_yTe$ crystals between $20 \leq T \leq 300$ K was studied using power law approach. These studies allowed to finds the exact scattering mechanisms which cause the metallic like resistivity behavior in $Ge_{1-x-y}Sn_xMn_yTe$ crystals. The exponent value $\kappa = 2.1 \pm 0.03$ obtained for the crystals $x \approx 0.2$, $y = 0.027$ is very close to $\sim T^2$ dependence which stems from electron–electron scattering mechanism in this sample. Two crystals with $y = 0.062$, 0.072 yielded values close to $\kappa = 1.5(0.02)$ which might be due to intraband electron-phonon scattering. Due to the above conflicting descriptions of the $\kappa = 1.5$, the true origin of such a temperature dependence of resistivity lack adequate interpretation for the $\rho_{xx}(T)$ curves of the samples with $x \approx 0.6$, 0.8, $y = 0.062$, 0.072.
- The smallest values of $\kappa = 1.15 \pm 0.02$ $\kappa = 1.14 \pm 0.02$ obtained for the samples with $y = 0.03$, 0.052, and 0.062 indicated the presence of pure phononic scattering. These results suggest that electron-electron and electron-phonon scatterings are two dominant mechanisms which contribute to the metallic like behavior of $\rho_{xx}(T)$ curves in $Ge_{1-x-y}Sn_xMn_yTe$ crystals.

- Finally, rather different behavior was shown by the sample with $y = 0.047$ spin glass state with $\kappa = 3.8 \pm 0.1$. The comparatively high value of $\kappa = 3.8$ suggest that the resistivity of the sample with $x \approx 0.2$, $y = 0.047$ takes contribution from either dominant $s-d$ scattering or electron-magnon interaction. The magnitude of $s-d$ scattering depends on the density of states of the materials.
- The transverse magnetoresistance results obtained at magnetic field up to 130 kOe demonstrated negative values for all compositions below the magnetic transition temperatures. Depending upon the concentration of alloying elements, the MR magnitude increases with increasing temperature for the samples with $x \approx 0.6$, 0.8 and $y = 0.062$, 0.086, 0.072. Except these three samples, the MR curves for the remaining alloys demonstrate opposite trend. Moreover, the sample with $x \approx 0.8$, $y = 0.072$ shows a positive upturn in the MR curve at $T \approx 1.6$ K which seems to be a broad minimum around 50 kOe. The magnitude of *MR* curves increases as a function of Mn content except the sample with $y = 0.086$. The decrease in *MR* for the sample with $y = 0.086$ occurs due to the localization effect which causes a drastic variation at low-fields.
- In order to find out the presence of spin glass state by analyzing *MR* curves, the square of magnetization curves were scaled to *MR* isotherms. The obtained results did not yield a straight line between the two quantities which excluded the presence of canonical spin glass state. Although, the sample with $y = 0.047$ presented different dependency as compared to other samples. This might be due to the spin glass state of this sample (as investigated in detail in chapter 5) though clear behavior of canonical spin glass systems cannot be confirmed.
- Further, *MR* curves for all samples were fitted to spin disorder model which reproduced the experimental results. The analysis of negative magnetoresistance with the spin disorder model determined the values of effective factor which is related to the magnetic moment of $Ge_{1-x-y}Sn_xMn_yTe$ alloys. For the samples with $x \approx 0.2$, 0.4, $y = 0.027$, 0.020, small values equal to $g_S \approx 2 \pm 0.4$ were obtained whereas $g_S \approx 8 \pm 0.4$ was obtained for the sample with $x \approx 0.8$, $y = 0.072$.
- The obtained values of the effective factor, g_S can be compared to the values of effective magnetic moment, μ_{eff}, calculated as a result of the Curie-Weiss law analysis. This comparison shows that the g_S and μ_{eff} values deviate by less than 5% for the samples with $x \approx 0.2$, $y = 0.027$, 0.047, $x \approx 0.4$, $y = 0.020$, $x \approx 0.6$, $y = 0.03$, 0.062. Though the remaining g_S and μ_{eff} values demonstrate large deviation for the remaining samples. Furthermore, the g_S

values exhibit temperature independent behavior for all samples below the magnetic transition temperatures.

- From the Hall resistivity curves, anomalous Hall effect, AHE, was observed in all $Ge_{1-x-y}Sn_xMn_yTe$ crystals whereas the samples with $y \leq 0.04$ showed small AHE magnitude only at $T \leq 4.2$ K. The AHE results for the samples with $y \leq 0.04$ are consistent with the paramagnetic behavior from magnetometric results since AC susceptibility and DC magnetization curves were obtained down to $T \approx 4.5$ K only. For the remaining samples with $y \geq 0.04$, Hall resistivity curves demonstrated AHE up to the magnetic transition temperatures. In all $Ge_{1-x-y}Sn_xMn_yTe$ samples, AHE is present at magnetic field $|H| \leq 4$ kOe.
- The identification of dominant scattering mechanism that causes AHE in $Ge_{1-x-y}Sn_xMn_yTe$ samples was performed. Two additive relations were used in order to analyze the AHE results; in the first scaling relation, two term relation was used consisting of linear and quadratic terms which represent skew scattering and side jump/intrinsic mechanisms, respectively. In the second scaling relation, the skew scattering term was modified to represent both impurity and phonon induced parts. The modified relation allowed the determination and comparison of the magnitudes of both impurity and phonon induced scattering mechanisms.
- After the scaling analysis of AHE with the above mentioned relations, the possibility of a single dominant scattering source is disregarded since the results cannot be scaled either with relations which represent only skew scattering or side jump mechanism. In order to examine the approximate contribution of each scattering mechanism to AHE, the interpretation of anomalous Hall resistivity identifies its scattering origin in the superposition of extrinsic sources. Although the scaling results hint towards superposition of skew scattering and side jump, the tendency of the obtained parameters signified that a large share of contribution comes from the later source.
- Since the scaling relations used in this thesis cannot separate the side jump mechanism from intrinsic mechanism, the AHE investigation was further extended to magnetoconductivity analysis. The magnetoconductivity of $Ge_{1-x-y}Sn_xMn_yTe$ alloys was determined to be in the bad metal hopping regime with $\sigma_{xx} < 10^4\ \Omega^{-1}.\mathrm{cm}^{-1}$. Therefore, scaling relation $\sigma_{\mathrm{AH}} \sim \sigma_{xx}^{\varepsilon}$ was used where the exponent values equal to $\varepsilon = 1.41 - 1.8$ were obtained. The conductivity regime $\sigma_{xx} < 10^4\ \Omega^{-1}.\mathrm{cm}^{-1}$ and proper scaling with the relation $\sigma_{\mathrm{AH}} \sim \sigma_{xx}^{\varepsilon}$ disregards the presence of intrinsic mechanism in $Ge_{1-x-y}Sn_xMn_yTe$ samples.
- Finally, the carrier mobility, $\mu_h(T)$, behavior of $Ge_{1-x-y}Sn_xMn_yTe$ alloys was studied to examine the scattering processes. The analysis of mobility curves was carried out with $1/T^{-\gamma}$

where γ is phonon related parameter. This $\mu_h(T)$ scaling resulted in $\gamma = 0.19 – 0.47$ for all $Ge_{1-x-y}Sn_xMn_yTe$ crystals. Maxima in $\mu_h(T)$ curves were observed for the samples with y = 0.027, 0.03, 0.062, 0.072, 0.086 which signified two scattering regimes in carrier mobility. The low temperature regime below $\mu_h(T)$ maxima resulted from ionized impurities whereas optically excited phonons or the presence of polarons dominate at $T \geq T_{\mathrm{max}}$.

Bibliography

[1] M. N. Baibich, J. M. Broto, A. Fert, F. N. V. Dau, F. Petroff, P. Etienne, G. Creuzet, A. Friederich, and J. Chazelas, **Phys. Rev. Lett. 61, 2472 (1988)**.

[2] G. Binasch, P. Grünberg, F. Saurenbach, and W. Zinn, **Phys. Rev. B 39, 4828 (1989)**.

[3] Y. Wu, Nano Spintronics for Data Storage, **Encyclopedia of Nanoscience and Nanotechnology, American Scientific Publishers, USA. 7, 493 (2003)**.

[4] D. Apalkov, B. Dieny and J. M. Slaughter, **Proc. IEEE 104, 1796 (2016)**.

[5] S. Parkin, S. H. Yang, **Nature Nanotechnol. 10, 195 (2015)**.

[6] T. J. Silva and W. H. Rippard, **J. Magn. Magn. Mater. 320, 1260 (2008)**.

[7] J. M. Kikkawa, I. P. Smorchkova, N. Samarth and D. D. Awschalom, **Science 277, 1284 (1997)**.

[8] M. E. Flatté and J. M. Byers, **Phys. Rev. Lett. 84, 4220 (2000)**.

[9] H. Ohno, D. Chiba, F. Matsukura, T. Omiya, E. Abe, T. Dietl, Y. Ohno, and K. Ohtani, **Nature 408, 944 (2000)**.

[10] R. T. Delves, **J. Phys. Chem. Solids, 24, 885 (1963)**.

[11] R. T. Delves, **Proc. Phys. Soc. 87, 809 (1966)**.

[12] S. Methfessel, and D.C. Mattis, H.P.J. Wijn (Ed.), **Encyclopedia of physics, vol. XVIII/1, magnetism, Springer-Verlag Berlin, pp. 389-562 (1968)**.

[13] J. K. Furdyna, Diluted magnetic semiconductors–an interface of semiconductor physics and magnetism, **J. Appl. Phys. 64, R29 (1988)**.

[14] H. Ohno, A. Shen, F. Matsukura, A. Oiwa, A. Endo, S. Katsumoto, and Y. Iye, **Appl. Phys. Lett. 69, 363 (1996)**.

[15] H. Ohno, H. Munekata, T. Penney, S. von Molnar, and L. L. Chang, **Phy. Rev. Lett. 68, 2664 (1992)**.

[16] T. Fukumura, Zhengwu Jin, A. Ohtomo, H. Koinuma and M. Kawasaki, **Appl. Phys. Lett. 75, 3366 (1999)**.

[17] M. Zając, R. Doradziński, J. Gosk, J. Szczytko, M. Lefeld-Sosnowska, M. Kamińska, A. Twardowski, M. Palczewska, E. Grzanka and W. Gębicki, **Appl. Phys. Lett. 78, 1276 (2001)**.

[18] T. Story, R. R. Gałązka, R. B. Frankel, and P. A. Wolff, **Phys. Rev. Lett. 56, 777 (1986)**.

[19] R. W. Cochrane, M. Plischke, and J. O. Ström-Olsen, **Phys. Rev. B 9, 3013 (1974)**.

[20] M. Escorne, A. Ghazalli, and P. Leroux-Hugon, in Proceedings of the Twelfth International Conference on the Physics of Semiconductors, edited by M. H. Pilkuhn **(Teubner, Stuttgart, Germany, 1974)**.

[21] L. Chen, X. Yang, F. Yang, J. Zhao, J. Misuraca, P. Xiong and S. von Molnar, **Nano Lett., 11, 2584 (2011)**.

[22] M. Hassan, G. Springholz, R. T. Lechner, H. Groiss, R. Kirchschlager, and G. Bauer, **J. Cryst. Growth, 323, 363 (2011)**.

[23] R. Tsu, W. E. Howard, and L. Esaki, **Phys. Rev. 172, 779 (1968)**.

[24] R. Fei, S. Yu, Y. Lu, L. Zhu, and L. Yang, **Nano Lett. 21, 2265 (2021)**.

[25] J. Ning, K. Men, G. Xiao, B. Zou, L. Wang, Q. Dai, B. Liu, and G. Zou, **CrystEngComm, 12, 4275 (2010)**.

[26] K. Chang, J. Liu, H. Lin, N. Wang, K. Zhao, A. Zhang, F. Jin, Y. Zhong, X. Hu, W. Duan, Q. Zhang, L. Fu, Q. K. Xue, X. Chen, and S. H. Ji, **Science 353, 274 (2016)**.

[27] T. H. Hsieh, H. Lin, J. Liu, W. Duan, A. Bansil, and L. Fu, **Nat. Commun. 3, 982 (2012)**.

[28] U. S. Shenoy, and D. K. Bhat, **J. Mater. Chem. C 8, 2036 (2020)**.

[29] X. Zhang, Z. Bu, S. Lin, Z. Chen, W. Li, and Y. Pei, **Joule 4, 986 (2020)**.

[30] C. Rinaldi, S. Varotto, M. Asa, J. Sławińska, J. Fujii, G. Vinai, S. Cecchi, D. D. Sante, R. Calarco, I. Vobornik, G. Panaccione, S. Picozzi, and R. Bertacco, **Nano Lett. 18, 2751 (2018)**.

[31] J. Krempaský, S. Muff, F. Bisti, M. Fanciulli, H. Volfová, A. P. Weber, N. Pilet, P. Warnicke, H. Ebert, J. Braun, F. Bertran, V. V. Volobuev, J. Minár, G. Springholz, J. H. Dil, and V. N. Strocov, **Nat Commun 7, 13071 (2016)**.

[32] J. M. Kikkawa and D. D. Awschalom, **Nature 397, 139 (1999)**.

[33] G. Salis, Y. Kato, K. Ensslin, D. C. Driscoll, A. C. Gossard and D. D. Awschalom, **Nature 414, 619 (2001)**.

[34] J. A. Gupta, R. Knobel, N. Samarth and D. D. Awschalom, **Science 292, 2458 (2001)**.

[35] Y. Kato, R. C. Myers, A. C. Gossard and D. D. Awschalom, **Nature 427, 50 (2003)**.

[36] N. P. Stern, S. Ghosh, G. Xiang, M. Zhu, N. Samarth, and D. D. Awschalom, **Phys. Rev. Lett. 97, 126603 (2006)**.

[37] S. P. Dash, S. Sharma, R. S. Patel, M. P. de Jong and R. Jansen, **Nature 462, 491 (2009)**.

[38] B. Dieny, V. S. Speriosu, S. S. P. Parkin, B. A. Gurney, D. R. Wilhoit, and D. Mauri, **Phys. Rev. B 43, 1297 (1991)**.

[39] N. F. Mott, **Proc. R. Soc. Lond. A 153, 699 (1936)**.

[40] J. S. Moodera, L. R. Kinder, T. M. Wong, and R. Meservey, **Phys. Rev. Lett. 74, 3273 (1995)**.

[41] M. Johnson, and R. H. Silsbee, **Phys. Rev. B 37, 5326 (1988)**.

[42] D. Awschalom, and M. Flatté, **Nature Phys. 3, 153 (2007)**.

[43] J. M. Kikkawa, and D. D. Awschalom, **Phys. Rev. Lett. 80, 4313 (1998)**.

[44] S. Datta, and B. Das, **Appl. Phys. Lett. 56, 665 (1990)**.

[45] R. Fiederling, M. Keim, G. Reuscher, W. Ossau, G. Schmidt, A. Waag and L. W. Molenkamp, **Nature 402, 787 (1999)**.

[46] Y. Ohno, D. Young, B. Beschoten, F. Matsukura, H. Ohno and D. D. Awschalom, **Nature 402, 790 (1999)**.

[47] P. Bruno, and J. Wunderlich. **J. Appl. Phys. 84, 978 (1998)**.

[48] D. Loss and D. P. DiVincenzo, **Phys. Rev. A 57, 120 (1998)**.

[49] W. Q. Chen, K. L. Teo, M. B. A. Jalil, and T. Liew, **J. Appl. Phys. 99, 08D515 (2006)**.

[50] Y. Fukuma, H. Asada, N. Nishimura, T. Koyanagi, **J. Appl. Phys. 93, 4034 (2003)**.

[51] S. K. Bahl and K. L. Chopra, **J. Appl. Phys. 41, 2196 (1970)**.

[52] Y. Fukuma, T. Murakami, H. Asada and T. Koyanagi, **Physica E 10, 273 (2001)**.

[53] Y. Fukuma, K. Goto, S. Senba, S. Miyawaki, H. Asada, T. Koyanagi, H. Sato, **J. Appl. Phys. 103, 053904 (2008)**.

[54] Y. Fukuma, M. Arifuku, H. Asada, T. Koyanagi, **J. Appl. Phys. 91, 7502 (2002)**.

[55] A. Khaliq, S. Lewińska, R. Minikaev, M. Arciszewska, A. Avdonin, B. Brodowska, V. E. Slynko, A. Ślawska-Waniewska, and L. Kilanski, **J. Alloy. Compd. 968, 171893 (2023)**.

[56] L. Kilanski, M. Arciszewska, W. Dobrowolski, V. Domukhovski, V. E. Slynko, and E. I. Slynko, **J. Appl. Phys. 105, 103901 (2009)**.

[57] L. Kilanski, R. Szymczak, W. Dobrowolski, K. Szałowski, V. E. Slynko and E. I. Slynko, **Phys. Rev. B 82, 094427 (2010)**.

[58] T. Dietl, **J. Phys. Soc. Jpn. 77, 031005 (2008)**.

[59] H. Ohno, **Science 281, 951 (1998)**.
[60] F. Matsukura, H. Ohno, Nanomagnetism and Spintronics (Second Edition), **Elsevier, 315 (2014)**.
[61] M. IIlegems, R. Dingle and L. W. Rupp Jr., **J. Appl. Phys. 46, 3059 (1975)**.
[62] T. Frey, M. Maier, J. Schneider and M. Gehrke, **J. Phys. C 21, 5539 (1988)**.
[63] H. Munekata, H. Ohno, S. von Molnar, A. Harwit, A. Segmüller, L. L. Chang, **J. Vac. Sci. Technol. B: Microelectron. Process. Phenomena, 8, 176 (1990)**.
[64] E. F. Kharakhorin, R. V. Lutziv, M. V. Pashkovskii, V. M. Petrov, **Phys. Status Solidi B, 5, 69 (1971)**.
[65] H. Savage, J. J. Rhyne, R. Holm, J. R. Cullen, C. E. Carroll, E. P. Wohlfarth, **Phys. Status Solidi B, 58, 685 (1973)**.
[66] R. L. Gunshor, L.A. Kolodziejski, N. Otsuka, B. R Gu, D. Lee, Y. Hefetz and A.V. Nurmikko, **Superlatt. Microstr. 3, 5 (1987)**.
[67] J. Spalek, A. Lewicki, Z. Tarnawski, J. K. Furdyna, R. R. Galazka, and Z. Obuszko, **Phys. Rev. B 33, 3407 (1986)**.
[68] Y. Shapira, S. Foner, D. H. Ridgley, K. Dwight, and A. Wold, **Phys. Rev. B 30, 4021 (1984)**.
[69] Y. Shapira, S. Foner, P. Becla, D. N. Domingues, M. J. Naughton, and J. S. Brooks, **Phys. Rev. B 33, 356 (1986)**.
[70] T. M. Giebultowicz, J. J. Rhyne, and J. K. Furdyna, **J. Appl. Phys. 61, 3537 (1987)**.
[71] D. V. Bartholomew, E.-K. Suh. S. Rodriguez, A. K. Ramdas and R. L. Aggarwal, **Solid State Commun. 62, 235 (1987)**.
[72] B. E. Larson, K. C. Hass, and R. L. Aggarwal, **Phys. Rev. B 33, 1789 (1986)**.
[73] R. R. Galazka, S. Nagata, and P. H. Keesom, **Phys. Rev. B., 22, 3344 (1980)**.
[74] S. Nagata, R. R. Galazka, D. P. Mullin, H. Akbarzadeh, G. D. Khattak, J. K. Furdyna, and P. H. Keesom, **Phys. Rev. B., 22, 3331 (1980)**.
[75] N. V. Joshi, S. Ray, G. Menk, **Appl. Phys. Lett.; 47, 1108 (1985)**.
[76] N. Samarth and J. K. Furdyna, **Proceedings of the IEEE, 78, 990 (1990)**.
[77] G. Bastard, C, Rigaux and A. Mycielski, **phys. stat. sol. (b) 79, 585 (1977)**.
[78] J. A. Gaj, J. Ginter and R. R. Galazka, **phys. stat. sol. (b) 89, 655 (1978)**.
[79] A. E. Turner, R. L. Gunshor and S. Datta, **Appl. Opt. 22, 3152 (1983)**.
[80] D. Wilson, **MRS Online Proceedings Library (OPL), 517, 541 (1998)**.
[81] W. E. Martin, **J. Appl. Phys. 44, 3703 (1973)**.
[82] H. T. Savage and J. J. Rhyne, **AIP Conf. Proc. 5, 879 (1972)**.
[83] T. Dietl and H. Ohno, **Rev. Mod. Phys. 86, 187 (2014)**.
[84] W. Giriat, J. Furdyna, Chapter 1 **Semiconductors and Semimetals, 25, 1-34 (1988)**.
[81] H. J. M. Swagten, C. E. P. Gerrits, A. Twardowski, and W. J. M. de Jonge, **Phys. Rev. B 41, 7330(R) (1990)**.
[86] A. Mycielski, M. Arciszewska, W. Dobrowolski, C. Rigaux, A. Mauger, C. Testelin, C. Julient, A. Lenard, M. Guillotb, B. Witkowska and M. Menant, **Physica Scripta. T39, 119 (1991)**.
[87] A. Mycielski, **J. Appl. Phys. 63, 3279 (1988)**.
[88] A. Lewicki, A. I. Schindler, J. K. Furdyna and W. Giriat, **Phys. Rev. B 40, 2379 (1989)**.
[89] M. Nawrocki, E. Hamdani, J. R. Lascaray, Z. Golacki and J. Deportes, **Solid State Commun. 77, 111 (1991)**.

[90] J. Kossut, W. Dobrowolski, Chapter 4 Diluted magnetic semiconductors, **7, 231-305 (1993)**.

[91] S. Datta, J. K. Furdyna, R. L. Gunshor, **Superlattices Microstruct. 1, 327 (1985)**.

[92] H. Alawadhi, I. Miotkowski, V. Souw, M. McElfresh, A. K. Ramdas, and S. Miotkowska **Phys. Rev. B 63, 155201 (2001)**.

[93] M. von Ortenberg, **Phys. Rev. Lett. 49, 1041 (1982)**.

[94] N. Dai, H. Luo, F. C. Zhang, N. Samarth, M. Dobrowolska, and J. K. Furdyna, **Phys. Rev. Lett. 67, 3824 (1991)**.

[95] B. König, U. Zehnder, D. R. Yakovlev, W. Ossau, T. Gerhard, M. Keim, A. Waag, and G. Landwehr, **Phys. Rev. B 60, 2653 (1999)**.

[96] A. Haury, A. Wasiela, A. Arnoult, J. Cibert, S. Tatarenko, T. Dietl, and Y. Merle d'Aubigné, **Phys. Rev. Lett. 79, 511 (1997)**.

[97] T. Dietl, H. Ohno, F. Matsukura, J. Cibert and D. Ferrand, **Science, 287, 1019 (2000)**.

[98] H. Saito, V. Zayets, S. Yamagata, and K. Ando, **Phys. Rev. Lett. 90, 207202 (2003)**.

[99] M. Ruderman, C. Kittel, **Phys. Rev. 96, 99 (1954)**.

[100] T. Kasuya, **Prog. Theor. Phys. 16, 45 (1956)**.

[101] K. Yoshida, **Phys. Rev. 106, 893 (1957)**.

[102] Y. Fukuma, H. Asada, S. Miyawaki, T. Koyanagi, S. Senba, K. Goto, H. Sato, **Appl. Phys. Lett. 93, 252502 (2008)**.

[103] H. Przybylińska, G. Springholz, R. T. Lechner, M. Hassan, M. Wegscheider, W. Jantsch, and G. Bauer, **Phys. Rev. Lett. 112, 047202 (2014)**.

[104] W. Eerenstein, N. Mathur, and J. Scott, **Nature 442, 759 (2006)**.

[105] R. Ramesh, N. Spaldin, **Nature Mater 6, 21 (2007)**.

[106] Y. Tokura and S. Seki, **Adv. Mater. 22, 1554 (2010)**.

[107] Y. Tanaka, Z. Ren, T. Sato, K. Nakayama, S. Souma, T. Takahashi, K. Segawa, Y. Ando, **Nat. Phys. 8, 800 (2012)**.

[108] H. Ohno, H. Munekata, S. von Molnar and L. L. Chang, **J. Appl. Phys. 69, 6103 (1991)**.

[109] H. Munekata, H. Ohno, S. von Molnar, A. Segmuller, L. L. Chang, and L. Esaki, **Phys. Rev. Lett. 63, 1849 (1989)**.

[110] S. Koshihara, A. Oiwa, M. Hirasawa, S. Katsumoto, Y. Iye, C. Urano, H. Takagi, and H. Munekata, **Phys. Rev. Lett. 78, 4617 (1997)**.

[111] G. Schmidt, G. Richter, P. Grabs, C. Gould, D. Ferrand, and L. W. Molenkamp, **Phys. Rev. Lett. 87, 227203 (2001)**.

[112] C. Gould, C. Rüster, T. Jungwirth, E. Girgis, G. M. Schott, R. Giraud, K. Brunner, G. Schmidt, and L. W. Molenkamp, **Phys. Rev. Lett. 93, 117203 (2004)**.

[113] M. Yamanouchi, D. Chiba, F. Matsukura, and H. Ohno, **Nature 428, 539 (2004)**.

[114] K. M. Rabe and J. D. Joannopoulos, **Phys. Rev. B 32, 2302 (1985)**.

[115] A. Bussmann-Holder, **Phys. Rev. B 40, 11639 (1989)**.

[116] T. Story, G. Karczewski, L. Świerkowski, and R. R. Gałązka, **Phys. Rev. B 42, 10477 (1990)**.

[117] J. N. Bierly, L. Muldawer and O. Beckman, **Acta Metallurgica, 11, 447 (1963)**.

[118] A. I. Lebedev, I. A. Sluchinskaya, V. N. Demin, and I. H. Munro, **Bull. Russ. Akad. Sci.: Phys. 60, 1533 (1996)**.

[119] J. M. Adamczyk, F. A. Bipasha, G. A. Rome, K. Ciesielski, E. Ertekin and E. S. Toberer, **J. Mater. Chem. A, 10, 16468 (2022)**.

[120] P. B. Pereira, I. Sergueev, S. Gorsse, J. Dadda, E. Müller, R. P. Hermann, **Phys. Status Solidi B 250, 1300 (2013)**.

[121] K. L. Jablonska, J. Kachniarz, Z. Spolnik, J. Libera, E. Dynowska, A. Nadolny and J. Sadowski, **J. Anal. At. Spectrom. 14, 461 (1999)**.

[122] S. Picozzi, **Front. Phys. 2, 10 (2014)**.

[123] S.Picozzi, Multiferroic and Ferroelectric Rashba Semiconductors, **Handbook of Materials Modeling, Springer International, 375 (2020)**.

[124] Y. H. Meng W. Bai, H. Gao, S. J. Gong, J. Q. Wang, C. G. Duan and J. H. Chu, **Nanoscale, 9, 17957 (2017)**.

[125] E. Plekhanov, P. Barone, D. Di Sante, and S. Picozzi, **Phys. Rev. B 90, 161108 (2014)**.

[126] D. D. Sante, P. Barone, R. Bertacco, S. Picozzi, **Adv. Mater. 25, 509 (2013)**.

[127] M. Liebmann, C. Rinaldi, D. D. Sante, J. Kellner, C. Pauly, R. N. Wang, J. E. Boschker, A. Giussani, S. Bertoli, M. Cantoni, L. Baldrati, M. Asa, I. Vobornik, G. Panaccione, D. Marchenko, J. S. Barriga, O. Rader, R. Calarco, S. Picozzi, R. Bertacco, M. Morgenstern, **Adv. Mater. 28, 560 (2016)**.

[128] A. Manchon, H. C. Koo, J. Nitta, S. M. Frolov and R. A. Duine, **Nat. Mater. 14, 871 (2015)**.

[129] C. Rinaldi, J. C. Rojas-Sánchez, R. N. Wang, Y. Fu, S. Oyarzun, L. Vila, S. Bertoli, M. Asa, L. Baldrati, M. Cantoni, J.-M. George, R. Calarco, A. Fert, R. Bertacco, **APL Mater. 4, 32501 (2016)**.

[130] P. S. Bednyakov, B. I. Sturman, T. Sluka, A. K. Tagantsev and P. V. Yudin, **npj Comput Mater 65, 1 (2018)**.

[131] G. F. Nataf, M. Guennou, J. M. Gregg, D. Meier, J. Hlinka, E. K. H. Salje and J. Kreisel, **Nature Rev. Phys. 2, 634 (2020)**.

[132] B. B. Van Aken, J.-P. Rivera, H. Schmid and M. Fiebig, **Nature 449, 702 (2007)**.

[133] C.-L. Jia, S. B. Mi, K. Urban, I. Vrejoiu, M. Alexe and D. Hesse, **Nat. Mater. 7, 57 (2008)**.

[134] C.-L. Jia, K. W. Urban, M. Alexe, D. Hesse, I. Vrejoiu, **Science 331, 1420 (2011)**.

[135] V. Stepkova, P. Marton, and J. Hlinka, **Phys. Rev. B 92, 094106 (2015)**.

[136] E. K. Salje and J. F. Scott, **Appl. Phys. Lett. 105, 252904 (2014)**.

[137] S. S. P. Parkin, M. Hayashi, L. Thomas, **Science 320, 190 (2008)**.

[138] M. Al Bahri, B. Borie, T.L. Jin, R. Sbiaa, M. Kläui, and S. N. Piramanayagam, **Phys. Rev. Appl. 11, 024023 (2019)**.

[139] J. K. Furdyna, and J. Kossut Semiconductors and Semimetals, **25**, **New York: Academic Press, (1988)**.

[140] T. Dietl, Handbook of Semiconductors, **3B**, Edited by Mahajan S. North Holland, **Amsterdam, 1251 (1994)**.

[141] Introduction to the theory of Ferromagnetism, **Oxford Science Publications, 2nd edition (2000)**.

[142] C. Karunakaran, and M. Balamurugan, **Spin Resonance Spectroscopy, Elsevier, 169-228 (2018)**.

[143] C. Zener, **Phys. Rev. 82 403 (1951)**.

[144] P. W. Anderson, and H. Hasegawa, **Phys. Rev. 100, 675 (1955)**.

[145] H. Akai, **Phys. Rev. Lett. 81, 3002 (1998)**.

[146] C. Zener, **Phys. Rev. 81, 440 (1951)**.

[147] J. Kanamori, and K. Terakura, **J. Phys. Soc. Japan 70, 1433 (2001)**.

[148] K. Sato, P. H. Dederichs, H. K. Yoshida and J. Kudrnovsky, **J. Phys.: Condens. Matter 16, S5491 (2004)**.

[149] G. M. Dalpian, S. H. Wei, X. G. Gong, A. J. R. da Silva and A. Fazzio, **Solid State Commun. 138, 353 (2006)**.

[150] J. Kanamori, **J. Phys. Chem. Solids 10, 87 (1959)**.

[151] J. B. Goodenough, **Phys. Rev. 100, 564 (1955)**.

[152] H. Fröhlich and F. R. N. Nabarro, **Proc. R. Soc. London Ser. A 175, 382 (1940)**.

[153] E. Dagotto, T. Hotta and A. Moreo, **Physics Reports 344, 153 (2001)**.

[154] B Belhadji, L Bergqvist, R Zeller, P H Dederichs, K Sato and H K. Yoshida, **J. Phys.: Condens. Matter 19, 436227 (2007)**.

[155] P. G. de Gennes, **Phys. Rev. 118, 141 (1960)**.

[156] F. C. Zhang and T. M. Rice, **Phys. Rev. B 37, 3759 (1988)**.

[157] C. Benoit à la Guillaume, D. Scalbert, and T. Dietl, **Phys. Rev. B 46, 9853 (1992)**.

[158] T. Dietl, H. Ohno, and F. Matsukura, **Phys. Rev. B 63, (2001)**.

[159] L. Bergqvist, O. Eriksson, J. Kudrnovsky, V. Drchal, P. Korzhavyi and I. Turek, **Phys. Rev. Lett. 93 137202 (2004)**.

[160] K. Sato, W. Schweika, P. H. Dederichs and Y. H. Katayama, **Phys. Rev. B 70, 201202(R) (2004)**.

[161] H. A. Kramers, **Physica 1, 182 (1934)**.

[162] P. W. Anderson, **Phys. Rev. 79, 350 (1950)**.

[163] J. B. Goodenough, **J. Phys. Chem. Solids 6, 287 (1958)**.

[164] Y. Shapira and V. Bindilatti, **J. Appl. Phys. 92, 4155 (2002)**.

[165] G. Karczewski, M. Sawicki, V. Ivanov, C. Ruester, G. Grabecki, F. Matsukura, L. W. Molenkamp, and T. Diet, **Journal of Superconductivity 16, 55 (2003)**.

[166] P. Kacman, **Semicond. Sci. Technol. 16, R25 (2001)**.

[167] J. Friedel, **Philos. Mag. 43, 153 (1952)**.

[168] T. Story, P. J. T. Eggenkamp, C. H. W. Swüste, H. J. M. Swagten, W. J. M. de Jonge, and L. F. Lemmens, **Phys. Rev. B 45, 1660 (1992)**.

[169] Y. Fukuma, H. Asada, M. Arifuku and T. Koyanagi, **Appl. Phys. Lett. 80, 1013 (2002)**.

[170] S. Blundell, Magnetism in Condensed Matter **(Oxford Univ. Press, Oxford, 2001)**.

[171] H. Kawamura and T. Taniguchi, **Handbook of Magnetic Materials, Elsevier, 24, 1-137 (2015)**.

[172] C. Bellouard, M. Hennion, I. Mirebeau and B. Hennion, **J. Magn. Magn. Mater. 104–107, 1627 (1992)**.

[173] J. K. Furdyna and N. Samarth, **J. Appl. Phys. 61, 3526 (1987) and references within**.

[174] V. Cannella and J. A. Mydosh, **Phys. Rev. B 6, 4220 (1972)**.

[175] C. A. M. Mulder, A. J. van Duyneveldt, and J. A. Mydosh, **Phys. Rev. B 23, 1384 (1981)**.

[176] A. Malinowski, V. L. Bezusyy, R. Minikayev, P. Dziawa, Y. Syryanyy, M. Sawicki, **Phys. Rev. B. 84, 024409 (2011)**.

[177] K. Binder and A. P. Young, **Rev. Mod. Phys. 58, 801 (1986)**.

[178] K. Binder, **Festkörperprobleme 17, 55 (1977)**.

[179] J. A. Mydosh, **Taylor & Francis, London and Washington, DC (1993)**.

[180] J. C. R. de Araújo, C. A. de Moraes Iglesias, R. B. da Silva, S. A. Barbosa, J. Xavier, E. D. da Silva Filho, J. L. C. Fonseca, P. B. Souza, C. C. Plá Cid, F. L. de Araujo Machado, E. F. da

Silva, M. Gamino, S. N. de Medeiros, M. A. Correa, F. Bohn, **J. Phys. D: Appl. Phys., 55, 365002 (2022)**.

[181] P. J. T. Eggenkamp, C. W. H. M. Vennix, T. Story, H. J. M. Swagten, C. H. W. Swüste, W. J. M. de Jonge, **J. Appl. Phys. 75, 5728 (1994)**.

[182] S. Kundu, T. Dey, A.V. Mahajan, N. Büttgen, **J. Phys. Condens. Matter 32, 115601 (2020)**.

[183] K. De, M. Patra, S. Majumdar, S. Giri, **J. Phys. D Appl. Phys. 40, 7614 (2007)**.

[184] P. Bag, P. R. Baral, and R. Nath, **Phys. Rev. B 98, 144436 (2018)**.

[185] C. A. Cardoso, F. M. Araujo-Moreira, V. P. S. Awana, E. Takayama-Muromachi, O. F. de Lima, H. Yamauchi, M. Karppinen, **Phys. Rev. B. 67, 020407(R) (2003)**.

[186] V. K. Anand, D. T. Adroja, A. D. Hillier, **Phys. Rev. B. 85, 014418 (2012)**.

[187] M. Itoh, I. Natori, S. Kubota, K. Motoya, **J. Phys. Soc. Jpn. 63, 1486 (1994)**.

[188] B. Martinez, X. Obradors, L. Balcells, A. Rouanet, C. Monty, **Phys. Rev. Lett. 80, 181 (1998)**.

[189] H. A. Katori, A. Ito, **J. Phys. Soc. Jpn. 63, 3122 (1994)**.

[190] E. H. Hall, **Am. J. Math. 2, 287 (1879)**.

[191] E. Hall, **Philos. Mag. 12, 157 (1881)**.

[192] N. Nagaosa, J. Sinova, S. Onoda, A. H. MacDonald, and N. P. Ong, **Rev. Mod. Phys. 82, 1539 (2010)**.

[193] R. Karplus and J. M. Luttinger, **Phys. Rev. 95, 1154 (1954)**.

[194] L. Berger, **Phys. Rev. B 2, 4559 (1970)**.

[195] J. Smit, **Physica, 21, 877 (1955)**.

[196] Y. Tian, L. Ye and X. Jin, **Phys. Rev. Lett. 103, 087206 (2009)**.

[197] J. Sinova, S. O. Valenzuela, J. Wunderlich, C. H. Back, and T. Jungwirth, **Rev. Mod. Phys. 87, 1213 (2015)**.

[198] M. I. Dyakonov and V. I. Perel, **Sov. Phys. JETP Lett. 13, 467 (1971); Phys. Lett. A 35(6), 459 (1971)**.

[199] J. E. Hirsch, **Phys. Rev. Lett. 83(9), 1834 (1999)**.

[200] S. Murakami, N. Nagaosa, and S.-C. Zhang, **Science 301, 1348 (2003)**.

[201] J. Sinova, D. Culcer, Q. Niu, N. A. Sinitsyn, T. Jungwirth, and A. H. MacDonald, **Phys. Rev. Lett. 92, 126603 (2004)**.

[202] C. X. Liu, S. C. Zhang and X. L. Qi, **Annu. Rev. Condens. Matter Phys. 7, 301 (2016)**.

[203] T. Ando, Y. Matsumoto and Y. Uemura, **J. Phys. Soc. Jpn. 39, 279 (1975)**.

[204] K. V. Klitzing, G. Dorda and M. Peper, **Phys. Rev. Lett. 45(6), 494 (1980)**.

[205] F. D. M. Haldane, **Phys. Rev. Lett. 61, 2015 (1988)**.

[206] R. Yu, W. Zhang, H. J. Zhang, S. C. Zhang, X. Dai, and Z. Fang, **Science 329, 61 (2010)**.

[207] H. Zhang, C. X. Liu, X. L. Qi, X. Dai, Z. Fang, S. C. Zhang, **Nat. Phys. 5, 438 (2009)**.

[208] Y. Xia, D. Qian, D. Hsieh, L. Wray, A. Pal, H. Lin, A. Bansil, D. Grauer, Y. S. Hor, R. J. Cava and M. Z. Hasan, **Nat. Phys. 5, 398 (2009)**.

[209] C. Z. Chang, J. S. Zhang, X. Feng, J. Shen, Z. C. Zhang, M. H. Guo, K. Li, Y. B. Ou, P. Wei, L. L. Wang, Z. Q. Ji, Y. Feng, S. H. Ji, X. Chen, J. F. Jia, X. Dai, Z. Fang, S. C. Zhang, K. He, Y. Y. Wang, L. Lu, X. C. Ma, and Q. K. Xue, **Science 340, 167 (2013)**.

[210] P. W. Anderson, **Phys. Rev. 109, 1492 (1958)**.

[211] A. Lagendijk, B. V. Tiggelen, D. S. Wiersma, **Phys. today. 62, 24 (2009)**.

[212] C. A. Müller and D. Delande, **arXiv:1005.0915 (2010)**.

[213] D. Vollhardt and P. Wölfle, **Phys. Rev. Lett. 48, 699 (1982)**.

[214] J. Chen, H. J. Qin, F. Yang, J. Liu, T. Guan, F. M. Qu, G. H. Zhang, J. R. Shi, X. C. Xie, C. L. Yang, K. H. Wu, Y. Q. Li and L. Lu, **Phys. Rev. Lett. 105, 176602 (2010)**.

[215] Y. A. Salawu, J. H. Yun, J. S. Rhyee, M. Sasaki and H. J. Kim, **Sci Rep 12, 2845 (2022)**.

[216] J. G. Checkelsky, Y. S. Hor, M. H. Liu, D. X. Qu, R. J. Cava and N. P. Ong, **Phys. Rev. Lett. 103, 246601 (2009)**.

[217] H. L. Peng, K. J. Lai, D. S. Kong, S. Meister, Y. L. Chen, X. L. Qi, S. C. Zhang, Z. X. Shen and Y. Cui, **Nature Mater. 9, 225 (2010)**.

[218] J. G. Checkelsky, Y. S. Hor, R. J. Cava and N. P. Ong, **Phys. Rev. Lett. 106, 196801 (2011)**.

[219] G. Bergmann, **Int. J. Mod. Phys. B 24, 2015 (2010)**.

[220] L. Kilanski, M. Arciszewska, W. Dobrowolski, V. Domukhovski, V. E. Slynko, E. I. Slynko, **J. Appl. Phys. 105, 103901 (2009)**.

[221] Y. Mozharivskyj, Comprehensive Inorganic Chemistry III (Third Edition), **Elsevier, 178-198 (2023)**.

[222] L. Kilanski, R. Szymczak, W. Dobrowolski, K. Szałowski, V. E. Slynko, E. I. Slynko, **Phys. Rev. B. 82, 094427 (2010)**.

[223] A. Khaliq, R. Minikayev, M. Arciszewska, A. Avdonin, B. Brodowska, A. Khan, V. E. Slynko, E. I. Slynko, L. Kilanski, **J. Magn. Magn. Mater. 544, 168695 (2022)**.

[224] K. T. Aust, B. Chalmers, **Can. J. Phys. 36, 977 (1958)**.

[225] G. S. Mann, L. H. Van Vlack, **Metall. Mater. Trans. B. 8, 53 (1977)**.

[226] D. R Lide, CRC Press LLC. (2000).

[227] H. C. I. Ankerhold, R. Ankerhold and G. P. C. Drummen, **Molecules, 17, 4047 (2012)**.

[228] C. V. Topping, and S. J. Blundell, **J. Phys.: Condens. Matter 31, 013001 (2019)**.

[229] H. M. Rietveld, **Acta Cryst. 22, 151 (1967)**.

[230] H. M. Rietveld, **J. Appl. Cryst. 2, 65 (1969)**.

[231] R. A. Young, P.E. Mackie, R. B. Von Dreele, **J. Appl. Cryst. 10, 262 (1977)**.

[232] R. J. Hill, **Am. Mineral. 69, 937 (1984)**.

[233] D. E. Cox, J. B. Hastings, W. Thomlinson, C. T. Prewitt, **Nucl. Instrum. Methods Phys. Res. 208, 573 (1983)**.

[234] D. L. Bish, **Clays and Clay Minerals 41, 738 (1993)**.

[235] L. Yue, T. Fang, S. Zheng, W. Cui, Y. Wu, S. Chang, L. Wang, P. Bai, H. Zhao, **ACS Appl. Energy Mater. 2, 2596 (2019)**.

[236] P. Boon-on, A. Tubtimtae, V. Vailikhit, P. Teesetsopon, S. Choopun, **Phys. Lett. A 381, 1807 (2017)**.

[237] M. Kriener, T. Nakajima, Y. Kaneko, A. Kikkawa, X. Z. Yu, N. Endo, K. Kato, M. Takata, T. Arima, Y. Tokura, Y. Taguchi, **Sci Rep. 6, 25748 (2016)**.

[238] K. R. Knox, E. S. Bozin, C. D. Malliakas, M. G. Kanatzidis, and S. J. L. Billinge, **Phys. Rev. B 89, 014102 (2014)**.

[239] I. Žutić, J. Fabian, S. Das Sarma, **Rev. Mod. Phys. 76, 323 (2004)**.

[240] K. Olejník, M. H. S. Owen, V. Novák, J. Mašek, A. C. Irvine, J. Wunderlich, T. Jungwirth, **Phys. Rev. B, 78, 054403 (2008)**.

[241] T. Fukushima, H. Shinya, H. Fujii, K. Sato, H. K. Yoshida, P. H. Dederichs, **J. Phys.: Condens. Matter, 27, 015501 (2015)**.

[242] M. Rodot, J. Lewis, H. Rodot, G. Villers, J. Cohen, P. Mollard, **J. Phys. Soc. Jpn. 21, 627 (1966)**.

[243] Y. D. Park, A. T. Hanbicki, S. C. Erwin, C. S. Hellberg, J. M. Sullivan, J. E. Mattson, T. F. Ambrose, A. Wilson, G. Spanos, B. T. Jonker, **Science, 295, 651 (2002)**.

[244] S. Von Molnár, H. Munekata, H. Ohno, L. L. Chang, **J. Magn. Magn. Mater. 93, 356 (1991)**.

[245] S. Satoh, N. Inoue, Y. Nishikawa, J. Yoshino, **3rd Symposium on Physics and Application of Spin-Related Phenomena in Semiconductors, Sendai, Japan, Eds. 23, (1997)**.

[246] M. Górska, J. R. Anderson, **Phys. Rev. B. 38, 9120 (1988)**.

[247] M. Escorne, A. Mauger, J. L. Tholence, R. Triboulet, **Phys. Rev. B. 29, 6306 (1984)**.

[248] H. J. M. Swagten, W. J. M. de Jonge, R. R. Gałązka, P. Warmenbol, J. T. Devreese, **Phys. Rev. B. 37, 9907 (1988)**.

[249] C. C. Paulsen. S. J. Williamson and H. Maletta, **Magn. Magn. Mater. 54, 209 (1986).**

[250] M. Balanda, **Acta physica polonica A, 124, 964 (2013)**.

[251] S. Süllow, G. J. Nieuwenhuys, A. A. Menovsky, J. A. Mydosh, S. A. M. Mentink, T. E. Mason, and W. J. L. Buyers, **Phys. Rev. Lett. 78, 354 (1997)**.

[252] P. Bag, K. Somesh, R. Nath, **J. Magn. Magn. Mater. 497, 165977 (2020).**

[253] D. X. Li, S. Nimori, Y. Shiokawa, Y. Haga, E. Yamamoto, and Y. Onuki, **Phys. Rev. B 68, 172405 (2003)**.

[254] D. X. Li, A. Dönni, Y. Kimura, Y. Shiokawa, Y. Homma, Y. Haga, E. Yamamoto, T. Honma, and Y. Onuki, **J. Phys.: Condens. Matter 11, 8263 (1999)**.

[255] X. Gui and W. Xie, **Chem. Mater. 32, 3922 (2020)**.

[256] E. M. Levin, V. K. Pecharsky, K. A. Gschneidner, Jr. **J. Appl. Phys. 90, 6255 (2001)**.

[257] A. F. May, S. Calder, C. Cantoni, H. Cao, and M. A. McGuire, **Phys. Rev. B 93, 014411 (2016)**.

[258] S. Arajs, and D. S. Miller, **J. Appl. Phys. 31, 986 (1960)**.

[259] D. Parsons, W. Sucksmith, and J. E. Thompson, **Phil. Mag. 3, 1174 (1958)**.

[260] M. Boulbazine, and A. G. Boudjahem, **J. Cluster Sci. 30, 31 (2019).**

[261] K. Eftimova, R. Laiho, E. Lähderanta, P. Nordblad, **J. Magn. Magn. Mater. 166, 179 (1997)**.

[262] M. Koyano, M. Suezawa, H. Watanabe, M. Inoue, **J. Phys. Soc. Jpn. 63, 1114 (1994)**.

[263] J. Massoudi, M. Smari, K. Khirouni, E. Dhahri, L. Bessais, **J. Magn. Magn. Mater. 528, 167806 (2021)**.

[264] J. Kroder, K. Manna, D. Kriegner, A. S. Sukhanov, E. Liu, H. Borrmann, A. Hoser, J. Gooth, W. Schnelle, D. S. Inosov, G. H. Fecher, C. Felser, **Phys. Rev. B. 99, 174410 (2019)**.

[265] S. Mukherjee, A. Garg, R. Gupta, **Appl. Phys. Lett. 100, 112904 (2012)**.

[266] S. Mukherjee, R. Ranganathan, P. S. Anilkumar, P. A. Joy, **Phys. Rev. B. 54, 9267 (1996)**.

[267] K. Vijayanandhini, Ch. Simon, V. Pralong, V. Caignaert, B. Raveau, **Phys. Rev. B. 79, 224407 (2009)**.

[268] D. X. Li, S. Nimori, T. Yamamura, Y. Shiokawa, **J. Appl. Phys. 103, 07B715 (2008)**.

[269] M. K. Sharma, K. Mukherjee, **J. Magn. Magn. Mater. 466, 317 (2018)**.

[270] M. H. Phan, N. A. Frey, H. Srikanth, M. Angst, B. C. Sales, D. Mandrus, **J. Appl. Phys. 105, 07E308 (2009)**.

[271] J. Souletie, J. L. Tholence, **Phys. Rev. B. 32, 516 (1985)**.

[272] S. Chatterjee, S. Giri, S. K. De, S. Majumdar, **Phys. Rev. B 79, 092410 (2009)**.

[273] M. Viswanathan, P. S. A. Kumar, **Phys. Rev. B 80, 012410 (2009)**.

[274] V. Kumar, R. Kumar, K. Singh, S. K. Arora, I. V. Shvets, R. Kumar, **J. Appl. Phys. 116, 073903 (2014)**.

[275] J. L. Tholence, **Physica B+C 126 157, (1984)**.

[276] A. P. Murani, **J. Phys. F: Met. Phys. 15, 417, (1985)**.

[277] E. Moreno, V. Sagredo, G. F. Goya, **Physica B 291, 190 (2000)**.

[278] L. Ma, W. H. Wang, J. B. Lu, J. Q. Li, C. M. Zhen, D. L. Hou, G. H. Wu, **Appl. Phys. Lett. 99, 182507 (2011)**.

[279] N. Hanasaki, K. Watanabe, T. Ohtsuka, I. Kezsmarki, S. Iguchi, S. Miyasaka, and Y. Tokura, **Phys. Rev. Lett. 99, 086401 (2007)**.

[280] W. Q. Chen, K. L. Teo, S. T. Lim, M. B. A. Jalil, T. Liew, and T. C. Chong, **Appl. Phys. Lett. 90, 142514 (2007)**.

[281] A. Grochot, W. Knoff, B. Taliashvili, W. Wołkanowicz, R. Minikayev, A. Pieniążek, E. Łusakowska M. Sawicki, W. Jantsch, T. Story and H. Przybylińska, **Acta Physica Polonica A 132, 340 (2017)**.

[282] D. Pajić, K. Zadro, R. Ristić, I. Živković, Ž. Skoko and E Babić, **J. Phys.: Condens. Matter 19, 296207 (2007)**.

[283] J. Tejada, X. X. Zhang, and E. M. Chudnovsky, **Phys. Rev. B 47, 14977 (1993)**.

[284] R. Ribas, B. Dieny, B. Barbara and A. Labarta, **J. Phys.: Condens. Matter 7, 3301 (1995)**.

[285] D. A. Read, T. Moyo and G. C. Hallan, **J. Magn. Magn. Mater. 44, 279 (1984)**.

[286] C. Jayaprakash and S. Kirkpatrick, **Phys. Rev. B 21, 4072 (1980)**.

[287] K. J. Buschow and A. M. Kraan, **J. Magn. Magn. Mater. 22, 220 (1981)**.

[288] D. R. Denholm and T. J. Sluckin, **Phys. Rev. B 48, 901 (1993)**.

[289] A. Cresswell and D. I. Paul, **J. Appl. Phys. 67, 398 (1990)**.

[290] C. N. Guy, *J. Phys*. **F: Met. Phys. 7, 1505 (1977)**.

[291] M. Ali, P. Adie, C.H. Marrows, D. Greig, B.J. Hickey, R. L. Stamps, **Nature Mater. 6, 70 (2007)**.

[292] T. Gredig, I.N. Krivorotov, P. Eames, E.D. Dahlberg, **Appl. Phys. Lett. 81, 1270 (2002)**.

[293] J. M. D. Coey, D. Givordi, A. Lienard and J. P. Rebouillat, **J. Phys. F: Met. Phys. 11, 2707 (1981)**.

[294] G. Bastard, C. Lewiner, **J. Phys. C Solid State Phys. 13, 1469 (1980)**.

[295] R. Jangid, K. B. Ainslie, R. Kukreja, **Journal of Materials Research, 35, 981 (2020)**.

[296] N. Marcano, J. C. Gómez Sal, J. I. Espeso, F. L. Barquín, C. Paulsen, **Phys. Rev. B, 76, 224419 (2007)**.

[297] Y. Tabata, T. Waki, H. Nakamura, **Phys. Rev. B. 96, 184406 (2017)**.

[298] T. L. Phan, D. Grinting, S. C. Yu, **J. Korean Phys. Soc. 61, 1439 (2012)**.

[299] W. Li, R. Zhao, L. Wang, R. Tang, Y. Zhu, J. H. Lee, H. Cao, T. Cai, H. Guo, C. Wang, L. Ling, L. Pi, K. Jin, Y. Zhang, H. Wang, Y. Wang, S. Ju, H. Yang, **Sci. Rep. 3, 2618 (2013)**.

[300] M. Górska, J. R. Anderson, G. Kido, S. M. Green, and Z. Gołacki, **Phys. Rev. B. 45, 11702 (1992)**.

[301] A. Hayrapetyan, **ICEF IV, 41, 2018**.

[302] J. R. Anderson, and M. Górska, **Solid State Commun. 52, 601 (1984)**.

[303] G. Braunstein, G. Dresselhaus, J. Heremans, and D. Partin, **Phys. Rev. B 35, 1969 (1987)**.

[304] J. A. Detwiler, G. M. Schmiedeshoff, N. Harrison, A. H. Lacerda, J. C. Cooley, and J. L. Smith Phys. Rev. B 61, 402 (2000).

[305] K. De, M. Patra, S. Majumdar, S. Giri, *J. Phys. D: Appl. Phys*. **40**, 7614 (2007).

[306] Z. Chen, Y. Su, Y. Li, D. Liu, C. Wang, J. Zhang, **IEEE transactions on magnetics, 45, 2616 (2009)**.

[307] D. Sherrington, B. W. Southern, **J. Phys. F: Met. Phys. 5, L49 (1975)**.

[308] R. W. Cochrane, F. T. Hedgcock, J. O. Ström-Olsen, **Phys. Rev. B 8, 4262 (1973)**.

[309] T. Shang, Y. Xu, D. J. Gawryluk, J. Z. Ma, T. Shiroka, M. Shi, and E. Pomjakushina, **Phys. Rev. B 103, L020405 (2021)**.

[310] E. M. Pugh and N. Rostoker, **Rev. Mod. Phys. 25, 151 (1953)**.

[311] E. M. Pugh, **Phys. Rev. 36, 1503 (1930)**.

[312] E. M. Pugh and T. W. Lippert, **Phys. Rev. 42, 709 (1932)**.

[313] M. V. Berry, **Proc. R. Soc. London 392, 45 (1984)**.

[314] A. Husmann, and L. J. Singh, **Phys. Rev. B 73, 172417 (2006)**.

[315] J. Smit, **Physica, 24, 39 (1958)**.

[316] E. A. Stern, **Phys. Rev. Lett. 15, 62 (1965)**.

[317] C. Zeng, Y. Yao, Q. Niu, and H. H. Weitering, **Phys. Rev. Lett. 96, 037204 (2006)**.

[318] P. N. Dheer, **Phys. Rev. 156, 637 (1967)**.

[319] A. Fert and O. Jaoul, **Phys. Rev. Lett. 28, 303 (1972)**.

[320] J. Lavine, **Phys. Rev. 123, 1273 (1961)**.

[321] S. Nakatsuji, N. Kiyohara, and T. Higo, **Nature 527, 212 (2015)**.

[322] Q. Wang, Y. Xu, R. Lou, Z. Liu, M. Li, Y. Huang, D. Shen, H. Weng, S. Wang, and H. Lei, **Nat Commun 9, 3681 (2018)**.

[323] S. Y. Yang, J. Noky, J. Gayles, F. K. Dejene, Y. Sun, M. Dörr, Y. Skourski, C. Felser, M. N. Ali, E. Liu, and S. S. P. Parkin, **Nano Lett. 20, 7860 (2020)**.

[324] A. Markou, D. Kriegner, J. Gayles, L. Zhang, Y. C. Chen, B. Ernst, Y. H. Lai, W. Schnelle, Y. H. Chu, Y. Sun, and C. Felser, **Phys. Rev. B 100, 054422 (2019)**.

[325] K. Sato, L. Bergqvist, J. Kudrnovský, P. H. Dederichs, O. Eriksson, I. Turek, B. Sanyal, G. Bouzerar, H. Katayama-Yoshida, V. A. Dinh, T. Fukushima, H. Kizaki, and R. Zeller, **Rev. Mod. Phys. 82, 1633 (2010)**.

[326] I. Turek, J. Kudrnovský, V. Drchal, and P. Weinberger, **J. Phys.: Condens. Matter. 16, S5607 (2004)**.

[327] V. A. Kulbachinskii, P. M. Tarasov, E. Bruck, **Physica B 368, 32 (2005)**.

[328] T. Schröder, T. Rosenthal, N. Giesbrecht, S. Maier, E-W. Scheidt, W. Scherer, G. J. Snyder, W. Schnick, and O. Oeckler, **J. Mater. Chem. A, 2, 6384 (2014)**.

[329] L. Ritchie, G. Xiao, Y. Ji, T. Y. Chen, C. L. Chien, M. Zhang, J. Chen, Z. Liu, G. Wu, and X. X. Zhang, **Phys. Rev. B 68, 104430 (2003)**.

[330] T. Masui, S. Lee, and S. Tajima, **Phys. Rev. B 70, 024504 (2004)**.

[331] H. Jiang, J. K. Bao, H. F. Zhai, Z. T. Tang, Y. L. Sun, Y. Liu, Z-C. Wang, H. Bai, Z. A. Xu, and G. H. Cao, **Phys. Rev. B 92, 205107 (2015)**.

[332] W. G. Baber. **Proc. Roy. Soc. London, Ser. A. 158, 383. (1937)**.

[333] M. J. Rice, **Phys. Rev. Lett. 20, 1439 (1968)**.

[334] R. Hartman, **Phys. Rev. 181, 1070 (1969)**.

[335] A. H. Thompson, **Phys. Rev. Lett. 35, 1786 (1975)**.

[336] W. E. Lawrence and J. W. Wilkins, **Phys. Rev. B 7, 2317 (1976)**.

[337] H. Takagi, B. Batlogg, H. L. Kao, J. Kwo, R. J. Cava, J. J. Krajewski, and W. F. Peck, Jr. **Phys. Rev. Lett. 69, 2975 (1992)**.

[338] M. Milewits, S. J. Williamson, and H. Taub, **Phys. Rev. B 13, 5199 (1976)**.

[339] J. Bass, W. P. Pratt, Jr., and P. A. Schroeder, **Rev. Mod. Phys. 62, 645 (1990)**.

[340] L. Ritchie, G. Xiao, Y. Ji, T. Y. Chen, C. L. Chien, M. Zhang, J. Chen, Z. Liu, G. Wu, and X. X. Zhang, **Phys. Rev. B 68, 104430 (2003)**.

[341] H. Jiang, J. K. Bao, H. F. Zhai, Z. T. Tang, Y. L. Sun, Y. Liu, Z. C. Wang, H. Bai, Z. A. Xu, and G. H. Cao, **Phys. Rev. B 92, 205107 (2015)**.

[342] G. K. White, and S. B. Woods, **Philos. Trans. R. Soc. London, A 251, 273 (1959)**.

[343] N. F. Mott, **Adv. Phys. 13, 325 (1964)**.

[344] R. K. Gopal, G. Sheet and Y. Singh, **Sci Rep 11, 12618 (2021)**.

[345] J. A. Peters, N. D. Parashar, N. Rangaraju and B. W. Wessels, **Phys. Rev. B. 82, 205207 (2010)**.

[346] M. Gacic, G. Jakob, C. Herbort and H. Adrian, **Phys. Rev. B. 75, 205206 (2007)**.

[347] Z. Yang, M. Biasini, W. P. Beyermann, M. B. Katz, O. K. Ezekoye, X. Q. Pan, Y. Pu, J. Shi, Z. Zuo and J. L. Liu, **J. Appl. Phys. 104, 113712 (2008)**.

[348] P. Xiong, G. Xiao, J. Q. Wang, J. Q. Xiao, J. S. Jiang, and C. L. Chien, **Phys. Rev. Lett. 69, 3220 (1992)**.

[349] A. K. Majumdar, **Phys. Rev. B. 28, 2750 (1983)**.

[350] P. Monod, **Phys. Rev. Lett. 19, 1113 (1967)**.

[351] R. W. Schmitt and I. S. Jacobs, **J. Phys. Chem. Solids 3, 324 (1957)**.

[352] S. Senoussi, **J. Phys. F: Met. Phys. 10, 2491 (1980)**.

[353] P. G. de Gennes and J. Friedel, **J. Phys. Chem. Solids 4, 71 (1958)**.

[354] M. E. Fisher and J. S. Langer, **Phys. Rev. Lett. 20, 665 (1968)**.

[355] A. Van Esch, L. Van Bockstal, J. De Boeck, G. Verbanck, A. S. van Steenbergen, P. J. Wellmann, B. Grietens, R. Bogaerts, F. Herlach, and G. Borghs, **Phys. Rev. B 56, 13103 (1997)**.

[356] L. Kilanski, R. Szymczak, W. Dobrowolski, A. Podgorni, A. Avdonin, V. E. Slynko, and E. I. Slynko, **J. Appl. Phys. 113, 063702 (2013)**.

[357] L. Ortenzi, H. Gretarsson, S. Kasahara, Y. Matsuda, T. Shibauchi, K. D. Finkelstein, W. Wu, S. R. Julian, Young-June Kim, I. I. Mazin, and L. Boeri, **Phys. Rev. Lett. 114, 047001 (2015)**.

[358] H. R. Child and J. W. Cable, **Phys. Rev. B 13, 227 (1976)**.

[359] K. Levin and K. H. Bennemann, **Phys. Rev. B 5, 3770 (1972)**.

[360] D. Alders, L. H. Tjeng, F. C. Voogt, T. Hibma, G. A. Sawatzky, C. T. Chen, J. Vogel, M. Sacchi, and S. Iacobucci, **Phys. Rev. B 57, 11623 (1998)**.

[361] A. W. Smith and R. W. Sears, **Phys. Rev. 34, 166 (1929)**.

[362] C. M. Hurd, The Hall Effect in Metals and Alloys; **Plenum Press, New York (1972)**.

[363] D. Yue and X. Jin, **J. Phys. Soc. Jpn. 86, 011006 (2016)**.

[364] A. Gerber, A. Milner, A. Finkler, M. Karpovski, L. Goldsmith, J. Tuaillon-Combes, O. Boisron, P. Mélinon, and A. Perez, **Phys. Rev. B 69, 224403 (2004)**.

[365] S. Zhang, **Phys. Rev. B 51, 3632 (1995)**.

[366] A. Granovsky, F. Brouers, A. Kalitsov, and M. Chshiev, **J. Magn. Magn. Mater. 166, 193 (1997)**. [367] Y. Zhang, W. B. Mi, X. C. Wang and X. X. Zhang, **Phys. Chem. Chem. Phys. 17, 15435 (2015)**.

[368] Y. E. I. Kondorskii, A. V. Vedyayev, and A. B. Granovskii, **Fiz. Met. Metalloved. 40, 455 (1975)**.

[369] A. Crépieux and P. Bruno, **Phys. Rev. B. 64, 014416 (2001)**.

[370] Z. Z. Du, C. M. Wang, S. Li, H. Z. Lu, and X. C. Xie, **Nat. Commun 10, 3047 (2019)**.

[371] J. Bass, **Advances in Physics, 21(91), 431 (1972)**.

[372] F. E. Maranzana, **Phys. Rev. 160, 421 (1967)**.

[373] L. Kilanski, M. Górska, R. Szymczak, W. Dobrowolski, A. Podgórni, A. Avdonin, V. Domukhovski, V. E. Slynko, and E. I. Slynko, **J. Appl. Phys. 116, 083904 (2014)**.

[374] B. Brodowska, W. Dobrowolski, M. Arciszewska, E. I. Slynko, V. K. Dugaev, **Journal of alloys and compounds 423, 205 (2006)**.

[375] K. Racka, I. Kuryliszyn, M. Arciszewska, W. Dobrowolski, J.-M. Broto, O. Portugall, H. Rakoto, B. Raquet, V. Dugaev, E. I. Slynko, and V. E. Slynko, **Journal of Superconductivity 16, 289 (2003)**.

[376] N. Manyala, Y. Sidis, J. F. D. Tusa, G. Aeppli, D. P. Young and Z. Fisk, **Nature Mater 3, 255 (2004)**.

[377] K. Kim, J. Seo, E. Lee, K.-T. Ko, B. S. Kim, B. G. Jang, J. M. Ok, J. Lee, Y. J. Jo, W. Kang, J. H. Shim, C. Kim, H. W. Yeom, B. I. Min, B-J. Yang and J. S. Kim, **Nature Mater 17, 794 (2018)**.

[378] T. Fukumura, H. Toyosaki, K. Ueno, M. Nakano, T. Yamasaki and M. Kawasaki, **Jpn. J. Appl. Phys. 46, L642 (2007)** (and references within).

[379] S. Onoda, N. Sugimoto and N. Nagaosa, **Phys. Rev. B. 77, 165103 (2008)**.

[380] H. Toyosaki, T. Fukumura, Y. Yamada, K. Nakajima, T. Chikyow, T. Hasegawa, H. Koinuma and M. Kawasaki, **Nature Mater 3, 221 (2004)**.

[381] S. Sangiao, L. Morellon, G. Simon, J. M. De Teresa, J. A. Pardo, J. Arbiol and M. R. Ibarra, **Phys. Rev. B. 79, 014431 (2009)**.

[382] X. J. Liu, X. Liu and J. Sinova, **Phys. Rev. B. 84, 165304 (2011)**.

[383] V. V. Rylkov, S. N. Nikolaev, K. Yu. Chernoglazov, V. A. Demin, A. V. Sitnikov, M. Yu. Presnyakov, A. L. Vasiliev, N. S. Perov, A. S. Vedeneev, Yu. E. Kalinin, V. V. Tugushev and A. B. Granovsky, **Phys. Rev. B. 95, 144202 (2017)**.

[384] Y. H. Cheng, R. K. Zheng, Hui Liu, Yong Tian and Z. Q. Li, **Phys. Rev. B. 80, 174412 (2009)**.

[385] T. Miyasato, N. Abe, T. Fujii, A. Asamitsu, S. Onoda, Y. Onose, N. Nagaosa and Y. Tokura, **Phys. Rev. Lett. 99, 086602 (2007)**.

[386] S. R. Kodigala, Chapter 6 - Electrical Properties of I-III-VI$_2$ Compounds, in: K. Subba Ramaiah (Ed.) Thin Films and Nanostructures, **Academic Press, 319 (2010)**.

[387] J. Mao, J. Shuai, S. Song, Y. Wu, R. Dally, J. Zhou, Z. Liu, J. Sun, Q. Zhang, C. dela Cruz, S. Wilson, Y. Pei, D. J. Singh, G. Chen, C-W. Chu and Z. Ren, **Proceedings of the National Academy of Sciences, 114, 10548 (2017)**.

[388] B. Chamlagain, Q. Li, N. J. Ghimire, H-J. Chuang, M. M. Perera, H. Tu, Y. Xu, M. Pan, D. Xaio, J. Yan, D. Mandrus, and Z. Zhou, **ACS Nano 8, 5079 (2014)**.

[389] R. Fivaz, and E. Mooser, **Phys. Rev. 163, 743 (1967)**.

[390] L. A. D. Irvine, A. B. Walker, and M. J. Wolf, **Phys. Rev. B 103, L220305 (2021)**.

[391] M. Zhang, X. Zhang, L.-Y. Huang, H.-Q. Lin, and G. Lu, **Phys. Rev. B 96, 195203 (2017)**.

[392] P. A. Mante, C. C. Stoumpos, M. G. Kanatzidis, and A. Yartsev, **Nat. Commun. 8, 14398 (2017)**.

[393] K. Kaasbjerg, K. S. Thygesen, and K. W. Jacobsen **Phys. Rev. B 85, 115317 (2012)**.

[394] R. W. Ure, J. R. Bowers, and R. C. Miller, In Properties of Elemental and Compound Semiconductors, **Metallurgical Society Conferences 5, 254. New York, London: Interscience Publishers, 1960**.